AD 740903

FUNDAMENTAL STUDIES IN THE USE OF SONIC POWER FOR ROCK CUTTING

Karl F. Graff

The Ohio State University
Research Foundation
Columbus, Ohio 43212

ANNUAL TECHNICAL REPORT

December, 1971

NATIONAL TECHNICAL
INFORMATION SERVICE

Sponsored By
Advanced Research Project Agency
ARPA Order No. 1979 Amend. 2
Program Code 1F10

D D C
RECEIVED
APR 20 1972
C

Monitored By
U.S. Bureau of Mines
Twin Cities Mining Research Center
Twin Cities, Minnesota

Best Available Copy

DISTRIBUTION STATEMENT A
Approved for public release;
Distribution Unlimited

Best
Available
Copy

Unclassified
Security Classification

14 KEY WORDS	LINK A ROLE	LINK A WT	LINK B ROLE	LINK B WT	LINK C ROLE	LINK C WT
Transducer						
Sonic Transducer						
Impact Drilling of Rock						
Intermittent-contact with Transducer						
Constant-frequency Power-supply						
Intermittent-crushing Action						
Sonic Energy Transmission						
Stored-energy in Resonant Systems						

Unclassified
Security Classification

Unclassified
Security Classification

DOCUMENT CONTROL DATA - R & D

(Security classification of title, body of abstract and indexing annotation must be entered when the overall report is classified)

1. ORIGINATING ACTIVITY (Corporate author)

The Ohio State University Research Foundation
Columbus, Ohio 43212

2a. REPORT SECURITY CLASSIFICATION
Unclassified

2b. GROUP

3. REPORT TITLE

Fundamental Studies in the Use of Sonic Power for Rock Cutting

4. DESCRIPTIVE NOTES (Type of report and inclusive dates)
Annual Report 12-30-70 to 12-30-71

5. AUTHOR(S) (First name, middle initial, last name)

Karl F. Graff

6. REPORT DATE
December 30, 1971

7a. TOTAL NO. OF PAGES
225

7b. NO. OF REFS
37

8a. CONTRACT OR GRANT NO
H0210010

b. PROJECT NO
1579

c.

d.

9a. ORIGINATOR'S REPORT NUMBER(S)

9b. OTHER REPORT NO(S) (Any other numbers that may be assigned this report)

10. DISTRIBUTION STATEMENT

Distribution of this document is unlimited

11. SUPPLEMENTARY NOTES

12. SPONSORING MILITARY ACTIVITY
Advanced Research Projects Agency
Military Geophysics Program
Washington, D.C. 20301

13. ABSTRACT

Preliminary studies in the penetration of rock faces with tools which are driven by sonic transducers, are reported in the system development section of this report. The high-power sonic transducers, which were developed in previous research programs, operate from fixed-frequency electrical supply systems, and are coupled to the tool by intermittent contact. Supply frequencies are in the 10 kHz range.

The system analysis portion of this report relates to two areas of fundamental investigation. A study of sonic tool impact on rock concludes that the use of a simple rigid-mass model of the impact tool is suitable; elastic wave-effects within the tool are not of primary importance if short tools are considered. A study of system interactions during sonic drilling describes stress levels and energy transfer into various types of work surfaces including rock. Results are also reported on experiments of tool impact on rock and on a sonic transducer tip.

DD FORM 1 NOV 65 1473

Unclassified
Security Classification

FUNDAMENTAL STUDIES IN THE USE OF SONIC POWER FOR ROCK CUTTING

Karl F. Graff
Principal Investigator (614)422-7920

The Ohio State University
Research Foundation
Columbus, Ohio 43212

ANNUAL TECHNICAL REPORT

December, 1971

Contract No. - H0-210010
Effective Date of Contract - December 30, 1970
Contract Expiration Date - December 30, 1971
Amount of Contract - $50,000
Technical Project Officer - Patrick J. Cain, Twin Cities Mining Research Center, Twin Cities, Minnesota

Period Covered: December 30, 1970 to December 30, 1971

This research was supported by the Advanced Research Projects Agency of the Department of Defense and was monitored by the U.S. Bureau of Mines, under Contract No. H0210010

The views and conclusions contained in this document are those of the authors and should not be interpreted as necessarily representing the official policies, either expressed or implied, of the Advanced Research Projects Agency or the U.S. Government.

PREFACE

This project on sonic rock cutting was sponsored by the Advanced Research Projects Agency and was monitored by U.S. Bureau of Mines, Twin Cities, Minnesota under Contract No. H0210010. James J. Olsen of the Twin Cities Mining Research Center was the ARPA Program Coordinator, with Patrick J. Cain of the Twin Cities organization acting as Project Officer. The work was initiated on December 30, 1970 and the first year of work completed on December 30, 1971.

The work was performed at The Ohio State University under the Research Foundation Project RF-3173. The work was done in the Departments of Welding Engineering and Engineering Mechanics. Dr. Karl F. Graff, Professor of Engineering Mechanics, was project supervisor and in charge of the System Analysis phase of work. Charles C. Libby, Assistant Professor of Welding Engineering, was in charge of the System Development phase of work. Ting-yu Lo and Tsai-chuang Ma, Graduate Research Associates in Engineering Mechanics, worked in the area of System Analysis. Gordon Smith and Gary Streby, Laboratory Technicians, worked in the area of System Development.

SUMMARY

Developments in powers sonics at The Ohio State University have led to a number of applications of industrial interest, including metal deformation, grinding and drilling. The development of high frequency (10 kHz), high power (12 kW) transducers, a unique means of impact coupling energy transfer and the results of preliminary drilling tests on concrete have shown that the application of sonics for rock cutting may be of considerable practical interest. The objective of the first year of work was to construct the hardware for, and to carry out, sonic rock drilling tests in the laboratory and, further, to accompany this work by the necessary fundamental studies of the sonic parameters to enable process improvement to be done.

Thus, the work on sonic rock cutting was divided into two parts, System Development and System Analysis. In the first part, a piece of apparatus was developed for performing sonic drilling tests. An extensive series of tests was then performed in which various sonic drilling tools were designed and tested and the influence of changes in excitation voltage and static force on drilling were assessed. Tests on achieving optimum drilling by varying the parameters of no load, low voltage resonance, excitation voltage and static force were also conducted. In the second part, System Analysis, analysis and experiments on tool-rock and tool-rod impact, transducer characteristics and the sonic interaction process were carried out. The specific aspects of the work done in System Development and Analysis is summarized in this report.

System Development

The sonic power laboratory equipment, instrumentation and power supplies which are illustrated in Part I: System Development, were applied to the impact-cutting of limestone rock and to the analysis of various aspects of sonic-impact cutting of rock.

The impact mode of rock penetration described herein utilizes a piezoelectric transducer (Model P-11) impacting a relatively short tool for intermittently fracturing and crushing the work surface. A static force is applied externally to the transducer at the transducer node.

The energy necessary for each successive impact of the transducer with the tool is drawn from the elastic energy stored in the resonant structure of the transducer. Electrical power supplied from a source of high-frequency electrical energy maintains the energy storage level. The energy witndrawal is accomplished in very short intervals during impacts, occurring several hundred or thousand times per second. The energy replacement occurs between impacts. By this means, it is possible to supply the input energy to the transducer at a fixed frequency.

Penetration rates up to eight inches per minute are attained with one-inch diameter tools. Parameters wich optimize penetration rates have been measured and are described. These parameters include initial resonant frequency of the transducer, power supply frequency, externally applied static force and excitation level of the transducer. Increasing the length of the acoustic transmission line solidly mounted to the transducer, and the effect on penetration rate were explored, with transmission lines up to 40 inches in length. The effect of tool geometries were investigated and relative penetration rates are included for tools of differing cutting face geometries and different masses.

System Analysis

In the impact coupling means of sonic energy transfer, the cutting tool impacts and rebounds from the vibrating transducer tip and then impacts and rebounds from the rock surface, with this a continuing sequence. In obtaining a fundamental understanding of sonic rock cutting, each of these events must be understood separately, as well as the interaction of these events, with the parameters of voltage, static force and transducer energy in the overall process. The work in Systems Analysis, reported in Part II of this report, Sections 1 through 6, is aimed at providing as many answers as possible to these questions.

A great deal of effort was put into the tool-rock impact stage of impact coupling. Thus, in Section 1, a purely theoretical analysis of the sonic impact tool on rock is reported. The results of the analysis provided the justification for modeling the tool as a rigid mass, instead of an elastic body, insofar as tool impact on rock is concerned. In Section 2 of the report, various simple impact situations are analyzed from the standpoint of wave transmission into rock.

In Section 4, the results of an experimental study of sonic tool impact on rock are reported. A special spring-gun apparatus was constructed capable of launching sonic tools into single impacts with rock at velocities up to 600 inches per second. In this work, the incident and rebound velocity of impacting sonic tools was measured by means of photocells. The resulting energy loss for the rock, as well as damage for the rock was determined for various sonic tool configurations.

Section 5, reports work conducted on the tool-rod (or transducer tip) stage of impact coupling. This work was largely experimental and again the impact apparatus used for tool-rod impact was used. The purpose of the work was to determine the influence of the local contact geometry at the tool-rod interface on the coefficient of restitution of the tool. Although the impacts were on a stationary rod, and not on a vibrating transducer tip, the information on the impact characteristics is applicable to the sonic case.

In Section 3, an extensive study of the vibrations, energy storage and loss characteristics of the sonic transducer is reported. The importance of these characteristics in impact coupling follows. A single tool-transducer tip impact removes a certain percentage of the total stored energy in the transducer. Hence, knowledge of transducer energy capacity is necessary in analyzing impact coupling. Also important is the speed of recovery of the transducer to a transient energy removal. This aspect is determined by the Q (quality factor) of the device. Extensive experiments were conducted on determining the energy capacity and Q of the transducer, and also on determining temperature rise and frequency shift during operation. Some tests were also conducted on the energy removal during tool impact, with this work supplementing that reported in Section 5.

Finally, in Section 6, a qualitative description of the overall sonic interaction process was given. This brought in the parameters of drive voltage, energy level, tip vibration and static force. It was shown how variations in the static force and voltage parameters affected rates and energy levels of sonic impact, and how the unloaded transducer energy capacity and Q-factor governed impact coupling under load.

Conclusions and Future Work

The major conclusion of the first year of work is that power sonics offers a potentially practical method of rock drilling and cutting on a major scale. This possibility has resulted due to the development of powerful transducers and the impact coupling technique of energy transfer. This is in contrast to the previously existing situation in ultrasonic drilling, where low power transducers and the slurry drilling principle generally limited applications to special cases of machining irregular shaped holes in brittle materials. It was further shown that the rather complex sonic rock cutting process could be subjected to rational analysis through selected experiments and theoretical calculations of the stages of impact coupling and of the general interaction problem.

Future work should be directed toward developing sonic cutting configurations directly amenable to tunneling applications, and should include techniques for layer cutting, for slot cutting and for spalling off thin layers of rock. Further, the work should be done on hard and medium hard rock grades. The method of investigation should continue to be along the lines of hardware development and basic studies of the system parameters.

TABLE OF CONTENTS

	Page
INTRODUCTION	1
PART I: SYSTEMS DEVELOPMENT	5
1. SONIC POWER LABORATORY FACILITIES	7
2. SONIC IMPACT DRILLING	18
3. LONG TRANSMISSION LINES	28
4. OPTIMIZING TRANSDUCER OUTPUT	40
PART II: SYSTEM ANALYSIS	59
1. ANALYSIS OF TOOL IMPACT ON ROCKS	61
2. STRESSES DEVELOPED DURING SONIC IMPACT	77
3. VIBRATIONAL CHARACTERISTICS OF A SONIC TRANSDUCER	96
4. TOOL IMPACT ON ROCK	147
5. TOOL IMPACT ON A TRANSMISSION LINE	166
6. A DESCRIPTION OF THE SONIC INTERACTION PROCESS	184

LIST OF TABLES

		Page
I	Impact Drilling Test Using Cylindrical-Shaped Flat-Faced Impact Tools	25
II	Impact Drilling Test Using Cylindrical-Shaped Flat-Faced Impact Tools	26
III	Impact Drilling Test Using Tools Illustrated in Figure 21	27
IV	P-11 Transducer, with Various Length Transmission Lines, Impact-Drilling Into Limestone Rock with Two Types of Short Tools	38
V	P-11 Transducers in Impact-Mode with Flat-Faced Tools	48
VI	P-11 Transducers in Impact-Mode with Flat-Faced Tools	49
VII	Penetration Rate Data on P-11 Transducers with 1" Flat-Faced Tools in Impact Mode on Limestone	55
1-1	Comparison of Impact of Elastic and Rigid Tools	69
1-2	Comparison of Impact of Elastic and Rigid Tools	69
3-4.1	Strain at Various Power Levels	127
3-4.2	Tip Acceleration at Various Power Levels	129
3-4.3	The Constant D for Various Power Level Strain Data	130
3-4.4	The Constant D from Acceleration Data	130
3-4.5	Comparison of the Different D Values	131
3-4.6	Displacement, Strain and Acceleration in the Transducer	131
3-4.7	Comparison of Theoretical and Experimental Stored Energies	133
3-5.1	Q-Factor for Different Tests	135
3-6.1	Percentage of Energy Removal After Impact and Stored Energy Recovery Time After Impact	146

LIST OF TABLES (Continued)

		Page
4-1	Stress Levels of Mahban's Experiment and Corresponding Incident and Rebound Velocity of a One-Dimensional Elastic Tool	153
5-1	Percentage of Rebound Energy from the Line	172
5-2	Values of Re for Three Different Transmission Line Tip Geometries	179

LIST OF FIGURES

		Page
1	Variable-frequency 10 kW broad-band electronic power-supply system with manually selected frequency. Meters are shown at right	8
2	Fixed-frequency, 100 kW, 9720 Hz motor-generator power supply. The 1200 rpm, 60 Hz driving motor on the left is of the synchronous type; therefore, the output frequency of the 3600 rpm generator is fixed regardless of load	9
3	Machine shop facilities in which transducers, jigs, fixtures are prepared for sonic power research studies	10
4	Variable-frequency, portable, 900 W power supply with manual control of driving frequency, on the right is a 15 HP piezoelectric transducer, rated [illegible] V at 10,000 Hz, model P-11C1	11
5	The electronic equipment for measuring resonant-frequency, figure of merit Q, and band width of piezoelectric transducers is illustrated. Variable-frequency sweep-frequency generator Dranetz impedance-admittance meter, X-Y plotter and frequency meter are shown here	12
6	Three P-11 transducer bodies, illustrating minor modifications. The basic design on the right has a 1/2 wave-length horn and a 1/2 wave-length long center-bolt. The P-11C incorporates a 2" long spacer into the horn body, thus shortening the center-bolt. The P-11C1 incorporates a 1/2 wave-length transmission line	14
7	The basic P-11C design transducer has been disassembled and all parts are shown in this exploded view	15
8	P-7A transducer drawing showing typical cross-section of the P-7 and P-7B types	16
9	Typical cross-section of P-11 transducer illustrating concentric ring construction which is responsible for hydraulic prestress on piezoelectric driving elements	17
10	Sonic motor-generator configuration for testing transducers. Two-P-11 transducers are coupled solidly together at the anti-nodes or working tips. The lamp	

LIST OF FIGURES (Continued)

		Page
	bank constitutes an electrical load to absorb the MG set output	19
11	Model P-31 transducer designed to deliver 30 kW continuously at a frequency of about 10,000 Hz	20
12	The console utilized for rock drilling is shown at the right. The P-11C transducer is supported at the node as shown in Figure 13. Instrumentation is shown at the left	21
13	Detail of P-11 transducer support is illustrated. See Figure 12 for overall assembly	22
14	A series of flat-ended cylindrical elements used as the penetrating tool for impact-mode rock drilling by sonic energy. Tables I and II include penetration rate data with these tools. Figure 15 illustrates alignment means used	23
15	The tools illustrated in Figure 14 are aligned with the tip of the driving transducer by a pin and socket arrangement illustrated here	24
16	The impact tools illustrated here are replacements for the cylindrical tools in Figures 14 and 15. These modifications in tool geometry were tested for penetration rate in limestone	29
17	Holes drilled into limestone by using cylindrical, flat-faced tools in the impact-mode driven by 10 kHz transducer. Figure 18 illustrates the back of the block, corresponding to the hole location pointed out above	30
18	Fracture of limestone block during penetration by impact-mode operation of flat-faced tool. See Figure 17 for front view of block	31
19	Fracture of Limestone rock during penetration by impact-mode operation of flat-faced tool. The wall of the hole drilled by the cylindrical tool has been blackened for clarity	32
20	Short disc-like tool with holes drilled in its periphery. Table I lists penetration data with this tool	33

LIST OF FIGURES (Continued)

		Page
21	Stem-type tool tested for penetration of limestone by impact-mode. Table III lists drilling information on this tool design	34
22	Model P-11C transducer with thumb-tack accelerometer fixed to free end by epoxy cement. Data in Figure 23 was prepared using this assembly	35
23	No-load acceleration amplitude versus frequency of supply voltage at terminals of P-11 transducer. Note vertical dotted line describing locus of resonant frequency points. This chart illustrates the variation in transducer resonant frequency caused by changes in terminal voltage	36
24	Overall view of console, P-11 transducer, and blocks of limestone used in the study of impact-penetration with long transmission lines	37
25	Detail view of P-11 transducer mounting in console illustrated in Figure 24	37
26	Detail view of work piece and transmission lines, shown in the overall view of Figure 24	37
27	Chart illustrating the impact-mode limestone-penetration rate in inches per minute, with sonic transmission lines of 10, 20, 30 and 40" in length. A P-11 transducer was used with an initial resonant frequency of 10,070 Hz. Power supply frequency 10,054 Hz. See Figure 24 for test assembly. See Table IV for detailed test data.	39
28	P-11 transducer characteristic curves used to determine optimum operation condition under impact-load, with 10,054 Hz fixed-frequency power-supply. Initial transducer resonant frequency versus terminal voltage for various static forces	41
29	Variations in transducer no-load resonant frequency due to voltage, related to transducer optimum operating condition. F_V and F_R are related for one voltage, one value of F_i and one static force. See also Figure 31	42
30	Extrapolated data relating F_V or change in transducer no-load resonant frequency, to the applied terminal voltage E. Refers to model P-11 transducer	43

LIST OF FIGURES (Continued)

		Page
31	Similar to Figure 29, but illustrating two values of F_i and the corresponding change in static force for optimum operation. Values of F_V are the same for both transducers, but F_R values differ. See Figure 32 to relate F_R to static force and voltage	44
32	Extrapolated data relating F_R to static force for various terminal voltages. The positive values of F_R shown here, indicate that the optimum operation of the transducer may be at a frequency higher than the no-load resonant frequency F_V at that voltage	45
33	Power input in watts versus static force in a lightly loaded P-11 transducer in impact-mode of operation using flat-faced tools on limestone rock. Power supply is fixed frequency 10,054 Hz. F_i is the initial resonant frequency of the transducer measured at 3 V, no-load	46
34	P-11 characteristic curves used to determine optimum operating conditions under impact load with 10,054 Hz fixed frequency power supply. This is similar to Figure 28 but is plotted F_i versus static force for various voltages	51
35	Instrumentation utilized in the sonic power laboratory in making measurements of transducer resonant frequency variations	52
36	Static force versus penetration-rate in limestone by impact-mode with P-11 transducer at 1500 V and with a fixed frequency 10,054 Hz supply. A 1" diameter flat-faced impact tool was used. Curves show static force effects penetration rate independently of the optimum operating point of transducer	53
37	Static force versus penetration rate as optimum transducer conditions are changed to approximately match the static force indicated by Figure 36. Note the scale is doubled in Figure 37	54
38	Drilling tests performed in the preparation of data for Figures 36 and 37	56
1-1	Bilinear contact force-penetration relation	63

LIST OF FIGURES (Continued)

		Page
1-2	Impact of a sonic tool against rock	64
1-3	Time variations of penetration for flat tip tool with V_o = 520 in./sec.	71
1-4	Time variation of contact force for flat tip tool with V_o = 520 in./sec.	72
1-5	Incident and reflected stress wave at flap tip tool with V_o = 520 in./sec.	73
1-6	Time variation of penetration for flat tip tool with V_o = 78.67 in./sec.	74
1-7	Time variation of contact force for flat tip tool with V_o = 78.67 in./sec.	75
1-8	Incident and reflected stress waves at flat tip tool with V_o = 78 67 in./sec.	76
2-1	Incident, reflected and transmitted waves at a rod discontinuity	78
2-2	(a) Transmitted and (b) reflected stress wave ratio for various impedance matches	79
2-3	(a) Transmitted and (b) reflected power for various impedance matches	82
2-4	Semi-infinite rod driven by a harmonic forcing function	82
2-5	Force-deformation characteristics of a work-hardening load	84
2-6	Force and velocity and conditions in a rod in the presence of incident and reflected stress waves	84
2-7	Contact force at rod end for linear region of force-deformation curve	86
2-8	Contact force at rod end for bilinear portion of force-deformation curve	88
2-9	Complete loading and unloading end force behavior for bilinear curve	91

LIST OF FIGURES (Continued)

		Page
2-10	Force pulses required to reach F_p	91
2-11	Force-deformation curve of an elastic, perfectly plastic load	91
2-12	Force pulse for an elastic, perfectly plastic load	92
2-13	(a) Force-deformation curve for a slug-die configuration as shown in (b)	93
2-14	Force pulse acting on slug governed by force-deformation curve as shown in Figure 2-13 (a)	93
2-15	Force-deformation curve for rock	94
2-16	Force pulses on a rock load for various durations of the applied pulse	95
2-17	Equivalent rock penetration vs various force-deformation paths	95
2-18	Contact force F(o,t) and force-penetration for a series of three incident pulses	97
2-19	Contact force F(o,t) and force-penetration for a series of three pulses having twice the amplitude of those shown in Figure 2-18	98
3-2.1	Coordinates system and dimensions of a stepped horn	100
3-2.2	Displacement profile of the P-7 unloaded transducer (cos ωt = 1)	102
3-2.3	Strain profile of the P-7 unloaded transducer (cos ωt = 1)	104
3-2.4	Acceleration profile of the P-7 unloaded transducer (cos ωt = 1)	104
3-3.1	Block diagram of apparatus	107
3-3.2	Sound-proof box used for P-7 noise reduction	108
3-3.3	(a) Bruel and Kjear 1013 oscillator and (b) McIntosh 275 amplifier and ultrasonic matching transformer	109

LIST OF FIGURES (Continued)

		Page
3-3.4	Bandwidth effects of ultrasonic matching transformer	110
3-3.5	Power transfer for different Z on ultrasonic matching transformer	111
3-3.6	Power transfer as a function of Z setting on ultrasonic matching transformer	112
3-3.7	Temperature calibration of the thermocouple temperature meter	114
3-4.1	Q, temperature and resonance frequency change as function of operation time	116
3-4.2	Q as a function of input power	117
3-4.3	Q as a function of input power	118
3-4.4	Basic setup for transducer temperature measurement	119
3-4.5	Temperature and Q as function of operation time at 10 watts input power	120
3-4.6	Temperature and Q as function of operation time at 10 watts input power	121
3-4.7	Temperature and Q as function of operation time at 20 watts input power	122
3-4.8	Temperature and Q as function of operation time at 20 watts input power	123
3-4.9	Temperature and Q as function of operation time at 30 watts input power	124
3-4.10	Temperature and Q as function of operation time at 30 watts input power	125
3-4.11	Basic experimental setup for strain measurement	126
3-4.12	Typical strain output observed from oscilloscope	127
3-4.13	Basic experiment setup for acceleration measurement	128
3-4.14	Typical acceleration output observed from oscilloscope	128

LIST OF FIGURES (Continued)

		Page
3-5.1	View of plate-post hardware	134
3-5.2	Detail of thick plate transducer holder	134
3-5.3	Transducer mounted in an enclosed case	135
3-5.4	Sectional drawing of enclosed case	136
3-5.5	Mounting scheme for Dranetz test	137
3-5.6	A uniform distributed reaction around the flange to support the transducer	137
3-5.7	Transducer mounted on a silastic rubber plate	138
3-5.8	Transducer supported by two knife edges, the knife edge is placed beneath (a) the flange (b) the thread	139
3-5.9	Transducer supported by two knife edges	139
3-5.10	Transducer supported by two wires	140
3-6.1	Basic experimental set-up for impact studies	142
3-6.2	Impact on transducer tip showing sudden energy decrease. Each horizontal division = 10 millisecond Vertical scale = 0.2 volt/division	143-144
3-6.3	(a), (b) - Amplitude of tip velocity increasing after tool-transducer impact	144
3-6.4	The amplitude of the tip velocity as the transducer is turned on(a) and turned off (b)	145
4-1	Mahban's experiment and his bilinear contact force-penetration relation	148
4-2	Impact of a sonic tool against rock	148
4-3	Experimental set-up	150
4-4	Tools of various tip geometry	151
4-5	Dimensions of tools used in the experiments	152

LIST OF FIGURES (Continued)

		Page
4-6	Incident velocity-rebound velocity of a flat tip tool (Type A)	155
4-7	Incident velocity-rebound velocity of Type B tool	157
4-8	Incident velocity-rebound velocity of Type D2 tool	158
4-9	Incident velocity-rebound velocity of Type E1 tool	159
4-10	Effect of number of impacts on the rebound velocity for Type B tool	160
4-11	Effect of number of impacts on the rebound velocity for Type D2 tool	161
4-12	Impact zone after twenty-five impacts (V_o = 550 in./sec.)	162
4-13	Variation of maximum shearing stress, (normalized), with ρ and ζ	163
4-14	Impact zone condition at different number of impacts	164-165
5-1	Stress wave in the transmission line due to tool-line impact	168
5-2	Impact of tool and transmission line	168
5-3	Experimental set-up (a)	171
5-3	Schematic diagram of experimental set-up (b)	171
5-4	Tools	173
5-5	Stress pulse resulting from tool impact	175-176
5-6	Transmission line tip used in this experiment	176
5-7	Transmission line tip dimension and tip-transmission line assemblies	177
5-8	Stress waves from tool impact	178

LIST OF FIGURES (Continued)

		Page
5-9	Stress waves from tool impact	178
5-10	Incident velocity-maximum stress for Type 1 tool	180
5-11	Incident velocity-maximum stress for Type 3 tool	181
5-12	Incident-rebound velocity relationship for Type 1 tool	182
5-13	Incident-rebound velocity relationship for Type 3 tool	183
6-1	Schematic diagram of a full wavelength transducer showing displacement and stress distribution along the length	188
6-2	Several examples of transient changes in the energy level of a sonic transducer	190
6-3	(a) Transducer acted upon by the static force F_s and the impact force f(t). (b) Time distribution of the forces in the transducer	192
6-4	Rigid body motion (velocity) of a sonic transducer acted upon by static force and impact	193
6-5	Velocities of the impact tool in the transducer-load gap	194
6-6	Variations in impact rate due to variations in static force level	196
6-7	Impact and energy removal from a transducer at various stages of recovery from a previous impact	198
6-8	Sequences of steady-state impact at various energy levels	200
6-9	Influence on impact rate of a voltage increase (a) without and (b) with increases of static force	202
6-10	Influence of various voltage overdrive conditions on the rate of impact	203

INTRODUCTION

Background

Developments in power sonics at The Ohio State University in the last several years have led to a number of applications of potential industrial interest. Using large sonic transducers, applications to metal deformation and grinding processes have been under investigation, as well as uses in treating fresh concrete and in welding. Certain crude experiments in drilling concrete suggested that use of sonic power for rock cutting might be possible.

The particular aspects of the work at Ohio State that made it possible to consider sonic rock cutting were twofold. In the first instance, the construction of large transducers, such as a 10 kW device (a prototype of a 30 kW unit has been constructed), has made power levels available to be of potential use in rock cutting. Secondly, a unique impact coupling means of transferring energy from the transducer to the rock has been developed. In this method, a small cutting tool is interposed between the transducer and the rock that impacts repeatedly between the two surfaces, picking up energy when impacting the transducer tip and causing fracture and crushing when impacting a rock work surface.

Excepting for the above developments, the use of ultrasonics for drilling brittle materials is still not new. Ultrasonic slurry drilling of very hard and brittle materials, such as glass, ceramics and gem stones, has been in use for many years. However, such applications were, in general, at very low power levels (100 W) and occurred at low penetration rates (fractions of an inch per minute). Thus, while slurry drilling has been a most useful process in selected applications, its value in large scale drilling processes would be questionable.

On the other hand, the use of ultrasonics for rock cutting is also not new. Thus, Maurer [1] has suggested ultrasonics as one of a large number of novel methods of rock removal. However, in reviewing this possible method of cutting, only the slurry drilling principle was considered. In a report on rapid excavation by the National Research Council [2], ultrasonics was again one of a variety of methods considered for rock removal. At the time of the cited reports, low transducer power levels and the inefficiency of the slurry drilling technique did not make ultrasonic rock cutting appear to be one of the more promising methods.

On the other hand, in the previously mentioned rather crude tests at Ohio State, drilling rates of several inches per minute were noted for 1 1/2-inch diameter holes in concrete. In these tests, the 10 kHz model P-11 transducer (rated at 12 kW) with a half-wavelength extension was coupled into the work surface using a very light impact tool.

Although no effort was made to vary or optimize the many process parameters, such as excitation voltage and tool configuration, the results were of sufficient interest to form the basis for the present work on sonic rock cutting.

Description of the Present Program

The present program has, of course, the objective of applying sonic power to rock cutting. Within this framework, there are many potential cutting and drilling applications and there are many grades of rock to consider. Furthermore, there are the many basic complexities of the sonic rock cutting process. What was done in the first year of work was to strive for simplicity in terms of rock cutting configurations and rock grades considered. To this end, only the drilling of single, circular holes into rock was investigated and only a single, medium grade of rock (Indiana Limestone) was considered. This enabled major attention to be given to determining the influence of the sonic parameters on the drilling process.

The sonic parameters that influence drilling are several, and include the transducer itself (of which the stored elastic energy, tip vibration amplitude and Q (Quality factor) are of greatest interest), the drive voltage to the transducer, the static force applied to the device, the tool characteristics (mass and geometry) and the characteristics of the rock. The sonic drilling process is fairly complicated because these various parameters interact, so that a change of one, such as drive voltage will change the others.

In order to investigate the fundamentals of sonic rock cutting, the program was divided into Systems Development and Systems Analysis phases. The work in the development phase was aimed at the performance of actual sonic drilling tests on a laboratory scale. In this work, various tool configurations were used, and the parameters of drive voltage and static force were varied and the resulting effects on drilling rate noted. In the analysis phase of the work, both laboratory experiments and theoretical analysis was carried out on selected aspects of sonic drilling to obtain a fundamental understanding of the process mechanics. Work here included studies of single tool and impacts on rock and on the transducer tip, determination of the energy storage and Q of the transducer and analysis of tool impact on rock.

The presentation of the material in this report follows the division of the work. Thus, in Part I, Systems Development, the results on drilling tests and on investigations to achieve an optimum drilling condition are reported. In Part II, Systems Analysis, the several sections report on analysis of tool impact on rock, stresses developed during impact, the vibration characteristics of the transducer, experiments on tool-rock and tool-rod impact and on the general interaction of sonic parameters in drilling.

Future Work

In proposed future work on sonic rock cutting, two major changes are suggested. In the one case, different modes of sonic cutting should be investigated. This would include sonic means of kerf cutting and layer cutting and would, in general, be directed toward configurations applicable to tunneling operations. Secondly, emphasis should be placed on sonic cutting of hard and medium hard rock grades.

In other regards, the basic delineation of the work into the hardware-oriented Systems Development and the fundamentally-oriented Systems Analysis phases should be continued. This latter aspect is important because at this early stage of sonic rock cutting, a number of questions remain on the process parameters and the optimum combination of these parameters.

References

1. Maurer, W. C., Novel Drilling Techniques, pp. 44-49, p. 105, Pergamon Press, 1968. Also, more briefly, Maurer, W. C., "Potential Application of Novel Rock Disintegration Techniques in Mining," 31st Annual Mining Symposium, 1970.

2. Rapid Excavation, National Research Council, Committee on Rapid Excavation, E. P. Pfleider, Chairman, 1968. Available as Publication 1690, National Academy of Sciences, Washington, D.C.

PART I: SYSTEM DEVELOPMENT

CONTENTS

1. SONIC POWER LABORATORY FACILITIES
2. SONIC IMPACT DRILLING
3. LONG TRANSMISSION LINES
4. OPTIMIZING TRANSDUCER OUTPUT

PRECEDING PAGE BLANK

1. SONIC POWER LABORATORY FACILITIES

The equipment illustrated in this section of the report is located in the Sonic Power Laboratory, in the Welding Engineering Laboratories Building of The Ohio State University campus. Some of the equipment illustrated was made available because of prior research in the sonic power field, and other equipment was developed for this project.

The electronic power source illustrated in Figure 1 enables the 15 hp transducer, which is located out in the laboratory, to be excited at any one of a range of manually selected voltages and frequencies. Typically, the range of frequencies employed in this program is from 9,700 to 10,500 Hz. Voltages in the range of 1000 to 2000 were employed in the first half of the program but higher voltages have been utilized in the second half of this program.

The fixed-frequency supply illustrated in Figure 2 is capable of delivering up to 100 kW of electrical power, through aluminum conduit and electrical outlets, to various locations in the sonic power laboratory. The output-frequency of 9720 Hz on this generator is fixed; it does not vary with load.

The several electrical outlets located in the laboratory, which are used to distribute 10 kHz electrical power, may be connected either to the 9720 Hz motor-generator or to an older unit which develops a frequency of 10,054 Hz. This second unit is driven by a squirrel-cage induction motor and for this reason, a maximum of about 20% of its rating (50 kW) is all that is considered useful for constant-frequency applications at 10,054 Hz. Transformers are employed in the laboratory to raise the 220 volts, at which power is distributed, to that necessary for satisfactory performance of the transducers.

An alternate power source for portable use is illustrated in Figure 4. This is a broad-band electronic frequency-converter rated 500 W electrical output. The transducer supported by the author is a model P-11C-1 piezoelectric sonic transducer rated 15 hp, 10 kHz, 3200 V with a peak-to-peak tip movement of 0.003".

Equipment used to evaluate large transducers and to determine their no-load characteristics under low levels of excitation, is illustrated in Figure 5. With this equipment it is possible to obtain a circular or polar diagram representing a locus of vectors produced as input or driving frequency is varied. This circle diagram may be prepared for transducer reactance and resistance measurements, in which case the measuring instrument would be acting as an impedance meter; or the circle diagram may be prepared for conductance and susceptance measurements, in which case the instrument would be acting as an admittance meter. The Draneiz impedance-admittance meter is seen in the lower center of background. The X-Y plotter which makes a record of the measured quantities is in the foreground. The frequency monitor

PRECEDING PAGE BLANK

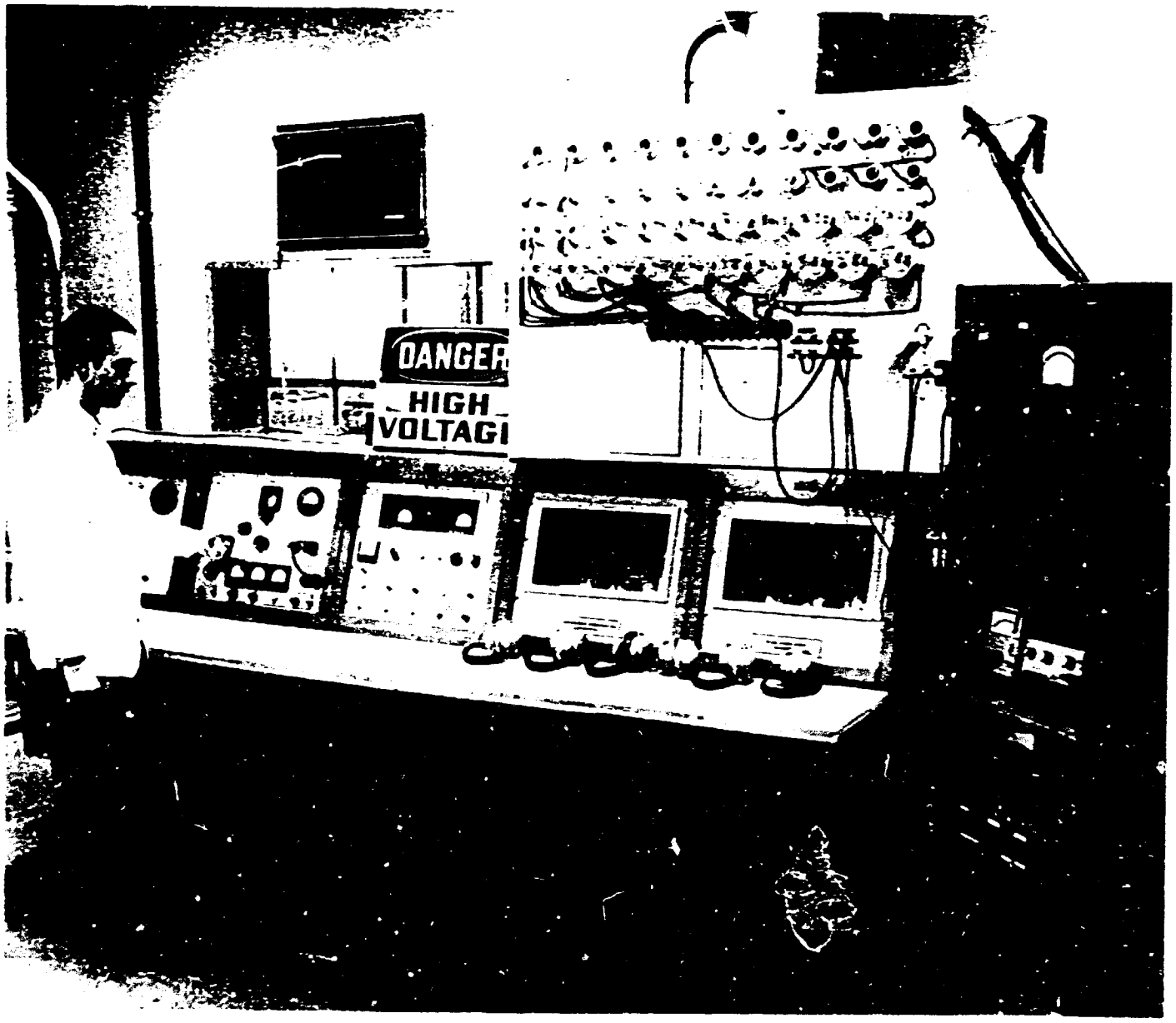

Figure 1 - Variable-frequency 10 kW broad-band electronic power-supply system with manually selected frequency. Meters are shown at right.

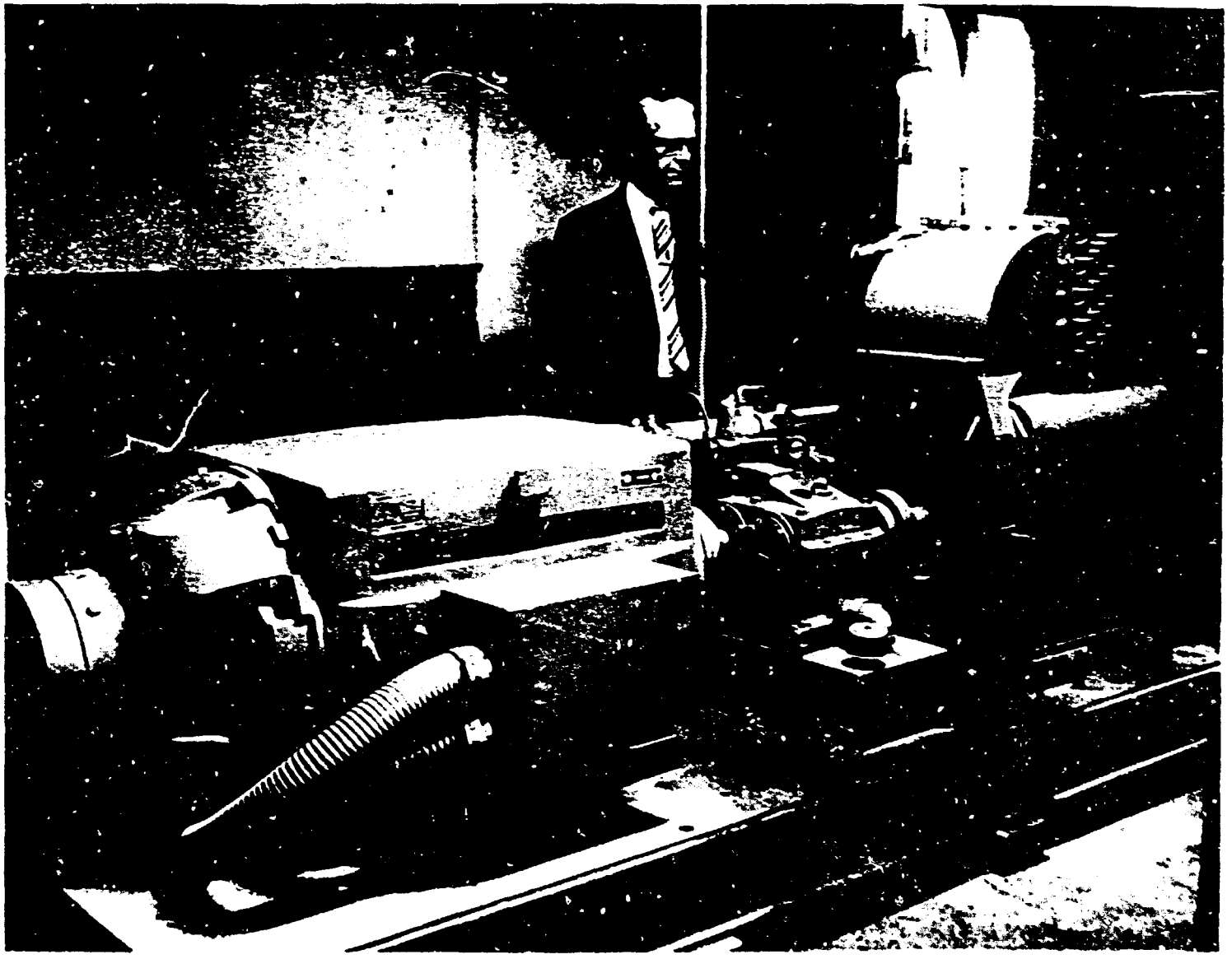

Figure 2 - Fixed-frequency, 100 kW, 9720 Hz motor-generator power supply. The 1200 rpm, 60 Hz driving motor on the left is of the synchronous type; therefore the output frequency of the 3600 rpm generator is fixed regardless of load.

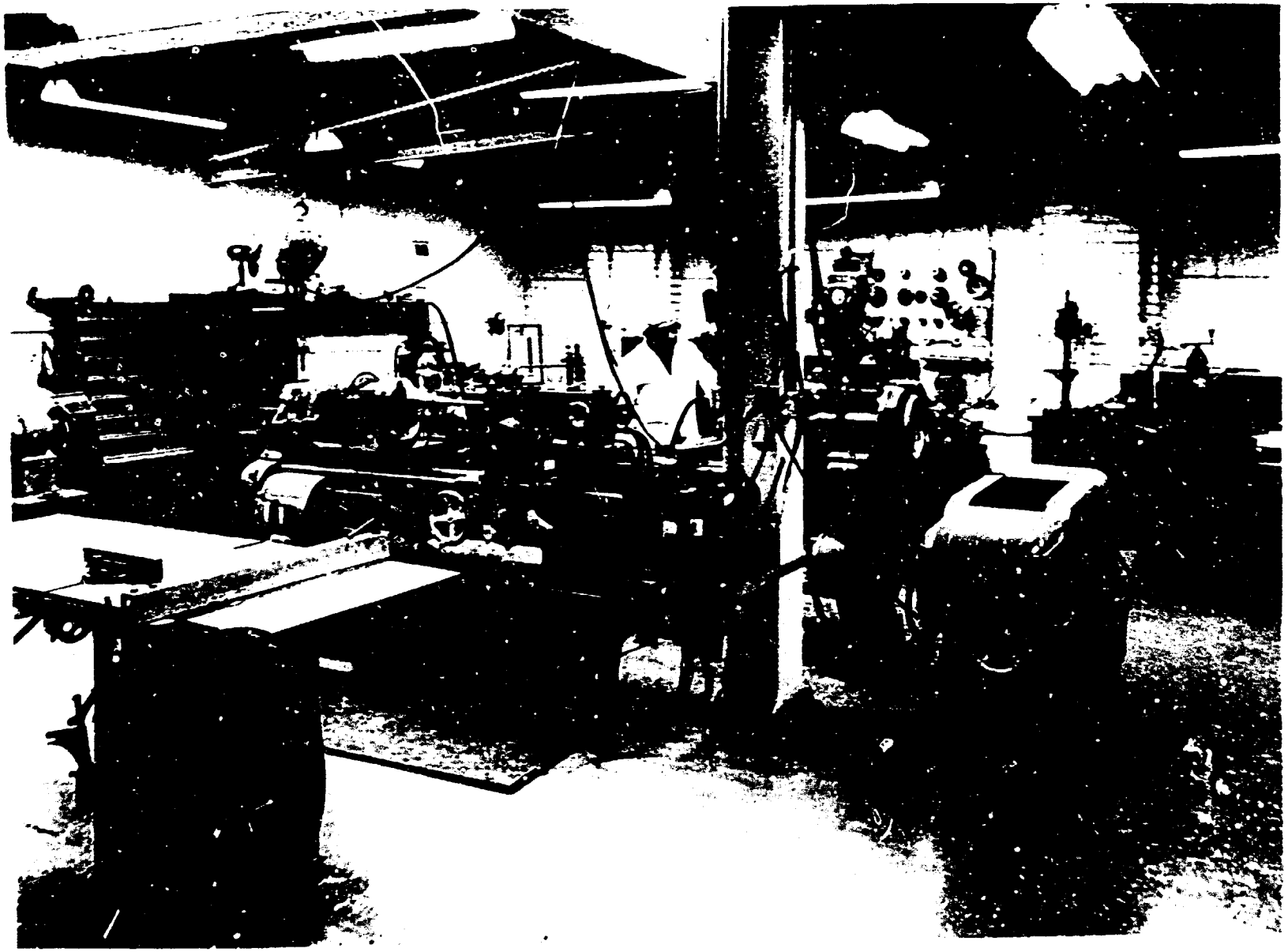

Figure 3 - Machine shop facilities in which transducers, jigs, fixtures are prepared for sonic power research studies.

Figure 4 - Variable-frequency, portable, 500 W power sypply with manual control of driving frequency. On the right is a 15 HP piezoelectric transducer, rated 3000 V at 10,000 Hz, Model P-11C1.

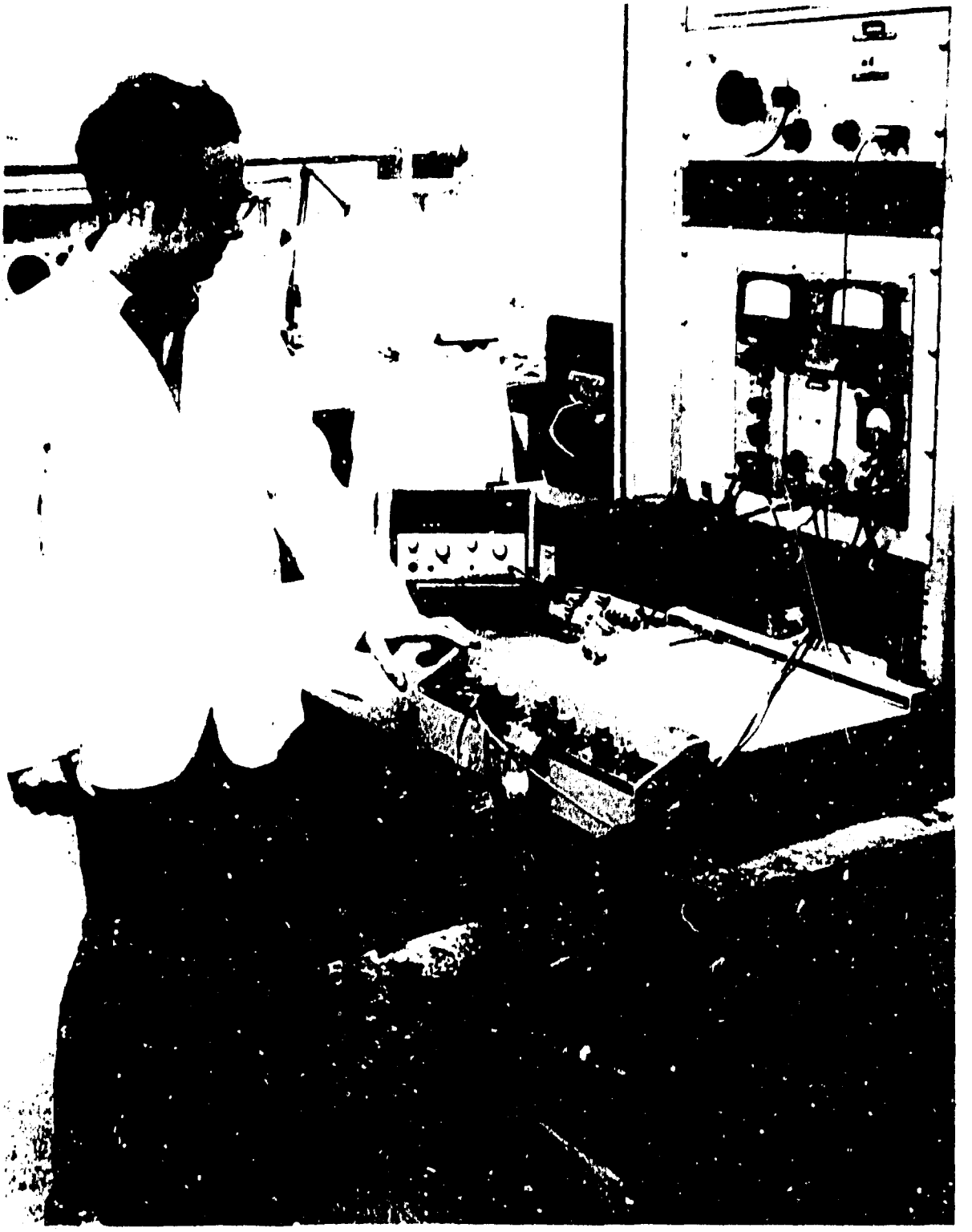

Figure 5 - The electronic equipment for measuring resonant-frequency, figure of merit Q, and band width of piezoelectric transducers is illustrated. Variable-frequency sweep-frequency generator Drametz impedance-admittance meter, X-Y plotter and frequency meter are shown here.

is at the left. The transducer, whose characteristics may be monitored, is typical of that shown in Figure 4.

Three models of the high-power sonic transducer known as a P-11 transducer, are illustrated in Figure 6. In each case, the full excitation of these transducers permits them to deliver up to 15 hp of vibratory energy at the tip (facing up in this illustration). The body or central structure of the transducers are shown here, the elements of the transducer assembly are shown in Figure 7.

The heart of the sonic transducer is shown in Figure 7 to be the piezoelectric rings which are shown mounted between rubber rings as a "packed crystal." The piezoelectric elements are located with at least one face in contact with an electrode and the other face in contact with the body of the transducer or "electrical ground." By applying an electric potential between the body of the transducer and the electrodes, the stack of piezoelectric crystals is excited. The crystals are thus in parallel electrically and in series mechanically. The excited transducer vibrates at its resonant frequency when excited with alternating voltages applied to these electrodes. When the supply frequency matches the transducer resonant frequency, a maximum capacity to do work results.

Much of the equipment illustrated in the preceding pages has been developed on previously sponsored research programs at The Ohio State University Sonic Power Laboratory. The research project EES 220, entitled "Development of Sonic and Ultrasonic Power Devices for Application in Highway Engineering," was active between 1962 and 1970. The final report on this work was made public in 1970 by the sponsor, The Ohio Department of Highways and the Federal Highway Administration. This two-volume report covers the development of the transducers utilized on this project. This development laid the foundation for the use of constant-frequency high-power sonic and ultrasonic transducer applications in the OSU Sonic Power Laboratory.

Between 1962 and the present time numerous industrial sponsors supported research in the Sonic Power Laboratory; this work is continuing. Sonic power applications thus supported have included cold-deformation or cold-heading of metals, hot-deformation of metals, penetrating building blocks for the construction industry, grinding and crushing both dry and slurry materials, cold-forming and welding of plastic materials, improving the engineering properties of fresh concrete as it is being laid, and grooving concrete surfaces with steel blades.

The development of the Model P-7 transducer, shown in Figure 8, was also carried out during this period. It is rated 380 W at 900 V and 10 kHz. The P-11 transducer of a larger size was also developed; an engineering drawing of which is shown in Figure 9. It is rated 15 kW at 3200 V 10 kHz nominal frequency. The accelerated life-test program which was utilized in the final stages of the transducer designs

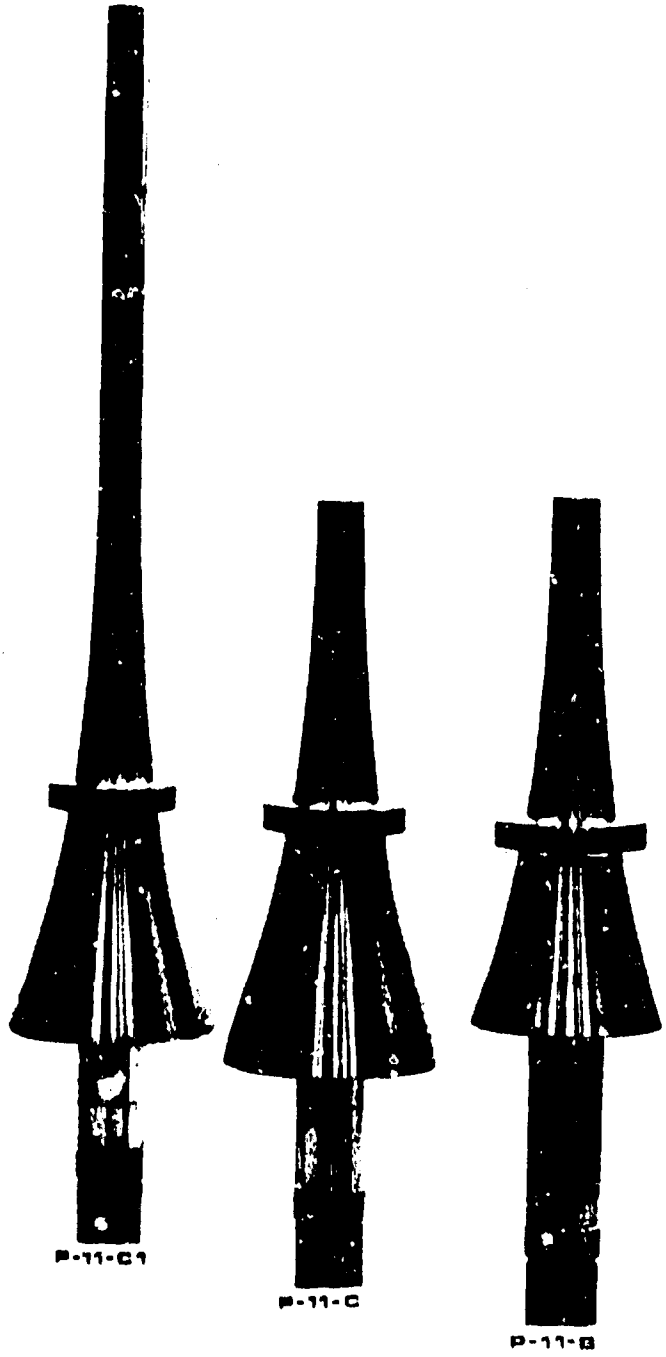

Figure 6 - Three P-11 transducer bodies, illustrating minor modifications. The basic design on the right has a 1/2 wavelength horn and a 1/2 wavelength long center bolt. The P-11C incorporates a 2-inch long spacer into the horn body, thus shortening the center bolt. The P-11C1 incorporates a 1/2 wavelength transmission line.

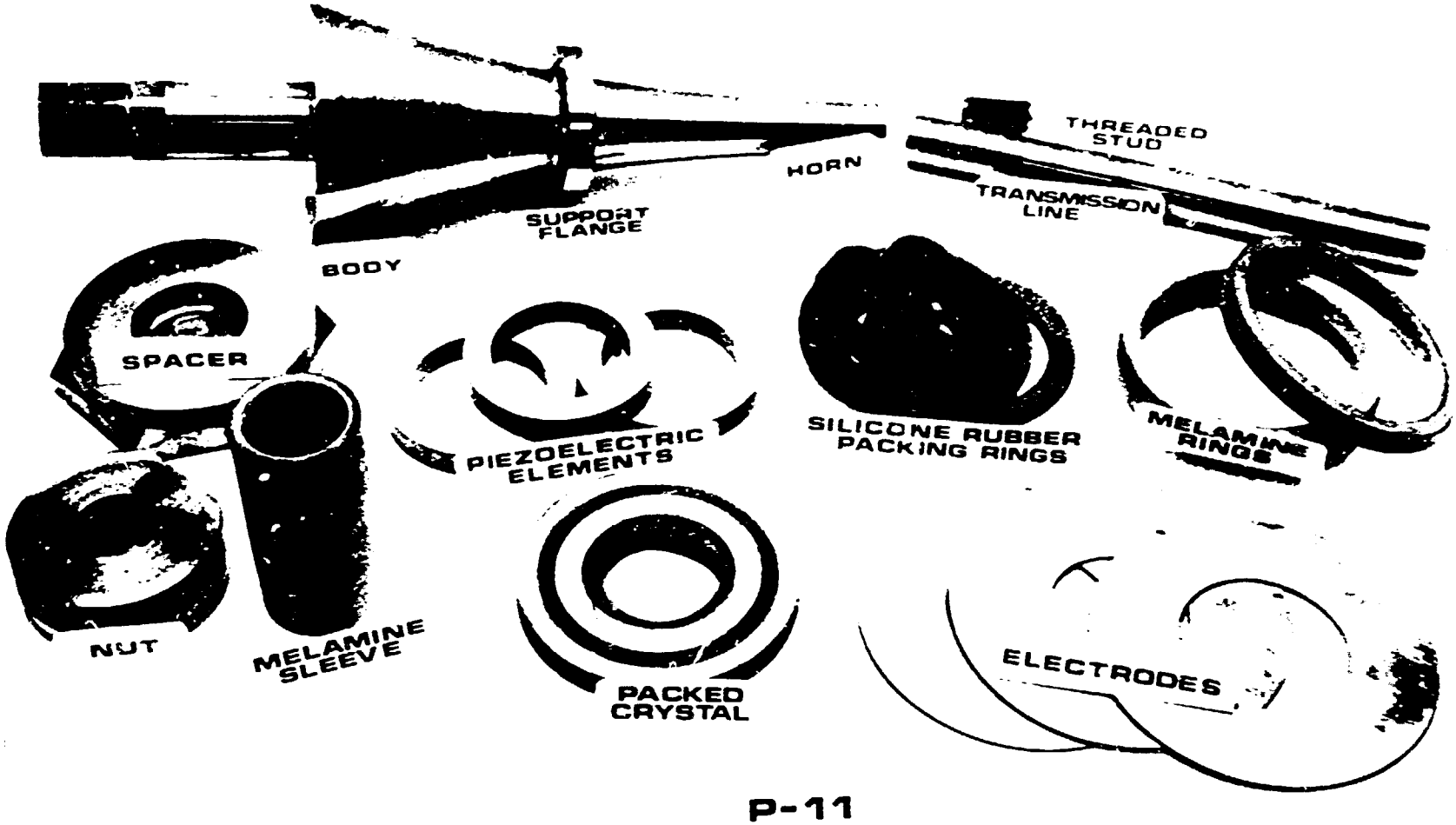

Figure 7 - The basic P-11C design transducer has been disassembled and all parts are shown in this exploded view.

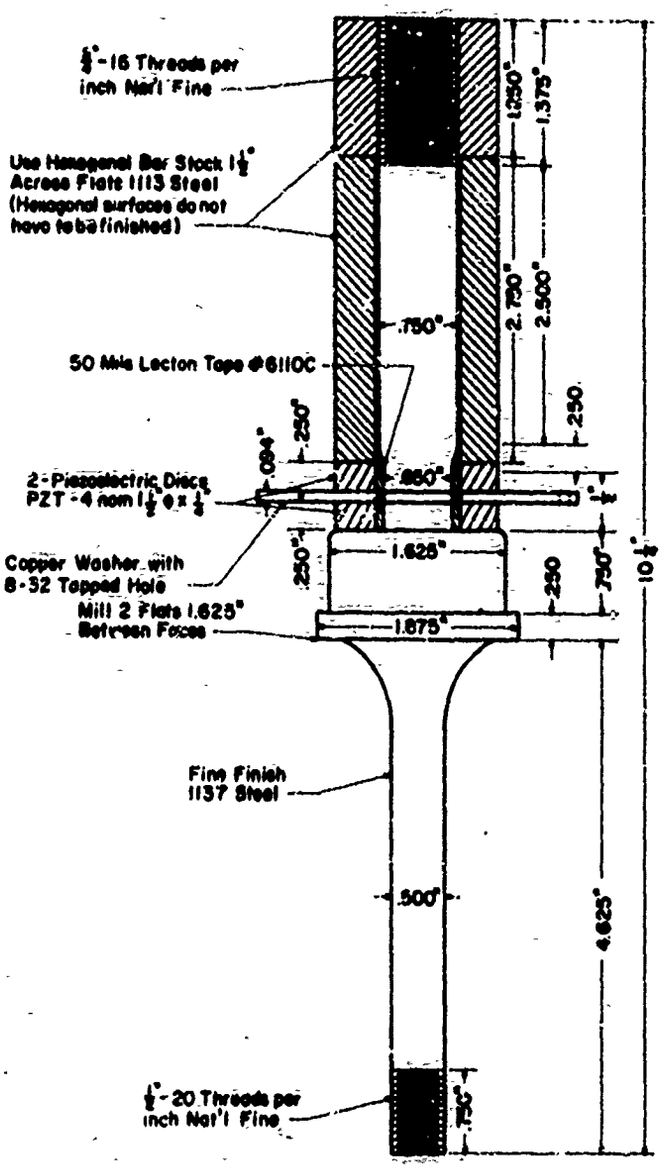

Fig. 8 - P-7A transducer drawing showing typical cross-section of the P-7 and P-7B types.

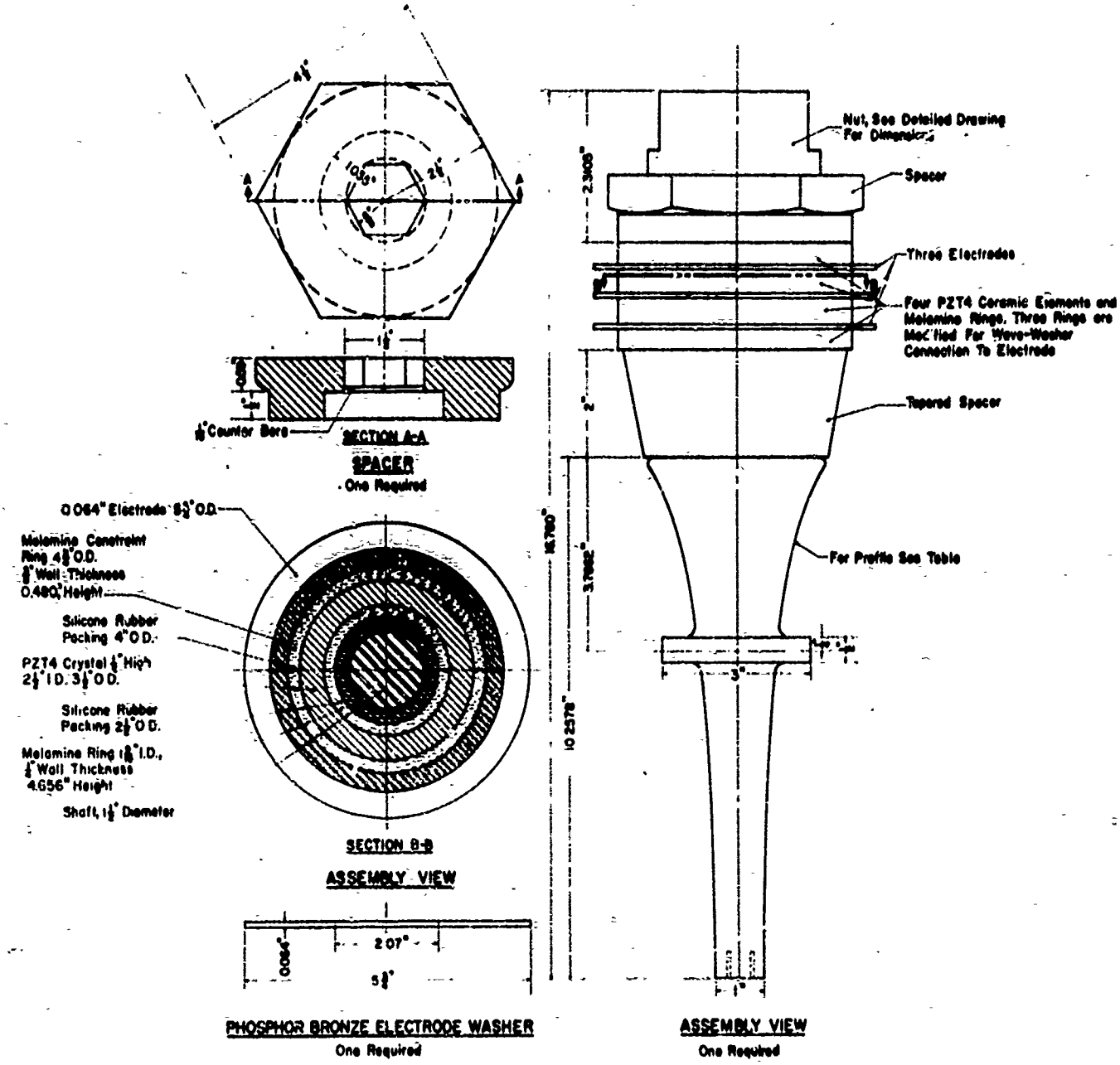

Fig. 9 - Typical cross-section of P-11 transducer illustrating concentric ring construction which is responsible for hydraulic prestress on piezoelectric driving elements.

is illustrated in Figure 10. Here we may see two Model P-11 transducers coupled together solidly, acting as a motor-generator set. The transducers resonate at the same frequency and one is connected to a power supply furnishing resonant frequency power to its terminals; the second transducer is connected to an electrical load, which in Figure 10 is a lamp band of 50 series-parallel connected 220 W bulbs. Finally, in Figure 11 is shown the prototype of a large, 30 kW transducer.

2. SONIC IMPACT DRILLING

The console assembly illustrated in Figure 12 shows the piezoelectric transducer, Model P-11, in position to do impact drilling. The instrumentation is shown at the left. The transducer is mounted to the console support plate, at the node of the transducer, by a rubber-lined clamp as seen in Figure 13.

The contact between the transducer (or its transmission line extension) and the work piece, is an intermittent contact tool of a cylindrical shape as shown in Figures 14 and 15. The tool bounces between the transducer tip and the work piece, crushing the brittle work surface and incrementally penetrating the rock face. The energy for the intermittent crushing action is supplied from the stored energy of the resonant transducer. The energy level is maintained by electrical energy input to the transducer during the interval between impacts.

The primary parameters which control the penetration rate caused by a specific tool configuration and a selected transducer rating, are, 1) the voltage or excitation amplitude applied at the transducer electrode terminals, 2) the frequency of this applied alternating voltage (as compared to the resonant frequency of the transducer) as the excited transducer is pressed against the work surface, and 3) the average static force (as contrasted to the dynamic force developed at the work surface) applied externally to the transducer in a direction which causes it to move toward the work surface. The dynamic forces which act to cause the tool to impact against the work surfaces, are a function of 1) the stored energy in the transducer, 2) the energy stored in the bouncing tool, and 3) the velocity of the tool as it moves between the transducer tip and the work surface in an impact mode.

In Tables I through III, these test parameters are illustrated. The transducer voltage is, of course, its excitation voltage as furnished from the frequency convertor or power supply. This impact energy is also monitored as kVA and power factor, or as kW input and as time of drilling. The depth of the hole and the volume of crushed rock are evidences of work done and the temperature rise of the transducer are evidences of transducer losses. In each table, the tool configuration, static force, initial resonant-frequency of the transducer and power-supply frequencies are listed.

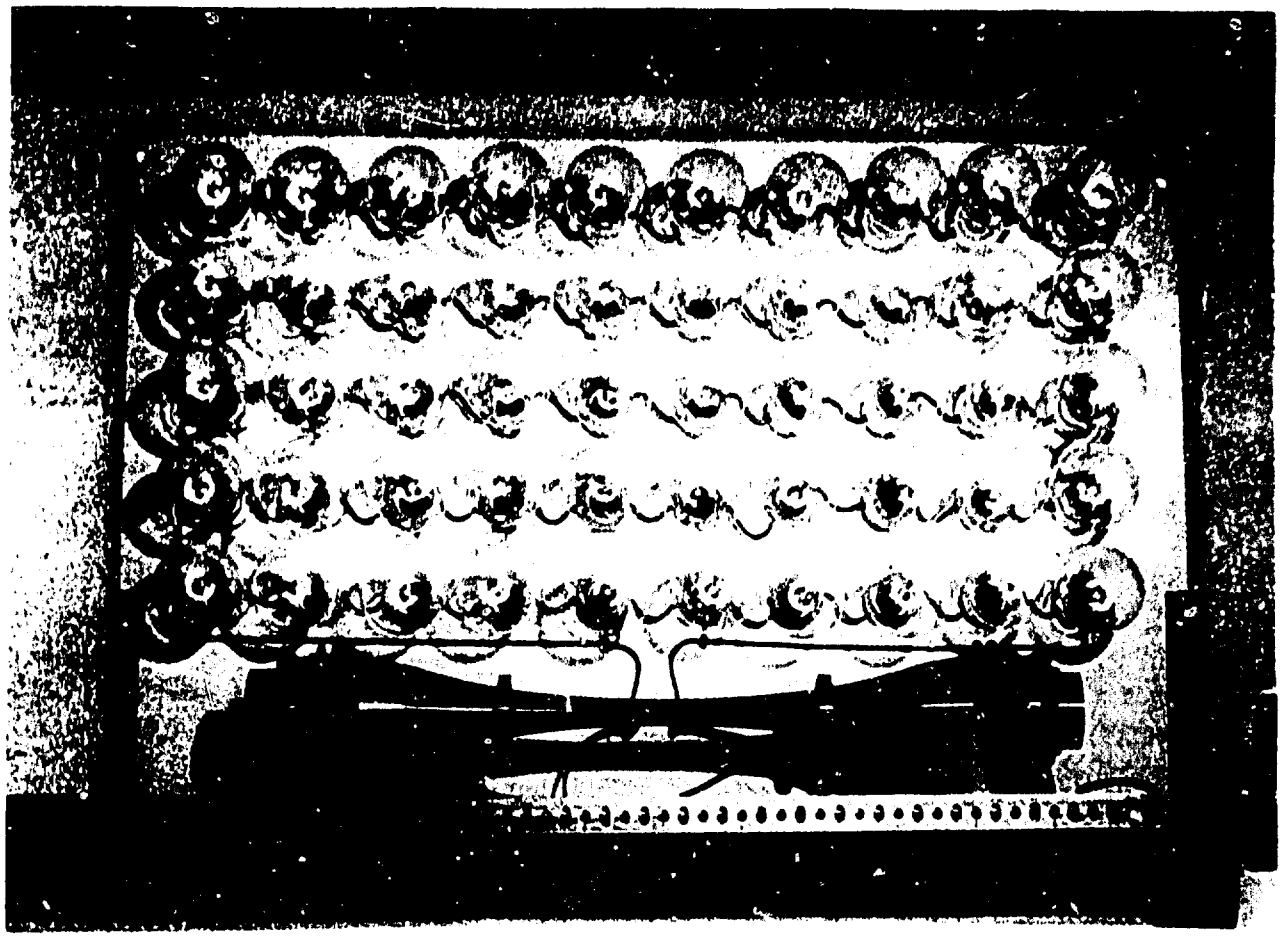

Figure 10 - Sonic motor-generator configuration for testing transducers. Two P-11 transducers are coupled solidly together at the anti-nodes or working tips. The lamp bank constitutes an electrical load to absorb the Mg set output.

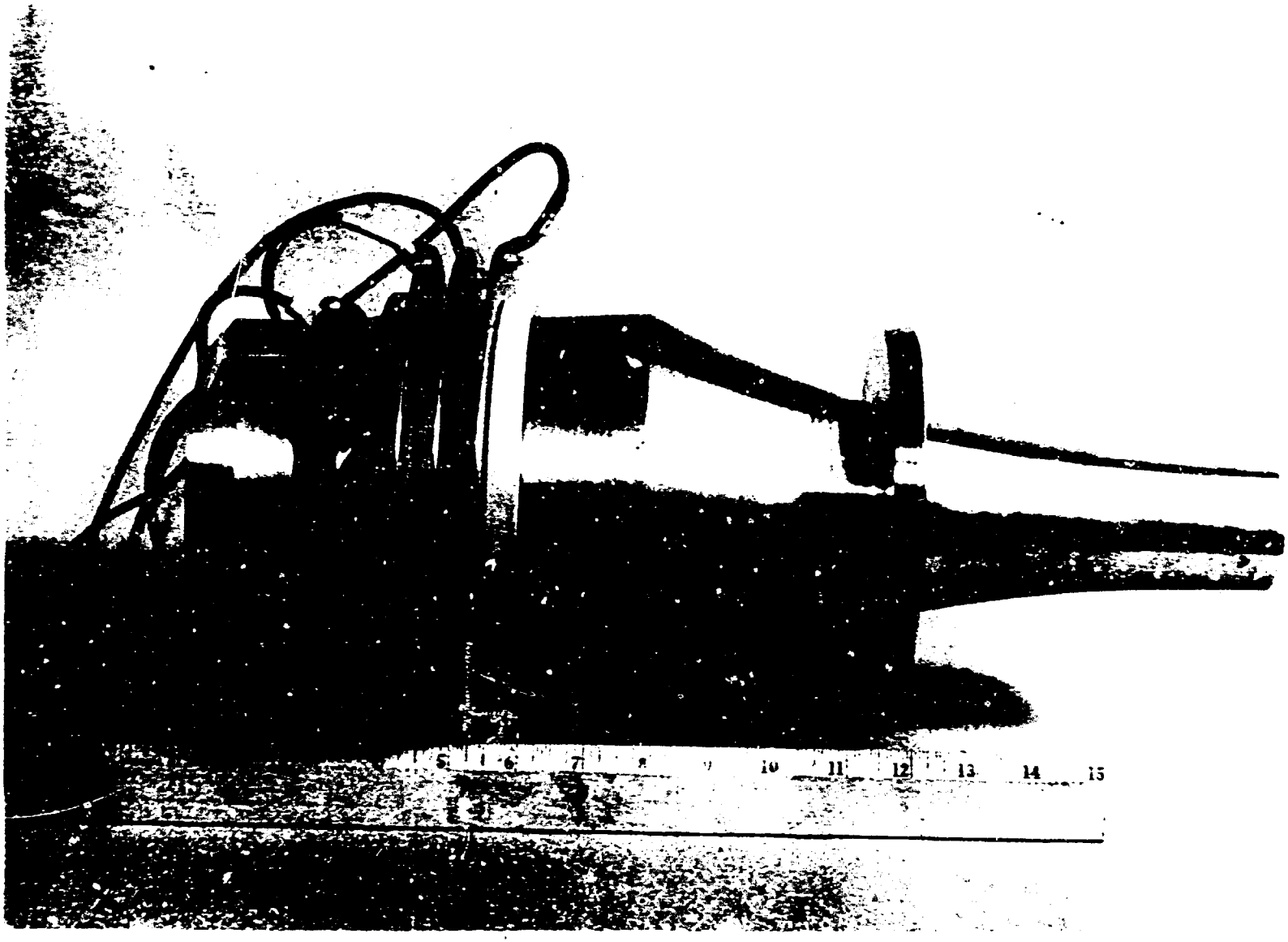

Figure 11 - Model P-31 transducer designed to deliver 30 kW continuously at a frequency of about 10,000 Hz.

Figure 12 - The console utilized for rock drilling is shown at the right. The P-11C transducer is supported at the node as shown in Fig. 13. Instrumentation is shown at the left.

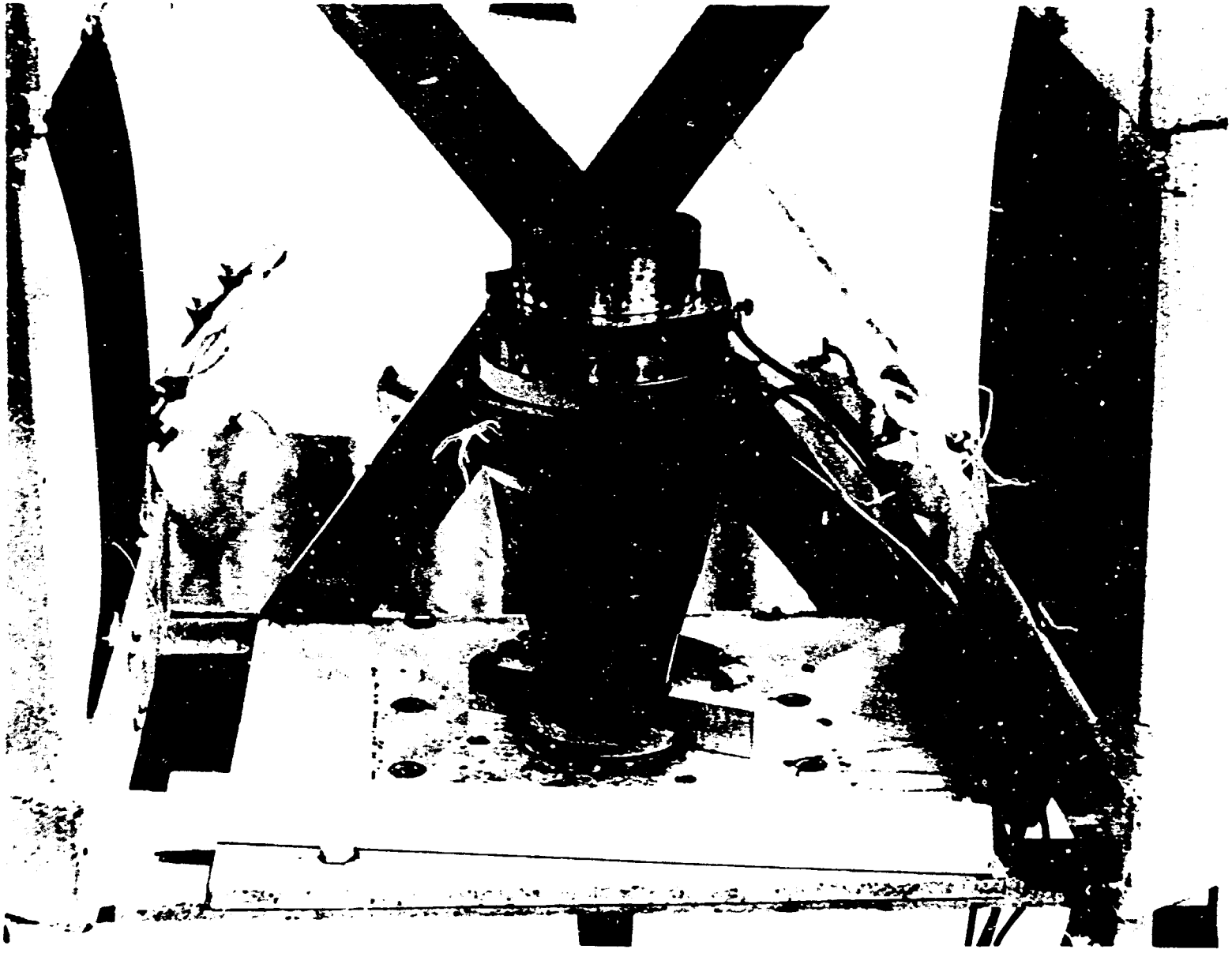

Figure 13 - Detail of P-11 transducer support is illustrated. See Fig. 12 for overall assembly.

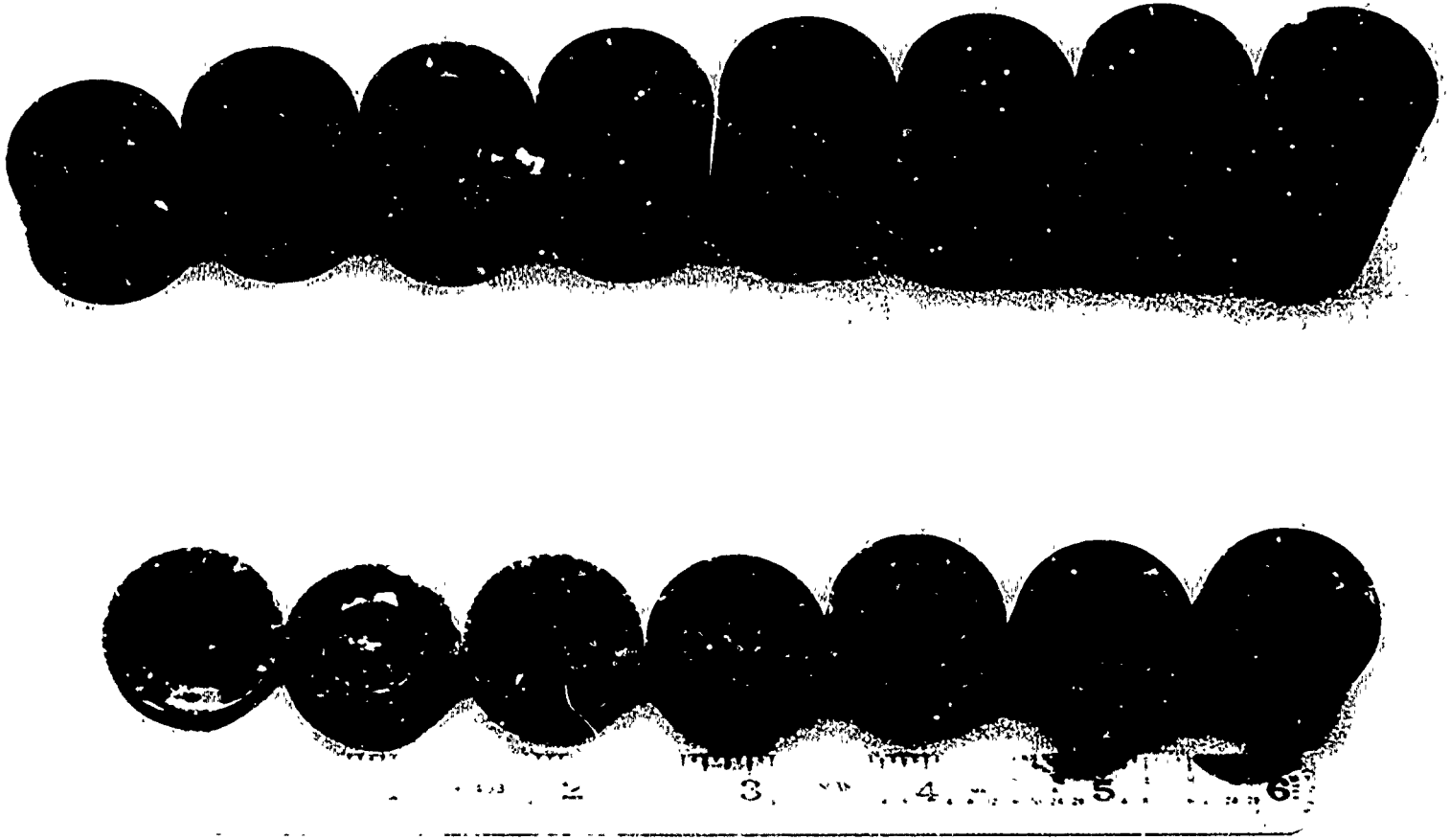

VARIOUS TOOL LENGTHS RF-3173-A1

Figure 14 - A series of flat-ended cylindrical elements used as the penetrating tool for impact-mode rock drilling by sonic energy. Tables I and II include penetration rate data with these tools. Figure 15 illustrates alignment means used.

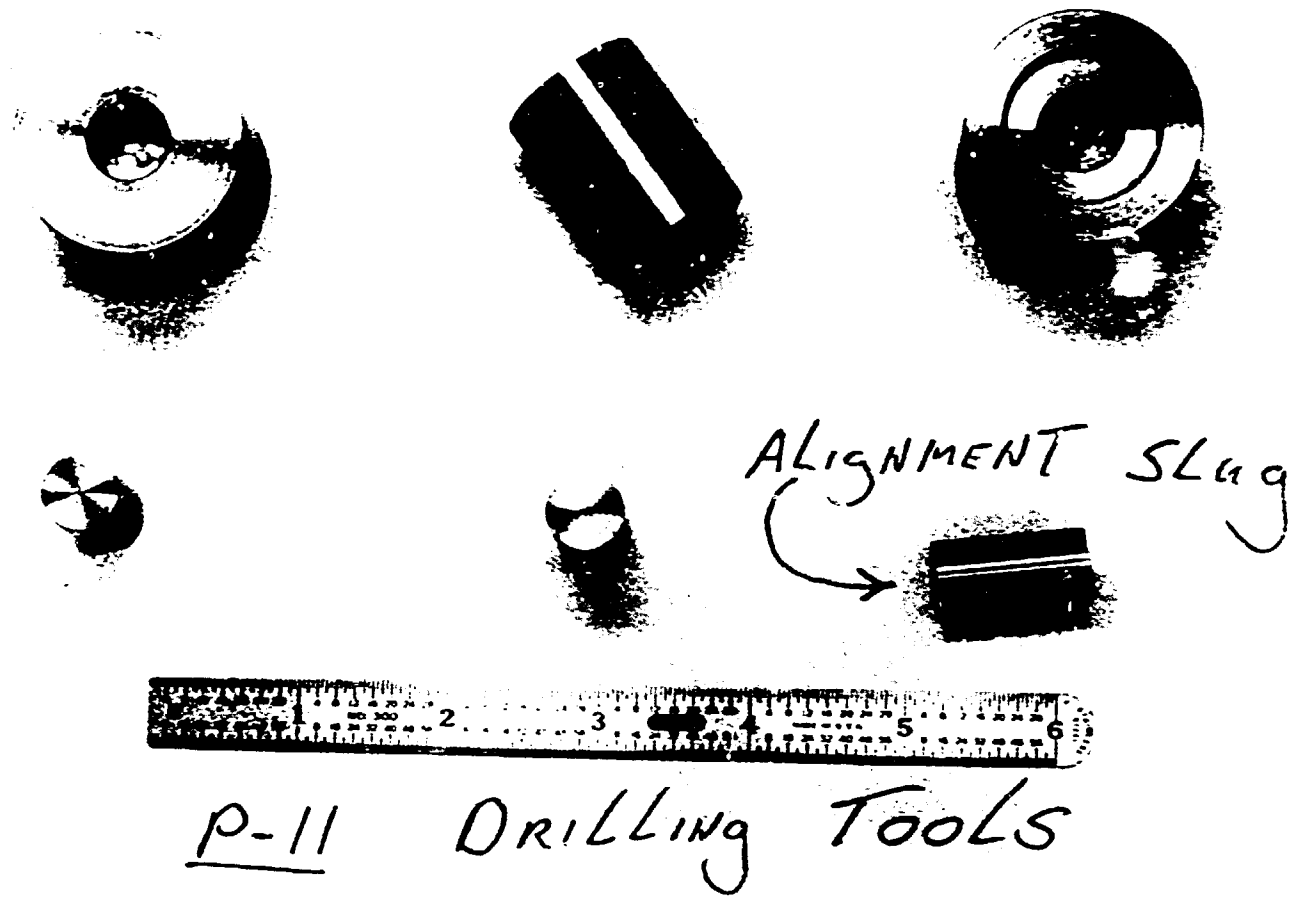

Figure 15 - The tools illustrated in Fig. 14 are aligned with the tip of the driving transducer by a pin and socket arrangement illustrated here.

Table I - Impact Drilling Test Using Cylindrical-Shaped Flat-Faced Impact Tools

Test Conditions: Material - Indiana Limestone
Dura' 'on of Each Test - 30 seconds
Sta' orce Applied Externally - 180#
Tra cer No-Load Resonant Frequency at 3 V, 10,097 Hz
Power Supply Frequency - 10,054 Hz
Solidly-Connected 10.25", Half-wave, 1" Diameter Transmission Line

Test No.	Transducer V	Generator Meter Readings A	kVA	% kVAR* Lag	Impact Tool Dimensions Dia. in.	Length, in.	Hole in Rock Depth, in.	Volume, in.^{3}	Transducer Body Temp. °C Start	°C Finish
M42171-1	1550	20	4	5	1	1/2	3-5/8	2.84	26	26
M42171-2	1800	20	4	8	1	1/2	3-7/8	3.05	31	32
M42171-3	2000	15	3.9	8	1	1/2	3-5/8	2.84	31	33
M42171-4	2450	15	5	4	1	1/2	4-1/6	3.19	36	38
M42271-1	1550	15	3.5	6	1	1/2	3-5/8	2.84	23	25
M42271-2	1550	14	2.5	6	1-1/4	3/4	2-3/4	3.38	26	28.5
M42271-3	1550	15	2	4	1	2	2	1.58	28	30
M42271-4	1550	15	2	4	1	2	1-3/4	1.38	30	30
M42271-5	1550	15	2	5	1	2	1-3/4	1.38	32	36
M42371-1	1550	25	2	12	1	4	0	0.00	23	24.5
M42371-2	2550	35	2	16	1	4	0	0.00	25	27
M42371-3	1550	10	2	4	1	1/2	1-3/4	1.38	34	33
M43071-1	1550	40	8	5	1	1/2	4-3/8	3.43	26	26
M43071-2	1550	35	7.5	7	1	1/4	3/4	.589	37	-

* Percent kVAR represents the reactive load expressed as a percent of the generator kW rating, or 50 kW in this case. 10% kVAR corresponds to 99.5% power factor.

Table II - Impact Drilling Test Using Cylindrical-Shaped Flat-Faced Impact Tools

Test Conditions: Material - Indiana Limestone
Duration of Each Test - 30 seconds
Static Force Applied Externally - 180#
Transducer - #BM-2 - No-load Resonant Frequency at 3 V, 10,086 Hz
Power Supply Frequency - 10,054 Hz
Solidly-Connected 10.25", Half-wave, 1" Diameter Transmission line

Test No.	Transducer V	Generator Meter Readings A	kVA	% kVAR* Lag	Impact Tool Dimensions Dia., in.	Length, in.	Hole in Rock Depth, in.	Volume, in.^{3}	Transducer Body Temp. °C Start	°C Finish
M60171-1	1600	20	4	2	1	1/4	5/8	0.491	28	30
M60171-2	1600	-	-	-	1	5/16	3/4	0.589	32	32
M60171-3	1600	15	3	2	1	3/8	7/8	0.687	35	35
M60171-4	1600	12	3	2	1	3/8	3/4	0.589	35	38
M60171-5	1600	12	3	2	1	1/2	5/8	0.491	38	38
M60171-6	1600	10	3	2	1	5/8	2-1/2	1.96	40	42
M60171-7	1600	10	3	2	1	3/4	2-1/8	1.67	44	48
M60271-1	1600	20	4	2	1	3/4	2-5/8	2.06	30	34
M60271-2	1600	17	3.5	2	1	7/8	1-7/8	1.47	32	34
M60271-3	16[illegible]	15	3.5	2	1	1	1-3/4	1.37	34	37
M60271-4	1[illegible]	12	2.5	2	1	1-1/8	1-5/8	1.275	37	37
M60271-5	1600	20	2.5	2	1	1-1/4	1-5/8	1.275	42	42
M60271-6	1600	15	2.5	2	1	1-3/8	1-1/2	1.18	37	40
M60371-1	1600	25	4	4	1	1-3/8	1-3/4	1.370	29	30
M60371-2	1600	20	2	2	1	1-1/2	1-1/4	1.275	34	34
M60371-3	1600	15	2.5	2	1	1-5/8	1-3/8	1.076	35	35
M60371-4	1600	15	2.5	2	1	1-3/4	1-5/16	1.028	36	40
M60371-5	1600	15	2	2	1	1-7/8	1	0.783	40	41
M60371-6	1600	12	2	2	1	2	1-7/16	1.125	34	36
M60371-7	1600	25	2	8	1	4	0	0.000	-	38
M60371-8	1600	15	2	2	1	3/4	1-5/8	1.275	40	42

* Percent kVAR represents the reactive load expressed as a percent of the generator kW rating, or 50 kW in this case. 10% kVAR corresponds to 99.5% power factor.

Table III - Impact Drilling Test Using Tools Illustrated in Figure 21

Test Conditions: Material - Indiana Limestone
Static Force Applied Externally - 180#
Transducer - #BM-4 - No-load Resonant Frequency at 3 V, 10,154 Hz
Power Supply Frequency - 10,054 Hz
Solidly-connected 10.25", Half-wave, 1" Diameter Transmission Line

Test No.	Test Duration, sec.	Operating Voltage	Input Power, W	Figure 21 Tool Dimensions		Hole in Rock		Transducer Body Temp.	
				Dia. in.	Length, in.	Depth in.	Volume in.^{3}	°C Start	°C Finish
M6147-1	10	1600	-	1	4	1.25	.980	31	31
M6147-2	8	1600	2,800	1	3	2.00	1.565	31	37
M6147-3	15	1600	17,600	1	3	2.75	2.15	37	55
M6147-4	15	1600	5,600	1	3	2.25	1.76	58	61

Several tentative conclusions were reached in this test series, some of which suggested that a further examination of the initial parameters should be undertaken. The test indicated that for these relatively short tools, the tool length of 1/2 inch appeared to be most effective. With tools shorter than this, tool destruction was quick. With longer tools, the rate of penetration decreased.

Some tests on modified tools were made in order to study experimentally the effect of the powdered rock cushioning successive tool impacts. These modifications are illustrated in Figures 16, 17, 20 and 21. Although insufficient tests were made to determine that changing tool geometry is not an effective means of improving the rate of penetration, these modifications did not improve the penetration rate.

Two illustrations of rock fracture during sonic penetration are also included. These are shown in Figures 18 and 19. Both fractures are caused by, and are immediately adjacent to, the hole formed in the rock by intermittent crushing under impact.

Figures 22 and 23 illustrate the beginning of an experimental test series on the P-11 model of piezoelectric transducer to examine the relationships between applied voltage and transducer resonant frequency, and between applied static force and transducer resonant frequency. As shown in Figure 23 the transducer resonant frequency drops about 120 Hz between 0 V and 1500 V. This fact is useful in determining the optimum resonant frequency of the transducer, measured at 3 V, which will be expected to match the supply frequency under full voltage excitation conditions.

The final section of Part I, entitled "Optimizing Transducer Output," includes additional information in reference to 1) the drop in resonant frequency due to increases in applied voltage, and 2) how this information may be utilized to maximize transducer output in the impact mode.

The two concluding sections of Part I, both include additional sonic rock drilling data under specialized conditions. In the next succeeding section drilling rates with various long transmissions lines are tabulated. In the last section drilling rates, as affected by static force and applied voltage, are tabulated.

3. LONG TRANSMISSION LINES

The test for impact-mode drilling with various lengths of acoustic transmission lines is detailed in Figures 24, 25 and 26 and the test results in Table IV are plotted in Figure 27.

TOOLS

FOR RF-3173-A1

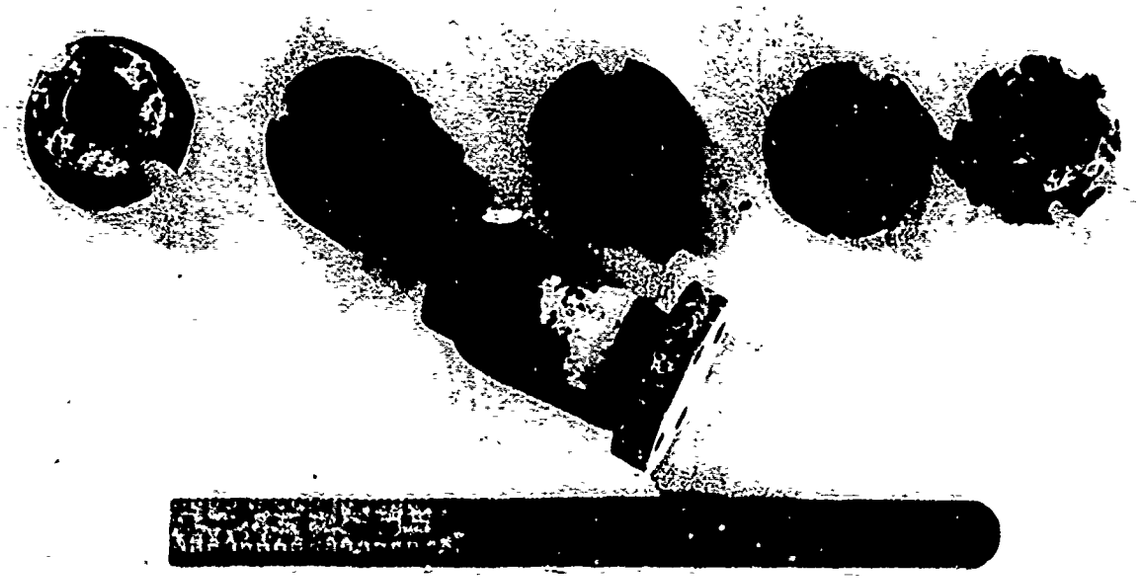

Figure 16 - The impact tools illustrated here are replacements for the cylindrical tools in Figs. 14 and 15. These modifications in tool geometry were tested for penetration rate in limestone.

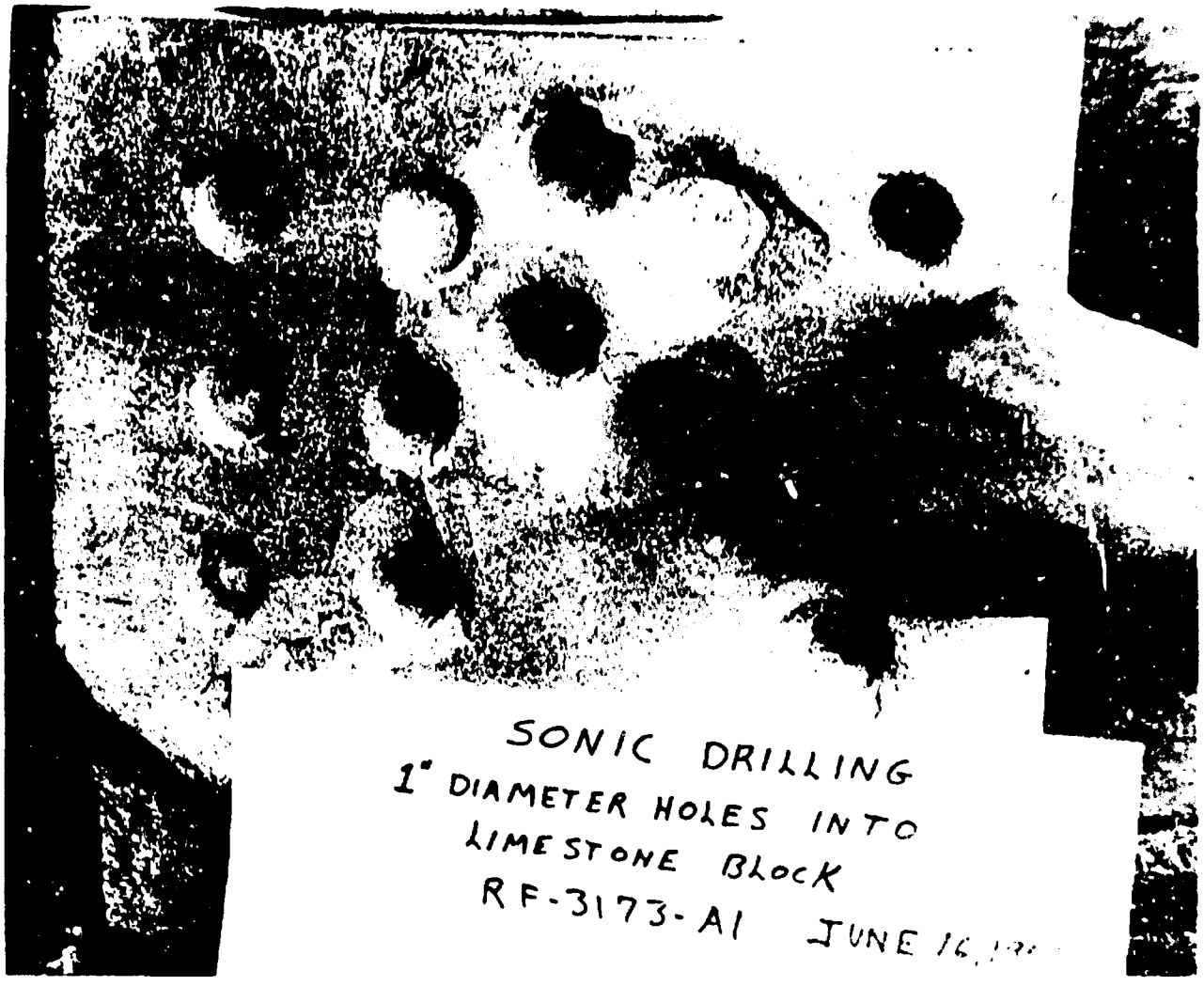

Figure 17 - Holes drilled into limestone by using cylindrical, flat-faced tools in the impact-mode driven by 10 kHz transducer. Figure 18 illustrates the back of the block, corresponding to the hole location pointed out above.

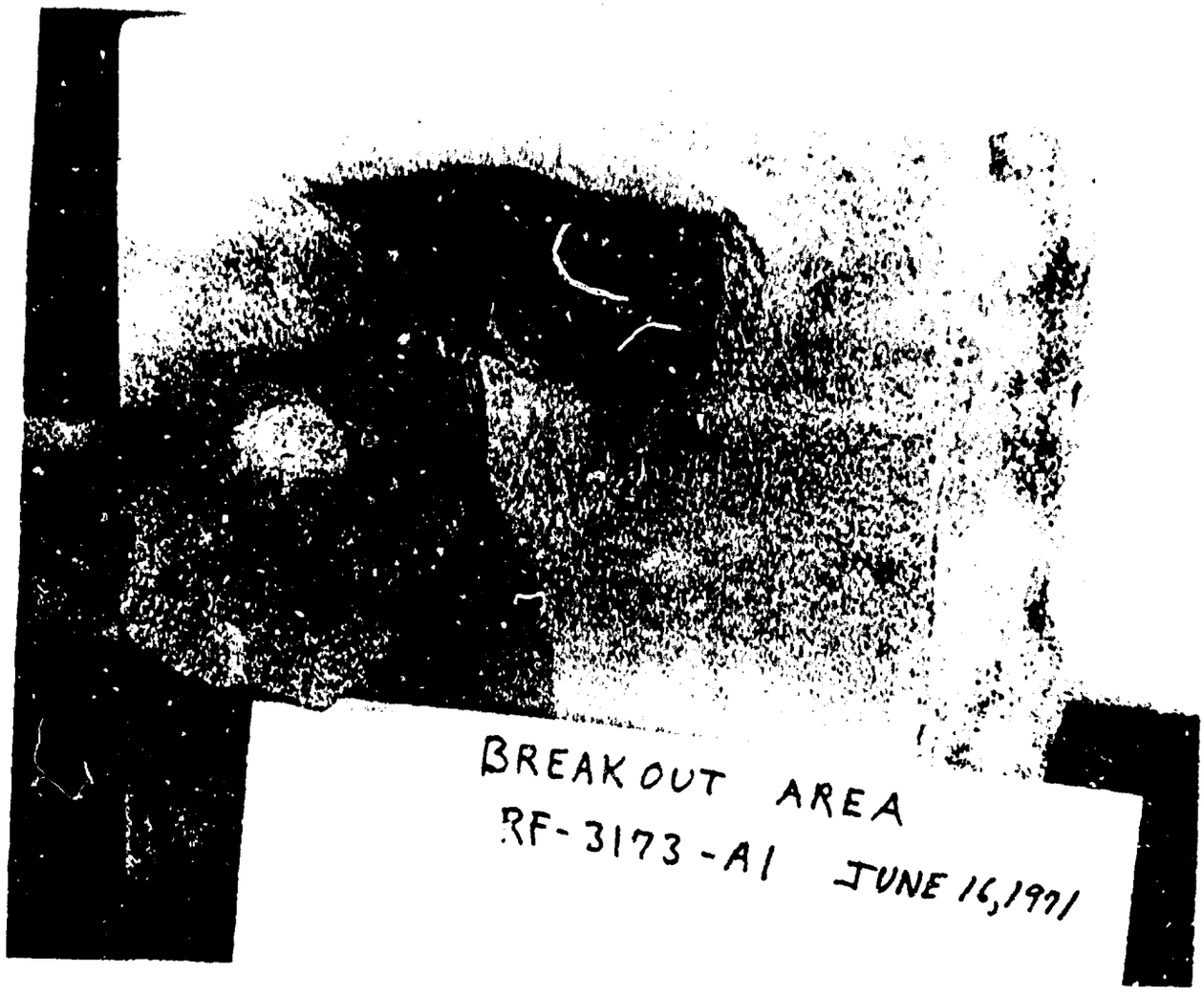

Figure 18 - Fracture of limestone block during penetration by impact-mode operation of flat-faced tool. See Fig. 17 for front view of block.

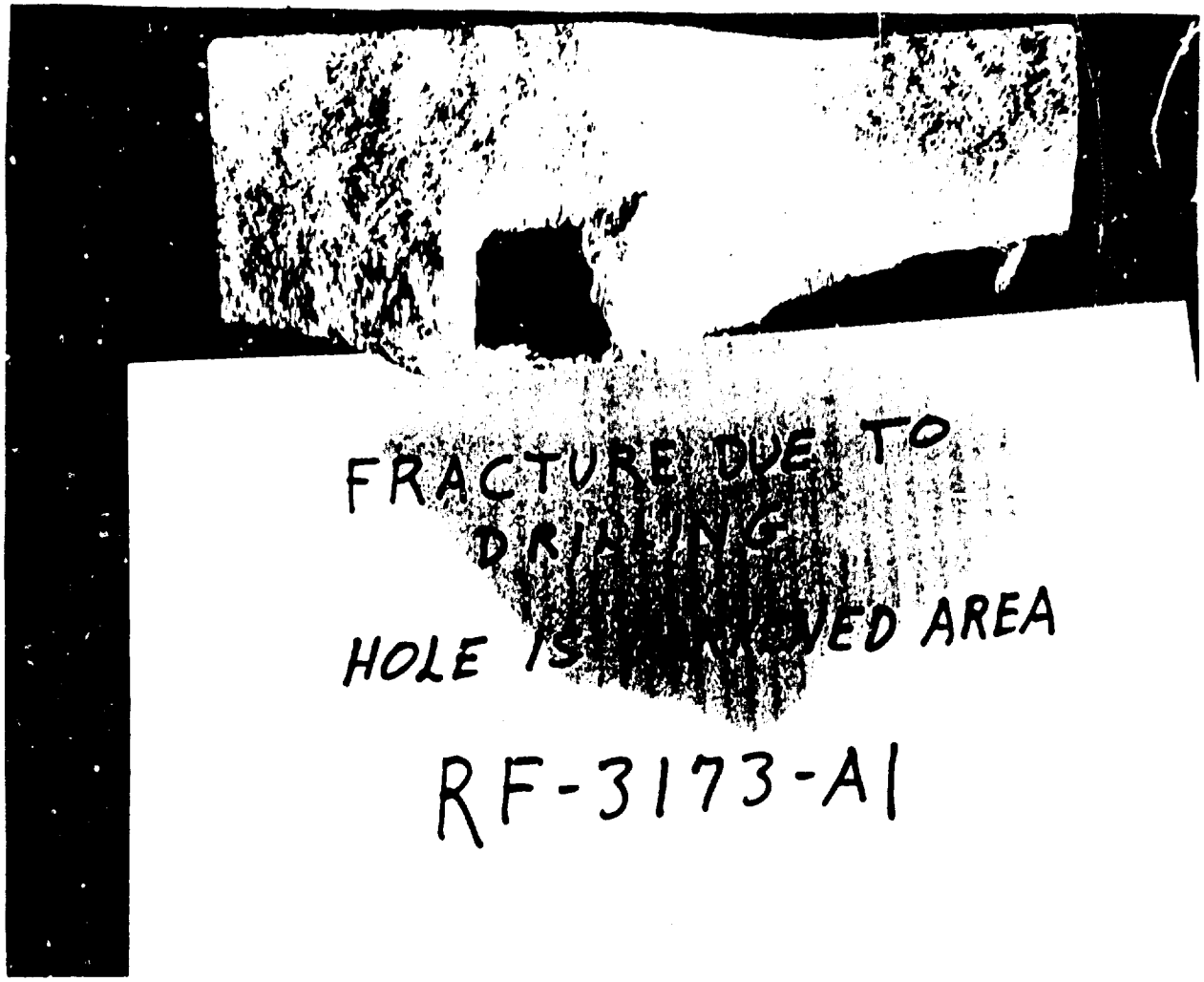

Figure 19 - Fracture of limestone rock during penetration by impact-mode operation of flat-faced tool. The wall of the hole drilled by the cylindrical tool has been blackened for clarity.

Figure 20 - Short disc-like tool with holes drilled in its periphery. Table I lists penetration data with this tool.

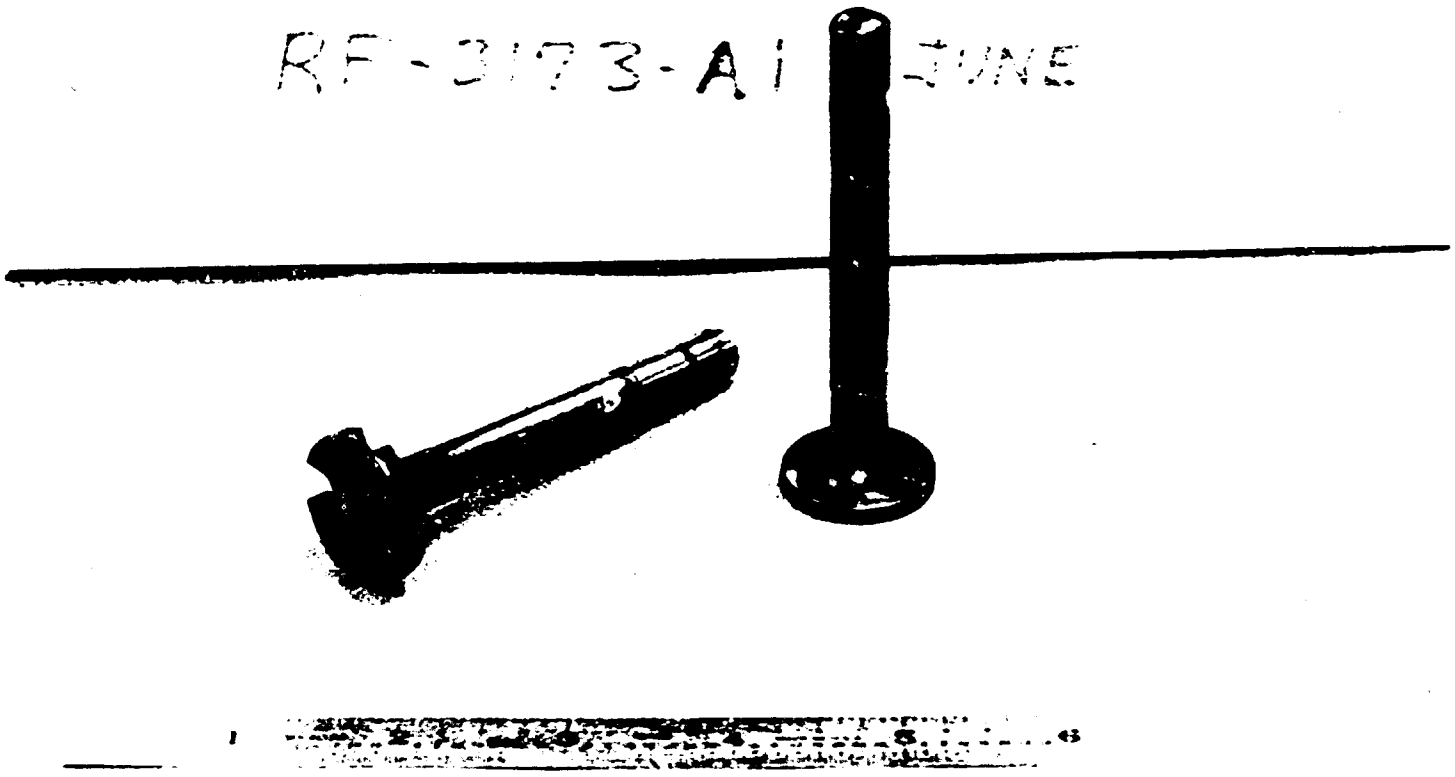

Figure 21 - Stem-type tool tested for penetration of limestone by impact-mode. Table III lists drilling information on this tool design.

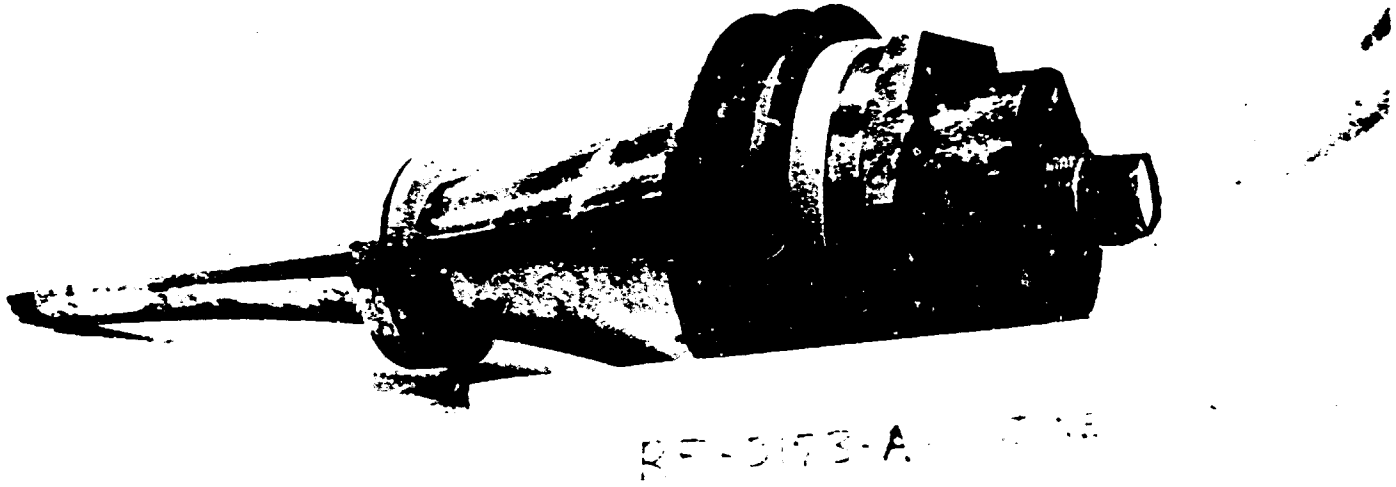

Figure 22 - Model P-11C transducer with thumb-tack accelerometer fixed to free end by epoxy cement. Data in Fig. 23 was prepared using this assembly.

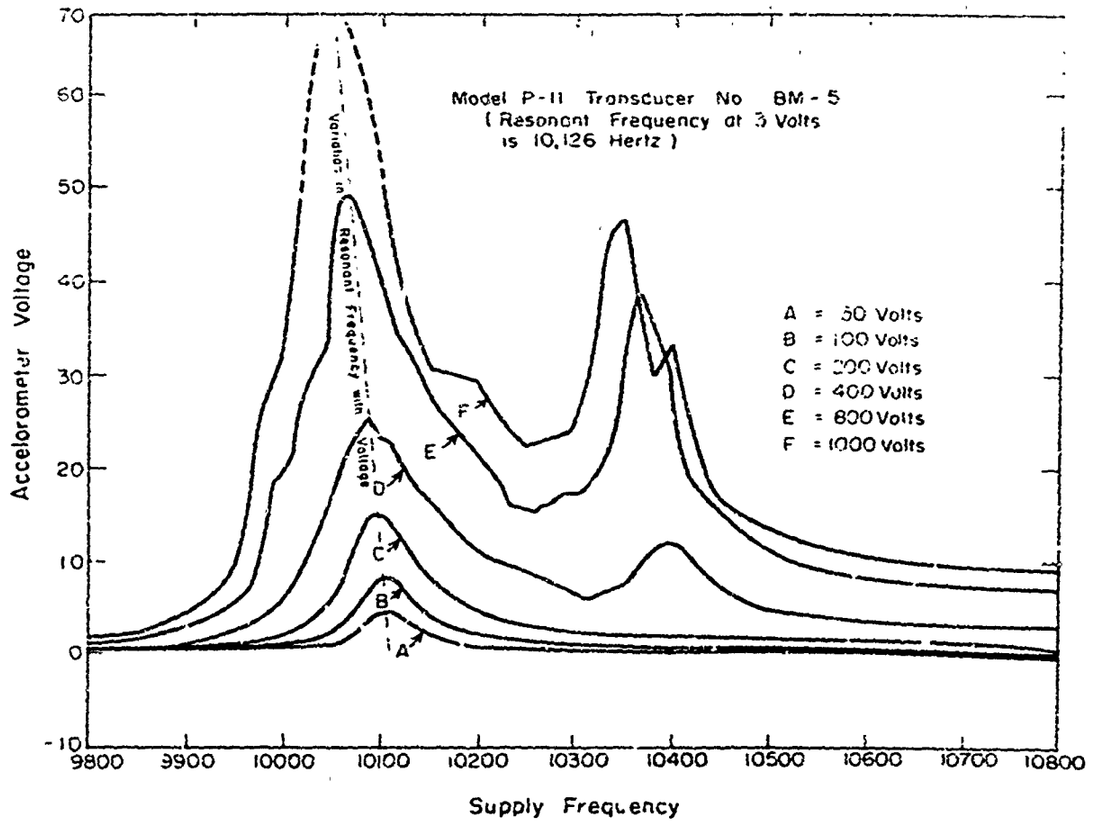

Figure 23 - No-load acceleration amplitude versus frequency of supply voltage at terminals of P-11 transducer. Note vertical dotted line describing locus of resonant frequency points. This chart illustrates the variation in transducer resonant frequency caused by changes in terminal voltage.

Figure 24 - Overall view of console, P-11 transducer, and blocks of limestone used in the study of impact-penetration with long transmission lines.

Figure 25 - Detail view of P-11 transducer mounting in console illustrated in Fig. 24.

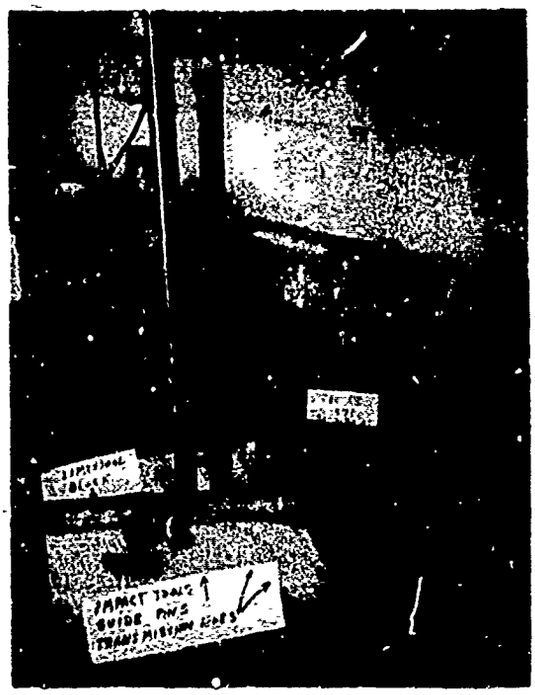

Figure 26 - Detail view of work piece and transmission lines, shown in the overall view of Fig. 24.

Table IV - P-11 Transducer, with Various Length Transmission Lines, Impact-Drilling Into Limestone Rock with Two Types of Short Tools. Supply Frequency 10,054 Hz, F_i 10,070 Hz.

Line Length (in.)	Terminal Excitation (V)	Tool Description Diameter (in.)	Tool Description Type	Static Force (lb)	1-Minute Penetration (in.)	Input Power (W)
10	1550	1	flat-faced 1/2" long	120	1	1080
20	1600	1	"	120	3/4	1080
30	1440	1	"	120	7/8	1312
40	1580	1	"	120	5/8	1120
10	1640	1	"	160	1/2	1660
10	2000	1	"	160	1	1440
20	2300	1	"	100	1	1720
20	2150	1	"	160	1/4	1400
20	1700	1	"	160	3/8	1240
30	1640	1	"	160	3/8	1480
30	1950	1	"	160	3/4	1680
40	1720	1	"	160	5/16	1200
40	1960	1	"	160	3/8	1440
10	1520	1-1/4	slotted, 1-1/4" long, centerhole	120	1-1/2	1080
20	2250	1-1/4	"	100	1	1520
20	1550	1-1/4	"	120	1	1280
30	1550	1-1/4	"	120	1-1/8	1088
40	1650	1-1/4	"	120	1/2	1500
10	2150	1-1/4	"	160	1-3/8	1440
10	1640	1-1/4	"	160	2-1/4	1240
20	2100	1-1/4	"	160	1-7/8	1560
20	1650	1-1/4	"	160	1-1/4	1400
30	2100	1-1/4	"	160	1-1/4	2080
30	1650	1-1/4	"	160	1-1/4	1192
40	2000	1-1/4	"	160	7/8	1600
40	1650	1-1/4	"	160	3/4	1500

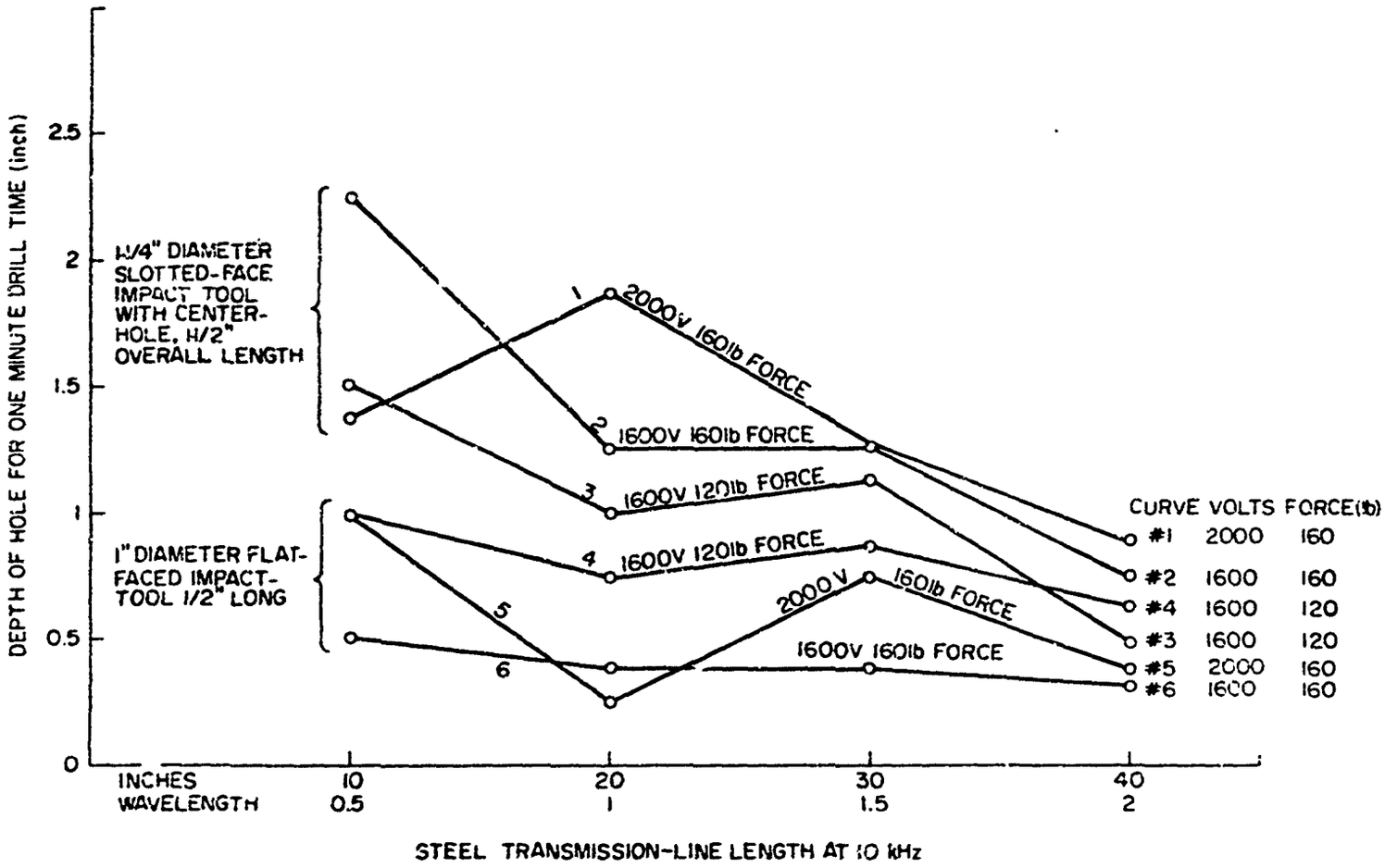

Figure 27 - Chart illustrating the impact-mode linestone-penetration rate in inches per minute, with sonic transmission lines of 10, 20, 30 and 40 inches in length. A P-11 transducer was used with an initial resonant frequency of 10,070 Hz. Power supply frequency 10,054 Hz. See Fig. 24 for test assembly. See Table IV for detailed test data.

As Figure 27 illustrates, these acoustic transmission lines showed a lower drilling rate with 40" lines than the 20" or 30" transmission lines. For a given static force applied externally to the transducer, increasing terminal voltage tended to increase the penetration rate, but this was not completely consistent. There is some evidence that there may be an optimum combination of static force and voltage for the best drilling rate of any one transducer design, and work material.

Based on observation of temperature rise in the transmission lines during drilling, it is very probable that stress-reversal losses at the nodes of the transmission lines account to a large degree for the reduced effectiveness of the longer lines. Increasing the yield point of the steel selected for the transmission lines will do much to improve the energy transmission efficiency of such acoustic transmission lines. The transmission lines described in Figures 24-27 (incl) are made of drill-rod.

4. OPTIMIZING TRANSDUCER OUTPUT

The research results, reported in this portion of the final report, were not anticipated when the research plan was instituted. The significance of the results herein reported is that new control parameters have been identified for impact-mode transducers operating with a "free-tool", i.e., a tool which is free and not restrained by diaphragms or other restraining elements fastened to the tool or bouncing mass.

The new control parameters make it possible, for example, to optimize the drilling rate for an impact-mode transducer operating from a fixed-frequency supply system. In a more general statement, the proper selection of 1) the initial transducer resonant frequency measured at no-load and at a very low voltage (3 to 10 V), 2) the externally applied static force, and 3) the excitation level applied to the terminals of the transducer, may make possible the optimization of the amplitude of motion of the transducer tip in the work environment, with a fixed-frequency supply system and an impact-mode method of delivering energy to the work surface. Charts have been prepared to illustrate this relationship, and to describe in detail the test methods utilized to determine the values of the parameters.

Figure 28 illustrates a set of curves for the P-11 transducer, in a free-tool impact-mode operation, which includes the data described in Figures 29 to 33. In Figure 28 a P-11 transducer tuned initially (at 3 V, no-load) to 10, 125 Hz is shown to have an optimum operating point at 300 pounds static force (applied externally) and 2500 V applied at its terminals from a 10,054 Hz fixed-frequency power source. The assumption in Figure 28 is that the work surface is being contacted intermittently by a free-tool, in impact-mode of operation, bouncing between the sonic transducer's tip and the work surface.

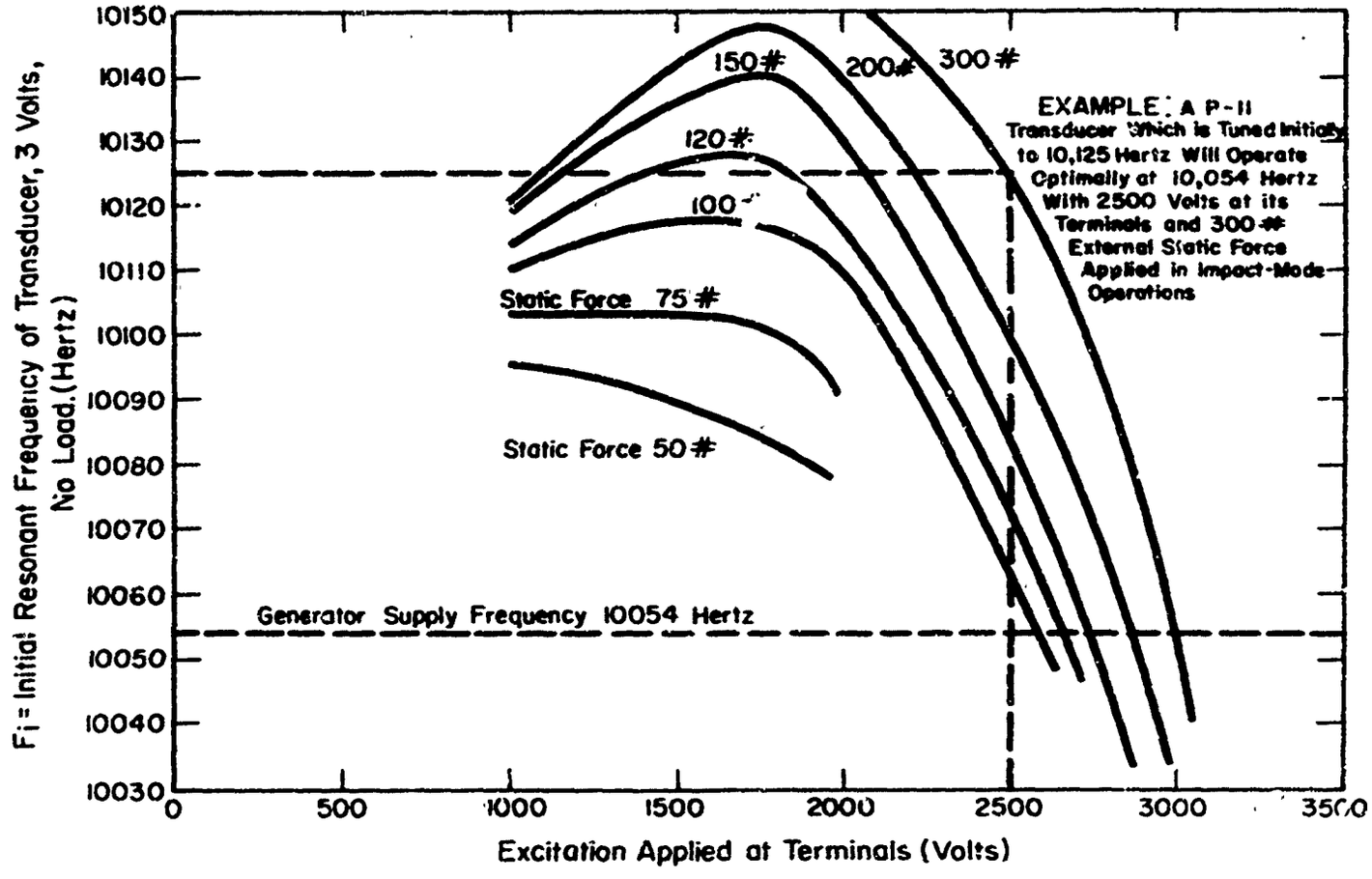

Figure 28 - P-11 transducer characteristic curves used to determine optimum operation condition under impact-load, with 10,054 Hz fixed-frequency power supply. Initial transducer resonant frequency versus terminal voltage for various static forces.

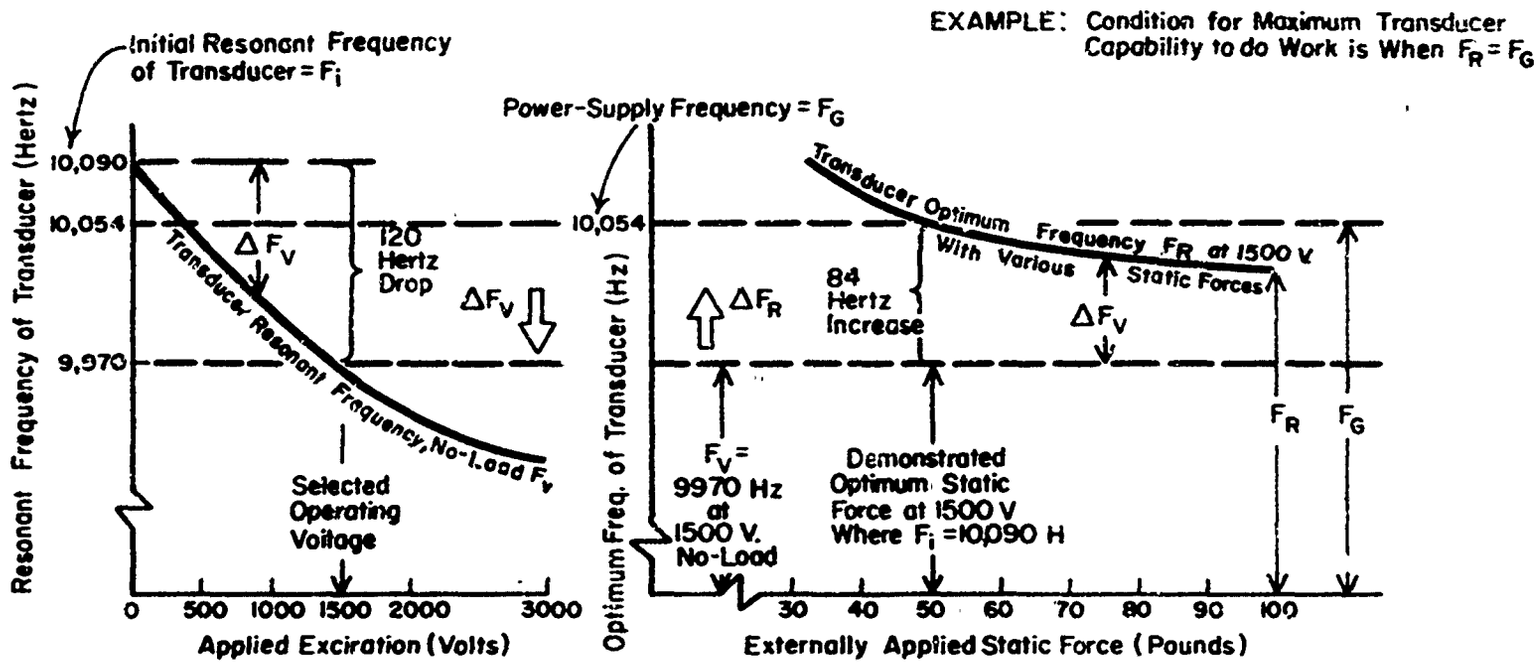

CHART A.
Increasing Terminal Voltage at No-Load, Reduces the Resonant Frequency of the Transducer

CHART B.
Increasing Static Force at any One Voltage Raises the Optimum Frequency in the Impact-Mode.

Figure 29 - Variation in Transducer no-load resonant frequency due to voltage, related to transducer optimum operating condition. F_V and F_R are related for one voltage, one value of F_i and one static force. See also Fig. 31.

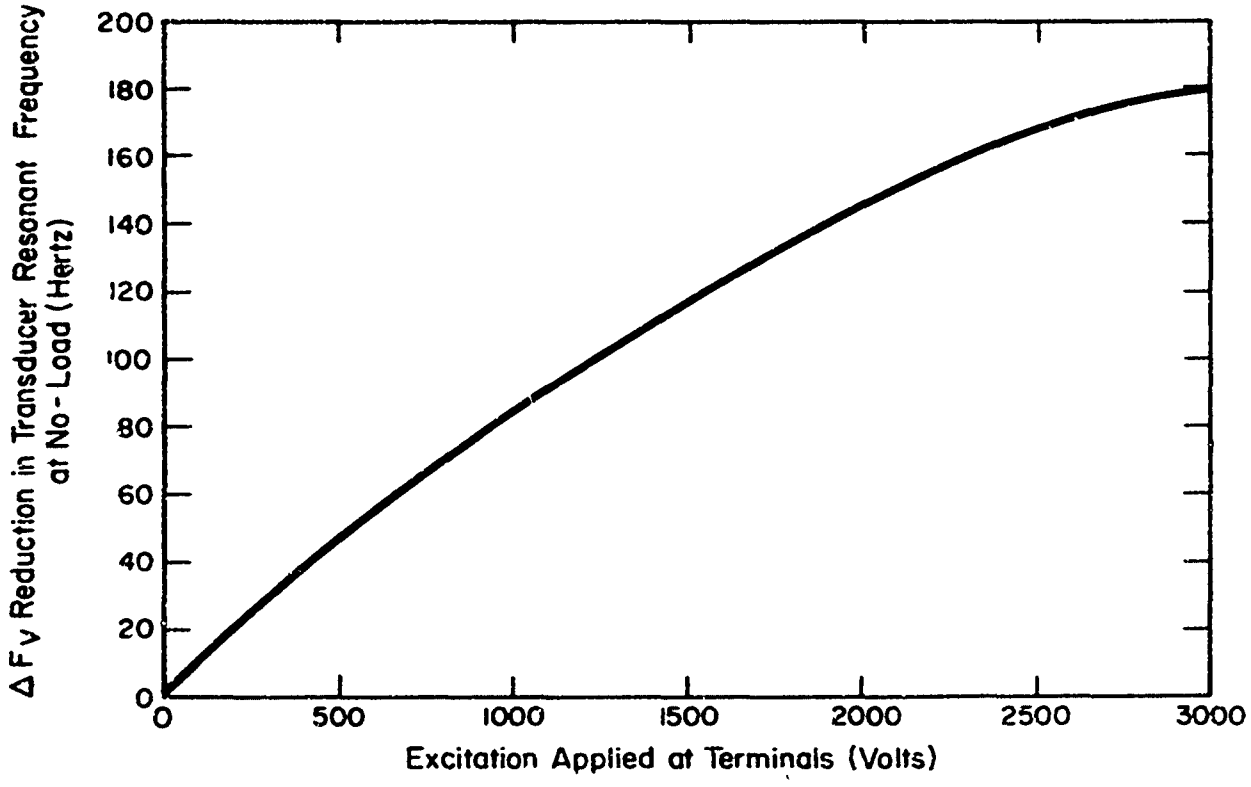

Figure 30 - Extrapolated data relating F_v or change in transducer no-load resonant frequency, to the applied terminal voltage, E. Refers to Model P-11 transducer.

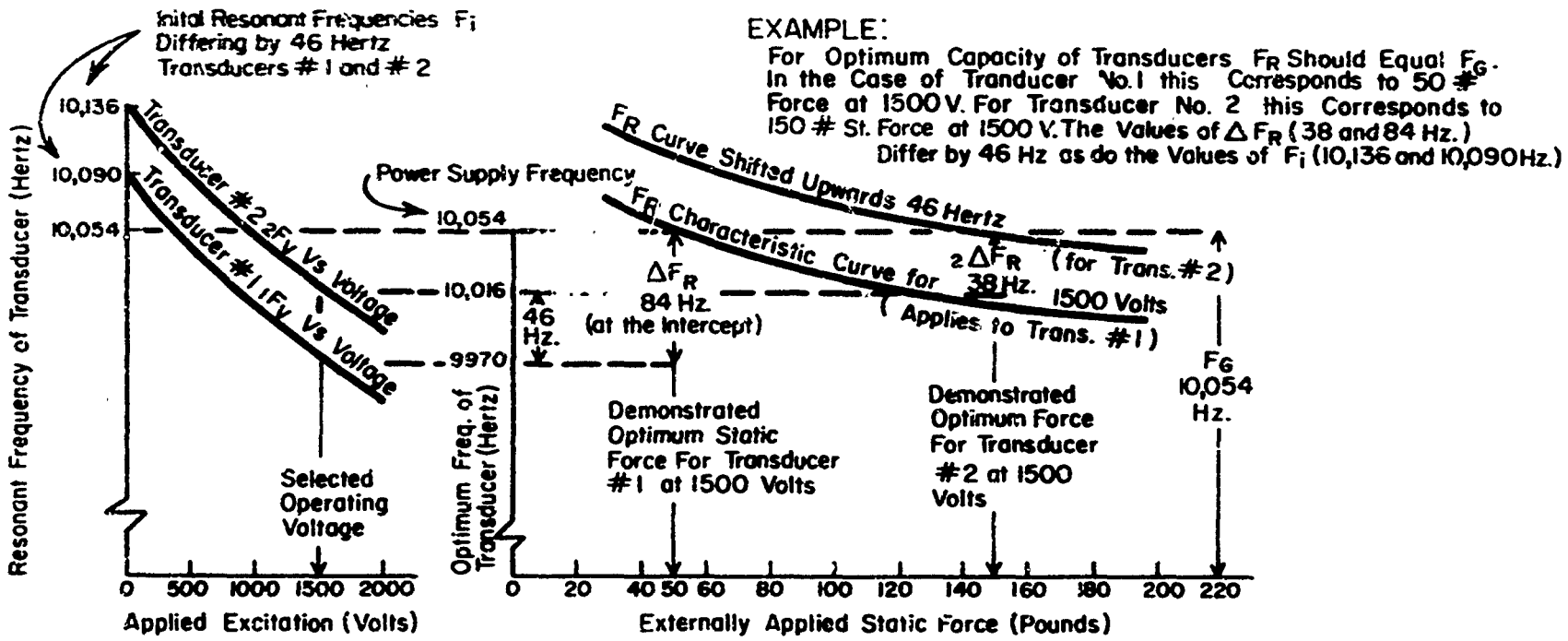

CHART A.

The Reduction in Resonant Frequency (120 Hz.) is the Same for Both Transducer # 1 and # 2, Since Each is to Operate at 1500 V.

CHART B.

The Optimum Increase in Frequency is not the Same (84 and 38 Hz) for Transducers No. 1 and No. 2, Consequently They Operate at Maximum Percent Capacity with Different Static Forces Applied

Figure 31 - Similar to Fig. 29, but illustrating two values of F_i and the corresponding change in static force for optimum operation. Values of F_v are the same for both transducers, but F_R values differ. See Fig. 32 to relate F_R to static force and voltage.

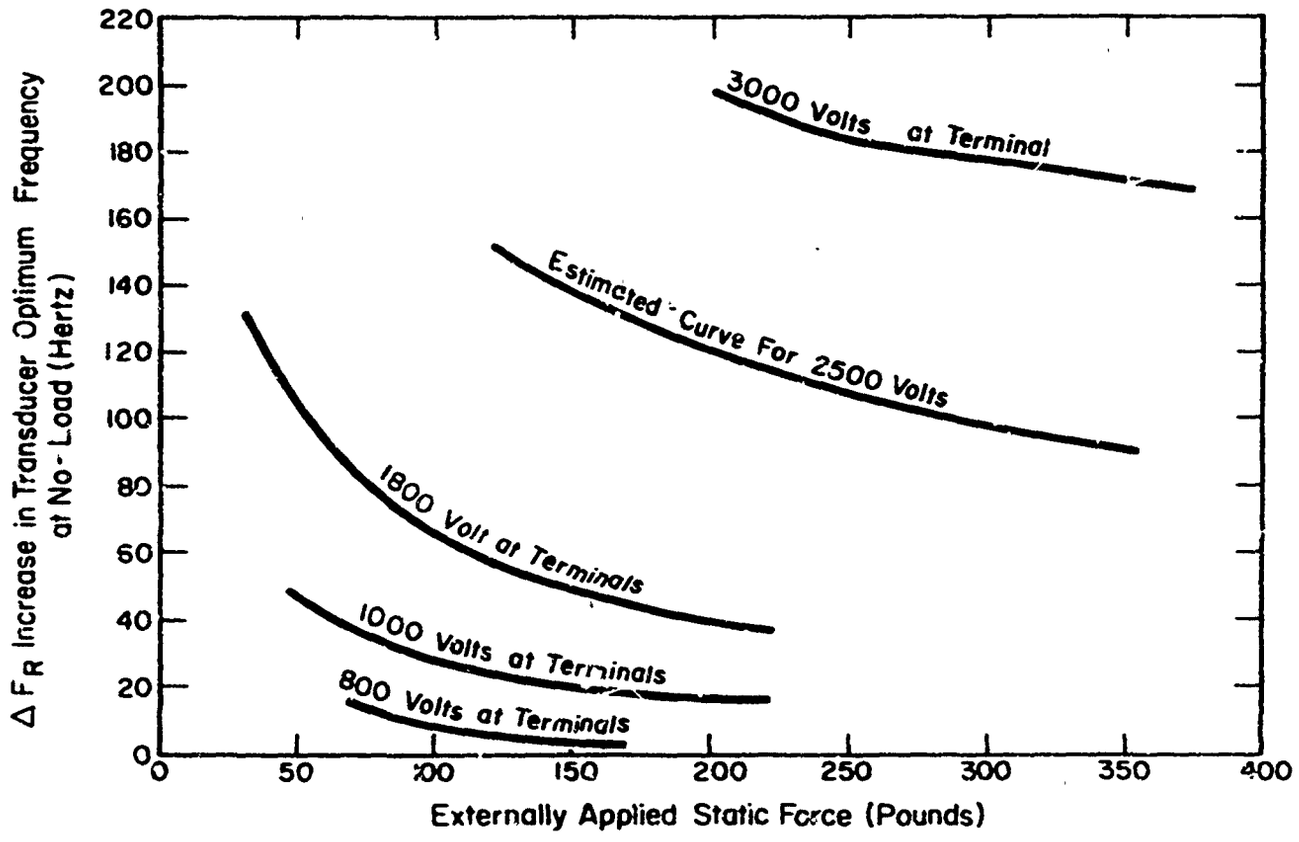

Figure 32 - Extrapolated data relating F_R to static force for various terminal voltages. The positive values of F_R shown here, indicate that the optimum operation of the transducer may be at a frequency higher than the no-load resonant frequency F_V at that voltage.

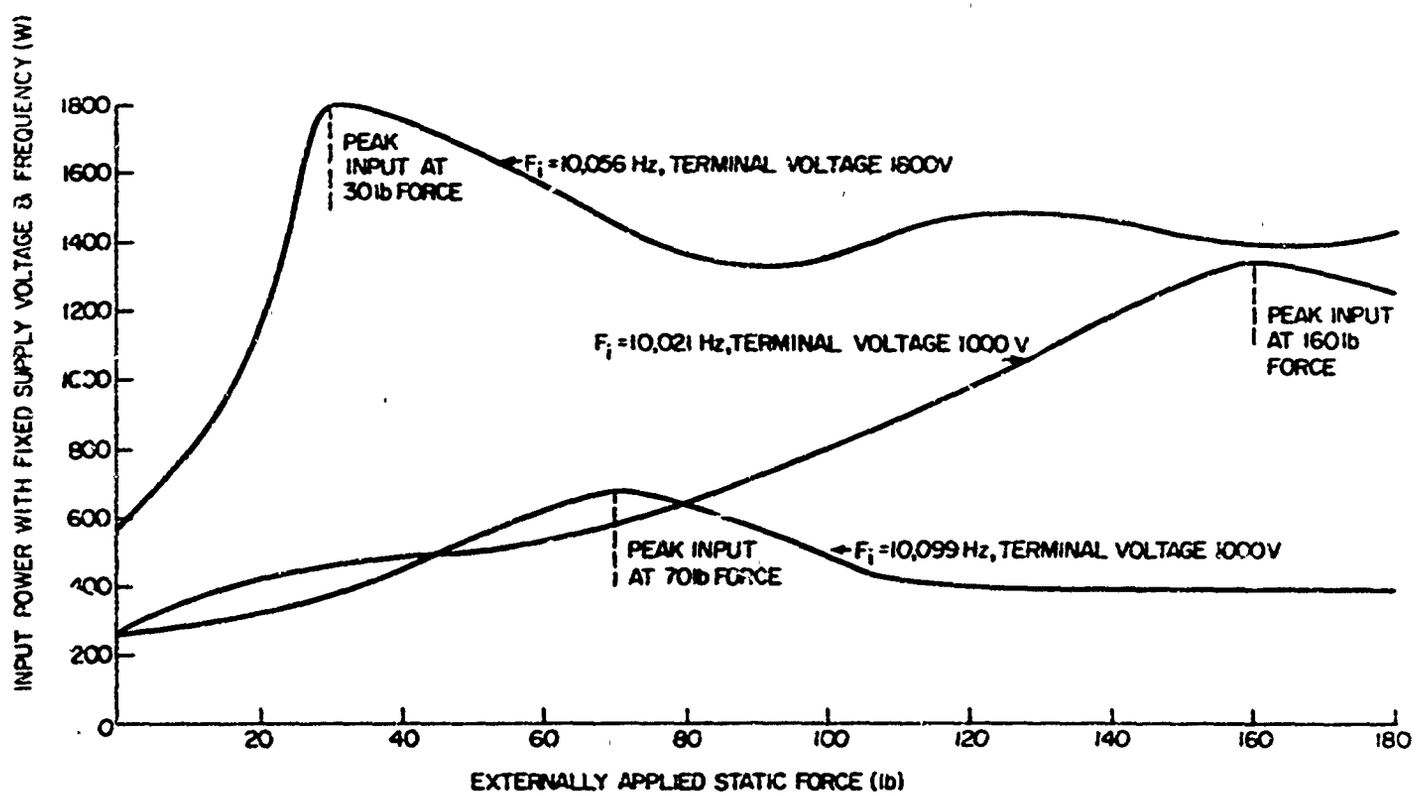

Figure 33 - Power input in watts versus static force in a lightly loaded P-11 transducer in impact-mode of operation using flat-faced tools on limestone rock. Power supply is fixed frequency 10,054 Hz. F_i is the initial resonant frequency of the transducer measured at 3 volts, no-load.

The research results illustrated in Figure 28, which include extrapolation of data described in the following pages, represent a significant contribution in the art and science of high-power transducer operation. It is believed that the effort expended in securing the data described in the following pages, to permit optimization of transducer output, represents an effective utilization of the man-hours of research effort expended on the system development portion of this research program. It would not have been possible to predict the existence of these control parameters at the time the research goals were established on this project.

The data from which Figure 28 was prepared is included in the following eight charts and three tables. In general, the concept involved here is that a transducer's resonant frequency may be expected to decrease at no-load, as the terminal voltage is increased. However, in the impact-mode of operation, optimum operation of the transducer has been observed to be at frequencies higher than those predicted from this no-load data. The increase in frequency, between F_V, the no-load resonant frequency at operating voltage, and F_r, the optimum frequency of the transducer, is designated as ΔF_r.

Figure 29 illustrates the drop in no-load resonant frequency ΔF_V, due to voltage, as being 120 Hz at 1500 V on a P-11 transducer. In Figure 29, the increase in frequency up to an optimum point is described as ΔF_r, or 84 Hz at 1500 V and 50 pounds externally applied static force. Figures 30 and 32 illustrate, respectively, the ΔF_V versus voltage curve at no-load and the ΔF_r versus static force at various load voltages. These charts have been extrapolated from test data described subsequently in this section

In Figure 31, the relationship described in Figure 30 is developed for two transducers differing in their initial resonant frequencies by 46 Hz. It becomes evident that, by varying the value of F_i, or initial resonant frequency, it is possible to control the static force at which optimum operation of the transducer will occur. In this illustration, a change in F_i of 46 Hz results in a change in the optimum static force from 50 pounds to 150 pounds. In this example, both transducers are assured to be operating at 1500 V, supplied by a 10,054 Hz power-supply. Figure 28 illustrates a practical utilization of this principle.

The data on which the values of ΔF_r were obtained experimentally is illustrated in Figure 33 and Tables V and VI. In Figure 33, the power input of a lightly-loaded P-11 transducer operating on fixed-frequency supply is plotted against the externally applied static force. Curves for various operating voltages are shown. Table V includes the complete data showning a range of voltages from 300 to 1800 V and a range of externally applied static forces between 10 and 160 pounds. Table V also indicates the means of calculating F_r for each of the six sets of data. The data in Table V contrasts to that in Table VI by the degree to which the transducers were loaded.

Table V - P-11 Transducers in Impact-Mode with Flat-Faced Tools
(Range of voltages and static forces selected for a low penetration rate; static forces determined at peak watts input with increasing static forces at fixed voltages)

F_G = Supply Frequency, 10,054 Hz
F_i = Initial Transducer Resonant Frequency on Dranetz Meter
F_v = Transducer No-load Resonant Frequency Calculated at Higher Voltage, $F_v = F_i - \Delta F_v$

Line No.	P-11 Transducer Model	P-11 Transducer No.	F_i Initial (Hz)	Static Force at Peak Input Power (lb)	E Terminal Voltage (V)	F_v Calculated Res. Freq. at E (Hz)	$\Delta F_R = (F_G - F_r)$ (Hz)
1	P-11C1	BM5	10,121	140	800	10,052	2
2	P-11C1	BM5	10,121	160	1000	10,037	17
3	P-11C1	BM2	10,099	70	1000	10,018	36
4	P-11C1	BM2	10,099	50	1800	9,964	90
5	P-11C1	BM2	10,056	[illegible]	1800	9,921	133
6	P-11C1	BM5	10,126	10	300	10,093	-39

Table VI - P-11 Transducers in Impact Mode with Flat-Faced Tools. Static Force Determined at Point of Minimum Impedance as Static Forces Were Increased with Fixed Voltage.

F_G = Supply Frequency, 10,054 Hz
F_i = Initial Transducer Resonance Frequency on Dranetz Meter
F_v = Transducer No-load Resonant Frequency Calculated at Higher Voltage = $F_i - \Delta F_v$

Line No.	P-11 Transducer Model	P-11 Transducer No.	F_i Initial (Hz)	Static Force at Min. Impedance (lb)	E Terminal Voltage (V)	F_v Calculated at E (Hz)	$\Delta F_R (F_G - F_v)$ (Hz)
1	P-11C	BM2	10,139	160	1500	10,022	32
2	P-11C	BM2	10,125	160	1500	10,008	46
3	P-11C1	BM6	10,120	126	1500	10,013	41
4	P-11C	BM2	10,105	63	1500	9,988	66
5	P-11C	BM2	10,091	63	1500	9,974	80
6	P-11C	BM2	10,036	50	1500	9,919	135

The peak power points in Figure 33 and Table V were found to correspond to points of peak current and minimum transducer impedance. In Table VI a loaded transducer was considered and the calculation of F_p was based on the assumption that the static force at the point of minimum impedance could be used in place of the static force at the point of maximum power. The correlation between Tables V and VI is judged to be sufficient to justify attempting to predict F_i for loaded transducers as well as lightly loaded transducers. The results of this endeavor is described in the following paragraphs under "applications of optimization principles."

Figure 34 shows the data in Figure 28, illustrated in a different mode. In this chart the initial resonant frequency F_i is shown in relation to optimum static force for several voltages. The 3000-V data is drawn from previous research in impact-tool operation. The 2500-V chart is estimated.

Figure 35 illustrates the instrumentation utilized in the preparation of data in this series of experimental measurements.

Application of Optimization Principles

In the application of impact-mode drilling of limestone using sonic transducers as a power source, there is a relationship between static force and drilling rate which appears to be independent of the optimum static force illustrated in previous pages of this report. Figures 36 and 37 illustrate variations in drilling rate due to both phenomena.

In Figure 36, the peak penetration rate of 1.2 to 1.3 inches per minute was found at 168 and 232 pounds in Curve 1. In Curve 2, it was 1.9 inches per minute at 105 pounds force. In neither case was the transducer operating at its minimum impedance. The static forces for minimum impedance are shown here to be related to the initial resonance frequency F_i of each transducer; this relationship was shown in Figure 34 in detail.

In Figure 37, Curve 2 is redrawn from Figure 36 and shown for comparison purposes only. In Figure 37, it is apparent that the selection of a value of F_i of 30 Hz higher than that in Curve #2 has more than doubled the penetration rate. The selection of the value 10,120 Hz as F_i in Curve #1, was made on the basis of the optimum values recommended by either Figure 28 or Figure 34.

Table VII illustrates in more detail the effect of gradually increasing the value of F_i or initial transducer resonant frequency upon the penetration rate at a fixed frequency and fixed terminal voltage. Note that the static force at minimum impedance rises with the increases in F_i.

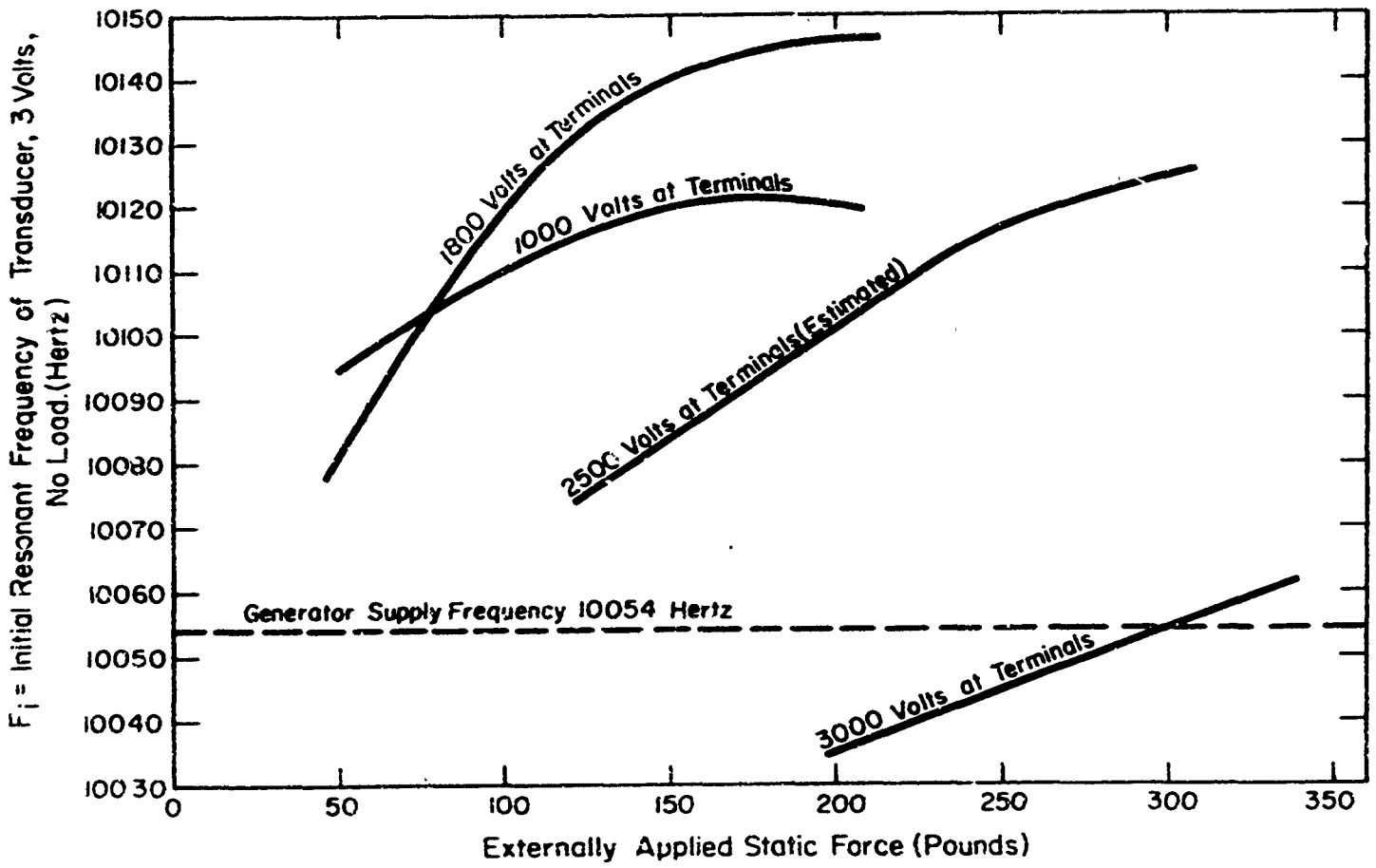

Figure 34 - P-11 characteristic curves used to determine optimum operating conditions under impact load with 10,054 Hz fixed frequency power supply. This is similar to Fig. 28 but is plotted F_i versus static force for various voltages.

Figure 35 - Instrumentation utilized in the sonic power laboratory in making measurements of transducer resonant frequency variations.

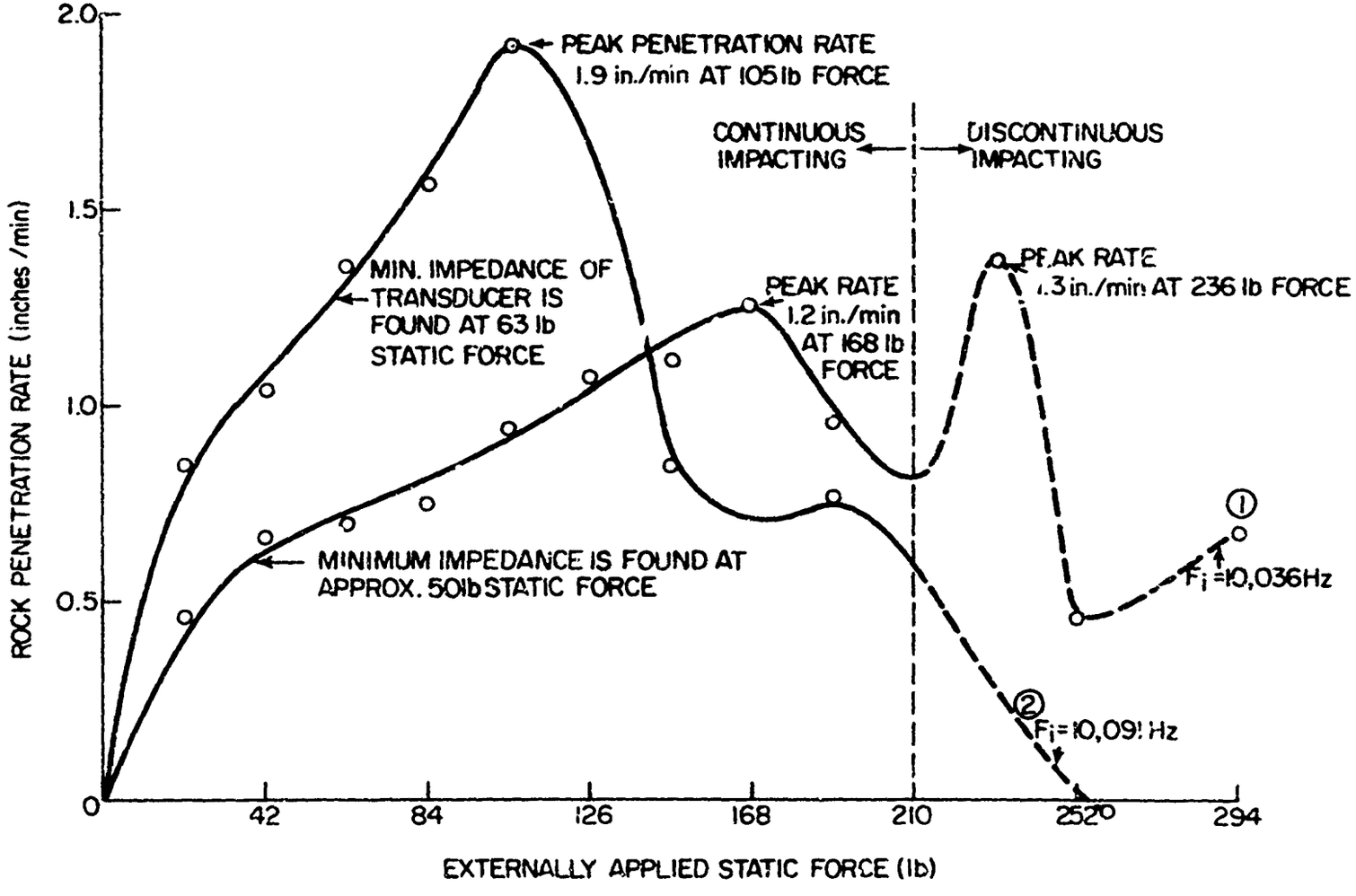

Figure 36 - Static force versus penetration-rate in limestone by impact-mode with P-11 transducer at 1500 V and with a fixed frequency 10,054 Hz supply. A 1-inch diameter flat-faced impact tool was used. Curves show static force effects penetration rate independently of the optimum operating point of transducer.

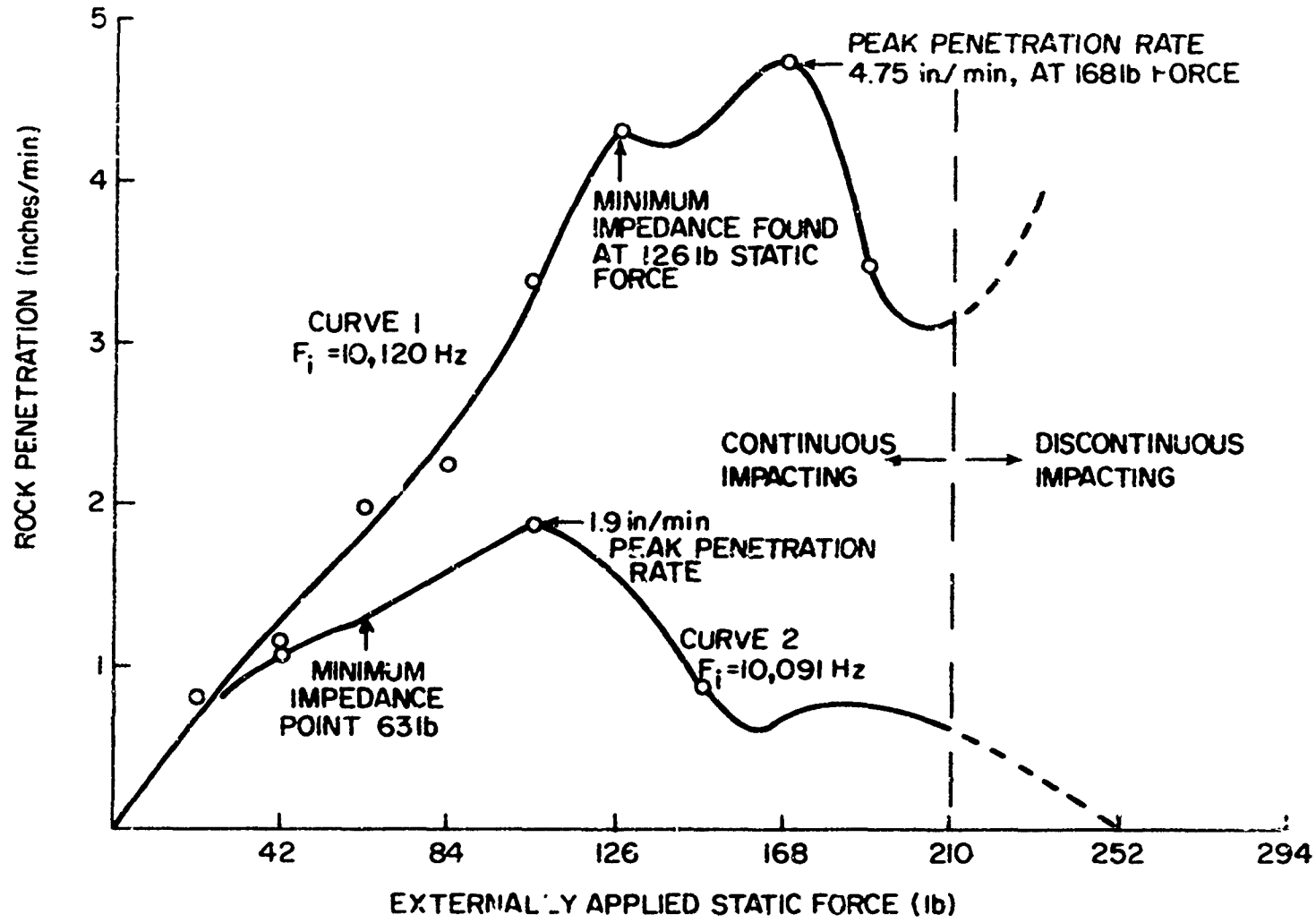

Figure 37 - Static force versus penetration rate as optimum transducer conditions are changed to approximately match the static force indicated by Fig. 36. Note the scale is doubled in Fig. 37.

Table VII - Penetration Rate Data on P-11 Transducers with 1" Flat-Faced Tools in Impact Mode on Limestone (Supply Frequency 10,054 Hz. Table Shows Successive Changes in F_i Made to Increase Penetration Rate)

Line No.	P-11 Transducer Model	P-11 Transducer No.	F_i Initial Res. Frequency (Hz)	Excitation Level (V)	Maximum Penetration Rate (in/min)	Maximum Penetration Force (lb)	Maximum Penetration Input (W)	Min. Impedance Point on Curve (Static Force)	Temperature Rise, °C
1	P-11C	BM2	10,036	1500	1.3	236	1380	50	8 to 12
2	P-11C	BM2	10,091	1500	1.9	105	1500	63	8 to 12
3*	P-11C	BM2	10,105	1500	2.1	105	1600	63	8 to 12
4	P-11C1	BM6	10,120	1500	4.75	168	2450	126	8 to 10
5**	P-11C1	BM6	10,120	1500	4.0	148	1800	126	8 to 10

* After test a fatigue crack was discovered in center shaft of transducer.
** Transducer crystals shorted out at peak power. Center-shaft showed crack after test completion.

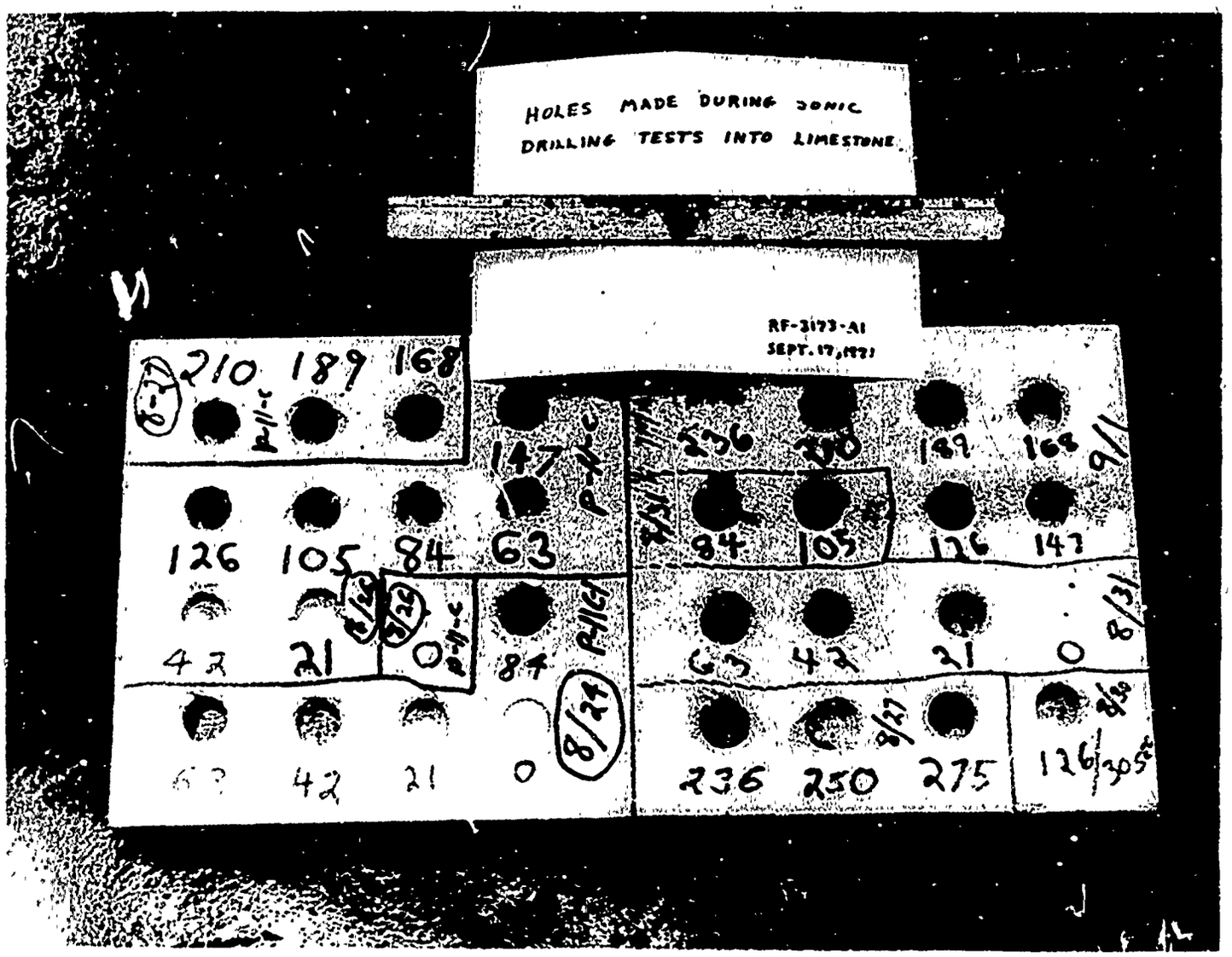

Figure 38 - Drilling tests performed in the preparation of data for Figs. 36 and 37.

In Figure 37, it is shown that a change of only 30 parts in 10,000 has effected a doubling of the penetration rate in limestone. This fact illustrates dramatically that the parameter relationships described in Figures 28 and 34 are of unique value in maximizing transducer output in impact-mode applications.

In fact, it has been observed, as indicated in the footnotes in Table VII, that the optimization of the transducer operation leads to a reduction in the transducer life. Apparently, it will be necessary to limit the force-impulses transmitted into the transducer body from the working tip of the transducer. Two designs of attachments to the transducer have been considered and will be applied during the second year of effort in impact-mode penetration of rock by sonic transducers, which should have this desired effect.

PART II: SYSTEM ANALYSIS

CONTENTS

1. ANALYSIS OF TOOL IMPACT ON ROCKS
2. STRESSES DEVELOPED DURING SONIC IMPACT
3. VIBRATIONAL CHARACTERISTICS OF A SONIC TRANSDUCER
4. TOOL IMPACT ON ROCK
5. TOOL IMPACT ON A TRANSMISSION LINE
6. A DESCRIPTION OF THE SONIC INTERACTION PROCESS

Preceding Page Blank

1. ANALYSIS OF SONIC TOOL IMPACT ON ROCKS

Previous studies of a rectangular stress wave propagating along a semi-infinite rod and incident on a rock show that the dynamic contact force-penetration characteristics can be approximately represented by a bilinear spring model as shown in Figure 1-1 where k_1 and k_2 are spring constants for the loading and unloading path of the bilinear spring. In the sonic drilling process, a short cylindrical bouncing tool is generally used for transmitting sonic energy from the sonic transducer to the rock by rapid impacts against the surface of the rock and the transducer tip. The problem of impact between the tool and the vibrating transducer tip has been studied extensively in previous reports. Based on previous work and the assumption that the wave propagation in the tool is essentially one-dimensional, a tool of given geometry and mass impacting on rock is studied in this report.

There are two ways of approaching this problem. One is to assume that the contact force-penetration character of the present problem is the same as that of a rectangular stress wave incident along a semi-infinite rod. Of course, the assumption just made needs justification. In this approach, it has the advantage of being simple in nature as well as in mathematical manipulation. The rebound velocity and maximum penetration can be obtained readily without involving complicated calculations. Another way of solving this problem is by considering the stress wave characteristics in the tool during impact. In this approach, we are able to obtain reasonable results at the price of the complicated numerical calculations involved. The differential equation governing the penetration of a tool against the rock was set up and solved. The results for the previous two approaches are found to be very close to each other. This justifies that, in solving the tool-load impact problem, the previous, simpler method can be used, i.e., one can assume a perfectly rigid tool impacting directly on a spring of bilinear character without invoking much error in the results.

1-1 RIGID TOOL IMPACT ON A BILINEAR SPRING

Mahban* suggested that when a rectangular stress wave is incident on rock along a semi-infinite rod, the contact force-penetration characteristics can be represented by a bilinear spring model. We should be careful here, since we still do not know whether the bilinear spring model for rock can be used for the present problem of impact of a tool against rock. However, it would be beneficial to make such an assumption at this stage of analysis, i.e., the contact force-penetration characteristic is the same for the present problem as for a rectangular stress wave incident on rock along a semi-infinite rod. In addition to that,

* Mahban, H., "Response of Rock to Impulse Loading," Ph.D. Dissertation, The Ohio State University, 1970.

PRECEDING PAGE BLANK

we assume the tool to be completely rigid. With the above assumptions, the problem of tool-load impact becomes a rather simple one-degree of freedom spring mass system with variable spring constant. The unloading of the tool is along a different path to the loading curve.

A rigid tool with initial velocity V_o before impact possesses a total energy

$$E = (\rho A l \ V_o^2)/2 \tag{1-1}$$

where ρ, A, and l are mass density, cross-sectional area and length of the cylindrical tool, respectively. The maximum contact force and penetration occurs when the velocity of the tool becomes zero and can be obtained by equating the tool energy, E, to the maximum potential energy of the spring.

$$E = (\rho A l \ V_o^2)/2 = 1/2 \ K_1 \ u_m^2 \tag{1-2}$$

This gives

$$u_m = V_o \sqrt{\frac{\rho A l}{K_1}} \tag{1-3}$$

where u_m is the maximum penetration. For the maximum contact force F_m, we have

$$F_m = K_1 u_m \tag{1-4}$$

or

$$\frac{F_m}{A} = V_o \sqrt{\frac{\rho K_1 l}{A}} \tag{1-5}$$

Part of the total energy is generally lost due to the impact. Unloading is along $K = K_2$. The energy loss, E_L, is the energy used to induce crack in the rock, and is equal to the shaded area between lines of loading and unloading in Figure 1-1, that is

$$E_L = 1/2 \ K_1 u_m^2 (1 - K_1/K_2) \tag{1-6}$$

The rebound velocity is obtained without difficulty by considering the energy after impact and is given by

$$V_r = \frac{K_1}{K_2} u_m \sqrt{\frac{K_2}{\rho A l}} \tag{1-7}$$

The time t_m required to reach the peak (maximum penetration) and the time required from peak to complete separation of tool and load, t_r,

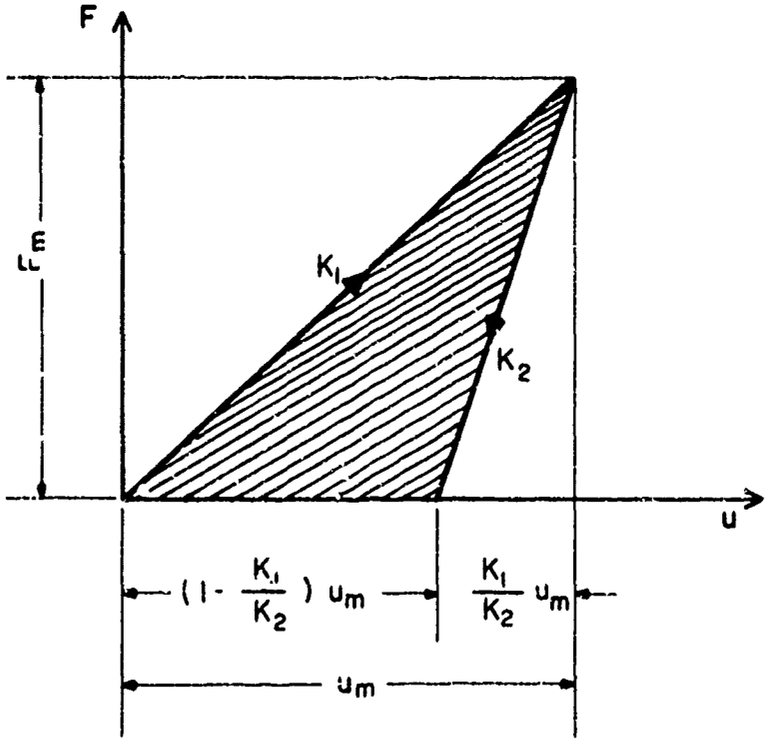

Figure 1-1. Bilinear contact force-penetration relation.

are, according to one-dimensional spring mass system, respectively

$$t_m = 1/4 \frac{2\pi}{\sqrt{\frac{K_2}{\rho A l}}} \tag{1-8}$$

$$t_r = 1/4 \frac{2\pi}{\sqrt{\frac{K_2}{\rho A l}}} \tag{1-9}$$

The total contact time is the sum of t_m and t_r. After the tool leaves the rock surface, there is a permanent deformation of the rock, as shown in Figure 1-1.

From previous discussion, it is easy to see that with the assumption made of a rigid tool, the problem of tool-load impact is much simplified and all the results can be obtained without complicated numerical calculations.

1-2 ELASTIC TOOL IMPACT ON A BILINEAR SPRING

In the previous section, the discussion is based upon the assumption that the contact force-penetration characteristics of tool-load impact is bilinear. No proof has yet been given. A more realistic approach is given here. It is based on Mahban's results obtained from incident stress wave along a semi-infinite rod.

(i) Initial Condition of a Tool with Constant Velocity

It can be proved that a cylindrical tool with velocity V_0 can be represented by two rectangular stress waves of opposite sign propagating in two different directions as shown in Figure 1-2. The magnitude of the stress waves are equal to $V_0 c\rho/2$, where c is the wave velocity in the tool. Since both ends of the tool are free, the wave is reflected back without distortion in shape, but with different sign.

(ii) Bilinear Spring Model and Governing Differential Equation

During impact of the tool and the load, the tip of the tool is compressed against the load and is no longer a free end. The reflected wave travels with velocity, c, away from the point of contact. When it reaches the other end of the tool, it is reflected back as an incident wave. There may be several incident-reflection wave cycles before the tool bounces back from the rock. A large force occurs between the load and tool. As a result, some fracture and penetration

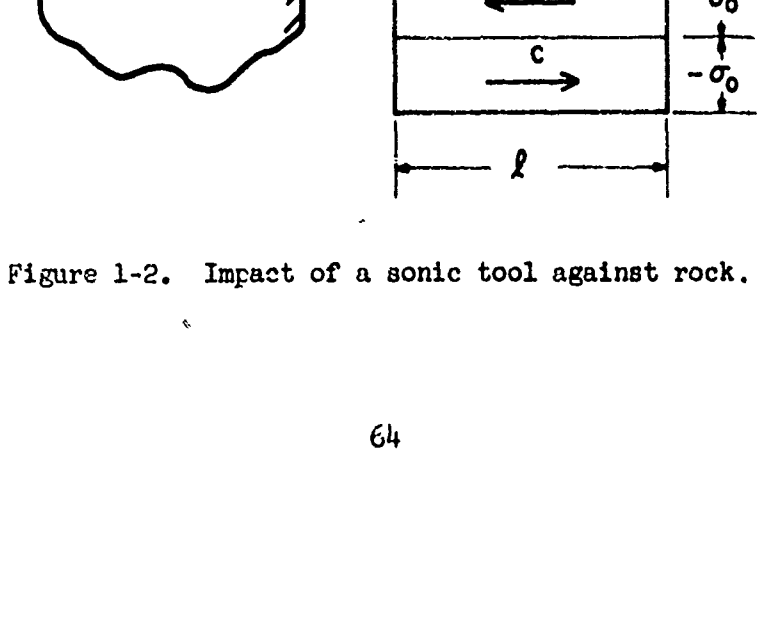

Figure 1-2. Impact of a sonic tool against rock.

occurs. The velocity of the tip, or the penetration, $\dot{u}$, according to one-dimensional theory of wave propagation in a rod is given by

$$\dot{u} = -\frac{c}{E}(\sigma_i - \sigma_r) \tag{1-10}$$

where E is Young's modulus, σ_i is the incident wave, and σ_r is the corresponding reflected wave. During the first wave cycle of contact, σ_i is equal to $-V_o c\rho/2$; thereafter, the shape of the incident wave becomes more and more complicated.

The contact force between tool and load is

$$F = A(\sigma_i + \sigma_r) \tag{1-11}$$

Eliminating σ_r in equation (1-10) and (1-11), we obtain the following differential equation

$$\dot{u} - \frac{c}{E}\frac{F}{A} = -\frac{2c\sigma_i}{E} \tag{1-12}$$

To solve the above differential equation, we can use the contact force-penetration characteristics pointed out by Mahban, and as already shown in Figure 1-1. This model can be expressed in the following form

$$F(t) = -\begin{cases} K_1 u(t) & \dot{u} > 0 \\ (K_1 - K_2)u_m + K_2 u(t) & \dot{u} < 0 \end{cases} \tag{1-13}$$

The problem can be solved with equation (1-12) and (1-13). The solution follows:

(a) <u>For $0 \leq t \leq t_1$</u>

$$u = A_1 + B_1 e^{-p_1 \bar{t}}$$

$$t_1 = \frac{2l}{c}$$

$$\bar{t} = t$$

$$p_1 = cK_1/EA$$

$$A_1 = 2\sigma_o A/K_1$$

$$B_1 = -A_1 = -2\sigma_o A/K_1$$

$$u_1 = u(t_1) \tag{1-14}$$

(b) <u>For $t_1 \leq t \leq 2t_1$</u>

$$u = A_2 + (B_2 + C_2\bar{t})e^{-p_1\bar{t}}$$

$$\bar{t} = t - t_1$$

$$A_2 = -2\sigma_o A/K_1$$

$$B_2 = u_1 + 2\sigma_o A/K_1$$

$$C_2 = 4c\sigma_o/E$$

$$u_2 = u(t_1) \qquad (1\text{-}15)$$

(c) <u>For $2t_1 \leq t \leq t_m \leq 3t_1$</u>

t_m = time required to reach maximum penetration

$$u = A_3 + (B_3 + C_3\bar{t} + D_3\bar{t}^2)e^{-p_1\bar{t}}$$

$$\bar{t} = t - 2t_1$$

$$A_3 = 2\sigma_o A/K_1$$

$$B_3 = u_2 - 2\sigma_o A/K_1$$

$$C_3 = -2p_1 u_1$$

$$D_3 = -\frac{4p_1 c\sigma_o}{E}$$

$$2t_1 \leq t_m = \left(\frac{-a \pm \sqrt{a^2 - 4b}}{2}\right) \leq 3t_1$$

$$a = \frac{1}{p_1}\left[\frac{u_1 K_1}{2\sigma_o A} - 2\right]$$

$$b = -\frac{E}{2p_1 c\sigma_o}\left(u_1 + \frac{u_2}{2}\right) + \frac{1}{2p_1^2}$$

$$u_m = u(t_m) \qquad (1\text{-}16)$$

(d) <u>For $t_m \leq t \leq 3t_1$</u>

$$u = A_4 + (B_4 + C_4\bar{t})e^{-p_1\bar{t}} + E_4 e^{-p_2\bar{t}}$$

$$A_4 = \alpha + \frac{2\sigma_o A}{K_2}, \qquad \alpha = (K_2 - K_1)u_m/K_2, \qquad \bar{t} = t - t_m$$

$$B_4 = \frac{2c}{E(p_2 - p_1)}\left[-\frac{K_1 u_1}{A} + \frac{4p_1\sigma_o}{p_2 - p_1}\right]$$

$$C_4 = \frac{8p_1 c\sigma_o}{E(p_2 - p_1)}$$

$$E_4 = e^{p_2\bar{t}_m}u_m - A_4 - \left(B_4 + C_4\bar{t}_m\right)e^{-p_1\bar{t}_m}$$

$$\bar{t}_m = t_m - 2t_1$$

$$u_4 = u(t_1) \tag{1-17}$$

(e) <u>For $3t_1 < t < 3t_1 + \bar{t}_m$</u>

$$u = A_5 + (B_5 + C_5\bar{t} + D_5\bar{t}^2)e^{-p_1 t} + E_5 e^{-p_2\bar{t}_m}$$

$$A_5 = \alpha - \frac{2\sigma_o A}{K_2}, \qquad \bar{t} = t - 3t_1$$

$$B_5 = \frac{2c}{E(p_2 - p_1)}\left\{\frac{p_2 + p_1}{p_2 + p_1}\left(2\sigma_o - \frac{K_1 u_1}{A}\right) + \frac{8p_1^2\sigma_o}{(p_1 - p_2)^2} - \frac{K_1 u_1}{A}\right\}$$

$$C_5 = \frac{4cp_1}{E(p_2 - p_1)}\left\{\frac{K_1 u_1}{A} - \left(\frac{p_2 + p_1}{p_2 - p_1}\right)2\sigma_o\right\}$$

$$D_5 = \frac{8cp_1^2\sigma_o}{E(p_2 - p_1)}$$

$$E_5 = u_4 - A_5 - B_5 \tag{1-18}$$

(f) For $3t_1 + \bar{t}_m \leq t \leq 4t_1$

$$u = A_6 + (B_6 + C_6\bar{t})e^{-p_1\bar{t}} + (E_6 + F_6\bar{t})e^{-p_2\bar{t}}$$

$$A_6 = \alpha - \frac{2\sigma_0 A}{K_2}, \qquad E = t - \left(3t_1 + \bar{t}_m\right)$$

$$B_6 = \frac{2c}{E(p_2 - p_1)^2}\left\{\frac{K_1 u_1}{A}(p_1 + p_2) - \frac{4p_1\sigma_0(3p_2 + p_1)}{p_2 - p_1}\right\}$$

$$C_6 = \frac{8cp_1\sigma_0(p_2 + p_1)}{E(p_2 - p_1)^2}$$

$$E_6 = e^{p_2\bar{t}_m}\left[u_6 - A_6 - \left(B_6 + C_6\bar{t}_m\right)e^{-p_1\bar{t}_m}\right] - F_6\bar{t}_m$$

$$F_6 = -2p_2E_4 \tag{1-19}$$

Once the value of u is known, the reflected stress, σ_r, can be obtained from equations (1-11) and (1-13).

It can be proved that the maximum penetration never occurs within the first cycle of the incident wave, nor within the second cycle if $K_1/A < 5.27 \times 10^6$ lb/in^3 for steel. This is usually satisfied for ordinary rocks. Generally, the maximum penetration, u_m, happens during the third cycle of the incident wave; at the same time, the penetration velocity becomes zero.

The approximate value of rebound velocity can be obtained by taking the mean value of the elastic waves in the tool when the tool is no longer in contact with the rock surface. A more detailed explanation is given in the following section.

1-3 NUMERICAL EXAMPLES AND ILLUSTRATION

Two example problems are given here to compare and illustrate the results discussed in Section 1-1 and 1-2. The value of K_1 and K_2 of the bilinear spring model represents mainly the effect of tip geometry, initial velocity V_0 (or equivalently stress level σ_0) and the rock properties. Only the flat tip tool with high equivalent stress level (V_0 = 520.0 in./sec or σ_0 = 39 ksi) and low stress level (V_0 = 78.67 in./sec or σ_0 = 5.9 ksi) will be discussed here. The same discussion can be applied to any other cases.

Example 1: Flat Tip Tool at High Equivalent Stress Level

$$\frac{K_1}{A} = 2.74 \times 10^6 \text{ lb/in}^3 \quad , \quad \frac{K_2}{A} = 9.10 \times 10^6 \text{ lb/in}^3$$

$$V_o = 520.0 \text{ in./sec (or } \sigma_o = \frac{V_o c \rho}{2} = 39 \text{ ksi)} \quad , \quad l = 1 \text{ in.} \tag{1-20}$$

Table 1-1 Comparison of Impact of Elastic and Rigid Tools

Tool	Maximum penetration $u_m(10^{-3}\text{in.})$	Max. contact force per unit area, F/A (ksi)	Rebound velocity (in./sec)	Time req. to reach peak (μsec)	Time from peak to 0 contact force (μsec)	Total contact time (μsec)
Elastic	8.459	23.18	287*	25.67	16.1	41.8
Rigid	8.603	23.57	285	25.99	14.26	40.25

*approximate value

Example 2: Flat Tip Tool at Low Equivalent Stress Level

$$\frac{K_1}{A} = 3.17 \times 10^6 \text{ lb/in}^3 \quad , \quad \frac{K_2}{A} = 6.67 \times 10^6 \text{ lb/in}^3$$

$$V_o = 78.67 \text{ in./sec (or } \sigma_o = \frac{V_o c \rho}{2} = 5.9 \text{ ksi)} \quad , \quad l = 1 \text{ in.} \tag{1-21}$$

Table 1-2 - Comparison of Impact of Elastic and Rigid Tools

Tool	Maximum penetration $u_m(10^{-3}\text{in.})$	Max. contact force per unit area, F/A (ksi)	Rebound velocity (in./sec)	Time req. to reach peak (μsec)	Time from peak to 0 contact force (μsec)	Total contact time (μsec)
Elastic	1.189	3.77	54*	24.31	17.1	41.4
Rigid	1.210	3.836	54.2	24.16	16.66	40.82

* approximate value

Figures 1-3 and 1-6 give the penetration of the tool against the rock surface for both cases. It is easy to see that the results obtained by considering the tool to be completely rigid and the contact force-penetration characteristics of rock under the impact of a rigid tool is the same as for stress wave incident along a semi-infinite rod is very close to the results obtained by the stress wave approach. With the closeness of u for the two approaches, we could imagine that there should not be much deviation for values of the contact forces. The results are shown in Figures 1-4 and 1-7 for high stress level and low stress level, respectively. There is not much difference between these two cases; i.e., the elastic tool and the rigid tool. In short, these two approaches give very close results as we can also plainly see from Table 1-1 and Table 1-2. The deviation of maximum penetration and maximum contact force for the rigid tool from the elastic tool is less than 2% for both problems.

To understand the wave propagation in the elastic tool, the incident and reflected stress waves at the tip for all time are plotted as shown in Figure 1-5 and Figure 1-8. The solid line gives the magnitude of the incident stress wave at the tip of the tool at any given time while the dashed line represents the corresponding value of the reflected stress. It is interesting to note that the maximum contact force or maximum penetration occurs at a time when incident and reflected waves have the same value; i.e., at a time when these two curves cross each other. The solid lines in the lower figure represent two waves propagating in opposite directions. The total stress in the tool is the sum of these two waves and is shown as the dashed line, which is maximum at the contact and is zero at the free end. The stress distribution is approximately linear. The above results are not surprising since, when the tool reaches maximum penetration, the particle velocity is equal to zero at the tip. We obtain $\sigma_i - \sigma_r$ by equation (1-10). At this stage, maximum stress occurs at the contact end while zero stress happens at the free end.

At the end of contact between tool and rock, the stress waves in the tool are approximately equal to two rectangular waves moving in opposite directions. The rebound velocity can be obtained by using the average value of the stress waves, σ_{av}, and the argument cited in Section 1-2. Thus

$$V_r = \frac{2\sigma_{av}}{c\rho} \tag{1-22}$$

The value of rebound velocity for both the elastic and rigid tool are given in Tables 1-1 and 1-2. The results are still in good agreement to each other.

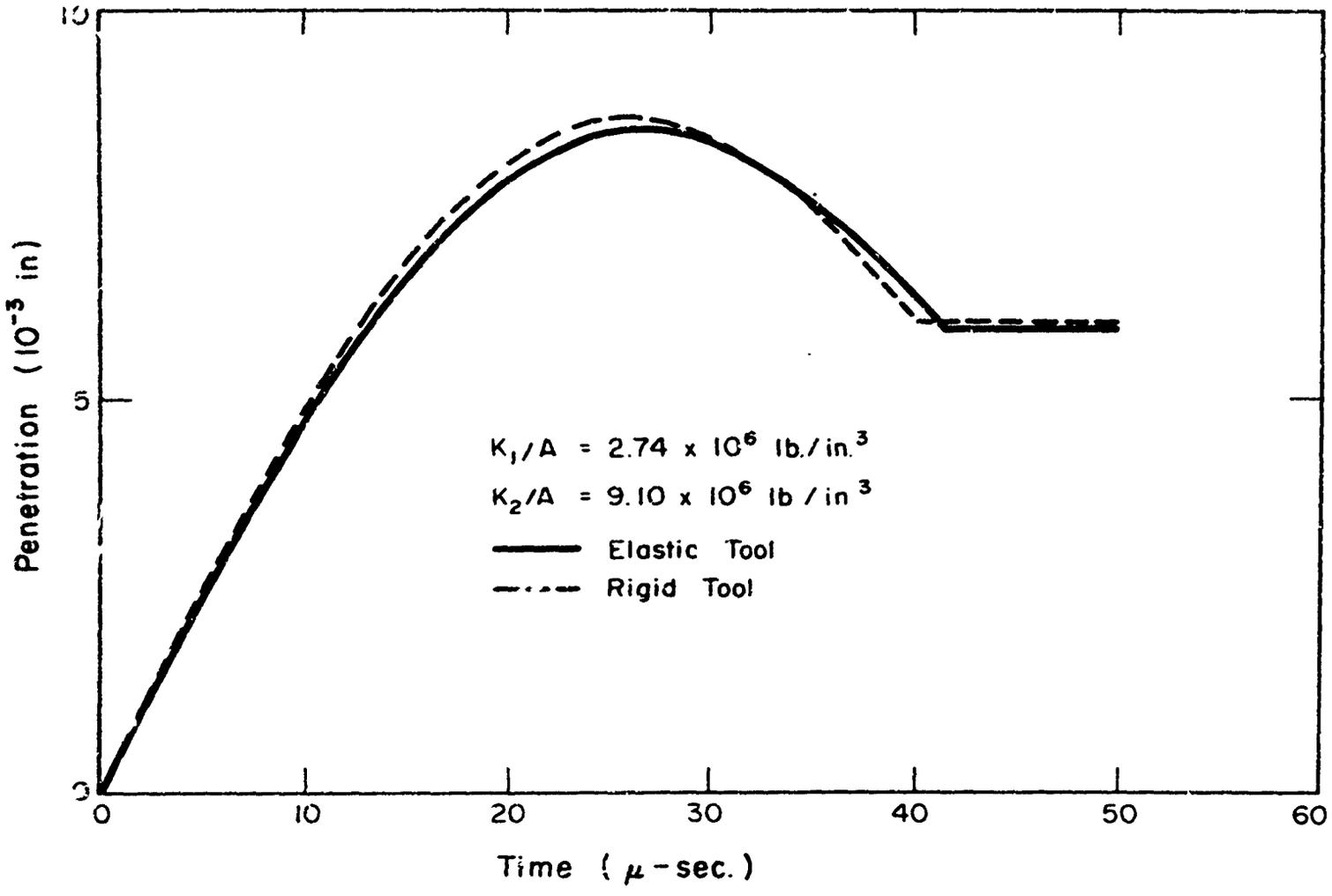

Figure 1-3. Time variation of penetration for flat tip tool with V_o = 520 in./sec.

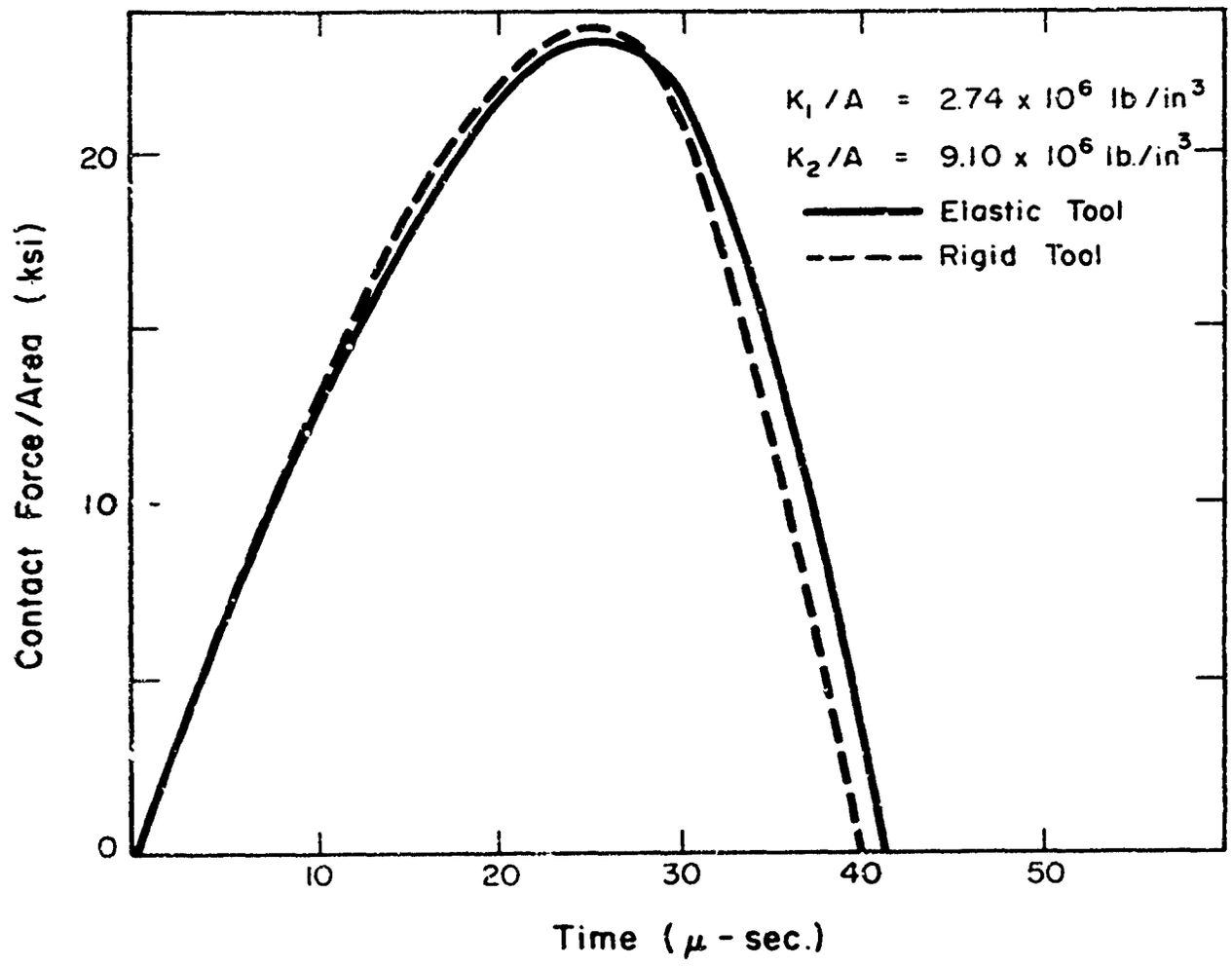

Figure 1-4. Time variation of contact force for flat tip tool with V_o = 520 in./sec.

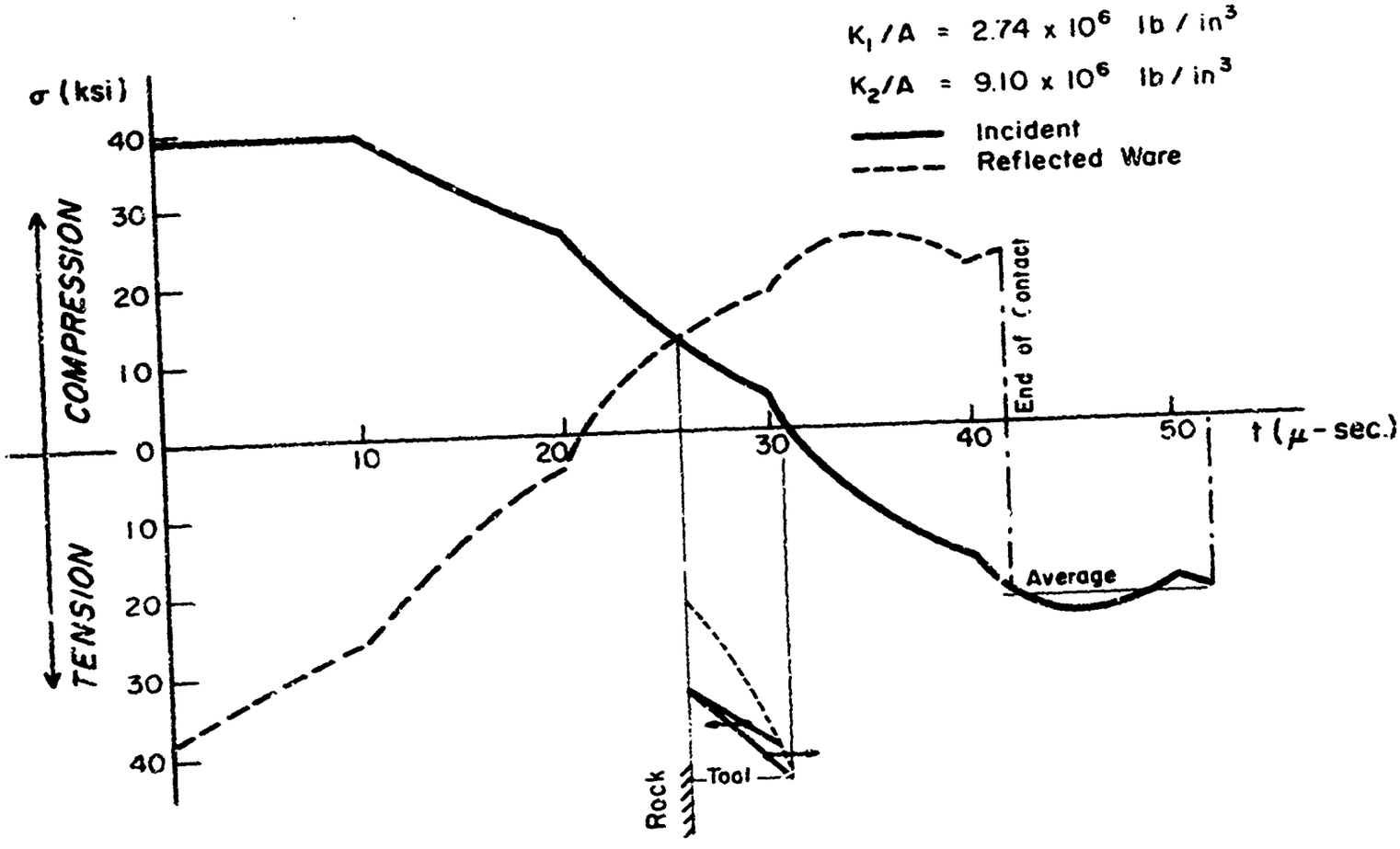

Figure 1-5. Incident and reflected stress wave at flat tip of tool with V_o = 520 in./sec.

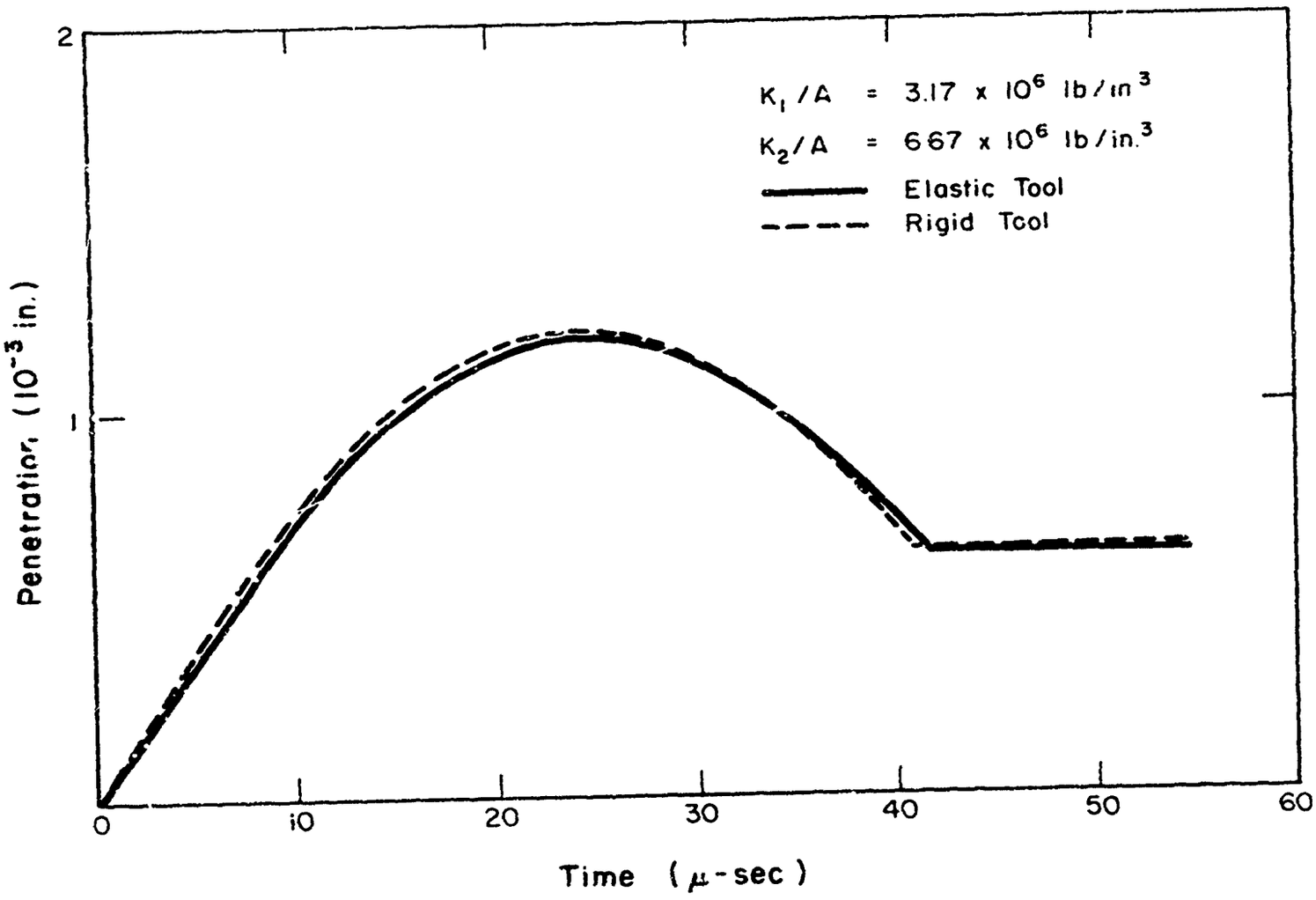

Figure 1-6. Time variation of penetration for flat tip tool with V_o - 78.67 in./sec.

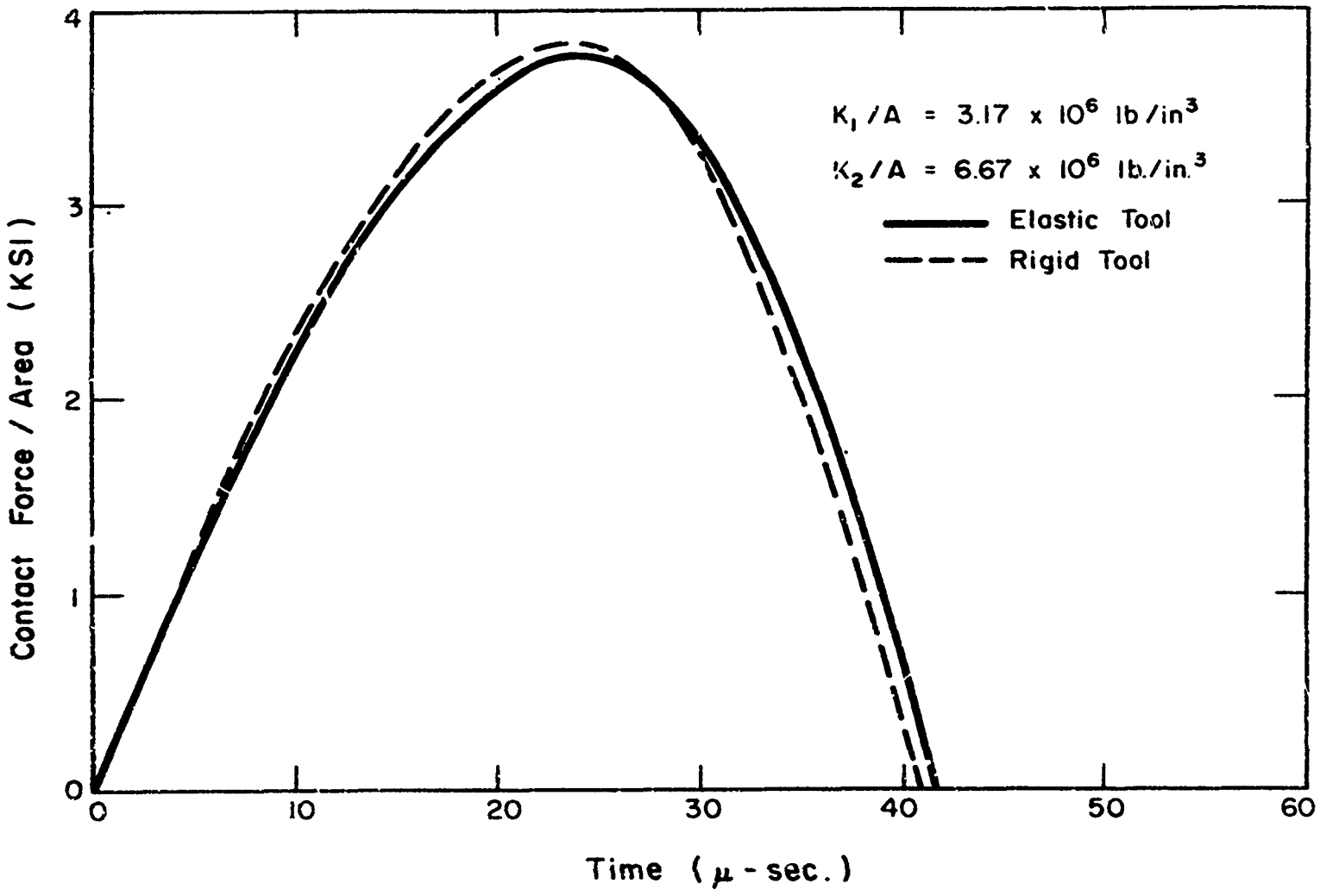

Figure 1-7. Time variation of contact force for flat tip tool with V_o = 78.67 in./sec.

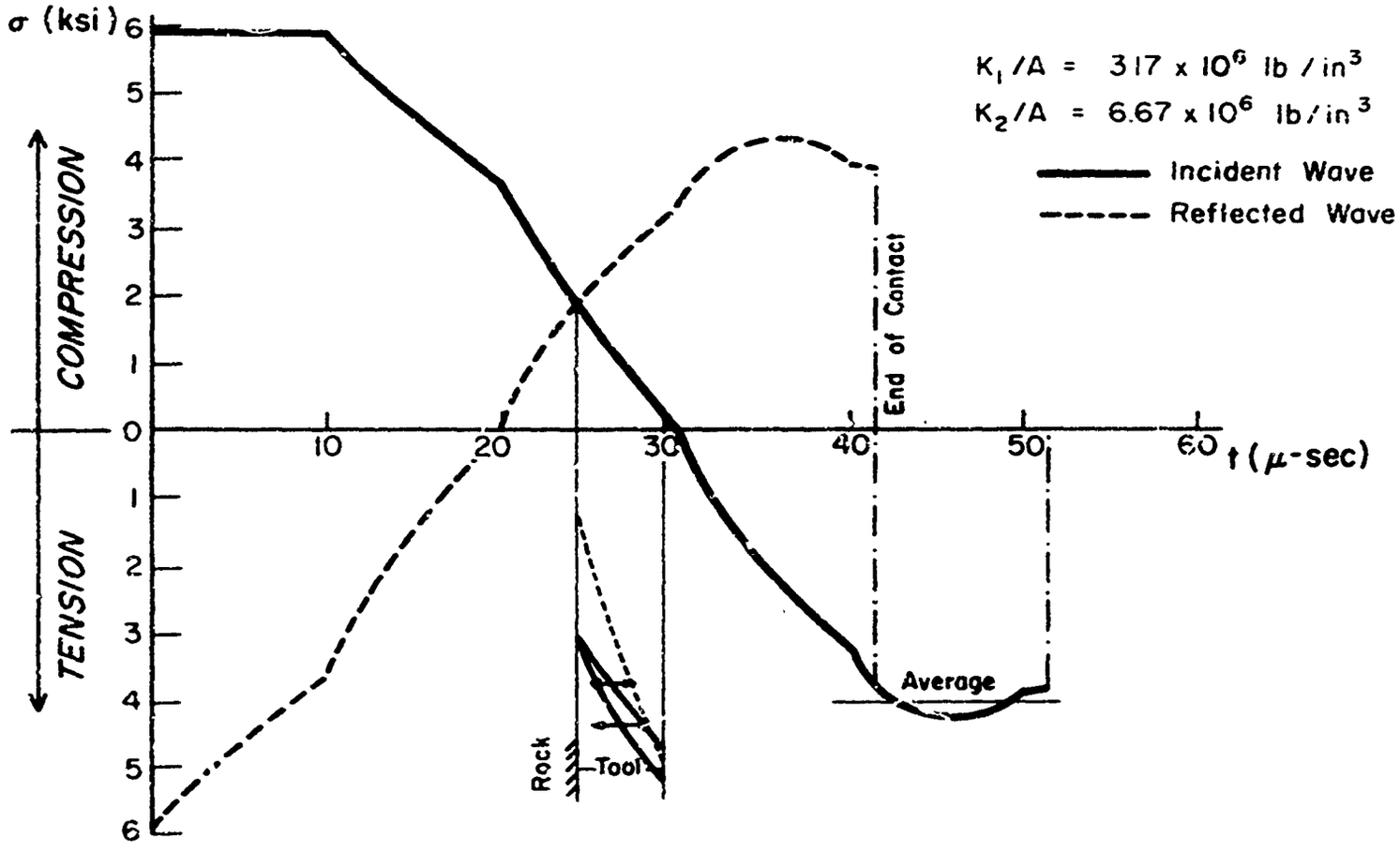

Figure 1-8. Incident and reflected stress waves at flat tip of tool with V_o = 78.67 in./sec.

1-4 CONCLUSION

By looking at the results obtained in Section 1-3, it shows that the rigid tool method yields very good results. This justifies the assumption made at the beginning of Section 1-1 and is acceptable from a practical point of view. By this assumption, it is possible for us to reduce a theoretically and numerically complicated problem to a simple problem whose solution is well-known to all engineers.

2. STRESSES DEVELOPED DURING SONIC IMPACT

Many sonic processes utilize impact coupling to transfer energy from the transducer to the load. The impact may occur directly between the transducer tip and the work surface, or between the tip and an intervening tool. By either way, the objective is to transfer sonic energy, in the form of standing waves in the transducer, to the load during a fraction of cycle of contact. The two major parameters of interest during this process are the amount of energy transfer into the load and the peak forces developed at the load-transducer tip interface.

In the following report, a number of sonic impact situations will be analyzed with the objective of determining such aspects as energy transfer and peak force.

2-1 IMPACT AGAINST A ROD

When a vibrating transducer tip impacts a load, the nature of the stress wave transmission and reflection is determined by the impedance matching of the tip and load. Various loads, such as springs, masses, dashpots, rock, etc., all present different impedances to the tip. The case of a load represented by another elastic rod is fairly simple to analyze and will be instructive for the present case. Thus, from an analytical basis, it enables the effects of impedance matching on stress and energy to be easily assessed. In addition, the rod on rod impact represents the configuration used in some sonic impact situations.

Given is two rods in contact as shown in Figure 2-1, with a stress wave incident on the function. It is well-known [1] that the transmitted and reflected waves will be given by

$$\sigma_T = \frac{2A_1\rho_2c_2}{A_1\rho_1c_1 + A_2\rho_2c_2}\,\sigma_I, \qquad \sigma_R = \frac{A_2\rho_2c_2 - A_1\rho_1c_1}{A_1\rho_1c_1 + A_2\rho_2c_2}\,\sigma_I \qquad (2\text{-}1.1)$$

From the definition of rod impedance, $Z = \rho cA$, the preceding equations may be written as

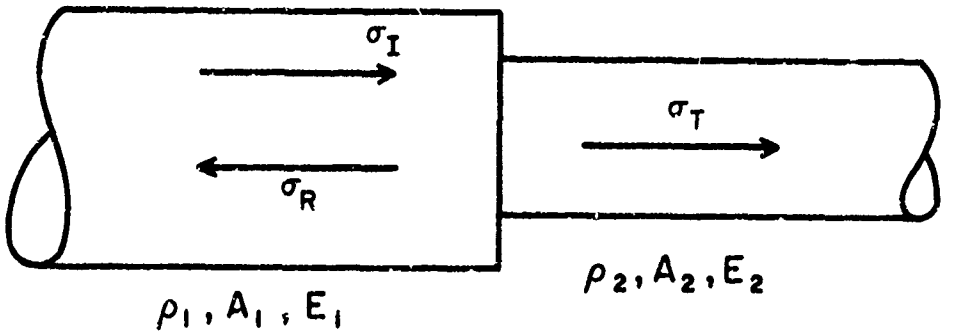

Figure 2-1. Incident, reflected and transmitted waves at a rod discontinuity.

$$\sigma_T = \frac{2Z_2(A_1/A_2)}{Z_1 + Z_2}\,\sigma_I = \frac{2(Z_2/Z_1)(A_1/A_2)}{1 + Z_2/Z_1}\,\sigma_I$$

$$\sigma_R = \frac{Z_2 - Z_1}{Z_1 + Z_2}\,\sigma_I = \frac{Z_2/Z_1 - 1}{1 + Z_2/Z_1}\,\sigma_I \qquad (2\text{-}1.2)$$

These may be written in terms of transmission and reflection coefficients,

$$\sigma_T = K_T\sigma_I \quad , \qquad \sigma_R = K_R\sigma_I \qquad (2\text{-}1.3)$$

where

$$K_T = \frac{2A_1\rho_2c_2}{A_1\rho_1c_1 + A_2\rho_2c_2} = \frac{2(Z_2/Z_1)(A_1/A_2)}{1 + Z_2/Z_1}$$

$$K_R = \frac{A_2\rho_2c_2 - A_1\rho_1c_1}{A_1\rho_1c_1 + A_2\rho_2c_2} = \frac{Z_2/Z_1 - 1}{1 + Z_2/Z_1} \qquad (2\text{-}1.4)$$

It is of interest to plot σ_T/σ_I and σ_R/σ_I for various ranges of impedance and area mismatches. The results are shown in Figure 2-2. The dependence of σ_T/σ_I on the area ratio as well as the impedance ratio points out how energy transfer and stress level are somewhat independent of one another. Thus, for $Z_2/Z_1 = 1$, the energy transfer will always be 100%. The induced stress level (transmitted stress level) may be adjusted by altering the A_1/A_2 ratio.

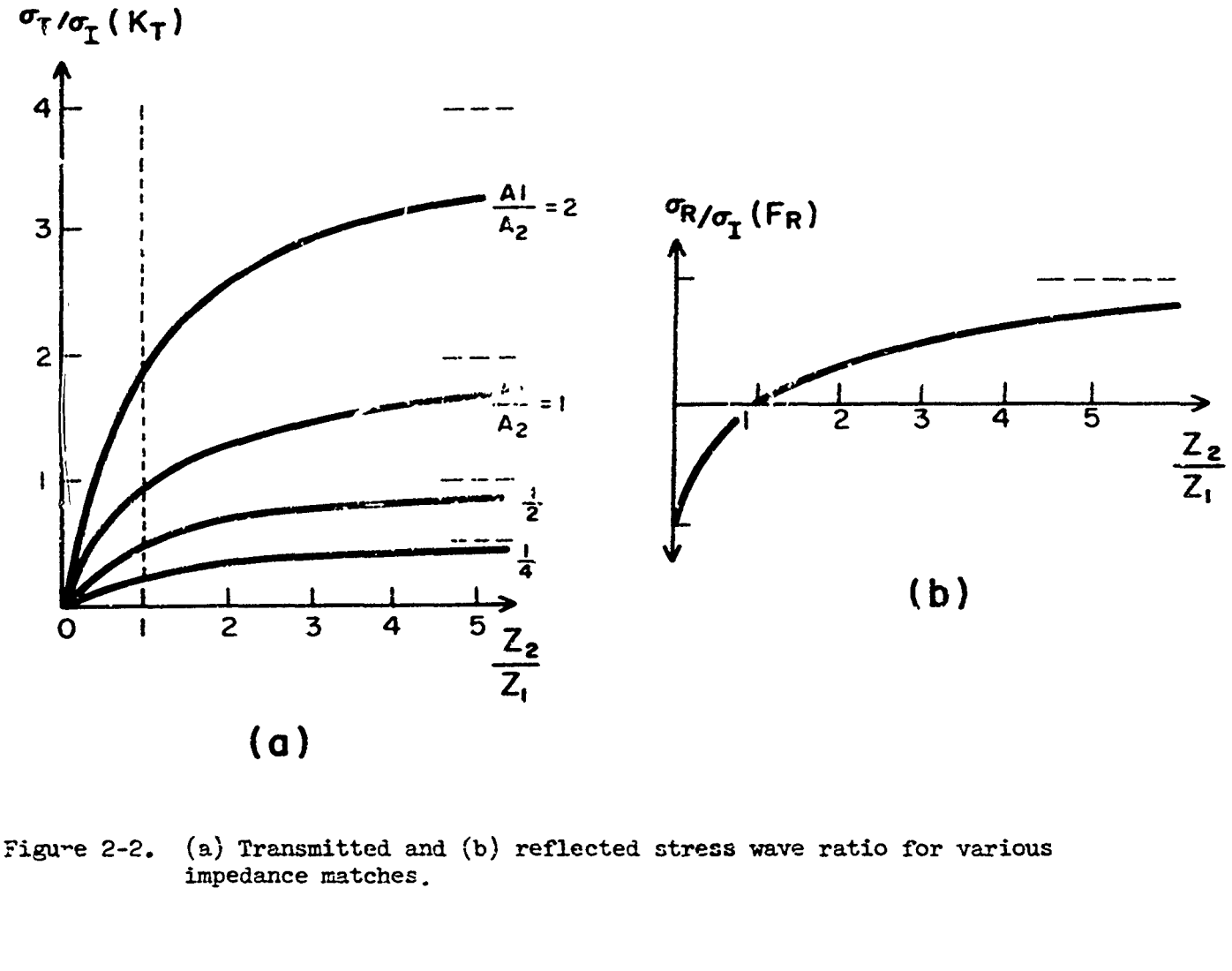

Figure 2-2. (a) Transmitted and (b) reflected stress wave ratio for various impedance matches.

The transmitted power is given by

$$P_T = -A_2\sigma_T v_2 \tag{2-1.5}$$

where

$$v_2 = \frac{\delta u_T}{\delta t} \qquad \sigma_T = E_2 \frac{\delta u_T}{\delta x} \tag{2-1.6}$$

If

$$u_T = f(x_2 - c_2 t) \tag{2-1.7}$$

then

$$v_2 = -c_2 f'_T \qquad \sigma_T = E_2 f'_T \tag{2-1.8}$$

The result for v_2 may be written as

$$v_2 = -\frac{c_2}{E_2}\sigma_T \tag{2-1.9}$$

Then the transmitted power is given by

$$P_T = \frac{A_2 c_2}{E_2}\sigma_T^2 \tag{2-1.10}$$

Using equation (2-1.3) this may be expressed in terms of the incident wave as

$$P_T = \frac{A_2 c_2}{E_2} K_T^2 \sigma_I^2 \tag{2-1.11}$$

The transmitted energy will be given by

$$E_T(t) = \int_0^t P_T(\xi)d\xi \tag{2-1.12}$$

The reflected power will be given by

$$\begin{aligned} P_R = P_I - P_T &= \frac{A_1 c_1}{E_1}\sigma_I^2 - \frac{A_2 c_2}{E_2} K_T^2 \sigma_I^2 \\ &= \frac{A_1 c_1}{E_1}\left(1 - \frac{A_2 c_2 E_1}{A_1 c_1 E_2} K_T^2\right)\sigma_I^2 \end{aligned} \tag{2-1.13}$$

Noting that $P_I = A_1 c_1 \sigma_I^2/E_1$, equations (2-1.11) and (2-1.13) may be written as

$$\frac{P_T}{P_I} = \frac{A_2 c_2 E_1}{A_1 c_1 E_2} K_T^2 \quad , \quad \frac{P_R}{P_I} = \left(1 - \frac{A_2 c_2 E_1}{A_1 c_1 E_2} K_T^2\right)$$

$$= \frac{Z_1}{Z_2}\left(\frac{A_2}{A_1}\right)^2 K_T^2 = \left(1 - \frac{Z_1}{Z_2}\left(\frac{A_2}{A_1}\right)^2 K_T^2\right) \qquad (2\text{-}1.14)$$

Noting the definition of K_T, given by equation (2-1.4), the preceding may be rewritten as

$$\frac{P_T}{P_I} = \frac{4(Z_2/Z_1)}{(1 + Z_2/Z_1)^2} \quad , \quad \frac{P_R}{P_I} = 1 - \frac{4(Z_2/Z_1)}{(1 + Z_2/Z_1)^2} \qquad (2\text{-}1.15)$$

It is seen that power transmission is dependent only on impedance matching, and is independent of area ratios. These quantities are plotted in Figure 2-3.

It is of interest to note that the transmitted power is relatively insensitive to the impedance match for $Z_2/Z_1 > 1/2$. For example, a minimum of 75% of the power is transmitted for $1/3 < Z_2/Z_1 \leq 3$.

The result for the rod impedance has been given as $Z = \rho Ac$. The derivation of this is given below. Consider the semi-infinite rod, as shown in Figure 2-4. The solution of the equation of motion

$$\frac{\delta^2 u}{\delta x^2} = \frac{1}{c^2}\frac{\delta^2 u}{\delta t^2} \qquad (2\text{-}1.16)$$

of the form

$$u = U e^{i\omega t} \qquad (2\text{-}1.17)$$

is

$$u = B e^{-i\gamma x} e^{i\omega t} \quad , \quad \gamma = \omega/c \qquad (2\text{-}1.18)$$

The constant B is given from the boundary condition,

$$-EA \left.\frac{\delta u}{\delta x}\right|_{x=0} = F_o e^{i\omega t} \qquad (2\text{-}1.19)$$

which gives

$$B = F_o/EAi\gamma \qquad (2\text{-}1.20)$$

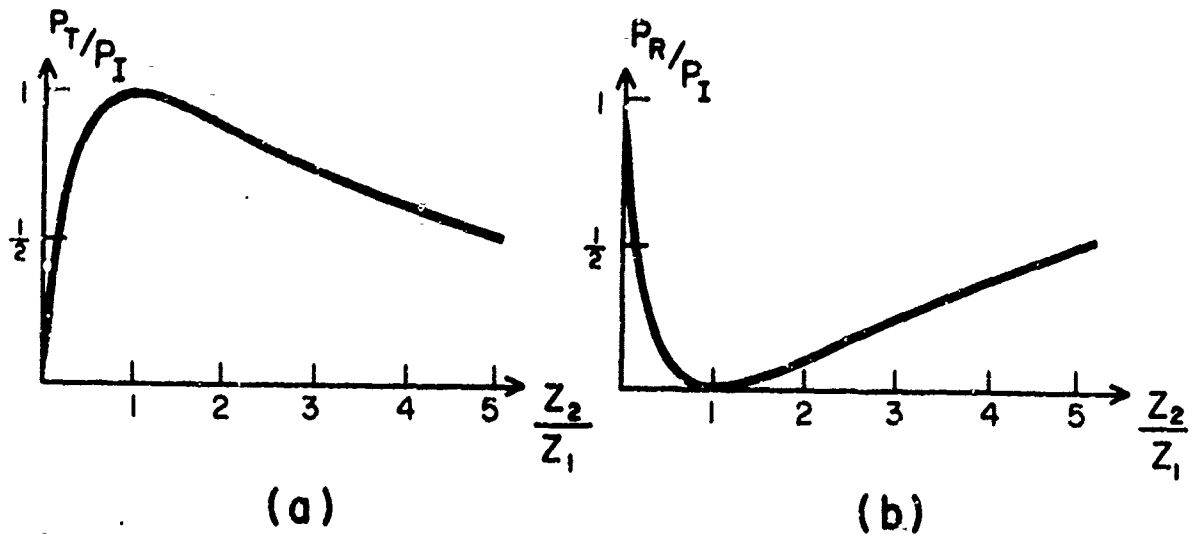

Figure 2-3. (a) Transmitted and (b) reflected power for various impedance matches.

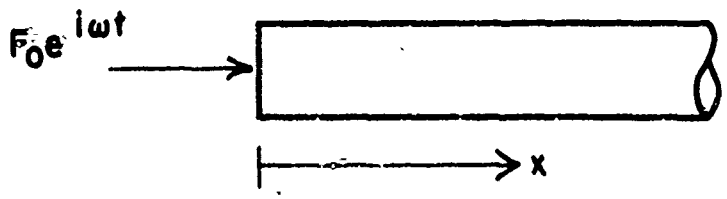

Figure 2-4. Semi-infinite rod driven by a harmonic forcing function.

then,

$$Z = \frac{F}{\dot{u}} = \frac{F_o\, e^{i\omega t}}{(F_o/EAi\gamma)\, i\omega e^{i\omega t}} = \frac{EA\gamma}{\omega} = \frac{EA}{c} = \rho Ac \qquad (2\text{-}1.21)$$

2-2 WAVE TRANSMISSION INTO A WORK-HARDENING LOAD

Processes in metal deformation involve loads that, under static conditions, involve elastic-plastic deformation characteristics of various degrees of complexity. For purposes of the present analysis, it will be assumed that the load may be characterized as shown in Figure 2-5. It is possible to obtain the force-deformation relation shown by quasistatic tests, or by dynamic tests, as have previously been done for rock drilling. Representing a complicated media by an idealized force-deformation curve, such as the above, essentially neglects inertia effects associated with the load, and incorporates only the stiffness effects.

The wave propagation situation is shown in Figure 2-6. At $x = 0$, we have

$$F = A\left[\sigma_i(o,t) + \sigma_r(o,t)\right] \qquad (2\text{-}2.1)$$

where

$$F = \begin{cases} +K_1\, u(o,t) & , \quad \dot{u}(o,t) < 0,\ -u_y < u(o,t) < 0 \\ +\left[K_2\, u(o,t) + b\right] & , \quad \dot{u}(o,t) < 0,\ -u_p < u(o,t) < -u_y \\ +\left[K_1\, u(o,t) - d\right] & , \quad \dot{u}(o,t) > 0,\ -u_p < u(o,t) \end{cases} \qquad (2\text{-}2.2)$$

and where

$$b = F_y - K_2 u_y \quad , \qquad d = K_2\left(u_p - u_y\right) + F_y - K_1 u_p \qquad (2\text{-}2.3)$$

The method for determining the reflected stress waves and deformation have been presented in other sources, such as Mahban [2]. Thus, in addition to equation (2-2.1), there is the velocity condition, given by

$$\dot{u}(o,t) = \frac{1}{\rho c_o}\left[\sigma_i(o,t) - \sigma_r(o,t)\right] \qquad (2\text{-}2.4)$$

Eliminating $\sigma_r(o,t)$ from (2-2.1), (2-2.4) gives

$$\frac{F(o,t)}{A} + \rho c_o \dot{u}(o,t) = 2\sigma_i(o,t) \qquad (2\text{-}2.5)$$

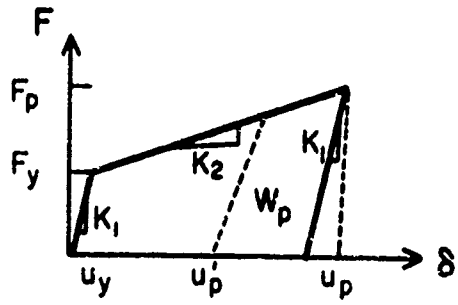

Figure 2-5. Force-deformation characteristics of a work-hardening load.

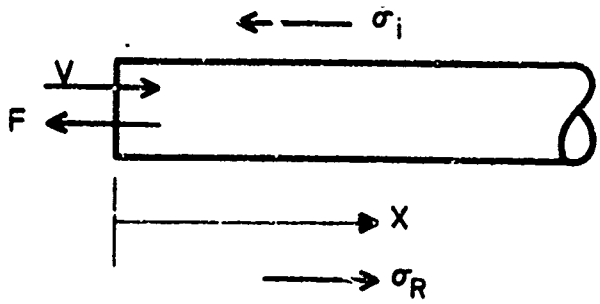

Figure 2-6. Force and velocity and conditions in a rod in the presence of incident and reflected stress waves.

or

$$\dot{u}(o,t) + \frac{1}{\rho c_o A} F(o,t) = \frac{2}{\rho c_o} \sigma_1(o,t) \tag{2-2.6}$$

Recalling the definition of rod impedance as

$$Z_o = \rho c_o A \tag{2-2.7}$$

then we have

$$\dot{u}(o,t) + \frac{F(o,t)}{Z_o} = \frac{2F_1(o,t)}{Z_o} \tag{2-2.8}$$

where $F(o,t)$ is prescribed according to equation (2-2.2).

Consider first the portion of the response in the elastic region. Thus, (2-2.8) becomes

$$\dot{u}(o,t) + \frac{K_1}{Z_o} u(o,t) = \frac{2F_1(o,t)}{Z_o} \tag{2-2.9}$$

This has the solution

$$u(o,t) = C\, e^{(-K_1/Z_o)t} + u_p \tag{2-2.10}$$

To obtain the particular solution, $F_1(o,t)$ must be specified. The case of $F_1(o,t)$ as a harmonic wave train is of practical value for sonics. The case of $F_1(o,t)$ as a rectangular pulse function is considerably simpler to analyze, however, and may be used to approximate practical wave shapes. We shall suppose

$$F_1(o,t) = \begin{cases} F_o\ , & o \leq t < t_1 \\ o\ , & t_1 < t < \infty \end{cases} \tag{2-2.11}$$

Depending on the magnitude and duration of the pulse, a variety of responses are possible. For the period $t < t_1$, (2-2.10) becomes

$$u(o,t) = C\, e^{(-K_1/Z_o)t} + \frac{2F_o}{K_1} \tag{2-2.12}$$

The constant C is determined from the condition,

$$u(o,o) = 0 \tag{2-2.13}$$

giving

$$C = -\frac{2F_o}{K_1} \tag{2-2.14}$$

Thus,

$$u(o,t) = \frac{2F_o}{K_1}\left(1 - e^{(-K_1/Z_o)t}\right) \tag{2-2.15}$$

The forces generated will be

$$F(o,t) = 2F_o\left(1 - e^{(-K_1/Z_o)t}\right) \tag{2-2.16}$$

The behavior of the generated force is shown in Figure 2-7.

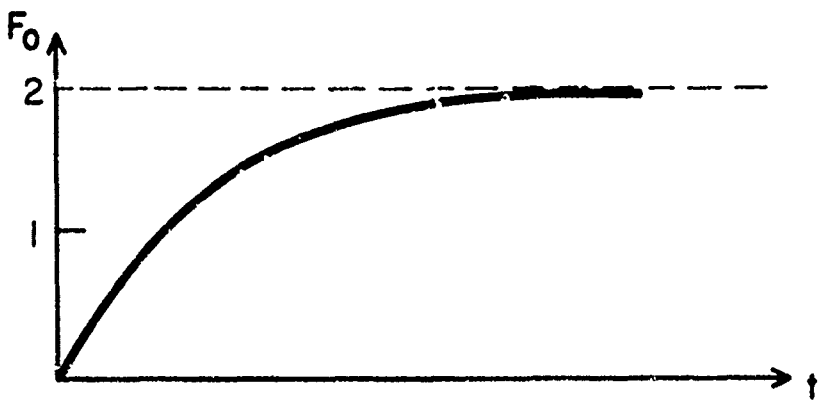

Figure 2-7. Contact force at rod end for linear region of force-deformation curve.

The first question of interest is whether the load will yield; i.e., referring to Figure 2-5, is F_y attained? It is obvious that this depends on two factors, (a) the magnitude of the incident pulse, F_o, and (b) the duration of the incident pulse, t_1. Assuming that F_o is sufficiently large, so that $F_y < 2F_o$, the time required for this to occur, t_y is

$$F_y = 2F_o\left(1 - e^{(-K/Z_o)t_y}\right) \tag{2-2.17}$$

or

$$t_y = -\frac{Z_o}{K_1} \ln\left(1 - F_y/2F_o\right) \qquad (2\text{-}2.18)$$

We now consider the behavior after the yield point is reached. The governing differential equation (2-2.8) takes the form

$$\dot{u}(o,t) + \frac{K_2}{Z_o} u(o,t) = \frac{2F_1(o,t)}{Z_o} - \frac{b}{Z_o} \qquad (2\text{-}2.19)$$

Again we have for the solution

$$u(o,t) = D\, e^{(-K_2/Z_o)t} + u_p \qquad (2\text{-}2.20)$$

Assuming that $F_1(o,t)$ is still acting, so that it is given by F_o, the particular solution is a constant, given by

$$u_p = \frac{2F_o - b}{K_2} \qquad (2\text{-}2.21)$$

The constant D is found from the conditions at $t - t_y$. Thus, at $t - t_y$, $u(o,t) = u_y$, so that

$$u_y = D\, e^{(-K_2/Z_o)t_y} + u_p \qquad (2\text{-}2.22)$$

or

$$D = e^{(-K_2/Z_o)t_y}\left(u_y - u_p\right) \qquad (2\text{-}2.23)$$

where

$$u_y - u_p = u_y - \frac{\left(2F_o - F_y + K_2 u_y\right)}{K_2} = u_y - \frac{2F_o}{K_2} + \frac{F_y}{K_2} - u_y$$

$$= \frac{-\left(2F_o - F_y\right)}{K_2} \qquad (2\text{-}2.24)$$

Then

$$u(o,t) = \left(\frac{2F_o - F_y}{K_2}\right)\left[1 - e^{(-K_2/Z_o)(t-t_y)}\right] + u_y \qquad (2\text{-}2.25)$$

The generated force, given by equation (2-2.2) is

$$F(o,t) = \left(2F_o - F_y\right)\left[1 - e^{(-K_2/Z_o)(t-t_y)}\right] + F_y, \ (t < t_y) \tag{2-2.26}$$

To plot the general behavior of (2-2.26), it is helpful to note that the time constant of the above is given by $T_2 = Z_o/K_2$, and that of the result (2-2.15) is $T_1 = Z_o/K_1$. Since $K_1 > K_2$, then $T_1 < T_2$. Thus, after yield occurs, the force rises less rapidly. This behavior is shown in Figure 2-8. The asymptotic value of the generated force is still $2F_o$.

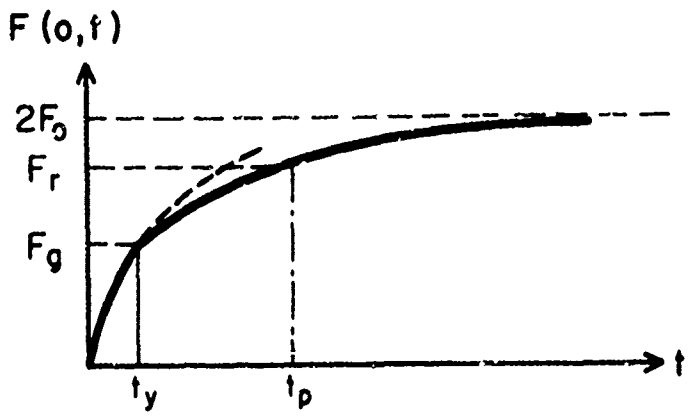

Figure 2-8. Contact force at rod end for bilinear portion of force-deformation curve.

In Figure 2-5, the force F_p is meant to indicate some necessary peak force level that must be attained in order to accomplish the process. It should be evident at this stage that $2F_o > F_p$ is thus one requirement for process accomplishment. If this condition is meant and the pulse duration, t_1 is sufficiently long, the peak force will be attained in some time, t_p, as shown in Figure 2-8.

A more likely occurrence in sonic processes is that the pulse will end before the process is accomplished and unloading will occur. During unloading, $F_1(o,t) = 0$ in (2-2.8), so that the equation of motion is

$$\dot{u}(o,t) + \frac{F(o,t)}{Z_o} = 0, \ , \qquad (t_1 < t < \infty) \tag{2-2.27}$$

The expression for $F(o,t)$ will be similar to (2-2.2) except for a difference in the value of d (as defined by (2-2.3) d corresponds to the value for u_p, F_p, and not an arbitrary value), u_1, F_1. Thus, we have

$$F(o,t) = K_1\, u(o,t) - d \tag{2-2.28}$$

where

$$d = K_1 u_1 - F_1 \tag{2-2.29}$$

The relation between F_1, u_1 is given from (2-2.2) as

$$F_1 = K_2 u_1 + F_y - K_2 u_y - K_2\,(u_1 - u_y) + F_y \tag{2-2.30}$$

Thus,

$$d = (K_1 - K_2) u_1 + F_y - K_2 u_y \tag{2-2.31}$$

noting that $F_y = K_1 u_y$, (2-2.31) simplifies to

$$d = (K_1 - K_2)\,(u_1 + u_y) \tag{2-2.32}$$

Thus, using (2-2.28), the equation of motion is

$$\dot{u} + \frac{K_1}{Z_o}\, u(o,t) = \frac{d}{Z_o} \tag{2-2.33}$$

having the solution

$$\dot{u}(o,t) = G\, e^{(-K_1/Z_o)t} + \frac{d}{K_1} \tag{2-2.34}$$

The constant G is established from the condition that at $t = t_1$, $u = u_1$. This gives

$$u(o,t) = \left(u_1 - \frac{d}{K_1}\right) e^{(-K_1/Z_o)(t-t_1)} + \frac{d}{K_1} \tag{2-2.35}$$

From the solution, as $t \to \infty$, $u(o,t) \to d/K_1$. This represents the residual, or permanent deformation of the system, as shown in Figure 2-5. This is the value given by (2-2.28) for $F(o,t) = 0$. Thus, as $t \to \infty$, we obtain

$$u_d = \frac{d}{K_1} \tag{2-2.36}$$

from (2-2.28) and from the solution (2-2.35). The generated force is given by

$$F(o,t) = (K_1 u_1 - d)e^{(-K_1/Z_o)(t-t_1)} \qquad (2\text{-}2.37)$$

A plot of this force as part of the total response is shown in Figure 2-9.

The results thus far show the generated force presuming that $2F_o > F_p$, but where also $F_1 < F_p$. Thus, unloading occurs before the process can be accomplished by the force pulse. We now consider what occurs when a new pulse strikes the material. It is possible to describe rather precisely the behavior without additional mathematical solutions. Thus, as the new pulse strikes the load, the initial force generation will be again governed by the elastic slope, K_1. However, due to the work-hardening, the force will have to rise to the previous maximum F_1 (instead of F_y as shown in Figure 2-9) before the response is governed by the slope K_2. The curve will continue to rise until $2F_o$ is attained, F_p is reached, or the pulse ends. A series of hypothetical pulses is shown in Figure 2-10. Thus, in the figure, the implication is that three pulses are required to attain F_p.

For subsequent cycles, increasing amounts of the deformation time are required just to overcome the elastic resistance of the system. Thus, pulses of increasing length might be required.

Numerous aspects of "time" could now be discussed, such as the total time required to do the process, optimum time, etc. However, further discussion of these, or other aspects, such as pulse superposition, will be postponed until later.

<u>Special Case:</u> <u>Elastic-perfectly Plastic Load</u>

Suppose the force-deformation characteristics of the load are characterized as in Figure 2-11. The work process is considered to be complete when the deformation reaches u_p. Again, supposing a rectangular pulse impinges on such a load, the initial responce, up to yield point, will be given by the previous analysis, results (2-2.16) and (2-2.18). After yield occurs, the governing equation is (2-2.19), where $K_2 = 0$. Thus,

$$\dot{u}(o,t) = \frac{2F_o}{Z_o} - \frac{b}{Z_o} \quad , \qquad b = F_y \qquad (2\text{-}2.38)$$

or

$$\dot{u}(o,t) = \frac{(2F_o - F_y)}{Z_o} \qquad (2\text{-}2.39)$$

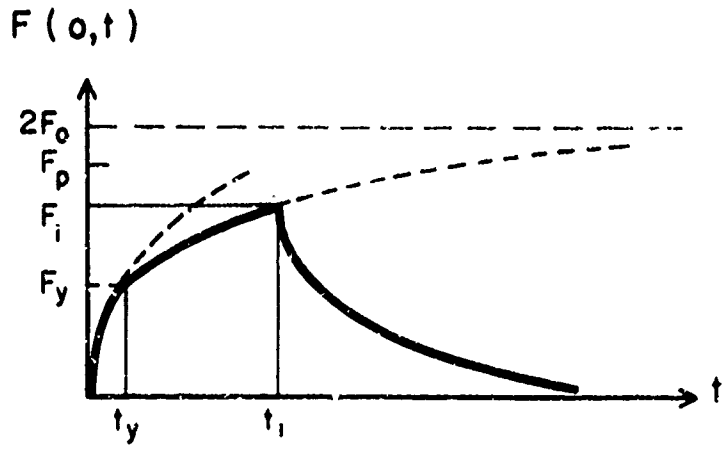

Figure 2-9. Complete loading and unloading end force behavior for bilinear curve.

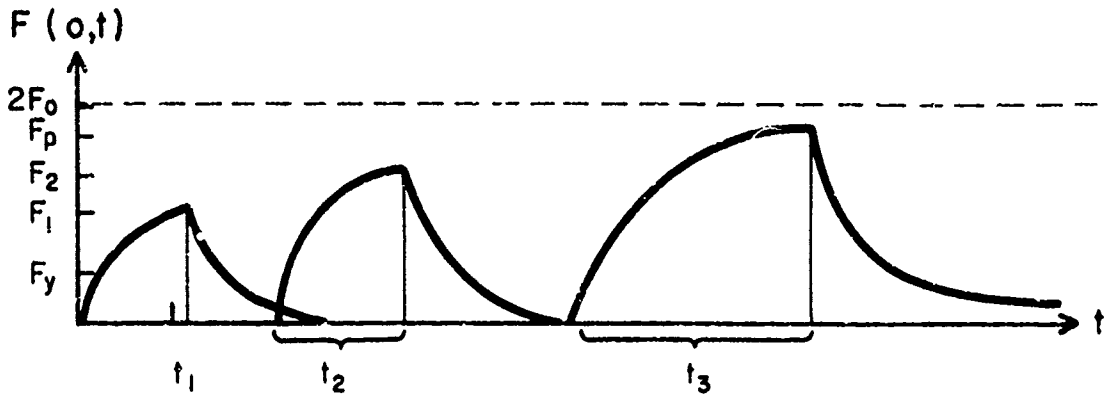

Figure 2-10. Force pulses required to reach F_p.

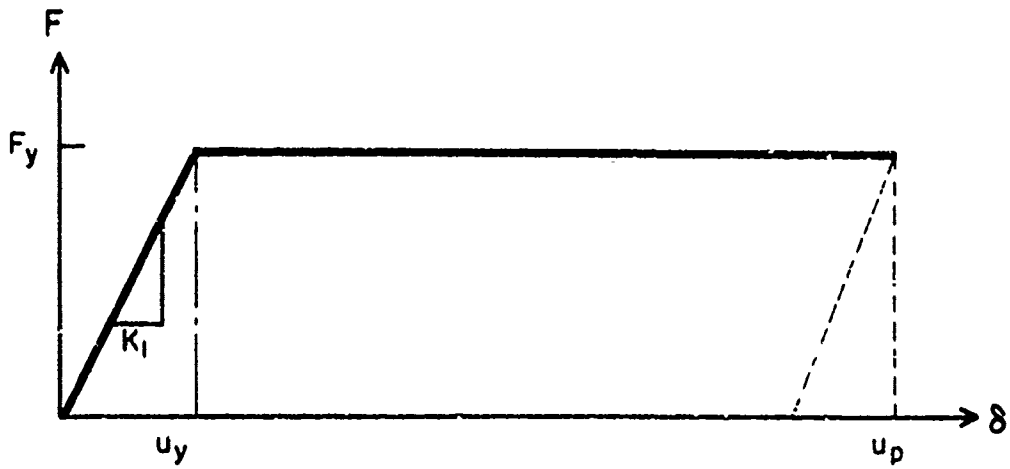

Figure 2-11. Force-deformation curve of an elastic, perfectly plastic load.

This has the solution

$$u(o,t) = \frac{(2F_o - F_y)}{Z_o} t + C \qquad (2\text{-}2.40)$$

where C is found from the condition that at $t = t_y$, $u(o,t) = u_y$. Thus,

$$C = u_y - \frac{(2F_o - F_y)}{Z_o} t_y \qquad (2\text{-}2.41)$$

and

$$u(o,t) = \frac{(2F_o - F_y)}{Z_o} (t-t_y) + u_y \qquad (2\text{-}2.42)$$

Of course, the generated force remains constant during this time. If the pulse ends, the system unloading is governed by the slope K_1 as previously shown. The behavior of the generated force would be as shown in the Figure 2-12. This response is perhaps seen as the logical limit of that shown in Figure 2-9, for smaller and smaller K_2.

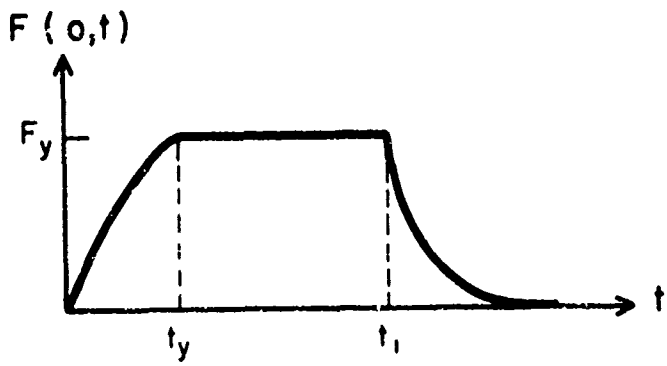

Figure 2-12. Force pulse for an elastic, perfectly plastic load.

More complex cases of force-deformation curves could be analyzed. Thus, the force deformation of a lead slug compressed in a cylindrical die was found [3] to be approximately that shown in Figure 2-13(a). The geometry of the slug-die system is shown in the Figure 2-13(b). Now, the initial region of the force-deformation curves, governed by K_1, is the elastic deformation of the slug. The portion of the curve governed by K_2 represents the work-hardening of the slug. At a certain point of loading, the expanded slug comes against the sidewalls of the

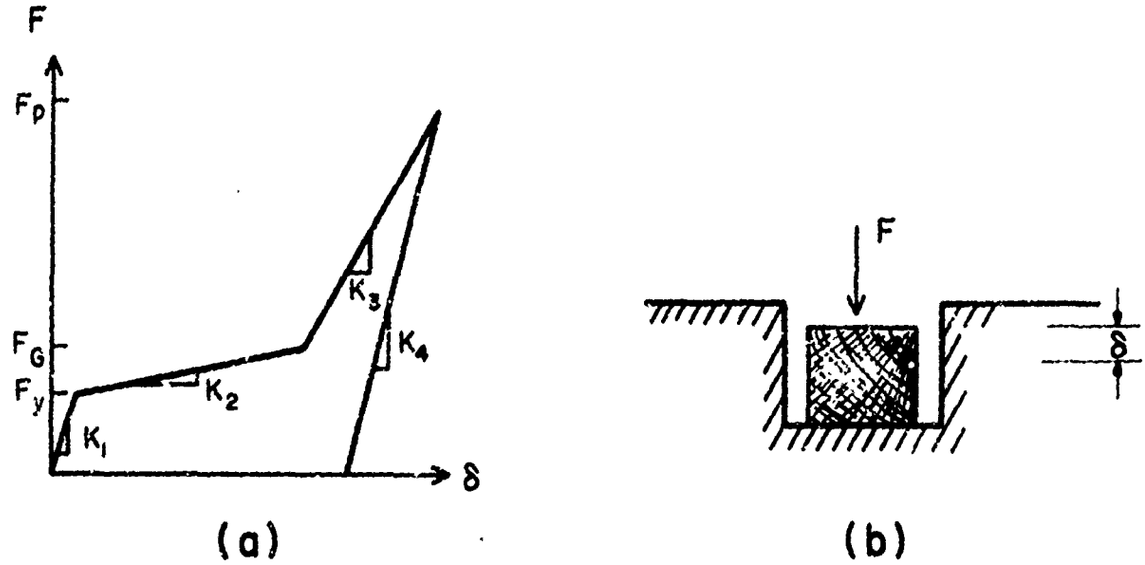

Figure 2-13. (a) Force-deformation curve for a slug-die configuration as shown in (b).

die. The additional constraint causes the slope of the force-deformation curve to sharply increase giving an equivalent work-hardening. On the basis of the previous work, it is possible to predict the nature of the generated force rather easily. Thus, suppose the pulse is of sufficient duration to pass from K_1, through K_2 and onto the K_3 portion. The response would be as shown in Figure 2-14.

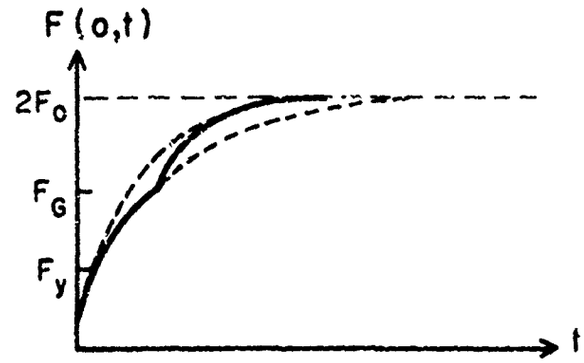

Figure 2-14. Force pulse acting on slug governed by by a force-deformation curve as shown in Figure 2-13(a).

2-3 WAVE TRANSMISSION INTO ROCK

This has been extensively analyzed by Mahban [4], but a few additional comments are in order. For a given rock and drill-tip geometry, we assume that the force-deformation relation is as shown in Figure 2-15. Now in rock, as implied by the force-deformation relation shown, there is no "perfectly-elastic" region (except for very low loads) as there is for metal loads. Thus, any force developed will cause some permanent deformation (or penetration). Every impact will perform some useful work, whereas for loads exhibiting a perfectly elastic region, a portion of the force pulse must overcome the elastic resistance. If the pulse level is too low or too short, it is entirely possible for no useful work to be done.

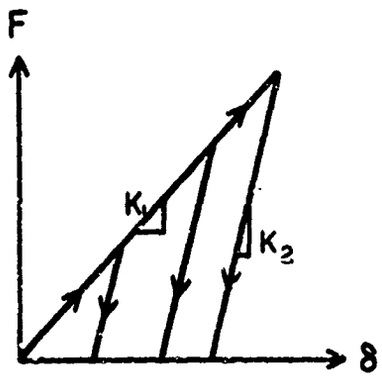

Figure 2-15. Force-deformation curve for rock.

With these remarks in mind, and the results of previous analyses available, it is possible to sketch the force generation curve directly. The time constants of the loading and unloading portions are governed by the slopes K_1, K_2. Since $K_2 > K_1$, the system will unload more rapidly than load, as shown in Figure 2-16. The figure actually depicts several possible responses, depending on the duration of the applied pulse.

Because of the markedly different force-deformation relation for rock in contrast to metal loads, the amount of energy and peak forces required to accomplish a rock penetration process may vary widely, whereas there are invariant quantities for the metal load. To illustrate this, a sonic rock penetration process may be considered "accomplished" when a net penetration, u_p, is attained. In Figure 2-17, it is shown how this may be attained by several combinations of paths. Thus, path 0-3-4 reaches u_p by one impact, path 0-2-7-9-4 represents two impacts, and the remaining path represents five impacts. Obviously, the peak forces attained and total energy required differ markedly for the three cases.

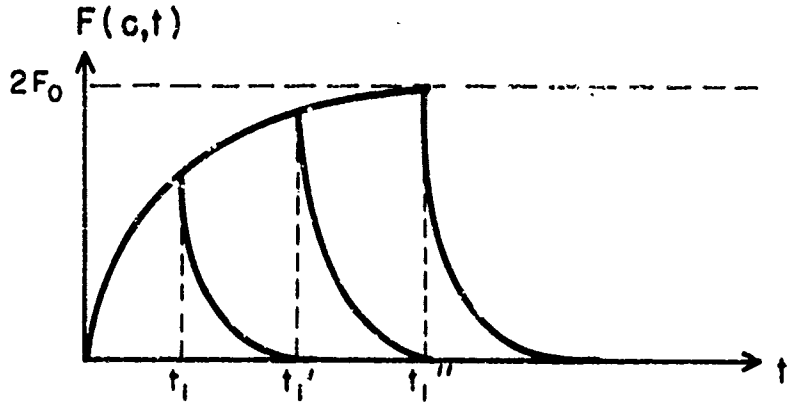

Figure 2-16. Force pulses on a rock load for various durations of the applied pulse.

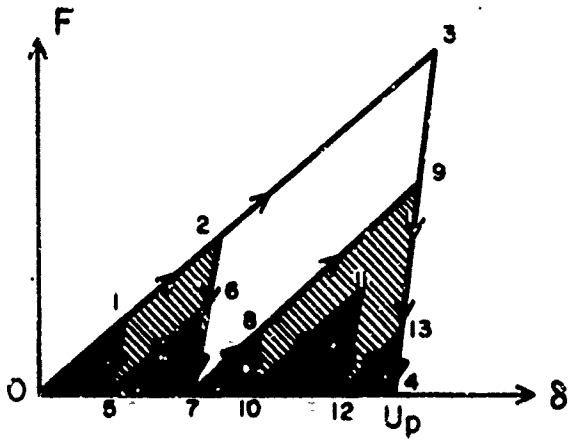

Figure 2-17. Equivalent rock penetration via various force-deformation paths.

Additional insight on the effects of varying the parameters of the input pulse may be obtained by considering a train of incident pulses, each of amplitude F_0 and duration t_1. The pulses, the force-time and force-deformation histories are shown in Figure 2-18.

One way of varying the pulse parameter is to assume that the amplitude has been increased to F_0', with the duration remaining the same. The behavior is shown in Figure 2-19., where the results of Figure 2-18 are also included as the dashed lines. It is obvious that the net penetration $3u_1$, after three pulses, is considerably greater than for the pulses of magnitude F_0.

Another method of parameter variation would be to hold the pulse amplitude constant, while increasing pulse duration from t_1 to t_1'. It is rather easy to deduce the consequences of this by referring to Figure 2-18. If the pulse is of greater duration, the generated force is increased since the duration of the exponential rise is prolonged. The result on the force penetration is the same as that for increasing pulse amplitude. Thus, a figure similar to Figure 2-19 results. The only difference between increasing amplitude and increasing duration is the time required to affect the penetration. Otherwise, the effects on the net penetration are the same.

2-4 REFERENCES

1. See, for example, Goldsmith, Impact, Edward Arnold, Ltd., 1960.

2. Mahban, H., "Rock Behavior Under Impulsive Loading," Ph.D. Dissertation, The Ohio State University, 1970.

3. Wei, T. Y., "Study of the Deformation of Lead and Aluminum Slugs Under Impact," Project EES 358, August, 1970.

4. Ibid.

3. VIBRATIONAL CHARACTERISTICS OF A SONIC TRANSDUCER

3-1 INTRODUCTION

The impact coupling process of sonic energy transfer involves the continual interaction of the sonic tool with the work surface and the sonic transducer through a series of impacts. The case of tool impact with the work surface (rock) is under separate investigation in the study of rock drilling. The case of tool impact on the transducer tip has been previously studied by Feng and Graff [1], Feng [2], [3] and Graff and Shieh [4]. These studies have been concerned with the single impact of tools of various shapes on vibrating transducer tips.

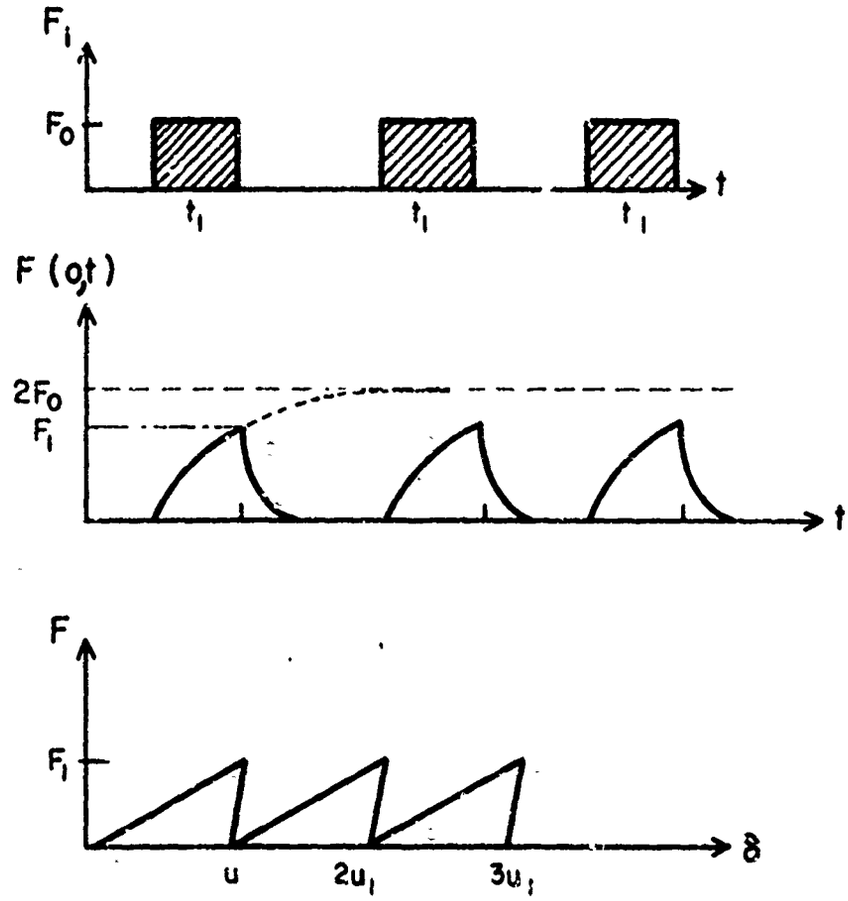

Figure 2-18. Contact force F(o,t) and force-penetration for a series of three incident pulses.

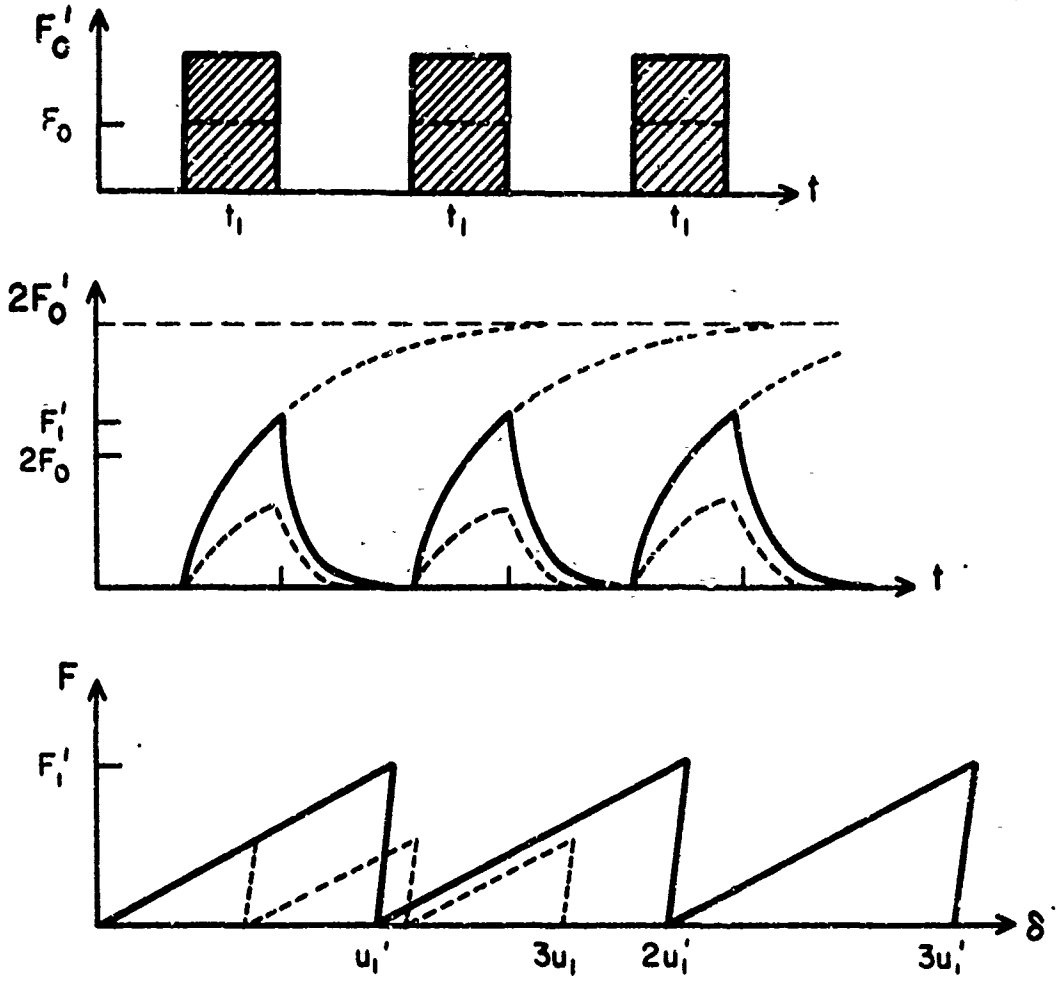

Figure 2-19. Contact force F(o,t) and force-penetration for a series of three pulses having twice the amplitude of those shown in Figure 2-18.

A major aspect of the tool-transducer impact that has not yet been considered is the energy removal per impact relative to the total stored energy of the transducer. This factor bears directly on the rapidity with which energy can be removed from a transducer in an impact coupling process; i.e., the number of impacts per second.

In studying this last phase of the problem, it is as important to determine the stored energy characteristics and Q of the transducer as it is to establish the energy removal per blow. For this reason, a major portion of the following study is devoted to studying the various transducer characteristics that enable these quantities to be determined.

Thus, one of the important factors in the use of a transducer for rock cutting is to understand the properties of the unloaded transducer, these properties including the study of the Q-factor (quality factor), strain at any point along the transducer, tip displacement of the transducer and the temperature variation during the operation. The understanding of the Q-factor will provide the information about the energy dissipated in each cycle of vibration. The information on strain at any point along the transducer and the tip displacement of the transducer will also enable the stored energy to be calculated. Finally, the study of the temperature changes during the transducer operation will provide some idea about the frequency shift and temperature versus operation time relationship. Some analytical calculations for the strain and the tip acceleration of the transducer are also presented.

Another important study that has been carried out is the investigation of the transiant response of a transducer caused by the impact of a tool and the influence on Q-factor for different methods of mounting the transducer. These findings will provide information about the energy recovery of the transducer in the impact coupling process and the Q change because of different transducer mounting. Each experiment will be presented and discussed in a separate section, and all experimental equipment set ups and procedures will be included in a single section.

3-2 THEORETICAL ANALYSIS OF THE P-7 TRANSDUCER

In order to theoretically calculate the stored energy in the P-7 transducer, knowledge of the longitudinal vibrational mode of the device is needed. Although the design principle of the P-7 is that of a half-wave-length stepped horn, having the node located at the step, the actual configuration of the transducer departs considerably from this. Thus, mounting shoulders and threads, the center bolt construction, the ceramic rings and electrode and other features represent significant departures of the actual transducer from the stepped horn.

A first step in analyzing the transducer consisted of considering a homogeneous stepped horn assembly where the horn dimensions were in

accord with the actual P-7, as shown in Figure 3-2.1. Thus, all inhomogenities of construction and materials are ignored in this still highly simplified model. However, the unequal lengths of the sections are accounted for.

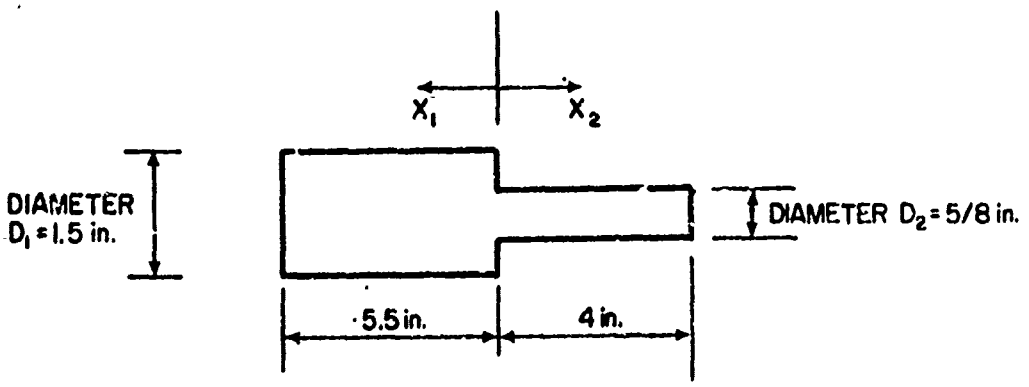

Figure 3-2.1 - Coordinates system and dimensions of a stepped horn.

To carry out the analysis, we have the governing differential equations for longitudinal wave propagation in a rod as

$$\frac{\partial^2 \mu_1}{\partial x_1^2} = \frac{1}{C^2}\frac{\partial^2 \mu_1}{\partial t^2}$$
$$\frac{\partial^2 \mu_2}{\partial x_2^2} = \frac{1}{C^2}\frac{\partial^2 \mu_2}{\partial t^2} \qquad (3\text{-}2.1)$$

where

$C = \sqrt{E/\zeta}$ = longitudinal wave velocity
E = elastic modulus
ζ = mass density

The solutions of the differential equations are

$$\mu_1 = (A \sin kx_1 + B \cos kx_1)\cos \omega t$$
$$\mu_2 = (C \sin kx_2 + D \cos kx_2)\cos \omega t \qquad (3\text{-}2.2)$$

where

$$k^2 = w^2/C^2 \qquad (3\text{-}2.3)$$

and w is the frequency in radians per second. The boundary conditions are

$$\begin{aligned}
&\mu_1 = -\mu_2 &&, \quad x_1 = 0\ , \quad x_2 = 0 \\
&A_1 \frac{\partial \mu_1}{\partial x_1} = A_2 \frac{\partial \mu_2}{\partial x_2} &&, \quad x_1 = 0\ , \quad x_2 = 0 \\
&\frac{\partial \mu_1}{\partial x_1} = 0 &&, \quad x_1 = L_1 = 5.5 \text{ in.} \\
&\frac{\partial \mu_2}{\partial x_2} = 0 &&, \quad x_2 = L_2 = 4.0 \text{ in.}
\end{aligned} \tag{3-2.4}$$

Substituting (3-2.2) into (3-2.4) we have

$$\begin{aligned}
&A \cos kL_1 - B \sin kL_1 = 0 \\
&C \cos kL_2 - D \sin kL_2 = 0 \\
&B = -D \\
&A_1 A = A_2 C
\end{aligned} \tag{3-2.5}$$

These last equations can be simplified to

$$\begin{aligned}
\frac{A_2}{A_1} C \cos kL_1 + D \sin kL_1 &= 0 \\
C \cos kL_2 - D \sin kL_2 &= 0
\end{aligned} \tag{3-2.6}$$

For a non-final solution, the following relation must be satisfied;

$$\begin{vmatrix} \frac{A_2}{A_1} \cos kL_1 & \sin kL_1 \\ \cos kL_2 & -\sin kL_2 \end{vmatrix} = 0 \tag{3-2.7}$$

This gives the frequency equation

$$\frac{A_2}{A_1} \cos kL_1 \sin kL_2 + \cos kL_2 \sin kL_1 = 0 \tag{3-2.8}$$

For the present case

$$\begin{aligned}
D_1 &= 1.5 \text{ in.} \quad , \quad D_2 = 0.625 \text{ in.} \\
L_1 &= 5.5 \text{ in.} \quad , \quad L_2 = 4 \text{ in.}
\end{aligned} \tag{3-2.9}$$

Then the frequency equation becomes

$$\left(\frac{0.625}{1.5}\right)^2 \cos 5.5k \sin 4k + \sin 5.5k \cos 4k = 0 \tag{3-2.10}$$

The first root (i.e., first mode) of (3-2.10) is $k = 0.3725$. The displacement relation can then be expressed as

$$\begin{aligned} \mu_1 &= (2.038 \sin kx_1 - \cos kx_1)D \cos \omega t \\ \mu_2 &= (11.72 \sin kx_2 + \cos kx_2)D \cos \omega t \end{aligned} \qquad (3\text{-}2.11)$$

Based on this last relation, the displacement profile of the transducer can be shown as in Figure 3-2.2.

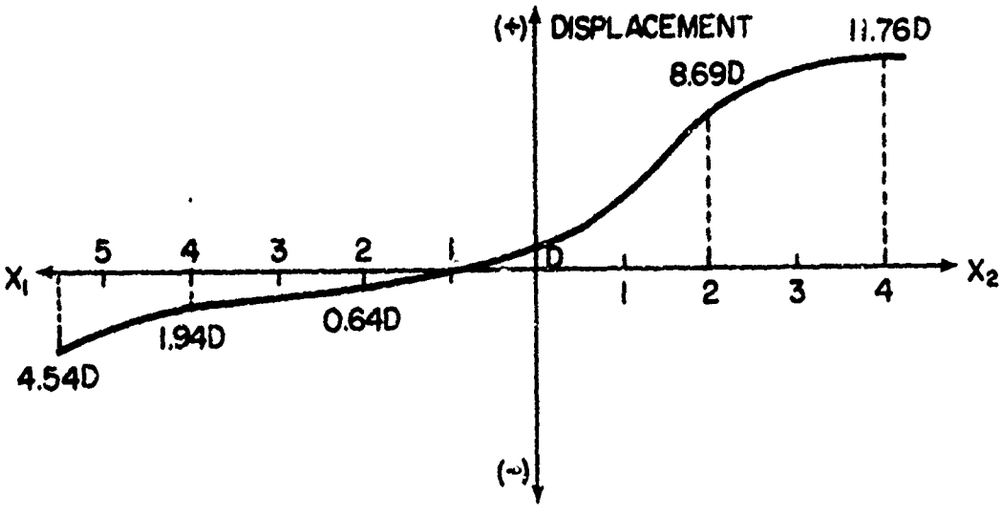

Figure 3-2.2 - Displacement profile of the P-7 unloaded transducer ($\cos \omega t = 1$).

It is observed that the maximum displacement occurs at the tip of the transducer, and zero displacement occurs at the section approximately 1.00 inches from the step. In the actual P-7 transducer, the piezoelectric crystals are located in this region.

The strain along the transducer can easily be obtained by differentiating the displacement expression with respect to x_1 and x_2, respectively, giving

$$\begin{aligned} \epsilon_1 &= \frac{\partial \mu_1}{\partial x_1} = kD(2.038 \cos kx_1 + \sin kx_1)\cos \omega t \\ \epsilon_1 &= \frac{\partial \mu_2}{\partial x_2} = kD(11.72 \cos kx_2 - \sin kx_2)\cos \omega t \end{aligned} \qquad (3\text{-}2.12)$$

The resulting strain profile is as shown in Figure 3-2.3.

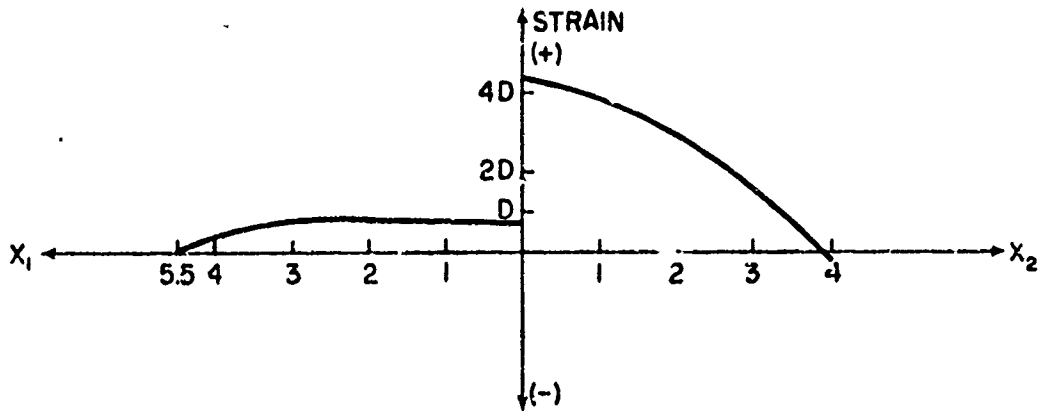

Figure 3-2.3 - Strain profile of the P-7 unloaded transducer ($\cos \omega t = 1$)

For the acceleration at any point in the transducer, we have

$$a_1 = \frac{\partial^2 \mu_2}{\partial t^2} = -Dw^2(2.038 \sin kx_1 - \cos kx_1)\cos \omega t$$

$$a_2 = \frac{\partial^2 \mu_2}{\partial t^2} = -Dw^2(11.72 \sin kx_2 + \cos kx_2)\cos \omega t \qquad (3\text{-}2.13)$$

The acceleration profile along the transducer is as shown in Figure 3-2.4.

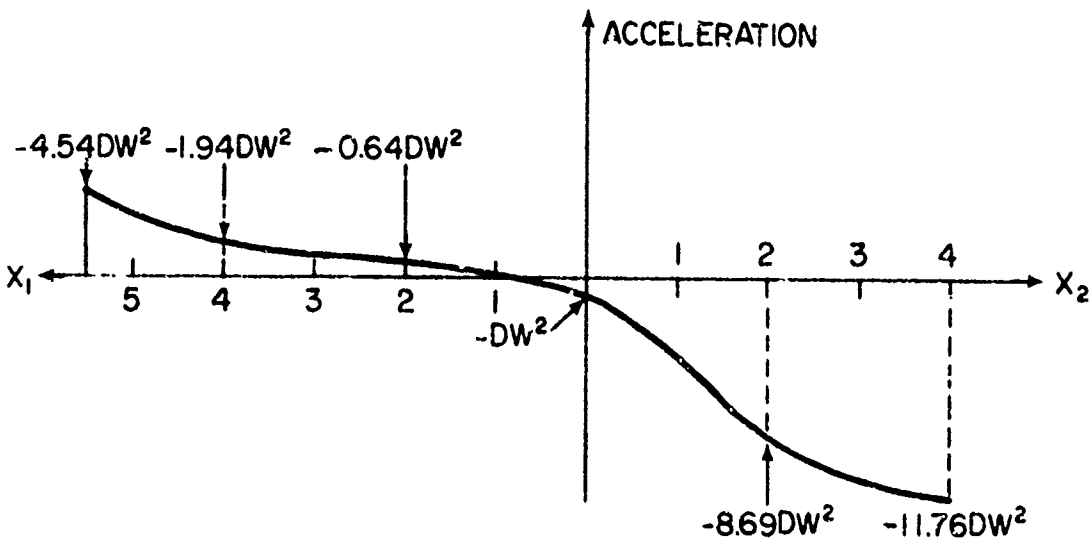

Figure 3-2.4 - Acceleration profile of the P-7 unloaded transducer ($\cos \omega t = 1$)

The major task in the present test is using the experimental results to determine the constant "D", either from the results of the strain readings or from the results of the acceleration data. Theoretically speaking, the D constant calculated either from the strain test or from the acceleration test should be the same, but actually some difference due to the experiment set up or instrumentation may be expected.

A second theoretical calculation pertains to the stored energy in the transducer. Thus, from a knowledge of the vibration profile of the transducer, it is posssible to compute this quantity as follows: When a transmission line is subjected to a longitudinal stress, σ, and strain, ϵ, the stored energy per unit volume, e, is given by

$$e = \tfrac{1}{2}\sigma\epsilon \qquad (3\text{-}2.14)$$

From previous calculations for the expression of displacement and strain, we have

$$\begin{aligned} \mu_1 &= (2.038 \sin kx_1 - \cos kx_1)D \cos \omega t \\ \mu_2 &= (11.72 \sin kx_2 + \cos kx_2)D \cos \omega t \end{aligned} \qquad (3\text{-}2.15)$$

where k = 0.3725. Assuming Hook's Law holds, so that $\sigma = E\epsilon$, then

$$e = \tfrac{1}{2}\sigma\epsilon = \tfrac{1}{2}E\epsilon^2 \qquad (3\text{-}2.16)$$

From $\epsilon = \partial u/\partial x$, we have

$$\begin{aligned} \epsilon_1 &= (2.038 \cos kx_1 + \sin kx_1)kD \cos \omega t \\ \epsilon_1 &= (11.72 \cos kx_2 - \sin kx_2)kD \cos \omega t \end{aligned} \qquad (3\text{-}2.17)$$

$$\begin{aligned} e_1 &= \tfrac{1}{2}Ek^2D^2(2.038 \cos kx_1 + \sin kx_1)^2\cos^2 \omega t \\ e_2 &= \tfrac{1}{2}Ek^2D^2(11.72 \cos kx_2 - \sin kx_2)^2\cos^2 \omega t \end{aligned} \qquad (3\text{-}2.18)$$

The average total strain energy in a transducer of length L and cross-sectional area A is given by

$$\bar{e} = \lim_{T \to \infty} \frac{1}{T} \int_0^T \left[A \int_0^L e \, dx \right] dt \qquad (3\text{-}2.19)$$

For the stepped transducer, this becomes,

$$\bar{e} = \bar{e}_1 + \bar{e}_2 \qquad (3\text{-}2.20)$$

where

$$\bar{e} = \lim_{T\to\infty} \frac{1}{T} \int_0^T \left[A_1 \int_0^{L_1} e_1 dx_1 \right] dt$$

$$\bar{e} = \lim_{T\to\infty} \frac{1}{T} \int_0^T \left[A_2 \int_0^{L_2} e_2 dx_2 \right] dt \qquad (3\text{-}2.21)$$

Substituting (3-2.18) into (3-2.21) and carrying out the integration, we obtain

$$\bar{e}_1 = \frac{A_1 E k^2 D}{4} \left[2.038^2 \left(\frac{L_1}{2} + \frac{1}{4k} \sin 2kL_1 \right) + \frac{2.038}{k} \sin^2 kL_1 + \left(\frac{L_1}{2} - \frac{1}{4k} \sin 2kL_1 \right) \right]$$

$$\bar{e}_2 = \frac{A_2 E k^2 D}{4} \left[11.72^2 \left(\frac{L_2}{2} + \frac{1}{4k} \sin 2kL_2 \right) - \frac{11.72}{k} \sin^2 kL_2 + \left(\frac{L_2}{2} - \frac{1}{4k} \sin 2kL_2 \right) \right] \qquad (3\text{-}2.22)$$

In the present case, the various parameters are

$$L_1 = 5.5 \text{ inches} \quad , \quad L_2 = 4.0 \text{ inches}$$

$$A_1 = \frac{\pi}{4} (1.5)^2 = 1.7672 \text{ in}^2 \quad , \quad A_2 = \frac{\pi}{4} (0.625)^2 = 0.3068 \text{ in}^2$$

$$E = 29 \times 10^6 \text{ lb/in}^2 \quad , \quad k = 0.3725 \qquad (3\text{-}2.24)$$

Substituting these values in (3-2.22) and (3-2.21) gives,

$$\bar{e}_1 = 29.7893 \times 10^6 D^2 \quad , \quad \bar{e}_2 = 80.3057 \times 10^6 D^2$$

$$\bar{e} = \bar{e}_1 + \bar{e}_2 = 110.095 \times 10^6 D^2 \qquad (3\text{-}2.24)$$

Thus, for a given value of D, which must be determined from experimental data, the transducer stored energy may be calculated.

3-3 EXPERIMENTAL EQUIPMENT AND PROCEDURES

A power source, an impedance matching device, and methods of measuring power, voltage, and temperature comprise the major elements of the system used in this work. The power source consisted of a Bruel and Kjear 1013 oscillator feeding into a McIntosh 275 power amplifier. A sonic matching transformer provided impedance matching between the amplifier and the transducer. The transformer had variable turns-

ratio settings to allow optimum matching between an amplifier and a given transducer. Watt and voltage meters were also included in the system for monitoring purposes. A schematic of the overall system is shown in Figure 3-3.1.

In an effort to silence the acoustic noise of the P-7 sonic transducer, a sound-proof box was constructed. The box was constructed of plywood with outside dimensions of 19" x 25" x 25", with the entire front being used as a door. The inside was lined with sound-proof panelling. The final inside dimensions were 19" x 20" x 20", giving a total volume of 7600 cubic inches. Two pieces of plexiglass separated by a one-inch dead air space provided a sound-proof window in the door for visual monitoring purpose. The resulting box is shown in Figure 3-3.2 with the door opened and a transducer in place.

A test was needed to determine the efficiency of the soundproofing. A speaker was connected to an amplifier-oscillator combination. The speaker was placed in the box and an audio level of 100 dB at 10 kHz was applied. The box door was closed and the level droped to 55 dB. This proved to be adequate soundproofing for the P-7 when operated below 100 watts.

The amplifier-oscillator combination consisted of a B and K 1013 voltage compression oscillator and a McIntosh 275 power amplifier. The oscillator operates over a range of 200 to 200,000 Hz. The amplifier holds a flat response from 50 to 25,000 Hz. This combination produced an output of from 200 to 25,000 Hz at 100 W ± 3 dB. These pieces of apparatus are shown in Figure 3-3.3 (a), (b).

An impedance matching device was needed to match the output of the power amplifier to the transducer. This piece of apparatus is shown in Figure 3-3.3 (b).

Several tests were performed to define the effects of the transformer on the parameters of the system. The transformer had an input impedance of 360 Ω and a switchable output impedance ranging from 360 to 5000 Ω. The effects of each of these settings on bandwith was the first test performed. The results are given in Figure 3-3.4. The power transfer curves are shown on Figure 3-3.5 and 3-3.6. The results of these tests indicated that a setting of 5000 Ω output impedance was optimum for power transfer to the P-7 transducer.

A variety of measurement devices were incorporated during the course of the test, including the F-W Bell wideband wattmeter, the Hewlett-Packard model 3400 A RMS voltmeter, and the Tektronic 549 oscilloscope. These instruments were used in monitoring the electrical input characteristic of the P-7 transducer.

An Advanced Product Inc. thermocouple temperature meter was used to monitor the thermal characteristics of the P-7; a calibration check

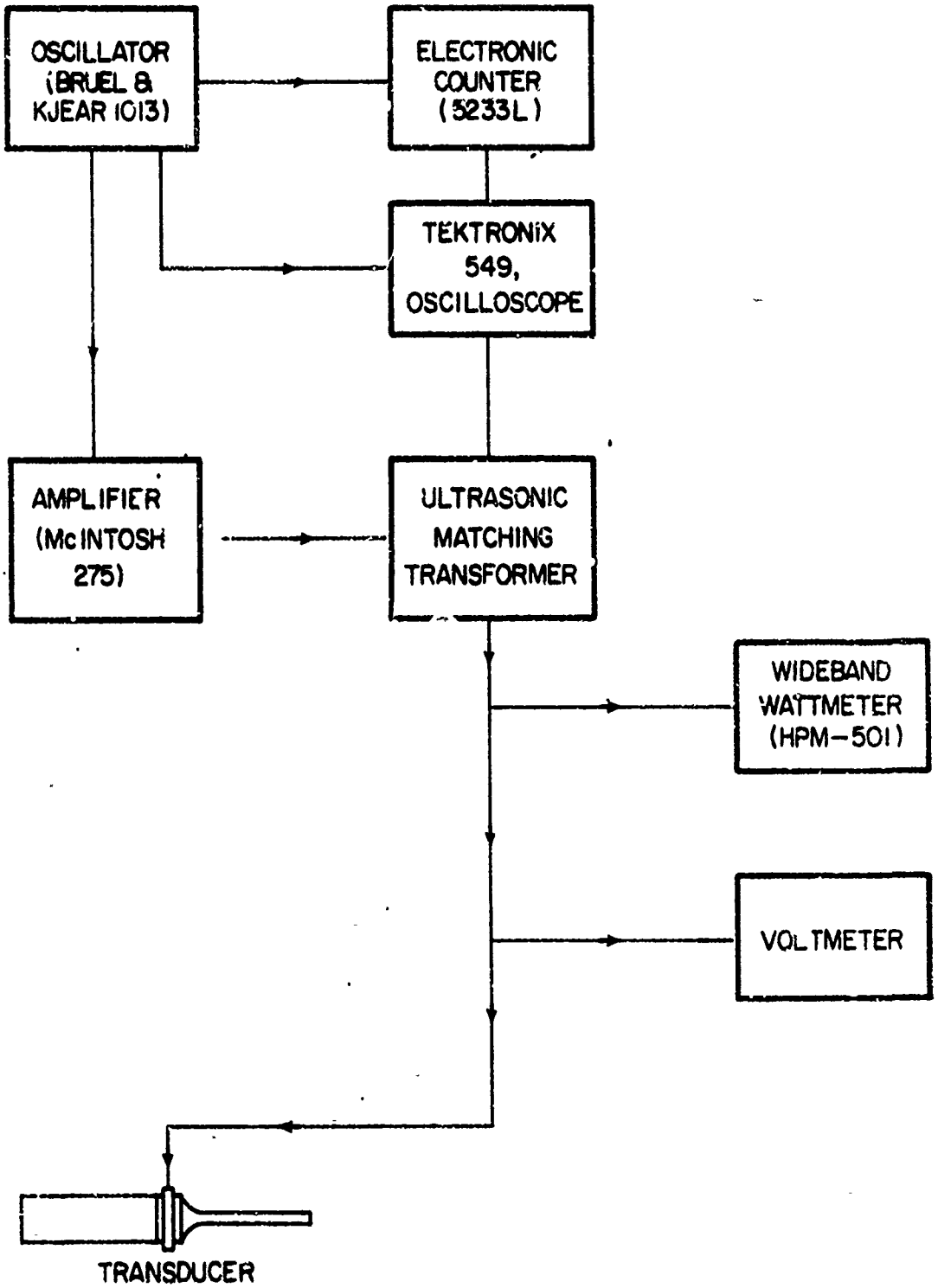

Figure 3-3.1 - Block diagram of apparatus.

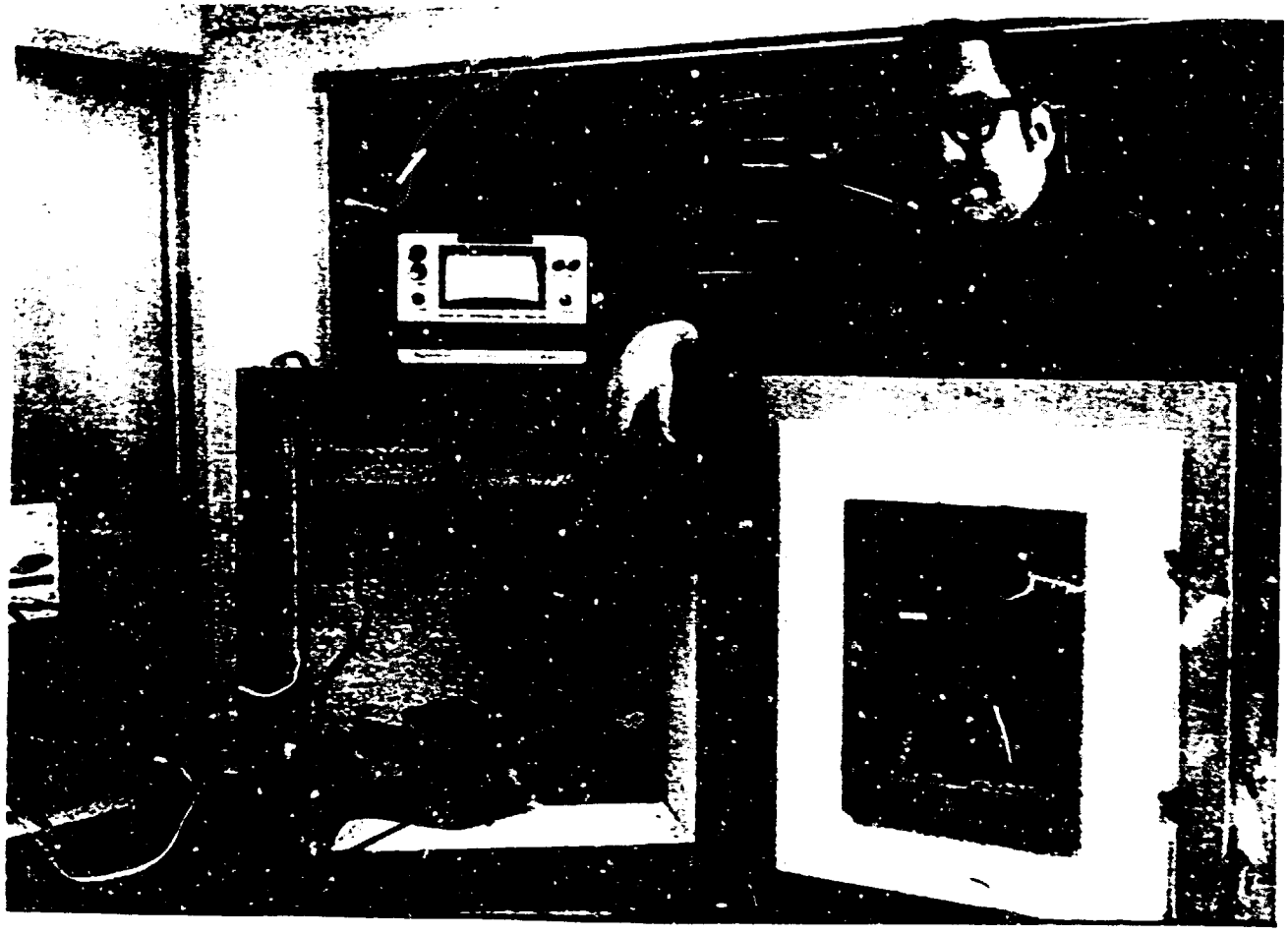

Figure 3-3.2 - Sound-proof box used for P-7 noise reduction.

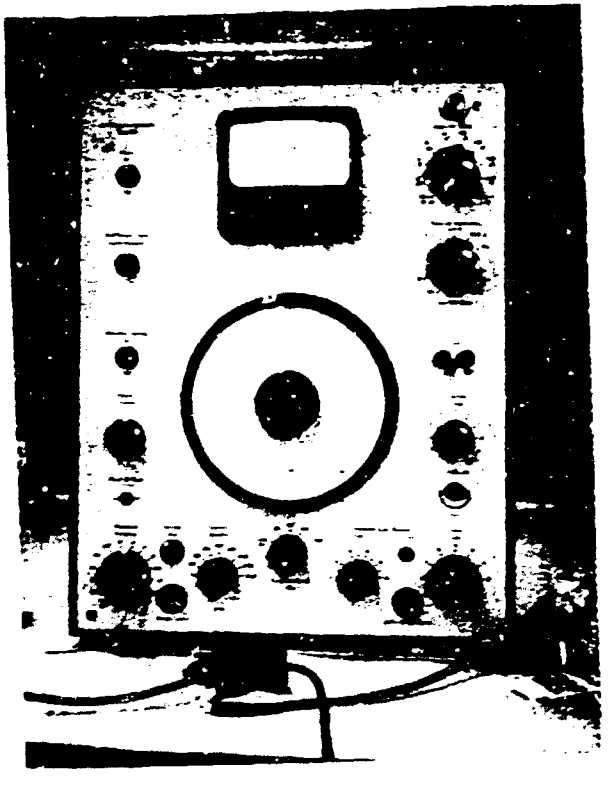

(a)

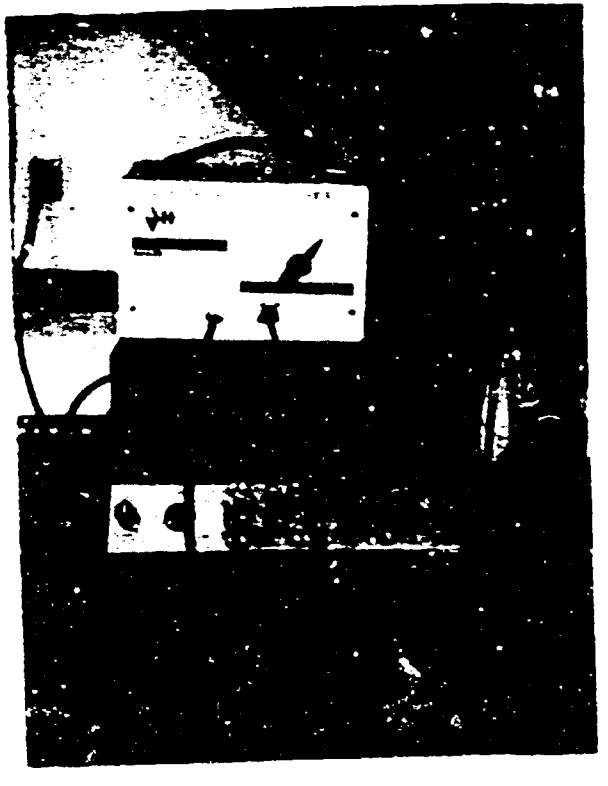

(b)

Figure 3-3.3 - (a) Bruel and Kjear 1013 oscillator and (b) McIntosh 275 amplifier and ultrasonic matching transformer.

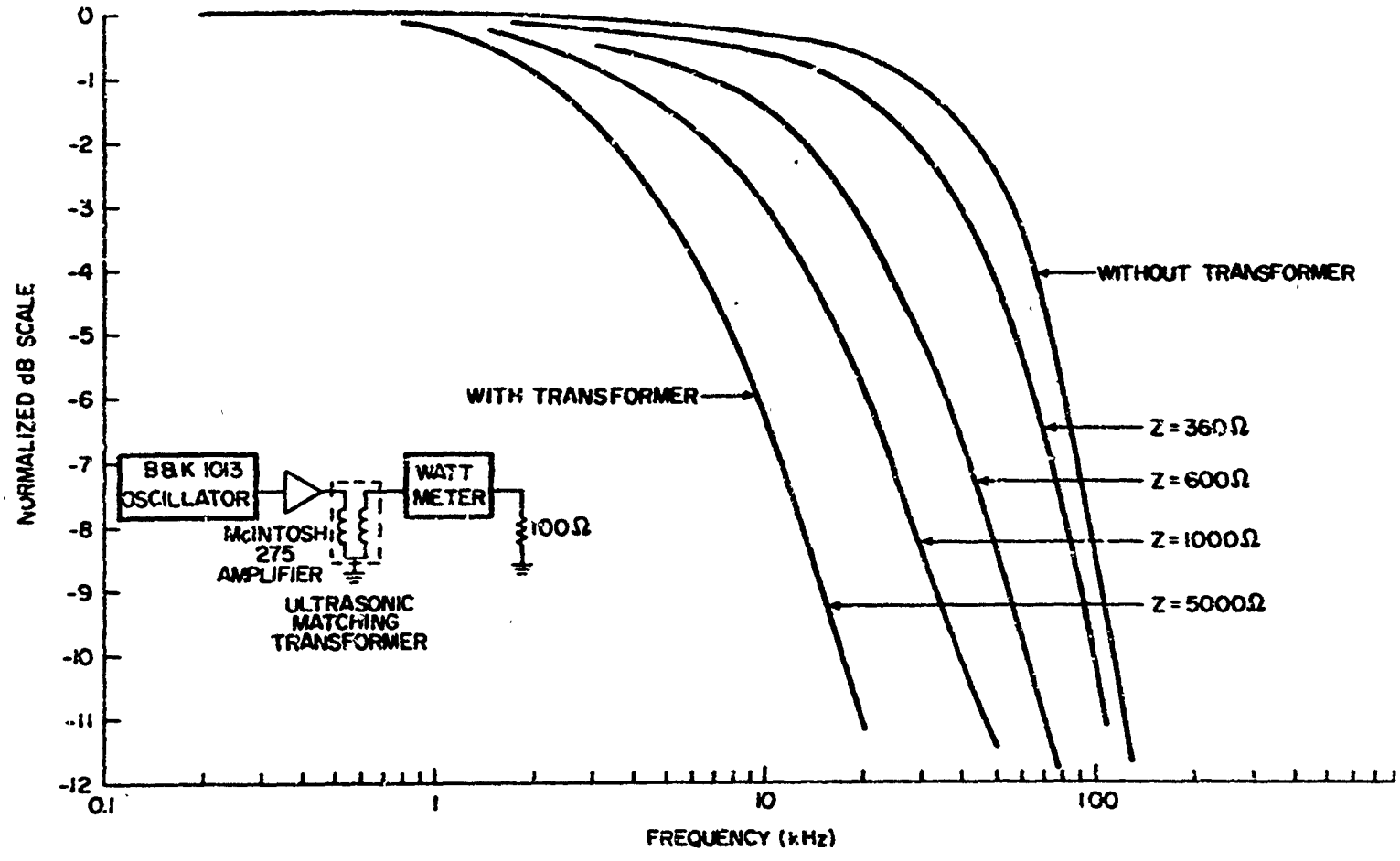

Figure 3-3.4 - Bandwidth effects of ultrasonic matching transformer.

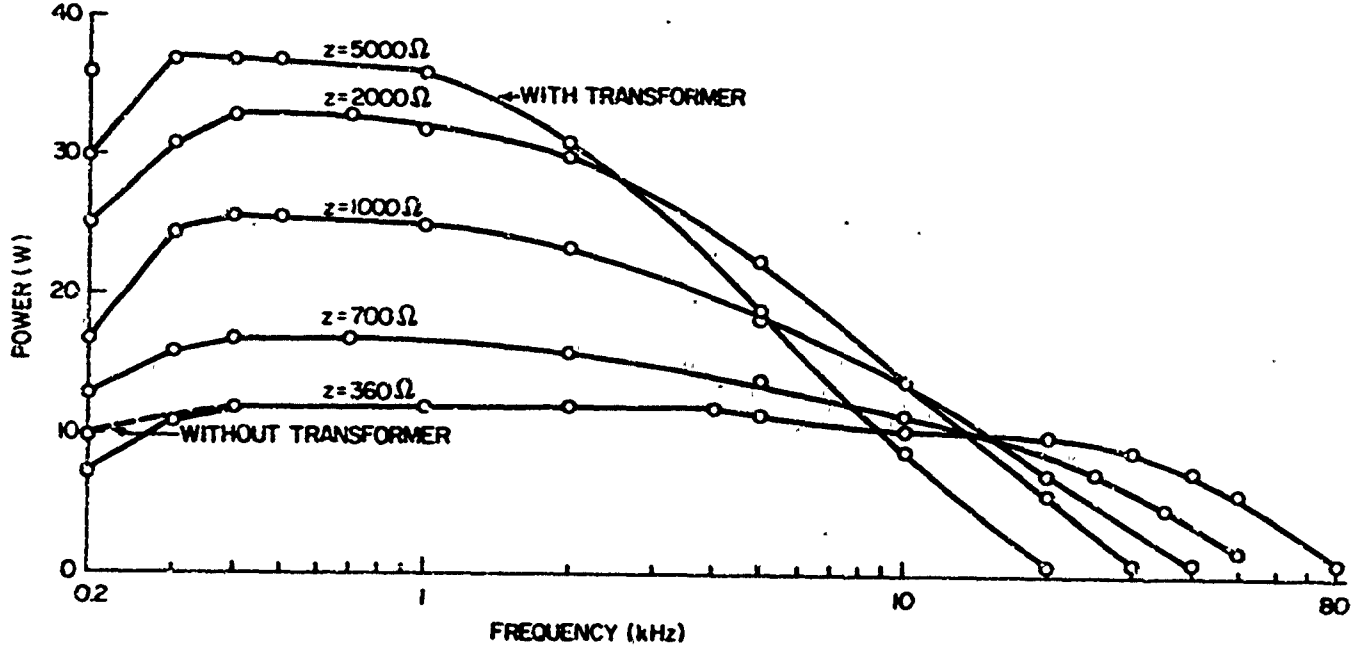

Figure 3-3.5 - Power transfer for different z on ultrasonic matching transformer.

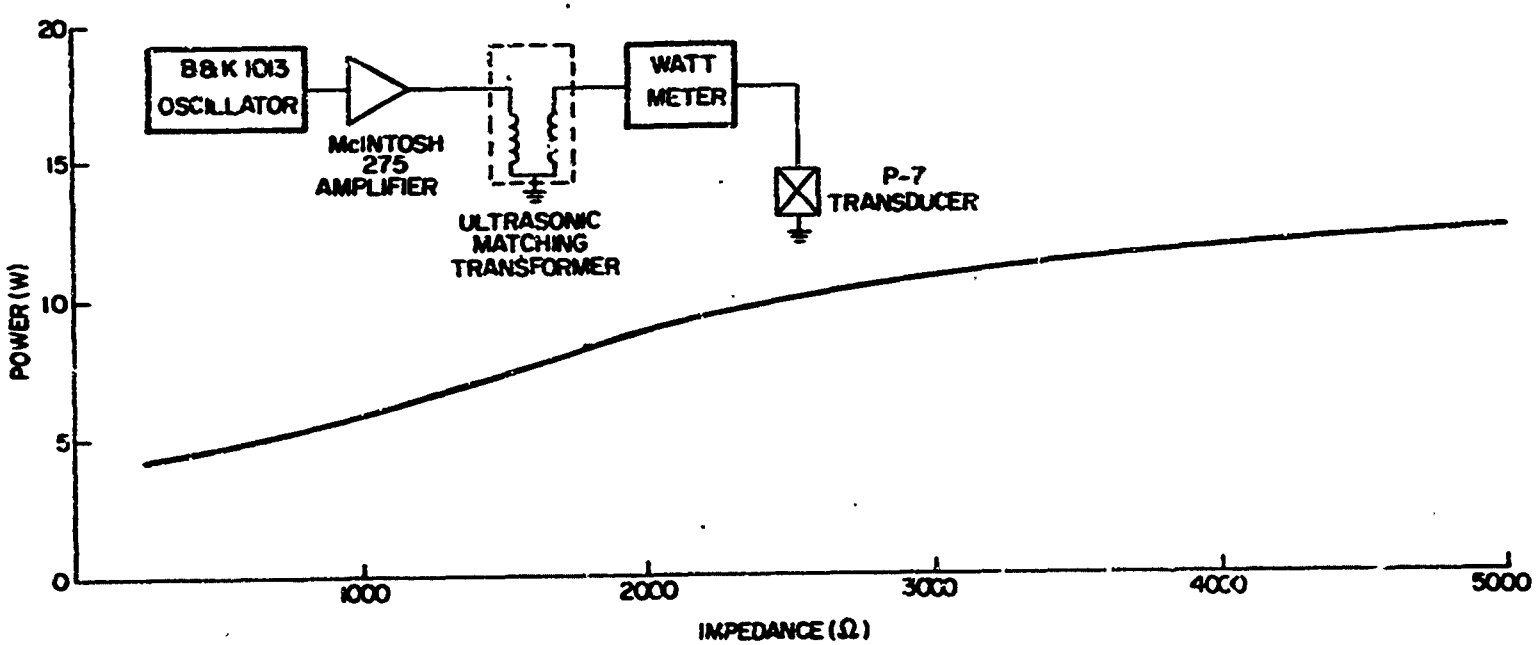

Figure 3-3.6 - Power transfer as a function of z setting on ultrasonic matching transformer.

was run on this device prior to the transducer tests. These results are given in Figure 3-3.7.

Finally, measurements of the mechanical vibration parameters of the transducer were accomplished using strain gages, accelerometers and a magnetic transducer pickup. Thus, a single Micro-measurements type EA-06-050AR-120 foil gage was mounted two inches from the step of the transducer (this location also being two inches from the tip). The gage was a single arm of a Wheatstone bridge strain gage circuit. During the course of the test, it was found that these gages failed rather rapidly due to fatigue. Transducer tip acceleration was measured using an Enderco 2222 microminature shock accelerometer. A Brüel and Kjaer type MM0002 magnetic transducer was used to monitor the transient response of tip movement of the P-7 transducer.

3-4 PROCEDURE, RESULTS AND DISCUSSION ON Q, STRAIN, TIP DISPLACEMENT AND TEMPERATURE STUDIES

(A) Q-Factor at Constant Power

The damping properties of forced or free vibrators are often specified by the quality factor Q, which has been defined as

$$Q = 2\pi \frac{\text{Maximum strain energy stored in vibration}}{\text{Energy dissipated per cycle of vibration}} \qquad (3\text{-}4.1)$$

For lightly damped systems, the bandwith method is also used to measure the Q-factor, where,

$$Q = \frac{f_r}{f_1 - f_2} \qquad (3\text{-}4.2)$$

and where

f_r = resonance frequency, and

f_2, f_1 = frequencies of the half power points.

The objective of this particular test was to measure the transducer Q at constant input power over a prolonged (90 minutes) time interval, during which the transducer temperature changed markedly. The experimental setup was as previously shown in Figure 3-3.1. The procedure was as follows: Starting at room temperature (approximately 72°F) the transducer was turned on and operated at resonance at a constant input power (20 W in the present case). Under continual operation the transducer temperature increased and this change was recorded at five-minute time intervals. The transducer resonance frequency would also shift with the passage of time. Compensation for this shift was made by varying the drive frequency so that the input power remained at 20 W.

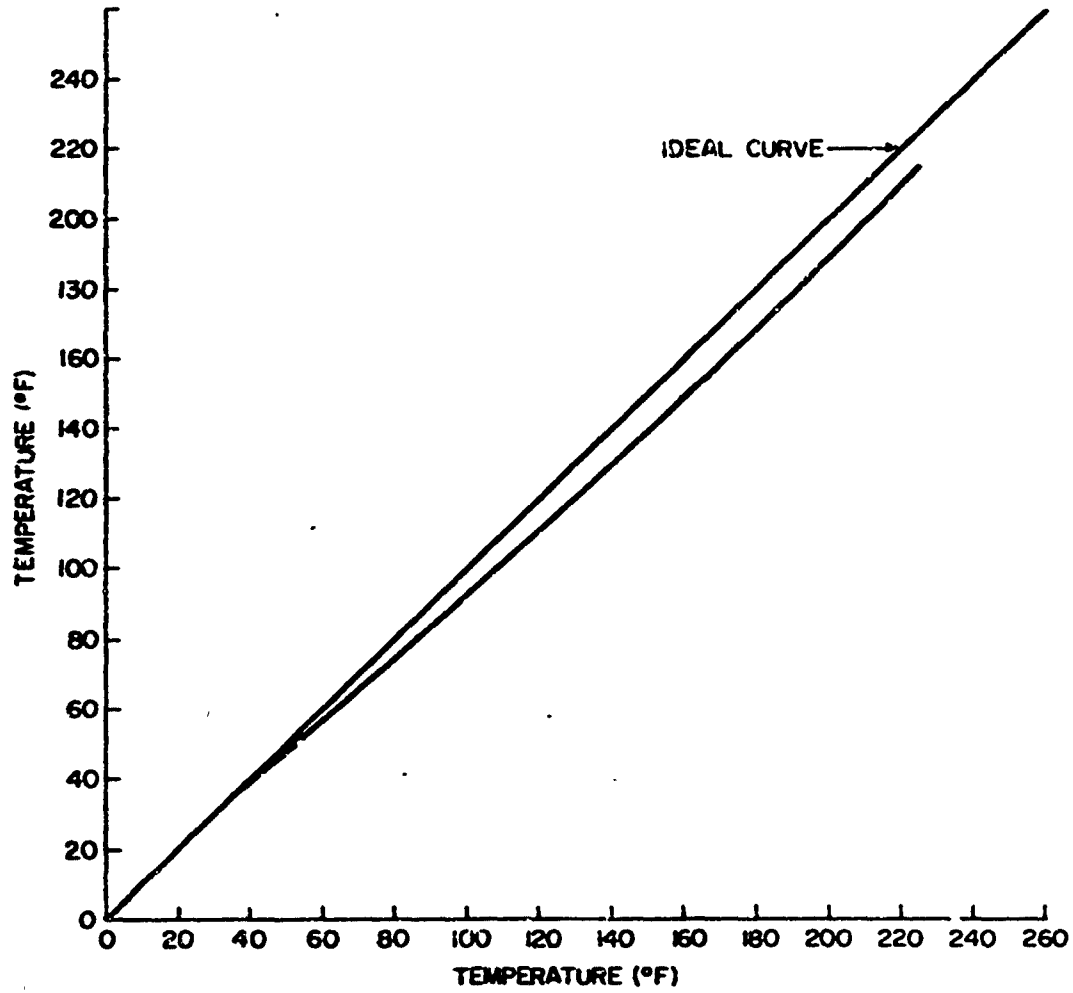

Figure 3-3.7 - Temperature calibration of the thermocouple temperature meter.

At five-minute intervals, the transducer Q was determined by quickly shifting frequency to the half-power points and, thus, determining the bandwidth at a given time and frequency. The results obtained from this test have been plotted in Figure 3-4.1. It is seen that the resonance frequency changes from 9720 Hz to 9665 Hz, with the temperature change being from 72°F to 138°F during the 90 minutes of operation. The important observation is made here that the Q-factor is practically constant at Q = 400 and is independent of the change in resonance frequency and temperature as well as time for a given power.

(B) Q as a Function of Input Power

For a fixed power (20 W) the results of the previously reported test showed transducer Q to be constant. An understanding of the variation of Q-factor with respect to the change of input power to a resonating transducer is also significant. A particular interest is focused on the change of Q for large values of input power. The instrumentation setup and procedures for this test are the same as the previous "Q" test. The transducer was operated at its resonance frequency (f_r) for a given input power. By means of the bandwidth method, the value of Q corresponding to a given value of input power was found by finding the half-power frequencies (f_1 and f_2) and using the relation $Q = f_r/(f_2-f_1)$. A crude result, due to not considering the temperature build up in the transducer during the test, is shown in Figure 3-4.2. Another more careful test was conducted and the result is presented in Figure 3-4.3. It is seen that at low power levels, the Q is quite high (thus, Q = 600 for an input power of 5 W). The Q then drops rapidly and appears to be approaching a limiting value of about 300 for input power of 40 to 50 W, although these power levels are far below the rated capacity of the transducer (700 W), the asymptotic behavior of the Q-factor suggests that it would not be drastically shifted at yet higher power levels.

(C) Transducer Temperature Measurement

It is a well known phenomenon that the resonance frequency of a sonic transducer will be shifted due to temperature changes in the transducer. The objective of the work reported in this section was to obtain extensive data on the temperature change--frequency shift characteristics during operation. The work elaborates on that given earlier in Figure 3-4.1 for a specific power level. The highest temperature is generated at the copper electrode (located at the exciting crystals). During the operation, the temperature is conducted from the general nodal region where the copper electrode is located to both ends of the transducer. Thus, it is desirable to have several pickups to measure the temperature change at different locations along the transducer. In the final setup, shown in Figure 3-4.4, three temperature pickups were utilized.

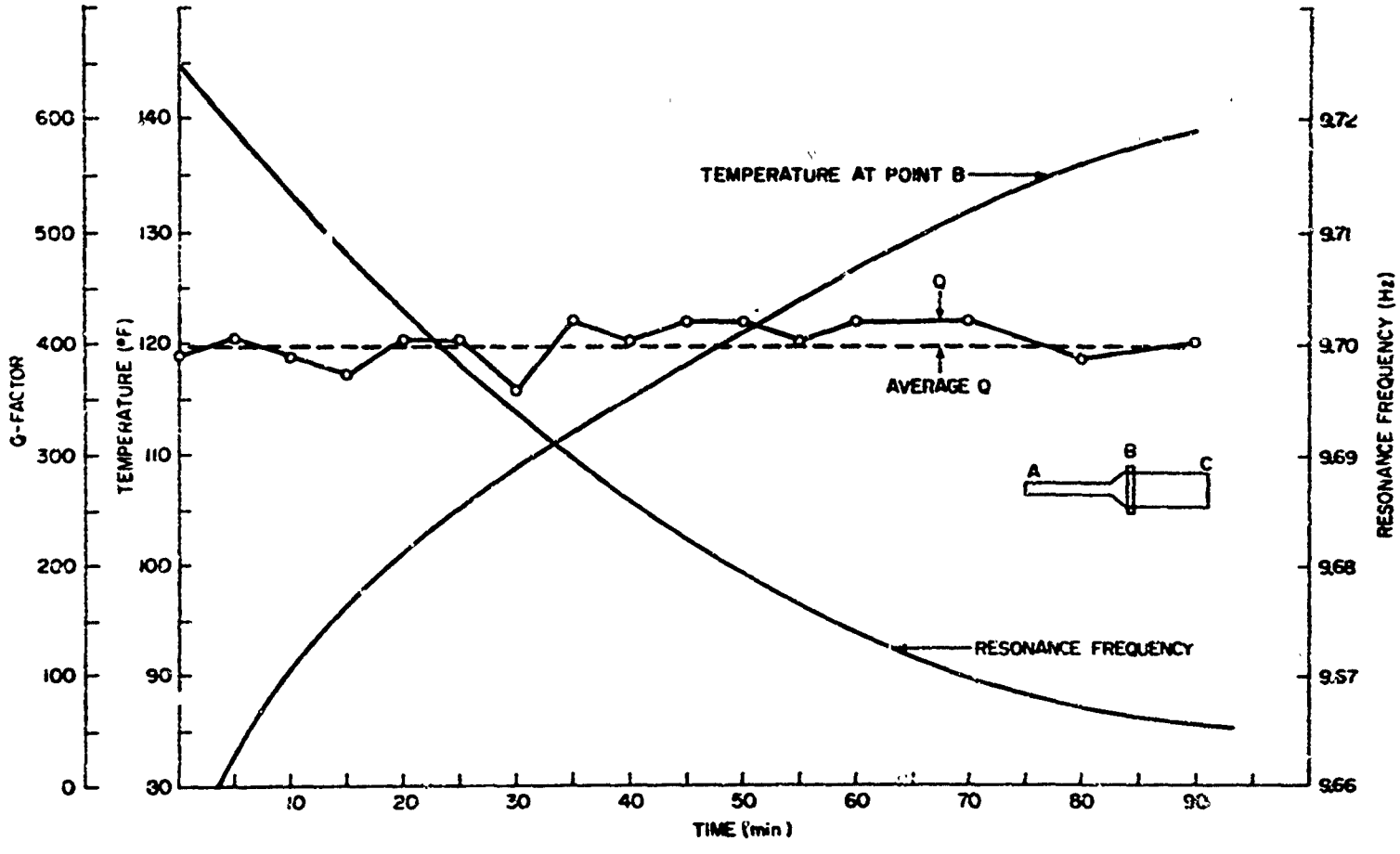

Figure 3-4.1 - Q, temperature and resonance frequency change as function of operation time.

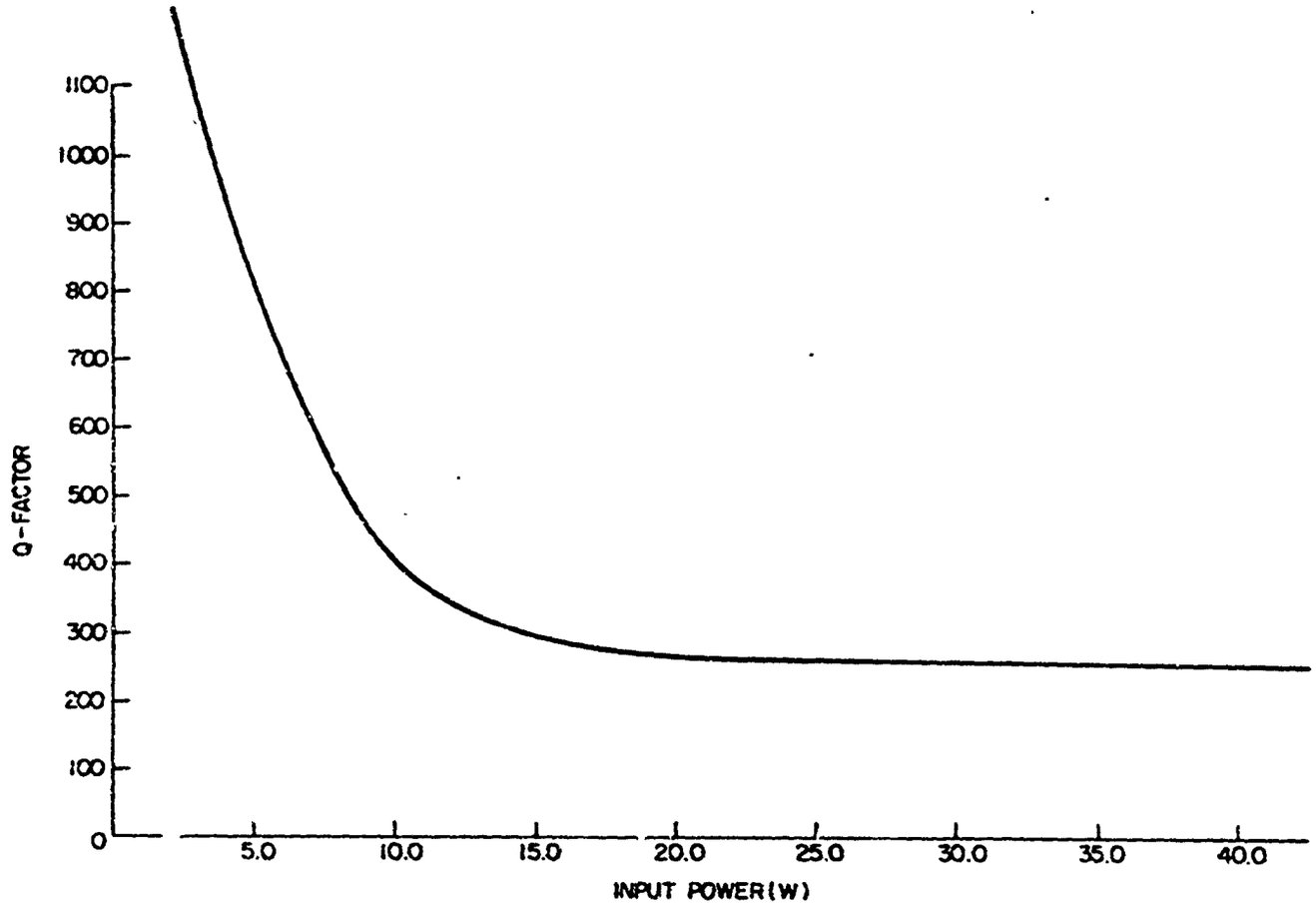

Figure 3-4.2 - Q as a function of input power.

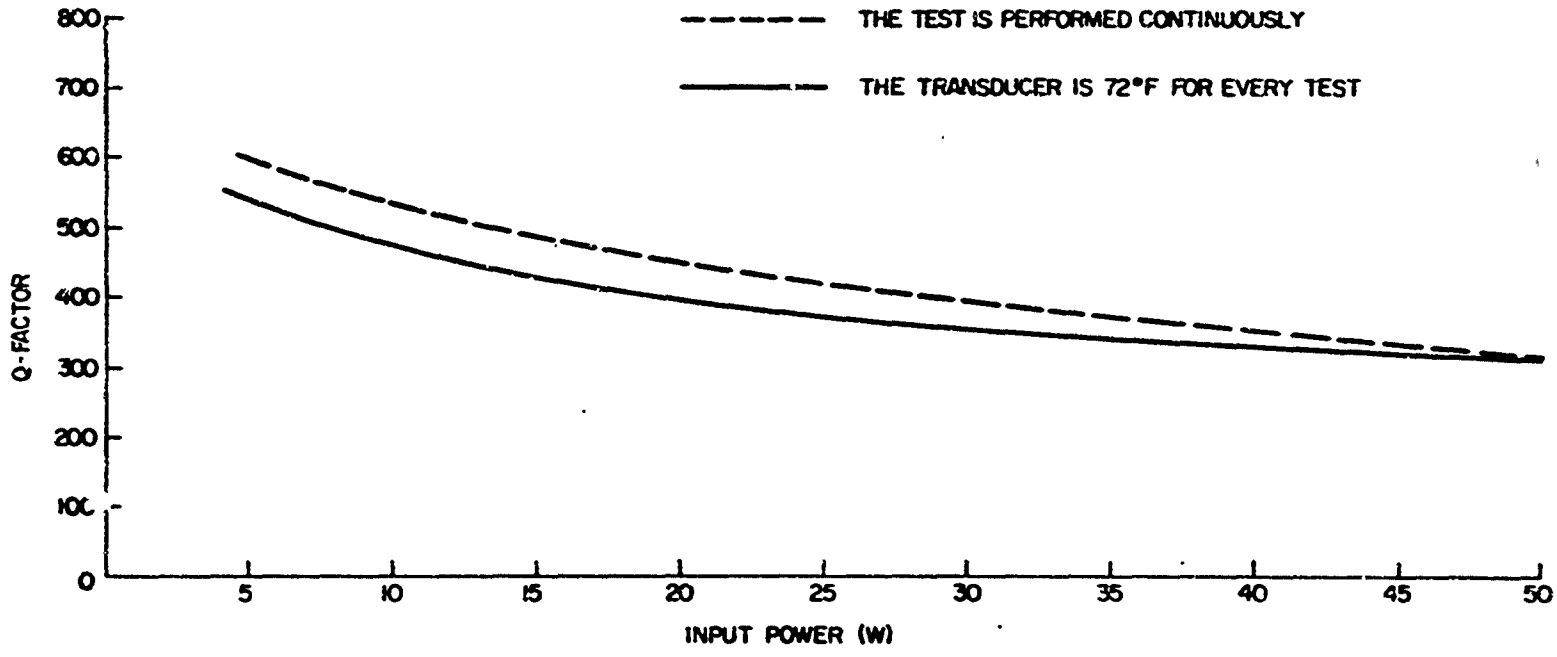

Figure 3-4.3 - Q as a function of input power.

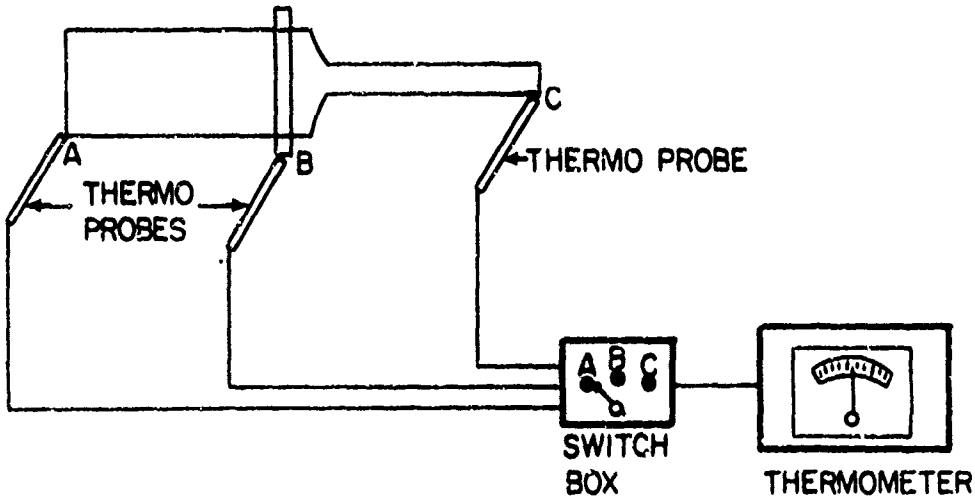

Figure 3-4.4 - Basic setup for transducer temperature measurement.

An "Advanced Product" model temperature pickup was used in the test. Between the tip of the temperature probe and the transducer, Dow Corning 340 silicone heat sink compound was used as a thermal bridge.

The test was conducted at several input power levels (10, 20, and 30 W). As the transducer operated at a specified input power and resonance frequency, the temperature rise at the three selected locations (A, B, and C) for different operating times was recorded. The results for the various tests are presented in Figures 3-4.5 through 3-4.10.

It should be recalled at this point that the transducer was operated in a closed sound-proof box. The box tended to act as an adiabatic container, so that heat conduction away from the transducer was altered compared to the open environment. However, the present test will provide a general picture for the temperature study of a transducer.

From the experimental results, it is observed that the highest temperature is always generated at point B (i.e., the copper electrode) and the temperature gradually decreases from B to point C and A. Further, the resonance frequency is seen to change as a function of operating time and temperature increase in a manner previously noted in Figure 3-4.1.

(D) Measurements of Strain and Acceleration

As part of the general objective of the test program of determining the energy storage and dissipation characteristics of the P-7, it became necessary to measure the tip acceleration of the transducer. Due

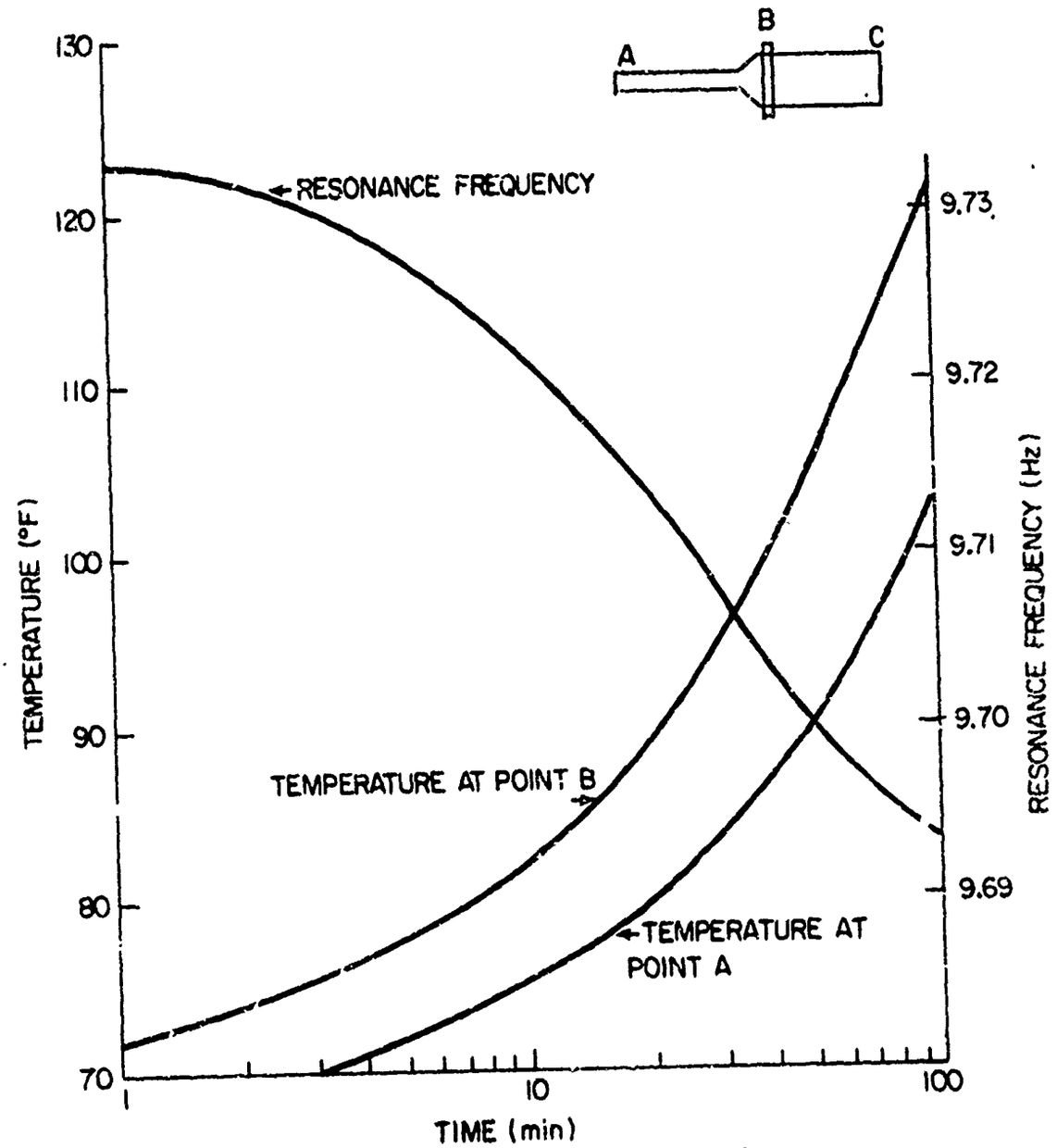

Figure 3-4.5 - Temperature and Q as a function of operation time at 10 watts input power.

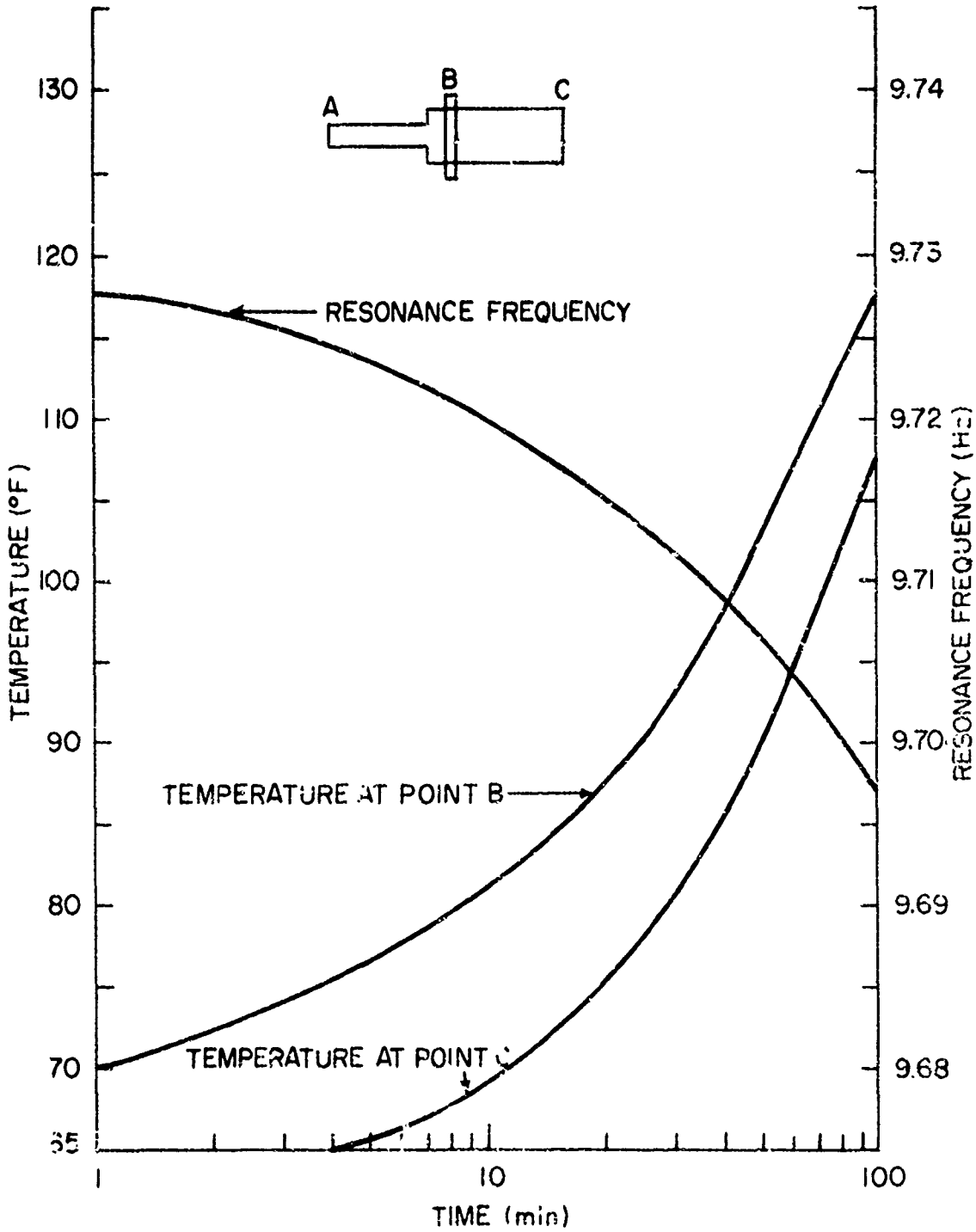

Figure 3-4.6 - Temperature and Q as function of operation time at 10 watts input power.

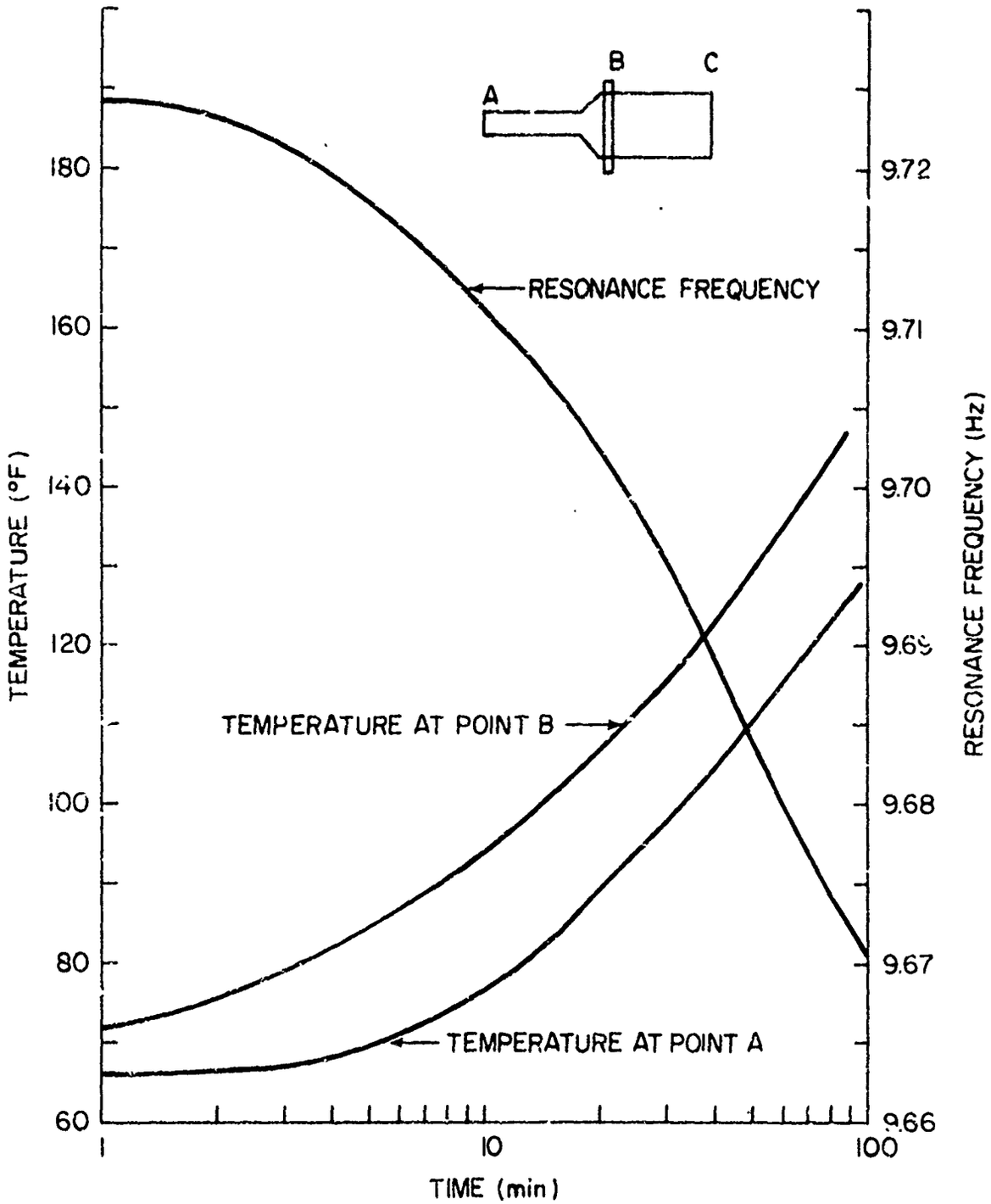

Figure 3-4.7 - Temperature and Q as function of operation time at 20 watts input power.

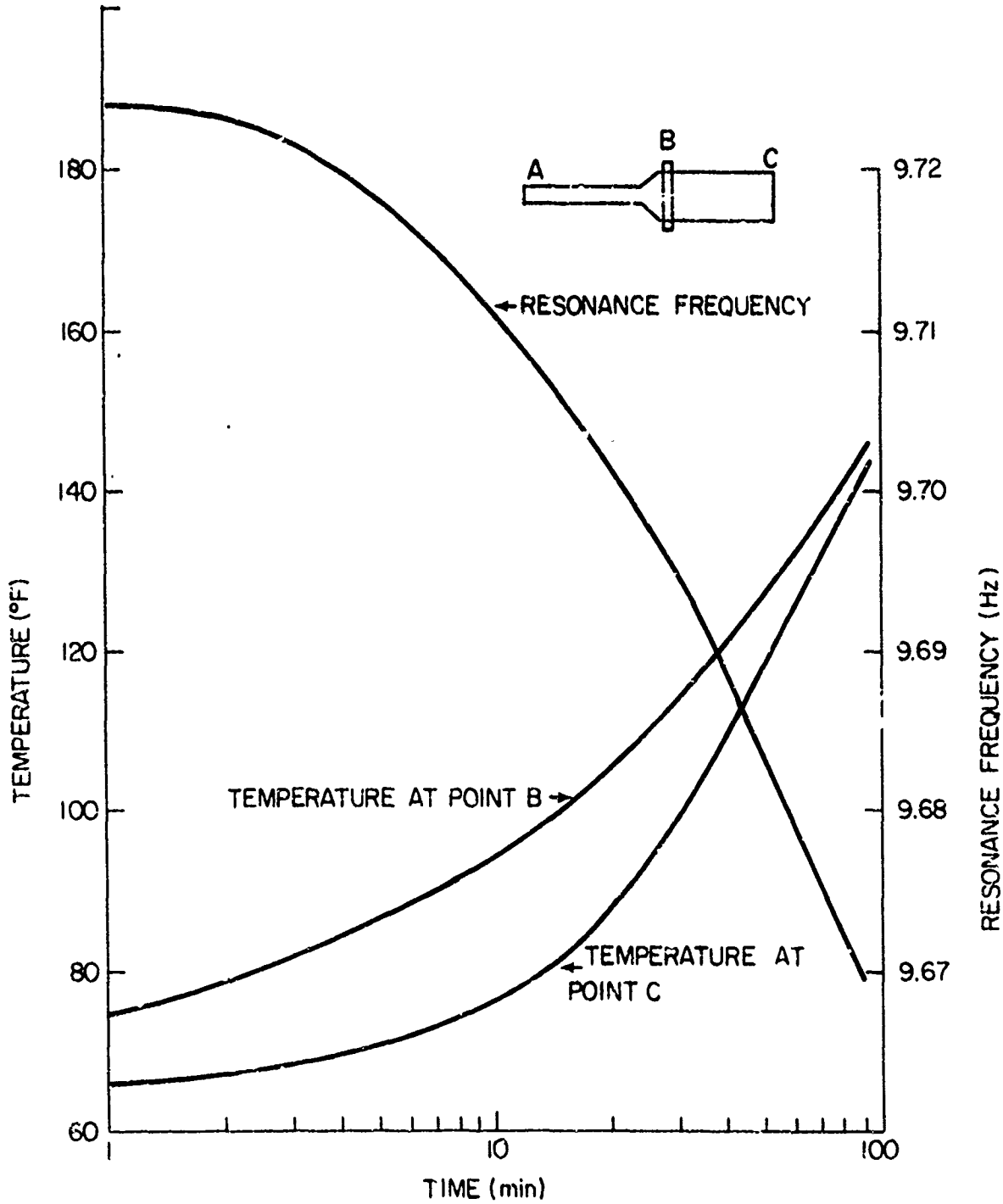

Figure 3-4.8 - Temperature and Q as function of operation time at 20 watts input power.

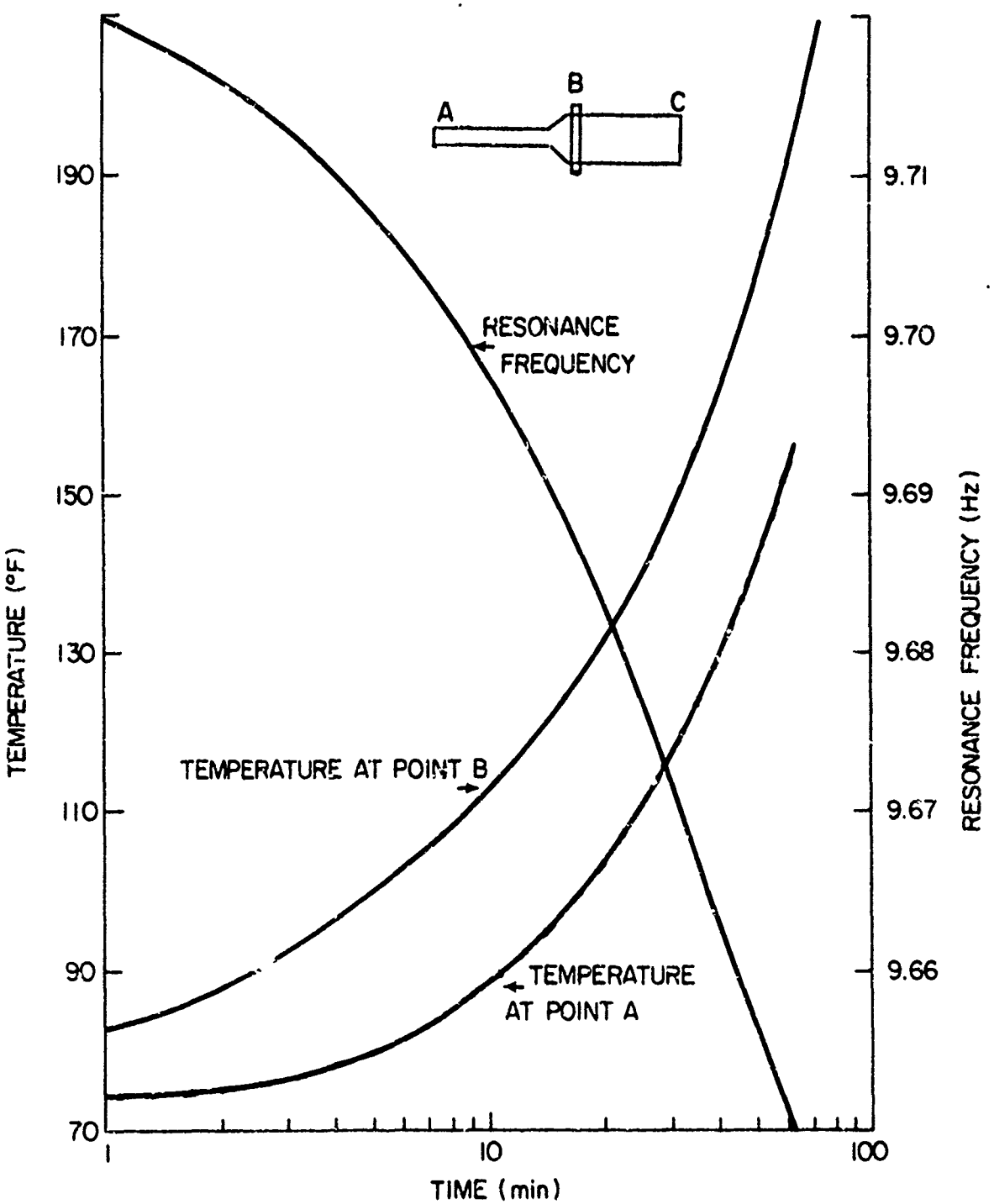

Figure 3-4.9 - Temperature and Q as function of operation time at 30 watts input power.

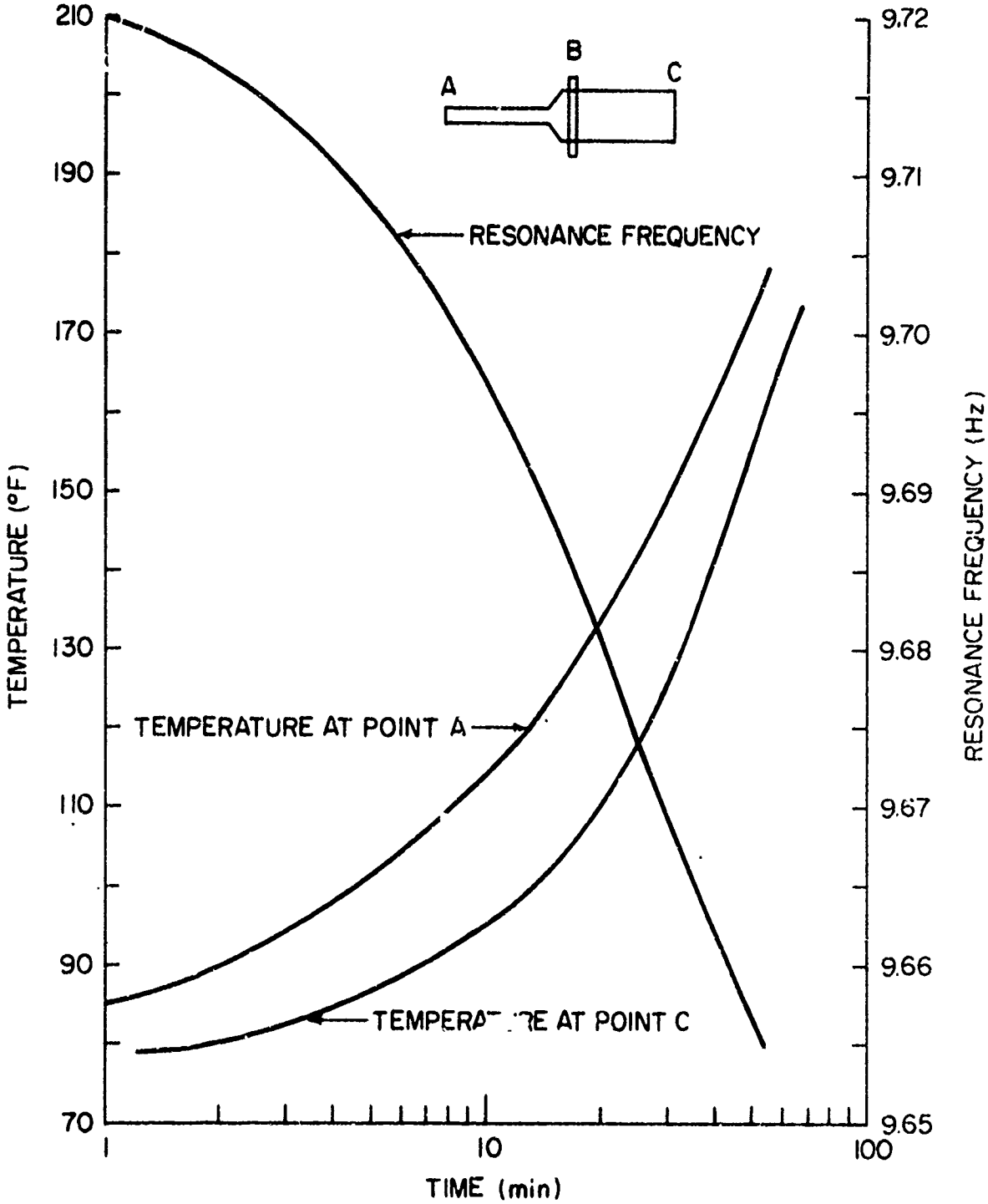

Figure 3-4.10 - Temperature and Q as function of operation time at 30 watts input power.

to the lack of availability of direct methods of measuring the small amplitude, high frequency vibrations, two indirect methods were used.

In the first method, a strain gage was mounted two inches from the transducer tip, as shown in the schematic of the setup in Figure 3-4.11. With the transducer operating at resonance frequency, the strain amplitudes were recorded for various input powers. A typical strain gage output is shown in Figure 3-4.12. The strain amplitudes measured for 5, 10, 20 and 30 W is given in Table 3-4.1. The resulting strain data was used in conjunction with a theoretical model of the transducer to obtain a value of tip displacement. These aspects are reported in a later section.

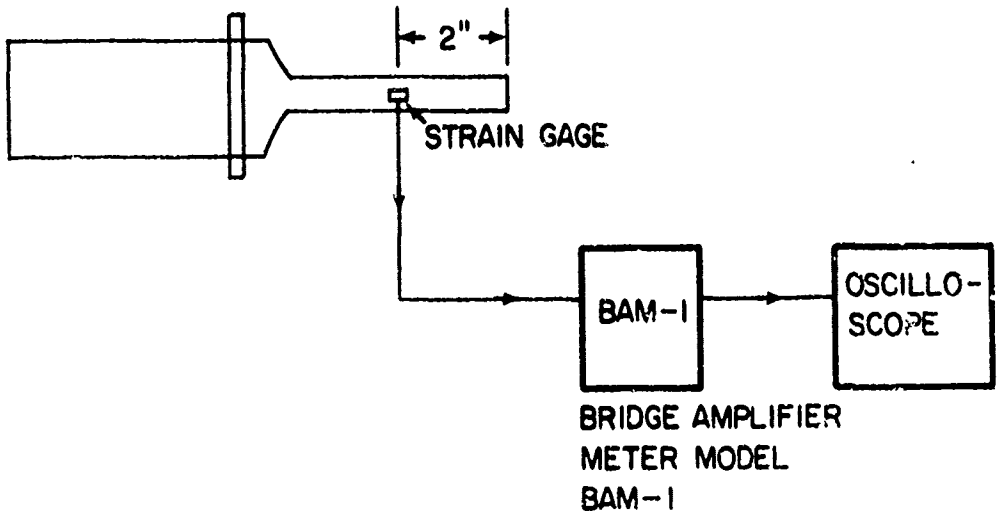

Figure 3-4.11 - Basic experimental setup for strain measurement

Strain gage used: Micro-Measurements Products
Gage type: EA-06-050AR-120
Gage Factor at 75°F: 2.035 ± 1.0%

Input power = 20 watts
Res. frequency = 9716 Hz
Each vert. div. = 0.2 volt
Each horiz. div. = 50 μsec

Figure 3-4.12 - Typical strain output observed from oscilloscope.

Table 3-4.1 - Strain at Various Power Levels

Input Power, W	Zero-Peak Strain Gage Reading
5	138×10^{-6}
10	206×10^{-6}
20	275×10^{-6}
30	334×10^{-6}

The second indirect method was to measure the tip acceleration. The experimental setup for this test was as shown in Figure 3-4.13. A typical acceleration output is shown in Figure 3-4.14. The data for the tip acceleration at 5, 10, 20 and 30 W is summarized in Table 3-4.2. The use of this data for establishing certain aspects of the mathematical model of the transducer and for obtaining the tip displacement is given in a later section.

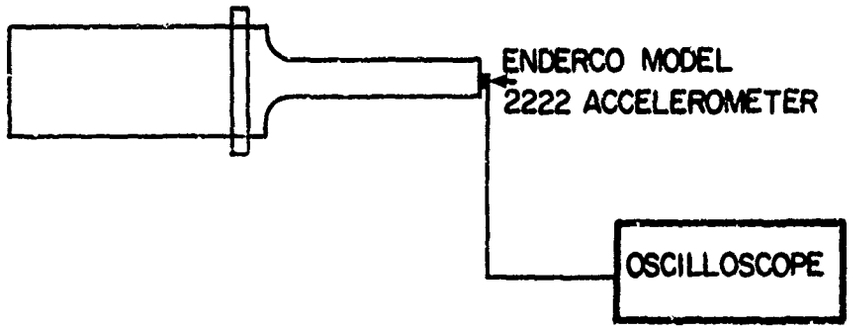

ACCELEROMETER VOLTAGE SENSITIVITY:
1.0 pk.mV/pk.g NOMINAL

Figure 3-4.13 - Basic experiment setup for acceleration measurement.

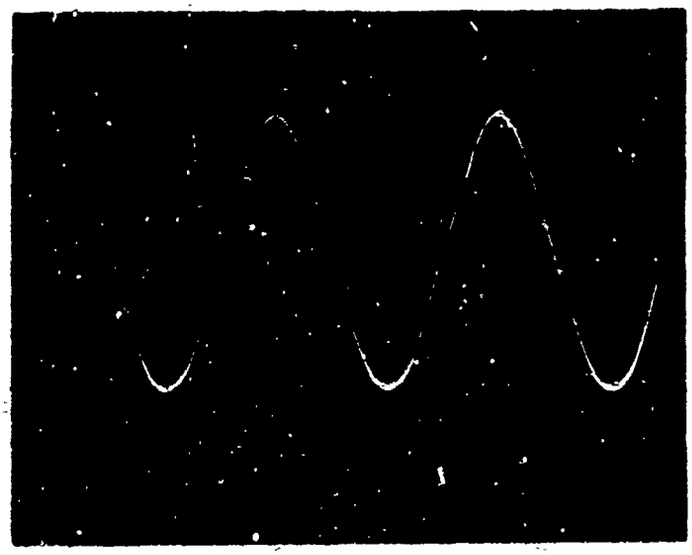

Input power = 30 watts
Res. frequency = 3705 Hz
Each vert. dir. = 5 volts
Each horiz. dir. = 20 μsec

Figure 3-4.14 - Typical acceleration output observed from oscilloscope.

Table 3-4.2 - Tip Acceleration at Various Power Levels

Input Power, W	Tip Acceleration	
	in./sec^2	g
5	0.21357×10^7	5.527×10^3g
10	0.27589×10^7	7.14×10^3g
20	0.37770×10^7	9.775×10^3g
30	0.45063×10^7	11.662×10^3g

(E) Comparison of Experimental and Theoretical Results

Theoretical calculations on the vibrational mode and energy storage of a transducer were reported in the earlier section (I-2). Experimental results on the Q, strain level, tip acceleration, frequency variation and the temperature changes occurring in a transducer operating at various power levels were reported in the previous section. It is of interest to make comparison between the two types of results, where possible.

We first consider the case of tip displacement of the transducer as obtained by strain and acceleration data. Referring to equation (3-2.11), it is seen that the constant D must be determined in order to predict tip displacement. Referring to equations (3-2.12) and (3-2.13), it is seen that this constant can be found if the strain or acceleration is known. In other words, these last formulas enable D to be obtained from experimental data. Thus, for the case of strain, we have the strain gage loacted at $x_2 = 2$ inches, so that

$$D = \frac{\epsilon_2}{K(11.72 \cos kx_2 - \sin kx_2)\cos \omega t} = \frac{\epsilon_2}{2.9567 \cos \omega t} \qquad (3\text{-}4.3)$$

where k = 0.3725, then

$$\begin{aligned} \epsilon_1 &= kD(2.038 \cos kx_1 + \sin kx_1)\cos \omega t \\ \epsilon_2 &= kD(11.72 \cos kx_2 - \sin kx_2)\cos \omega t \end{aligned} \qquad (3\text{-}4.4)$$

For the various input power levels, the value of the constant D as determined from the strain data is given in Table 3-4.3.

Table 3-4.3 - The Constant D for Various Power Levels from Strain Data

Input Power, W	D
5	4.63×10^{-5}
10	6.97×10^{-5}
20	9.296×10^{-5}
30	11.288×10^{-5}

For the case of acceleration data, the constant D is given from equation (3-2.13) as

$$a_2 = -Dw^2(11.72 \sin kx_2 + \cos kx_2)\cos \omega t \qquad (3\text{-}4.5)$$

or

$$D = \frac{-a_2}{w^2(11.72 \sin kx_2 + \cos kx_2)\cos \omega t} \qquad (3\text{-}4.6)$$

At the tip, $x_2 = 4$ inches, for $\cos \omega t = 1$, the maximum value of acceleration is determined for comparison with experimental data. The resulting value D for various input powers is given in Table 3-4.4.

Table 3-4.4 - The Constant D from Acceleration Data

Input Power, W	D
5	5.066×10^{-5}
10	5.617×10^{-5}
20	7.94×10^{-5}
30	9.276×10^{-5}

From a theoretical point of view, the D constant calculated from the strain test and the acceleration test should be the same, but actually, due to the approximations made in the transducer model, there are some differences between the two calculated D constants. The comparison of the D constant is shown in Table 3-4.5. Considering the mathematical idealizations and the widely different measuring techniques, the results are in fairly good agreement.

Table 3-4.5 - Comparison of the Different D Values

Input Power, W	D from Strain Test (D_1)	D from Acc. Test (D_2)	$\frac{D_2-D_1}{D_1}$ %	Average D
5	4.68×10^{-5}	5.066×10^{-5}	8.2	4.873×10^{-5}
10	6.97×10^{-5}	5.617×10^{-5}	-19.4	6.295×10^{-5}
20	9.296×10^{-5}	7.94×10^{-5}	14.6	8.618×10^{-5}
30	11.285×10^{-5}	9.276×10^{-5}	17.7	10.282×10^{-5}

After substituting the average value of D into equations (3-2.11), (3-2.12), (3-2.13) and setting cos wt equal to 1, the numerical value for maximum tip displacement, strain and acceleration can be found and are shown in Table 3-4.6.

Table 3-4.6 - Displacement, Strain and Acceleration in the Transducer

Input Power, W	Tip Displacement, in.	Strain in Transducer	Tip Acceleration (in./sec^2)
5	0.5731899×10^{-3}	$-0.92271235 \times 10^{-6}$	$-0.213569456 \times 10^{7}$
10	$0.74044764 \times 10^{-3}$	$-1.19197168 \times 10^{-6}$	$-0.275891712 \times 10^{7}$
20	$1.01368964 \times 10^{-3}$	$-1.63183635 \times 10^{-6}$	$-0.377701888 \times 10^{7}$
30	$1.20941699 \times 10^{-3}$	$-1.94691878 \times 10^{-6}$	$-0.450630144 \times 10^{7}$

The procedure used to compare theoretical and experimental values of the stored energy is given. Using the average value of the constant D for the various power levels (see Table 3-4.6), the theoretical value of stored energy was computed from equation (3-2.24). Actually, it will be recalled that D resulted from utilizing experimental strain and acceleration data in conjunction with a purely theoretical model of the transducer, so that the computed stored energy is not a purely theoretical expression. The experimental value of stored energy was then calculated from the defining expression for Q,

$$Q = 2\pi \frac{U}{D} \qquad (3\text{-}4.7)$$

where

U = The total strain energy (stored energy) at maximum displacement

D = The energy dissipated per cycle

Then

$$U = \frac{QD}{2\pi} \text{ lb-in./cycle} \tag{3-4.8}$$

Now, the transducer was operated in the unloaded condition so that all of the energy input into the transducer was equal to the energy dissipated in the system. The various levels of power dissipation were

$$\begin{aligned} D_5 &= 5 \text{ watts} = 4.546 \times 10^{-3} \text{ lb-in./cycle} \\ D_{10} &= 10 \text{ watts} = 9.1116 \times 10^{-3} \text{ lb-in./cycle} \\ D_{20} &= 20 \text{ watts} = 18.2232 \times 10^{-3} \text{ lb-in./cycle} \\ D_{30} &= 30 \text{ watts} = 27.3348 \times 10^{-3} \text{ lb-in./cycle} \end{aligned} \tag{3-4.9}$$

From previous experimental results reported in Section (3-4(b)), the Q for different input levels was,

$$\begin{aligned} Q_5 &= 800 \;, \quad Q_{10} = 400 \\ Q_{20} &= 265 \;, \quad Q_{30} = 255 \end{aligned} \tag{3-4.10}$$

Then

$$\begin{aligned} U_5 &= \frac{Q_5 D_5}{2\pi} = 0.59 \text{ in.-lb} = 0.067 \text{ watt-sec.} \\ U_{10} &= \frac{Q_{10} D_{10}}{2\pi} = 0.58 \text{ in.-lb} = 0.066 \text{ watt-sec.} \\ U_{20} &= \frac{Q_{20} D_{20}}{2\pi} = 0.77 \text{ in.-lb} = 0.087 \text{ watt-sec.} \\ U_{30} &= \frac{Q_{30} D_{30}}{2\pi} = 1.11 \text{ in.-lb} = 0.124 \text{ watt-sec.} \end{aligned} \tag{3-4.11}$$

A summary of the theoretical and experimental values of stored energy is presented in Table 3-4.7 for direct comparison

Table 3-4.7 - Comparison of Theoretical and Experimental Stored Energies

Input Power, W*	D	Theoretical Stored Energy (in.-lb)	Experimental Stored Energy (in.-lb)
5	4.873×10^{-5}	0.261	0.59
10	6.295×10^{-5}	0.436	0.58
20	8.618×10^{-5}	0.817	0.77
30	10.282×10^{-5}	1.163	1.11

* The average operating frequency is 9715 cps

At the lowest power level, 5 watts, the agreement between theoretical and experimental values is quite poor. At higher power levels, however, the agreement improves considerably.

3-5 PROCEDURE, RESULTS AND DISCUSSION OF THE INFLUENCE ON Q DUE TO TRANSDUCER MOUNTING

From experience in various tests on the transducer, it is known that the Q value may change due to different transducer mounting methods. Thus, it becomes necessary to understand the influence on Q due to transducer mounting so that a better mounting scheme may be developed in the future.

Six mounting schemes are investigated in the present tests ranging from an almost completely free mounting to a rigid mounting scheme. These tests provide some idea about the magnitude of Q variation and the sensitivity of Q to different mounting schemes. All tests were conducted under a constant 30 watts input power. The bandwith method was used to measure the Q factor where

$$Q = \frac{f_r}{f_1 - f_2} \qquad (3\text{-}5.1)$$

and where

f_r = Resonance frequency

f_1, f_2 = Frequencies of the half power points.

Each mounting scheme is presented in a separate paragraph and the final results of all schemes are shown in Table 3-5.1 for the sake of easy comparison.

TEST A--Plate-Post Mounting

A P-7 transducer is screwed into a thick plate and then secured by a set screw and lock nut. This assembly is fastened to a one-inch diameter steel post as shown in Fig. 3-5.1 and Fig. 3-5.2. The corresponding f_r, f_2 and f_1 are monitored and shown in Table 3-5.1.

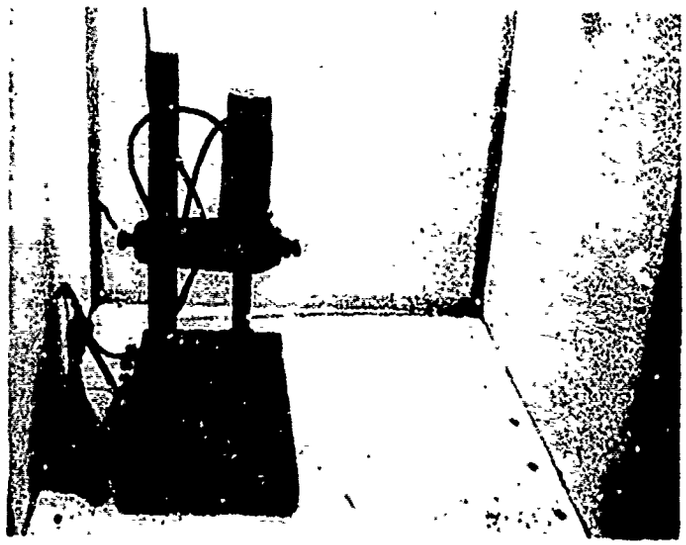

Figure 3-5.1 - View of plate-post hardware.

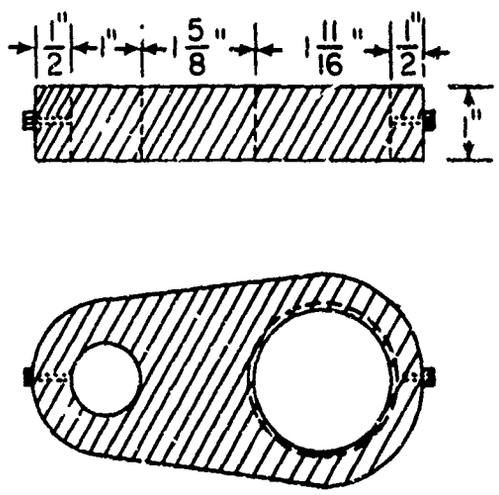

Figure 3-5.2 - Detail of thick plate transducer holder.

Table 3-5.1 - Q-Factor for Different Tests

Test	f_r, cps	f_2, cps	f_1, cps	$Q = \frac{f_r}{f_2 - f_1}$
A	9760	9775	9747	349
B	9740	9753	9730	423
C	9735	9747	9726	465
D	9748	9760	9737	424
E (a)	9719	9734	9710	405
E (b)	9715	9732	9702	323
F	9739	9754	9732	442

TEST B--Transducer Mounted in an Enclosed Case

An enclosed case shown in Figure 3-5.3 (sectional drawing is shown in Figure 3-5.4 was used to mount the P-7 transducer with the threaded flange located approximately at the node point of the transducer. It is seen from Table 3-5.1 that the Q value for this mounting scheme is relatively high.

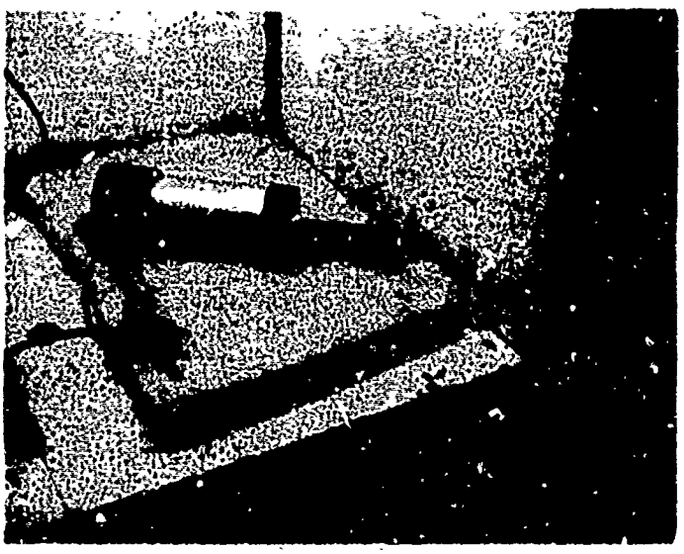

Figure 3-5.3 - Transducer mounted in an enclosed case.

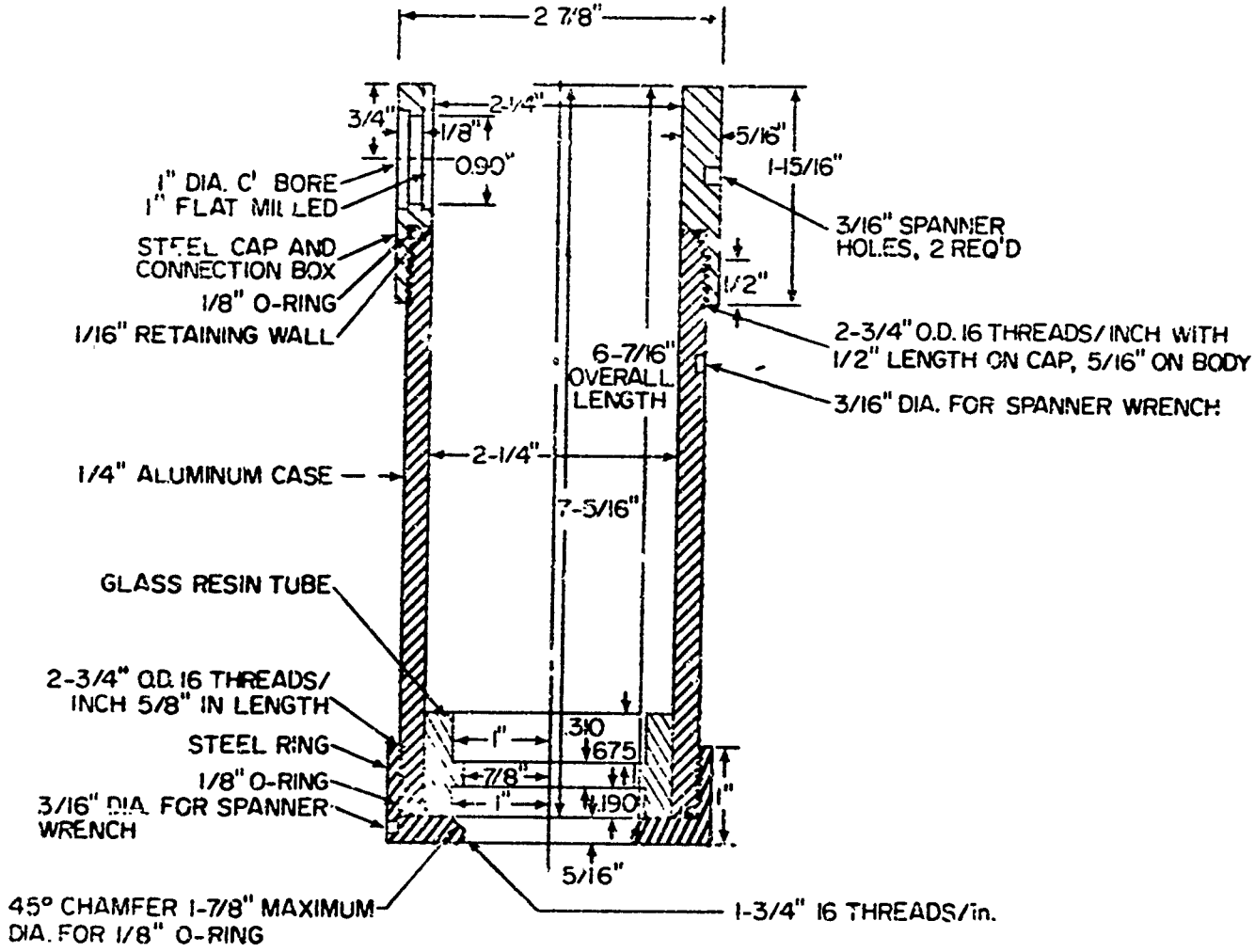

Figure 3-5.4 - Sectional drawing of enclosed case.

TEST C--Mounting Scheme Used for Dranetz Test

For the Dranetz test, a 2-inch diameter fiberglass ring and steel tube are used to support the transducer as shown in Figure 3-5.5. This mounting scheme can be described by the drawing in Figure 3-5.6. From the final results in Table 3-5.1, it is seen that the highest Q is obtained from this mounting scheme.

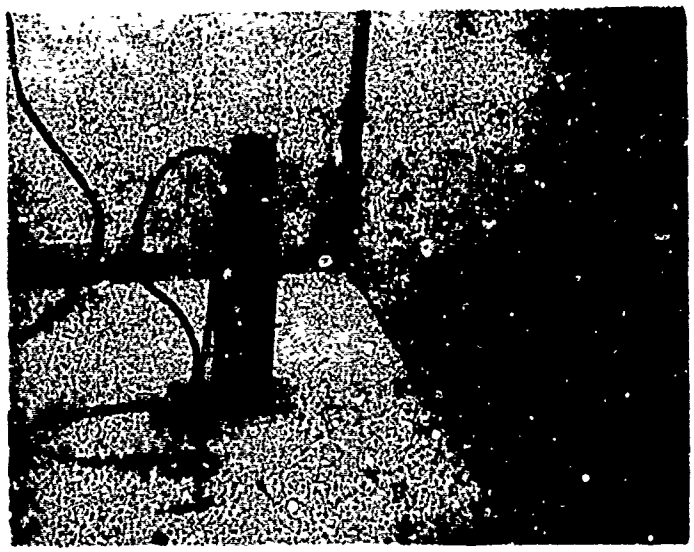

Figure 3-5.5 - Mounting scheme for Dranetz test.

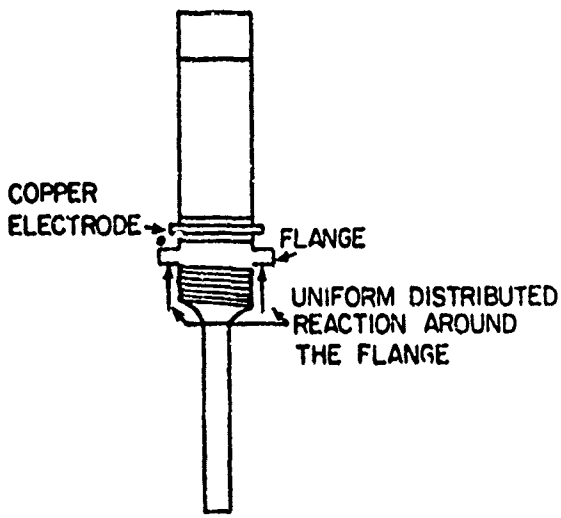

Figure 3-5.6 - A uniform distributed reaction around the flange to support the transducer.

TEST D--Transducer Mounted on a Silastic Rubber Plate

A 2-1/2" x 2-1/2" x 1/4" silastic rubber plate with a 1-3/4" diameter hole at the center was used to support the transducer. The whole assembly was placed on a flat glass plate so that the friction force between the large end of the transducer and its contact surface was reduced to a minimum. A relatively high Q was obtained, as shown in Table 3-5.1, for this mounting assembly.

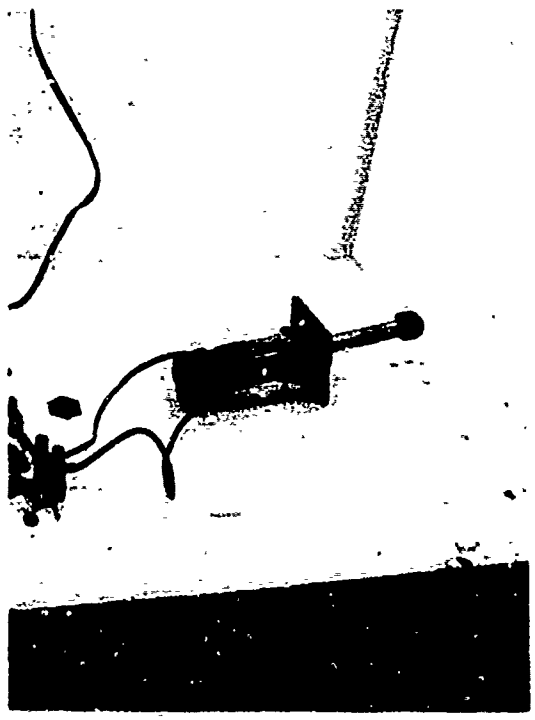

Figure 3-5.7 - Transducer mounted on a silastic rubber plate.

TEST E--Transducer Supported by Two Knife Edges

Two kinds of tests with different knife edge arrangements were conducted, as shown on Figure 3-5.8 (a) and (b). It is interesting to notice that the value of Q for case (a) is approximately 25% higher than the value for case (b). This suggests that the tightness of mounting around the node point substantially changes the value of Q.

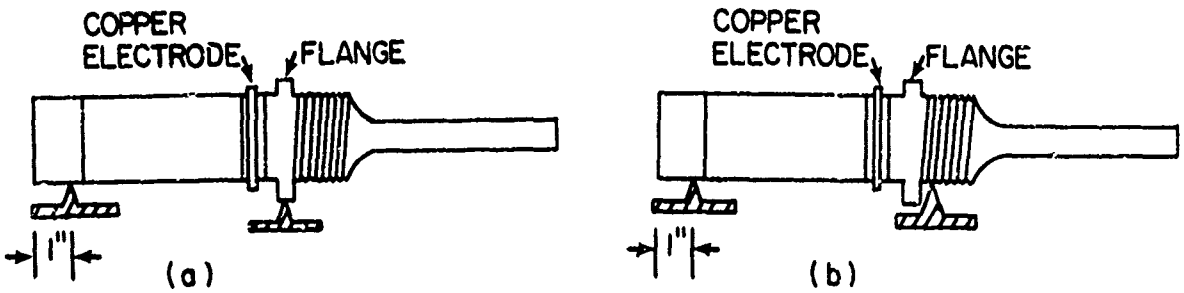

Figure 3-5.8 - Transducer supported by two knife edges, the knife edge is placed beneath (a) the flange (b) the thread.

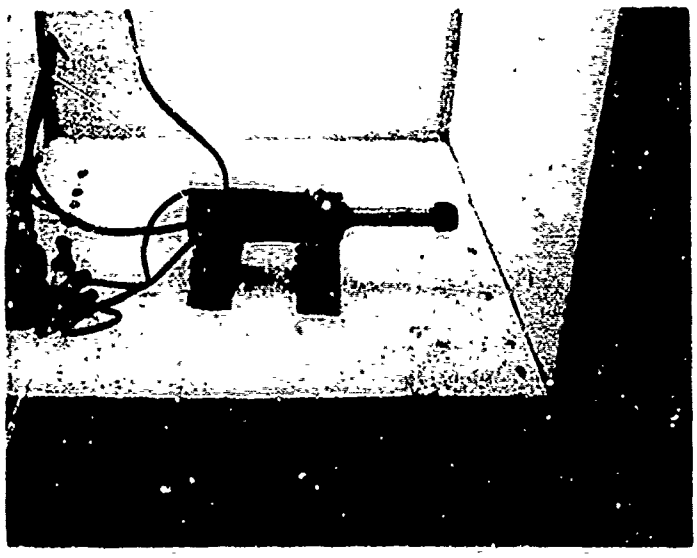

Figure 3-5.9 - Transducer supported by two knife edges.

TEST F--Transducer Supported by Two Wires

Two thin metal wires, as shown in Figure 3-5.10, were used to suspend the transducer. One wire is located 1 inch from the large end of the transducer, and the other wire is located at the inner thread at the step. The Q value obtained from this test is rather high.

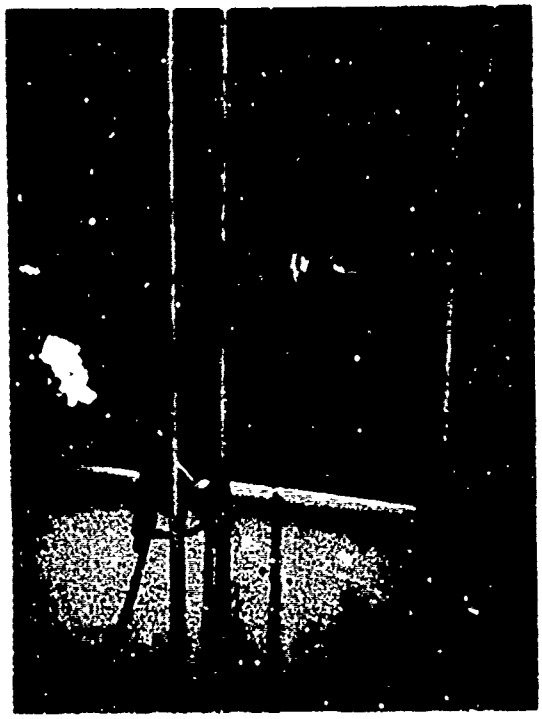

Figure 3-5.10 - Transducer supported by two wires.

To compare the Q value for each test from the previous table, it is easily seen that the Q factor for the less constrained mountings, such as Test C, are higher than the ones with more constraint, such as Test A. The sensitivity of the variation of Q due to mounting is largely based on the degree of tightness and contact area of the mounting around the node point. The lower and upper bound of Q for 30 watts input power are approximately from 325 to 450.

3-6 PROCEDURE, RESULTS AND DISCUSSION ON THE TRANSIENT RESPONSE DUE TO TOOL IMPACT

Two aspects of the tool-transducer impact that have not yet been covered in the previous work is the transient response of a transducer due to a tool impact. It is the objective here to study the energy removal per impact relative to the total stored energy of the transducer and the rapidity of energy recovery of a transducer from a tool impact.

Due to the lack of availability of direct methods of measuring the energy removal per impact and the rapidity of energy recovery from a tool impact, a indirect method of monitoring the tip vibration of a transducer is used. A Brüel and Kjaer type MM-0002 magnetic transducer pickup is placed in the vicinity of the tip of the P-7 transducer and connected to an oscilloscope to monitor the amplitude of the tip vibration. A one half-inch diameter steel ball and a 9/16-inch diameter tungsten-carbide ball are used to simulate a tool impact on the transducer. Figure 3-6.1 shows the basic features of the setup.

Two kinds of output are observed from the oscilloscope. One is that the amplitude of tip velocity decreases after the impact, the other is that the amplitude of the tip velocity increases after impact. Both cases are shown in Figures 3-6.2 (a) to (e) and Figures 3-6.3 (a), (b). Figure 3-6.4 shows the amplitude of tip velocity when the transducer is turned on and off.

The percentage of the stored energy removed from the transducer are calculated based on the relation from Section 3-2 and presented in Table 3-6.1. The time required for the stored energy of the transducer to recover to the level before the impact is calculated and also shown in Table 3-6.1. With the understanding of the present experimental results, it is possible to determine the size of the gap between the transducer tip and the working surface such that an optimum utilization of the transducer in the rock cutting process can be achieved.

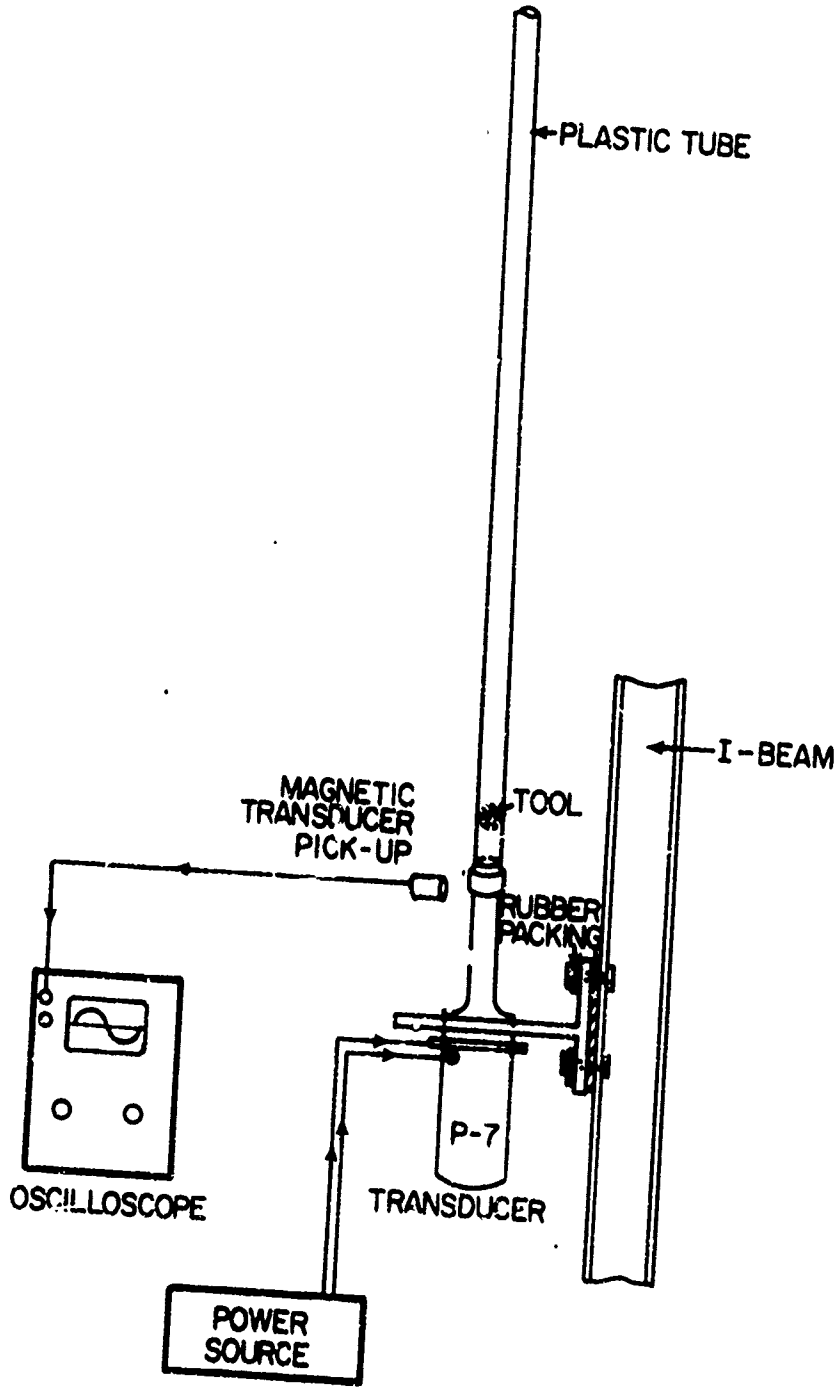

Figure 3-6.1 - Basic experimental set-up for impact studies.

(a) Res. freq. = 9700 cps
$\frac{1}{2}$" φ steel ball

(b) Res. freq. = 9700 cps
$\frac{1}{2}$" φ steel ball

(c) Res. freq. = 9678 cps
$\frac{1}{2}$" φ steel ball

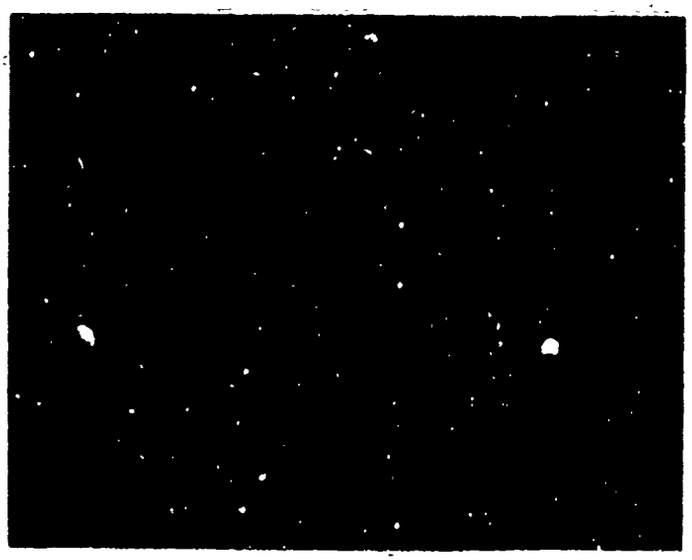

(d) Res. freq. = 9695 cps
$\frac{1}{2}$" φ steel ball

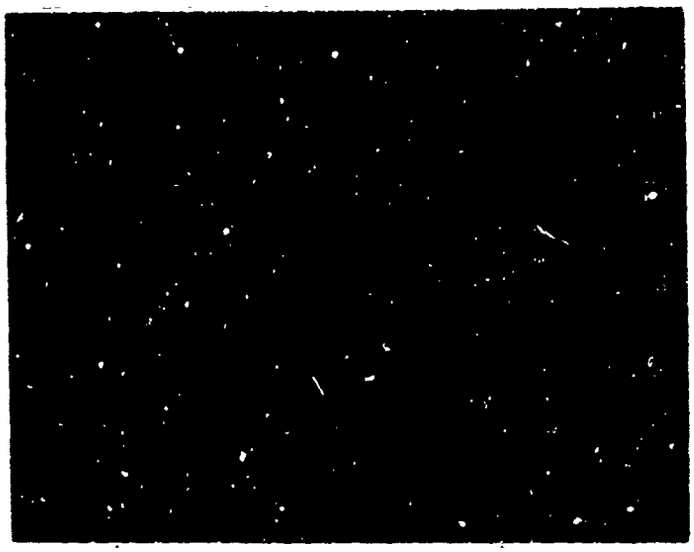

(e) Res. freq. = 9703 cps
9/16" φ Tungsten-carbide ball

Figure 3-6.2 - Impact on transducer tip showing sudden energy decrease. Each horizontal division = 10 millisecond. Vertical scale = 0.2 volt/division.

(a) Res. freq. = 9703 cps (b) Res. freq. = 9705 cps

9/16" Tungsten-carbide ball
Each vert. dir. = 0.2 volt
Each horiz. dir. = 10 millisecond

Figure 3-6.3 (a), (b) - Amplitude of tip velocity increasing after tool-transducer impact.

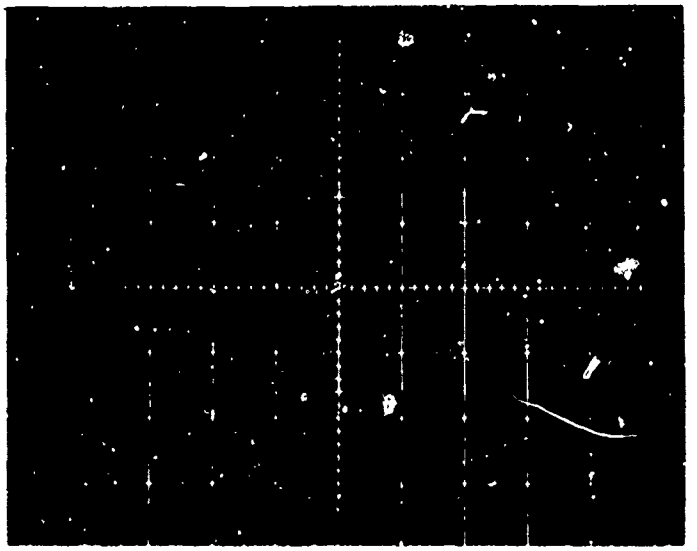

(a) Start up of the transducer

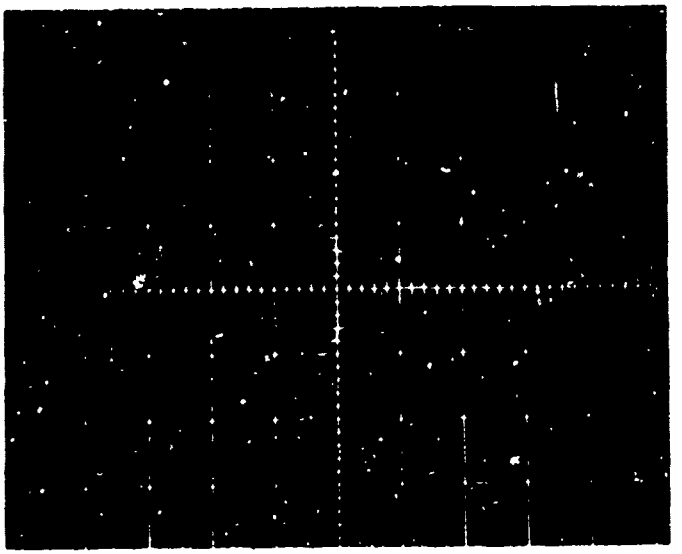

(b) Turn off of the transducer

Res. freq. = 9680 cps
Each vert. dir. = 0.2 volt
Each horiz. dir. = 20 millisecond

Figure 3-6 4 - The amplitude of the tip velocity as the transducer is turned on (a) and turned off (b).

Table 3-6.1 - Percentage of Energy Removal After Impact and Stored Energy Recovery Time After Impact

Cases (Fig. 3-6.2)	Resonance Frequency cps	Vel. Amplitude Removed After Impact	Stored Energy Removed After Impact	Recovery Time After Impact	
				msec.	cycles
(a)	9700	14%	26%	12	116.4
(b)	9700	17%	31.1%	12	116.4
(c)	9678	15%	28%	11.5	111.3
(d)	9695	15%	28%	10	97
(e)	9703	36.2%	59.3%	10	97

3-7 CONCLUSION

The investigation reported represented the initial phase of a theoretical-experimental study of the influence on the total stored energy of the transducer of the input power, temperature, mounting technique and the tool impact. In the course of the investigation, the observation made enabled a number of conclusions to be drawn regarding the vibrational characteristics of a sonic transducer.

(1) The Q value is constant and is independent of the change in resonance frequency and temperature as well as operating time for a given power level.

(2) For different input power levels, the Q for a P-7 transducer tends to approach a limiting value of about 250 as the power increases.

(3) The highest temperature is generated at the copper electrode and the resonance frequency is shifted as a function of operating time.

(4) The total stored energy, displacement, strain and acceleration along the transducer may be obtained from theoretical analysis and experiments.

(5) The Q value is inverse to the degree of constraint imposed from the mounting. The upper and lower bound of Q for 30 watts input power level was 450 and 325.

(6) The stored energy removal after impacted by a half-inch steel ball is about 30 percent of the original stored energy.

3-8 REFERENCES

1. Feng, C. C. and Graff, K. F., "Impact on a Sonic Transmission Line," Engineering Experiment Station Report 220-Q3-68, see also final report on "Development of Basic and Ultrasonic Power Devices for Application in Highway Engineering," Final Report EES-220, Vol. 2, Chapter 22, 1970.

2. Feng, C. C., "Energy Transfer in Sonic Impact Coupling," M.S. Thesis, The Ohio State University, 1969.

3. Feng, C. C., "Analysis of Spring-Assisted Impact Coupling," Final Report on Engineering Experiment Station Project WE 17, 1970.

4. Graff, K. F., and Shieh, L. C., "Investigation of Engineering Aspects of The Sonic Cement Grinding Process," Final Report on Engineering Experiment Station Project EES-380, 1971.

4 TOOL IMPACT ON ROCK

4-1 INTRODUCTION

A previous study of a rectangular stress wave propagating along a semi-infinite rod and incident on a rock surface by Mahban [1] shows that the dynamic contact force-penetration characteristics can be approximately represented by a bilinear spring model as shown in Figure 4-1, where k_1 and k_2 are spring constants for the loading and unloading paths of the bilinear model. Based on Mahban's model for rock, the problem of tool-rock impact has been theoretically analyzed and reported [2]. We know that in the sonic rock drilling process, the length of the tool is usually very short. The behavior of the tool during impact is very complicated according to the three dimensional theory of elasticity. To simplify the problem, an assumption was made that one dimensional theory of elastic wave propagation in long rods could still be applied to tools of short length (Fig. 4-2a). In this approach, a rather complicated analysis is still involved. To further simplify the problem, another approach was given, assuming that the tool was perfectly rigid and the contact force-penetration character was the same as that of a rectangular stress wave propagating along a semi-infinite rod. By these assumptions, the problem becomes very simple. It is just as a rigid mass impacting on a spring of bilinear character (Fig. 4-2b). The results were found to be very close to those obtained by the former approach. The agreement of the above two approaches does not mean that we have exactly solved the tool-rock impact problem because assumptions were made in both approaches. It only indicates that one can replace the former approach which is very complicated in numerical manipulation by a very simple rigid mass-spring system which is well known but with assumptions of weaker theoretical basis. To study the actual tool-rock

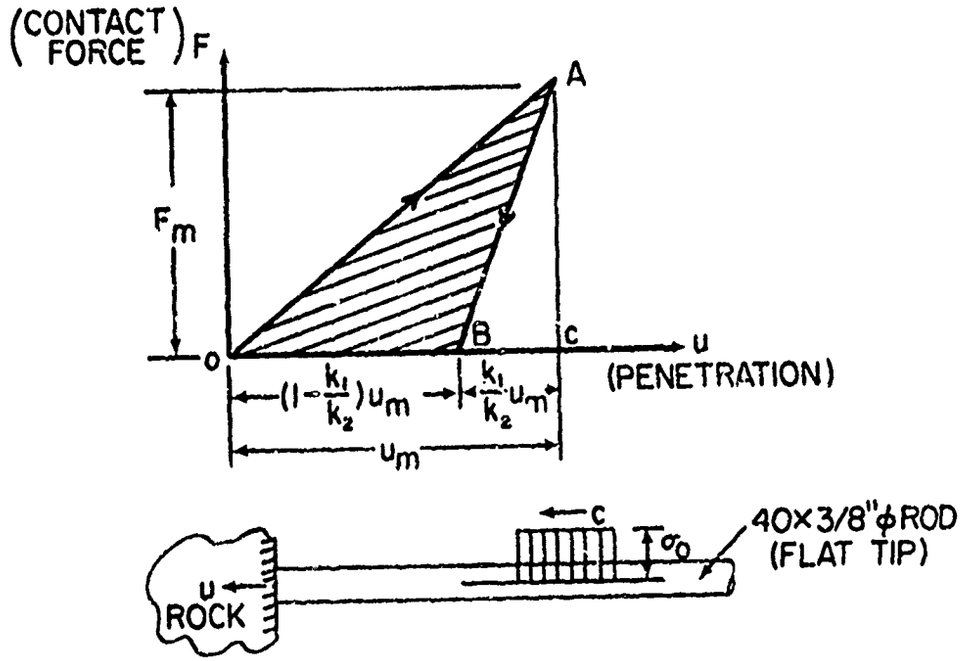

Figure 4-1 - Mahban's experiment and his bilinear contact force-penetration relation.

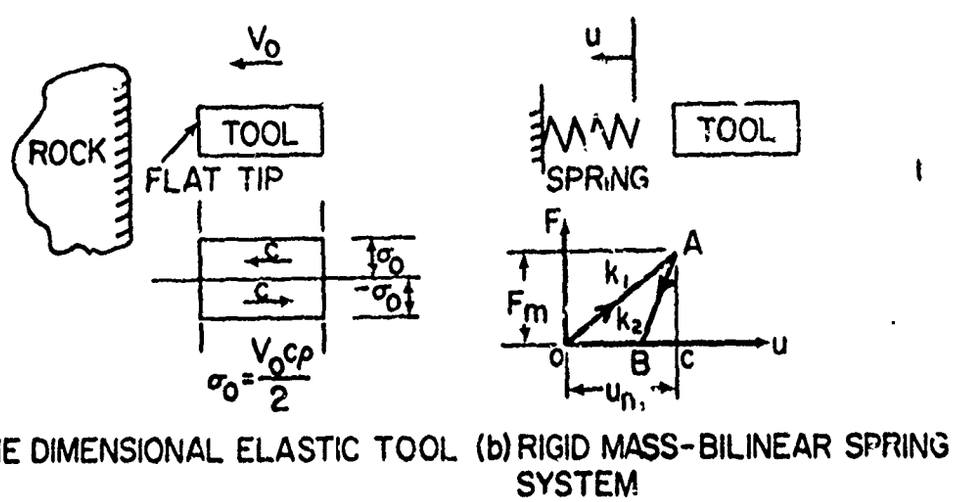

(a) ONE DIMENSIONAL ELASTIC TOOL (b) RIGID MASS-BILINEAR SPRING SYSTEM

Figure 4-2 - Impact of a sonic tool against rock.

impact problem, a series of experiments was conducted. Attempts were made toward finding the impact-rebound velocity relationship; then the actual results were compared with the analytical results obtained from the two approaches cited previously. Special emphasis was also given to the fracture zone characteristics, energy loss, and the effect of various tool geometries and number of impacts.

4-2 EXPERIMENTAL PROCEDURE

A photograph and schematic diagram of the experimental set-up are shown in Figure 4-3. A spring gun, which can deliver tools at a specific velocity by adjusting the spring deformation, is placed directly in front of the surface of a rock specimen. The movement of tools of various tip geometry is guided by the gun barrel, therefore the direction of incidence and rebound of the tool can be adjusted to be approximately perpendicular to the rock surface. The incident and rebound velocities of tools are measured by the use of two photo cells which are attached to the end of the spring gun. The photo cells are one inch apart; they pick up the signal when the tool passes. Two oscilloscopes are used to record the time required for the tool to pass the one-inch distance both in incidence and rebound movement. The velocity of the tool is just equal to the reciprocal of the time measured. The incident velocity of the tool ranged from 200 in./sec. to 600 in./sec.

The tools were made of cold-rolled steel. Figure 4-4 shows tools with various tip geometries. The dimensions and latter designations of the tools used are shown in Figure 4-5. All of the tools are of one inch in diameter and length.

4-3 THEORETICAL CONSIDERATIONS AND RESULTS

(A) Incident and Rebound Velocity Relationship of a Flat Tool (Type A):

As stated in Section 4-1, the tool-rock impact problem was presented in reference [2] and was based on Mahban's experimental results and the assumption that wave behavior in the tool is one-dimensional. It was also found that the tool-rock impact analysis can be replaced approximately by a rigid mass-spring system. We will now compare the experimental and analytical results.

Mahban obtained the values of k_1 and k_2 in his experiment on limestone for four different stress levels (σ_o) of incident rectangular stress waves along a 40-inch rod. The incident velocities (V_o) of a tool corresponding to his stress levels can be obtained according to the equation for one-dimensional elastic wave in the tool (Fig. 4-2a),

$$V_o = \frac{2\sigma_o}{c\rho} \qquad (4\text{-}3.1)$$

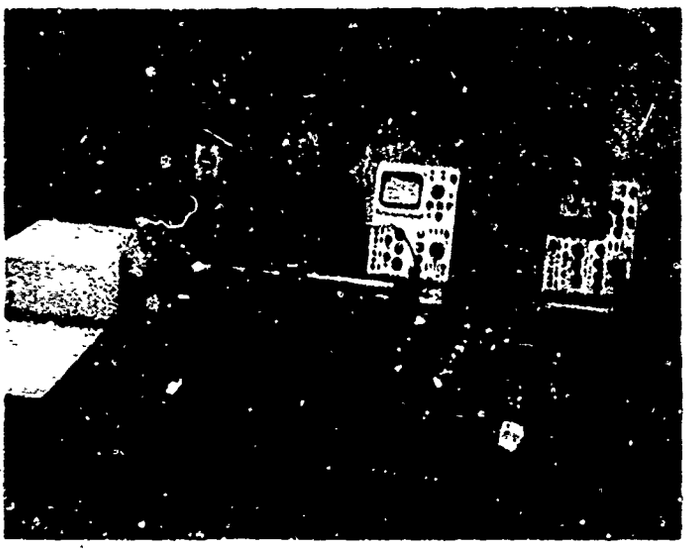

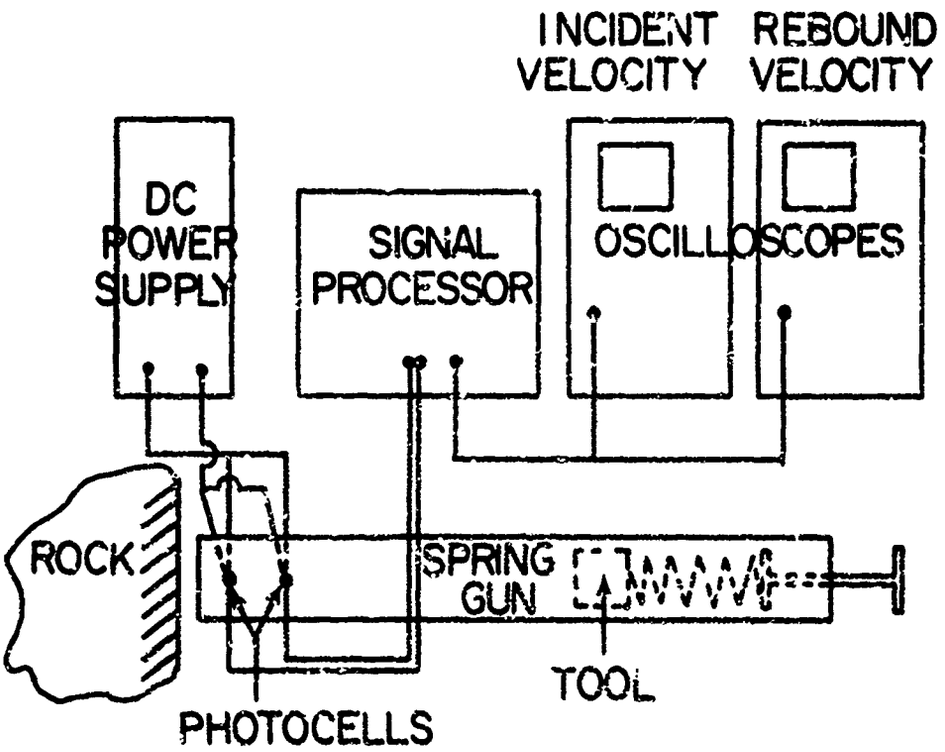

Figure 4-3 - Experimental set-up.

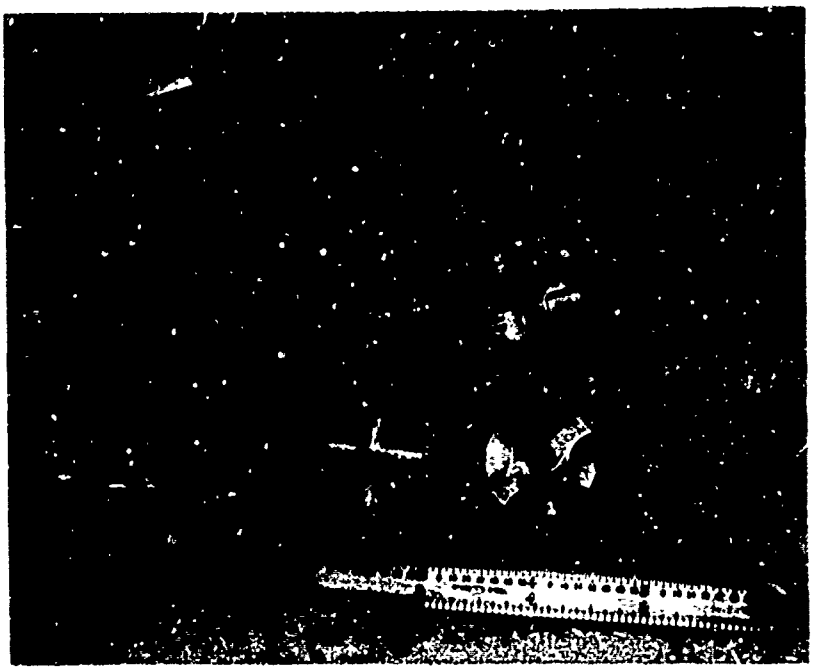

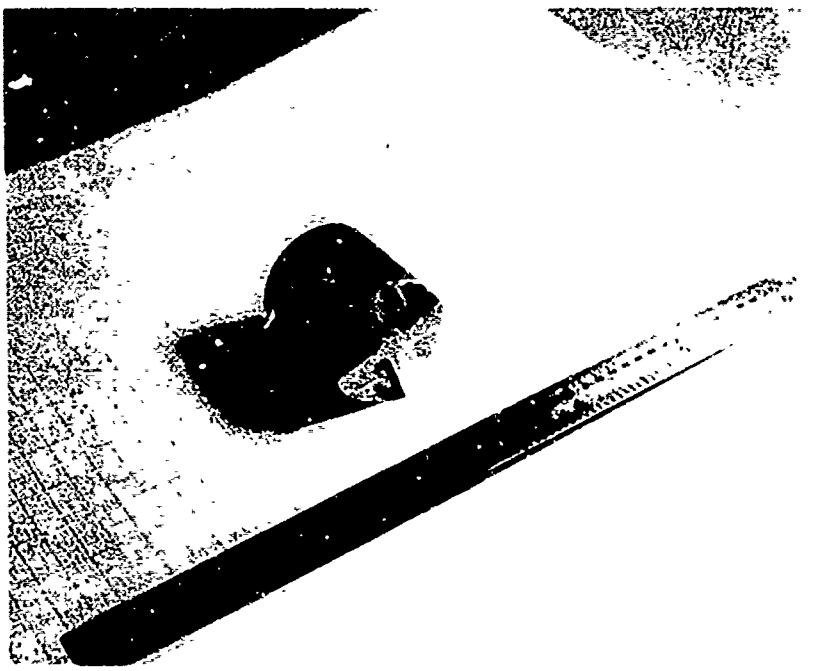

Figure 4-4 - Tools of various tip geometry

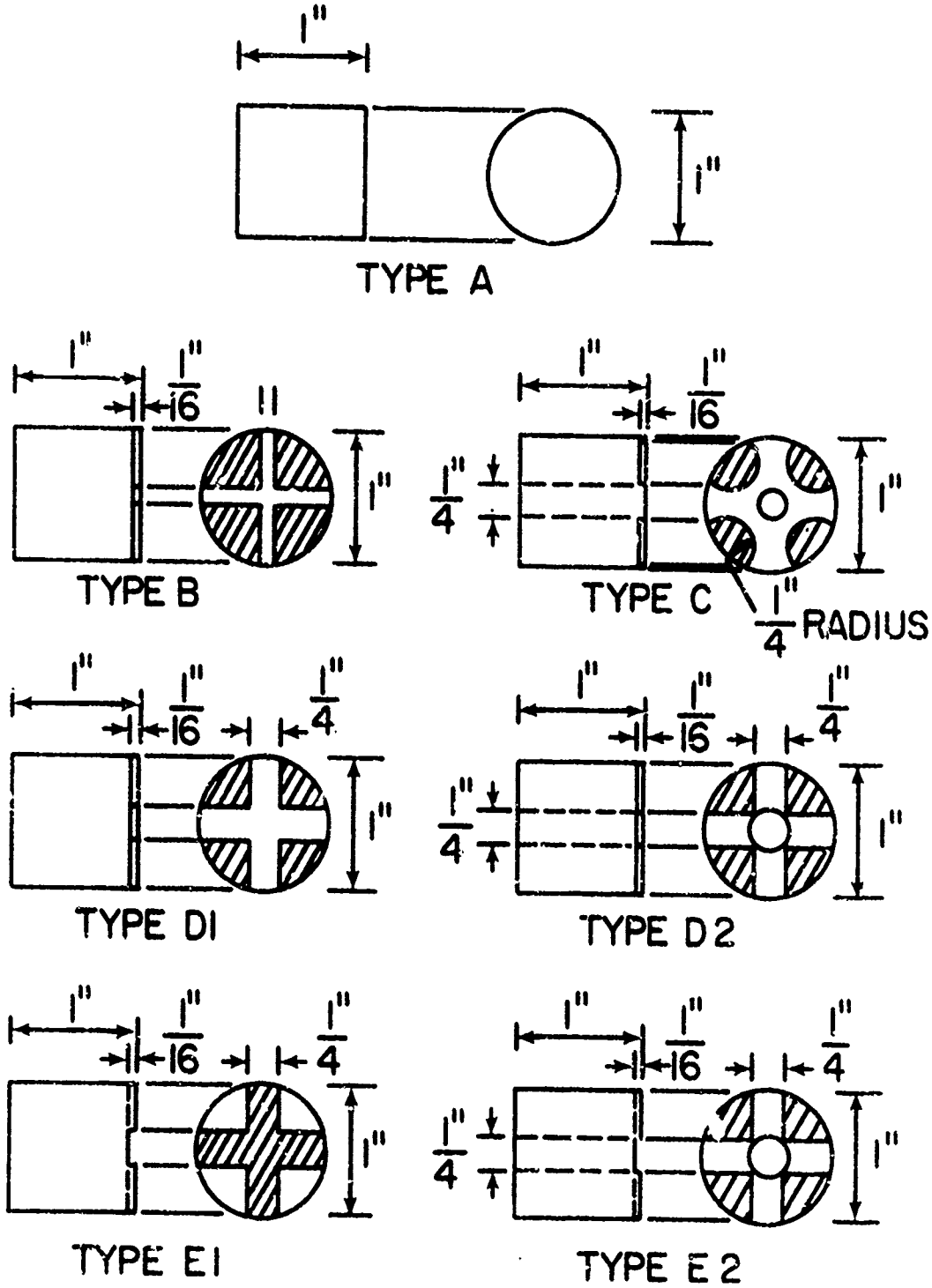

Figure 4-5 - Dimensions of tools used in the experiments.

where c and ρ are one-dimensional wave velocity and the mass density of the tool, respectively.

The values of stress levels (σ_0) and bilinear spring constants (k_1/A and k_2/A) obtained by Mahban, and the corresponding incident velocities of a tool are shown in the following table.

Table 4-1 - Stress Levels of Mahban's Experiment and Corresponding Incident and Rebound Velocity of a One-Dimensional Elastic Tool

	σ_0(ksi) Stress Level		39 High	24.5 Med-High	7.8 Medium	5.9 Low
Mahban's Experiment	k_1/A (10^6 lb./in^3)	Rock Model	2.74	2.89	3.69	3.17
	k_2/A (10^6 lb./in^3)		9.10	7.21	6.82	6.67
One-Dimensional Elastic Tool	V_0 (Incident Velocity in./sec.)		520.0	326.5	104.0	78.7
	V_r (Rebound Velocity in./sec.)		3	207	76.4	54

The rebound velocity V_r of the one-dimensional elastic tool can be calculated approximately by considering the energy of the rigid mass-bilinear spring system. Thus,

$$\frac{1}{2} u_m(k_1 u_m) = \frac{1}{2} mV_0^2$$

$$u_m \text{ (maximum penetration)} = V_0\sqrt{\frac{m}{k_1}} \qquad (4\text{-}3.2)$$

Since the rebound energy of a rigid tool is equal to the area of the triangle ABC as shown in Figure 4-2 (b), we have

$$\frac{1}{2}mV_r^2 = \frac{1}{2}\left[\frac{k_1}{k_2} u_m\right]\left[k_1 u_m\right]$$

or

$$V_r = u_m\sqrt{\frac{k_1}{k_2 m}} \qquad (4\text{-}3.3)$$

Substituting the value of u_m in equation (4-3.2) into equation (4-3.3) we obtain

$$V_r = V_o\sqrt{\frac{k_1}{k_2}} \qquad (4\text{-}3.4)$$

The calculated values of V_r is also shown in Table 4-1.

Figure 4-6 is a plot of incident tool velocity versus the rebound velocity for a flat tool (Type A) according to the analytical results presented in Table 4-1 and the results obtained in this experiment. The figure shows that the actual rebound velocity is always lower than calculated, i.e., the value of V_r calculated based on one-dimensional elastic wave propagation in tool and bilinear model of rock is the upper bound of the actual case. The reasons for a lower actual value may be due to the following factors:

(1) One-dimensional elastic wave propagation theory can not describe the behavior of tools of small length to radius ratio accurately.

(2) The values of k_1 and k_2 are chosen approximately. Therefore, the calculated V_r is only an approximation according to equation (4-3.4).

(3) The actual rebound velocity can not be measured accurately due to the friction between the tool and the spring gun in the experiment. The actual value V_r is higher than measured value. This effect is especially important when the rebound velocity is small.

(4) Misalignment of the axis of tool and the normal line of rock surface will make the impact starting with a point on the periphery of the tool before the surfaces come into complete contact with each other, i.e., two impacts actually occur in one single incident-rebound process. This would increase the energy loss. The direct result would be a lower rebound velocity than a perfect surface-to-surface single impact as we assumed in evaluating the value of V_r by analytical means. Work is also done in compressing the air between the tool and rock surface.

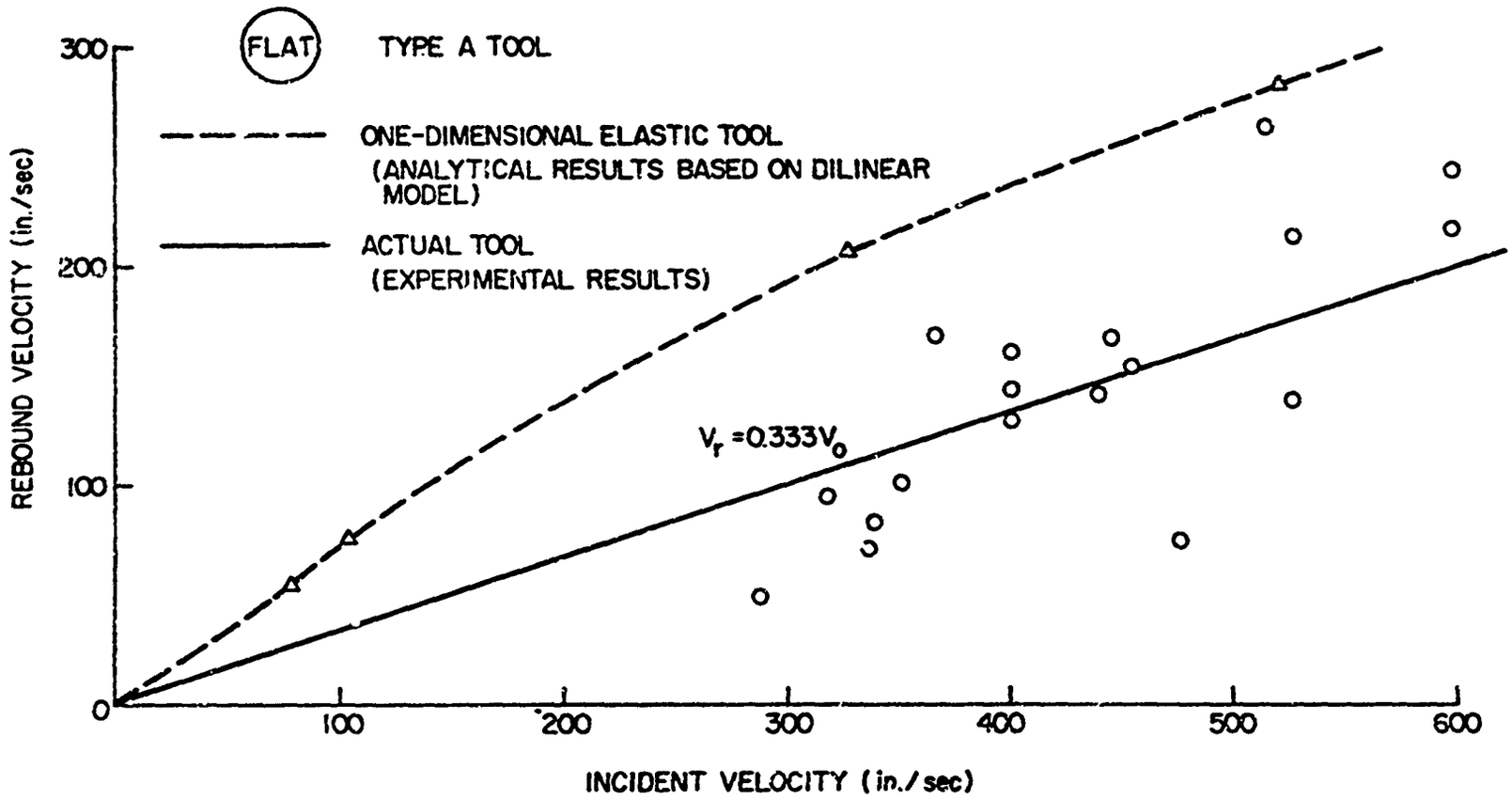

Figure 4-6 - Incident velocity-rebound velocity of a flat tip tool (Type A).

(B) Effect of Tool Tip Geometry on the Rebound Velocity

Figures 4-6 through 4-9, are plots of incident versus rebound velocity for various tools. All the figures show a fairly wide scatter in the rebound velocity data. This may be due to the irregularity of both the rock surface and the impact conditions. In these figures, we can find a general trend that the rebound velocity increases as the contact area of the tool reduces. This has been indicated by an approximate best fit straight line. The Type B tool has the highest rebound velocity among all of the tools tested.

(C) Effect of Number of Impacts on the Rebound Velocity

Figures 4-10 and 4-11 show the variation of rebound velocity as the number of impacts at a specific location increases for Type B and Type D2 tools, respectively. The incident velocity of the tools was kept constant for all impacts and was equal to 550 in./sec. The figures show that the rebound velocity decreases as the number of impacts increases. The possible explanation for this trend follows. It is the effect of chips caused by continuous impact. For each impact, fracture occurs in the impact zone and part of the chips remain in that region, while part of them leave the impact zone and rebound with it. When the tool again impacts against the rock, part of the energy of the tool is lost in further crushing of the chips between tool and rock. In sonic drilling, we usually call this the powdering effect. The more chips between tool and rock the more energy is absorbed, and the less the rebound velocity. Therefore, solving the problem of chip removal is one of important tasks in improving the rock cutting process. Figure 4-12 shows the impact zone condition after twenty-five impacts.

(D) Characteristics of the Impact Zone

I. N. Sneddon [3] has solved for stresses produced by a circular flat punch on a half-space. Based on his analysis, a chart* (Fig. 4-13) on the variation of maximum shearing stress can be obtained. The figure shows that maximum shearing stress goes to infinity at the boundary of the punching surface. It decreases either inward or outward along the radial direction. According to the failure theory of maximum shear strength, failure starts at the periphery of the punch. In our problem of flat tool-rock impact, we have a situation similar to Sneddon's except that the contact force P between tool and rock is a time varying function, but the maximum shearing stress distribution pattern should not vary greatly from that shown in Figure 4-13. The experimental result shown in Figure 4-14 (a) proves the above argument as we observe that the heaviest damage is done at the edge. Other punch problems solved show the stress concentration at sharp edges.

* Reference [1], p. 120, Fig. 55.

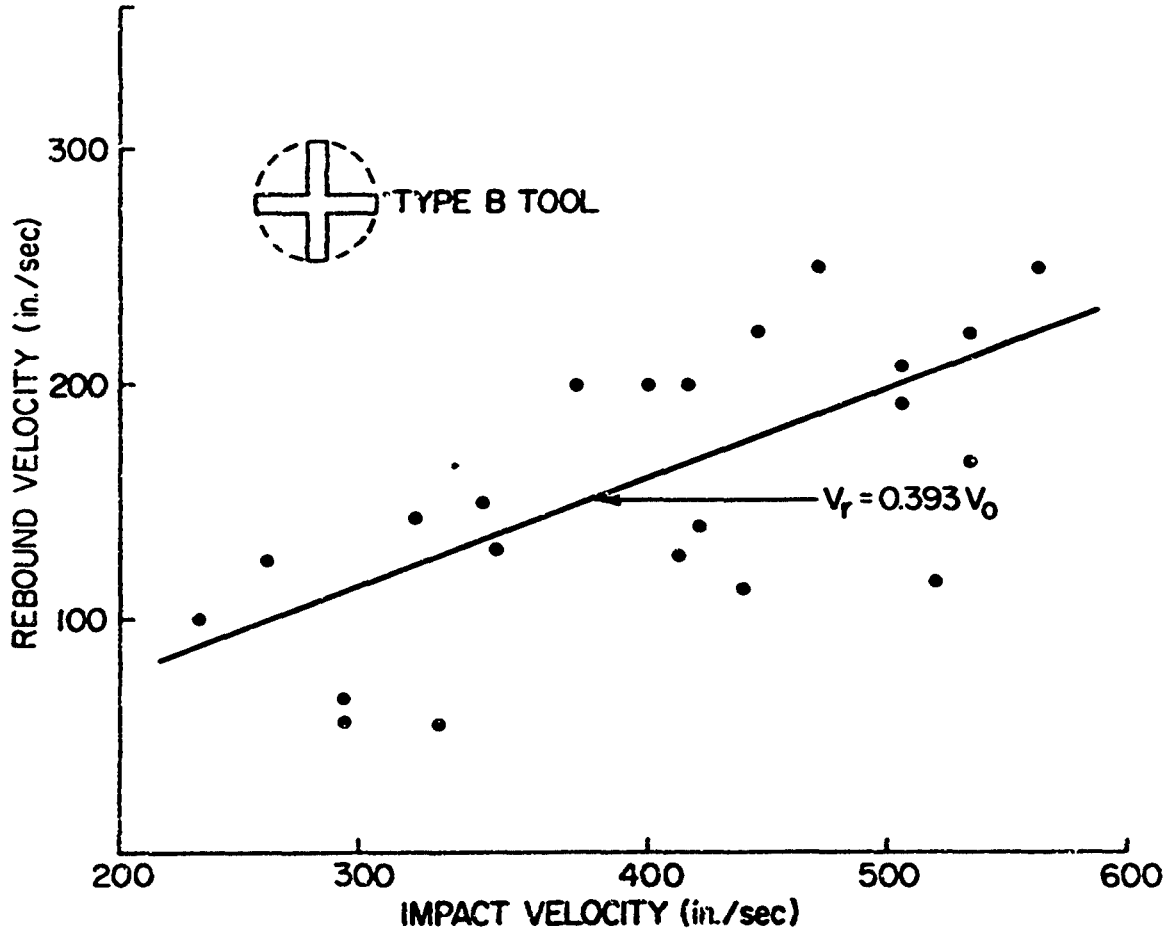

Figure 4-7 - Incident velocity-rebound velocity of Type B tool.

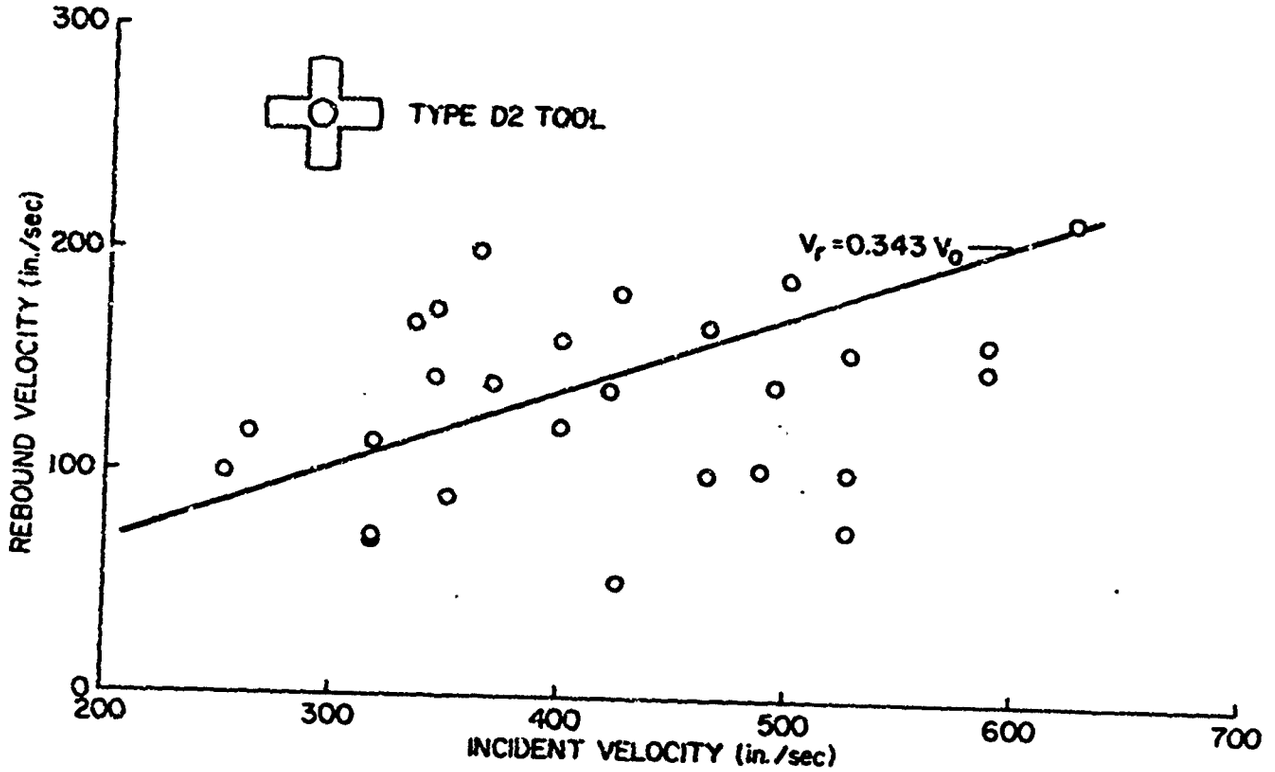

Figure 4-8 - Incident velocity-rebound velocity of Type D2 tool.

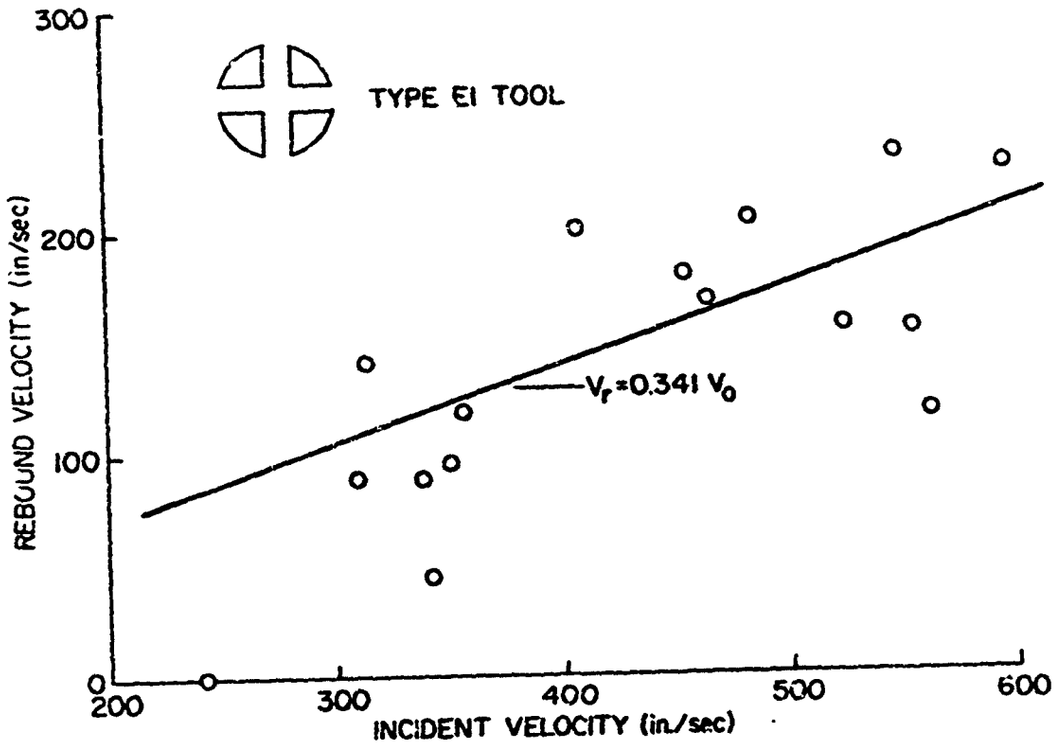

Figure 4-9 - Incident velocity-rebound velocity of Type E1 tool.

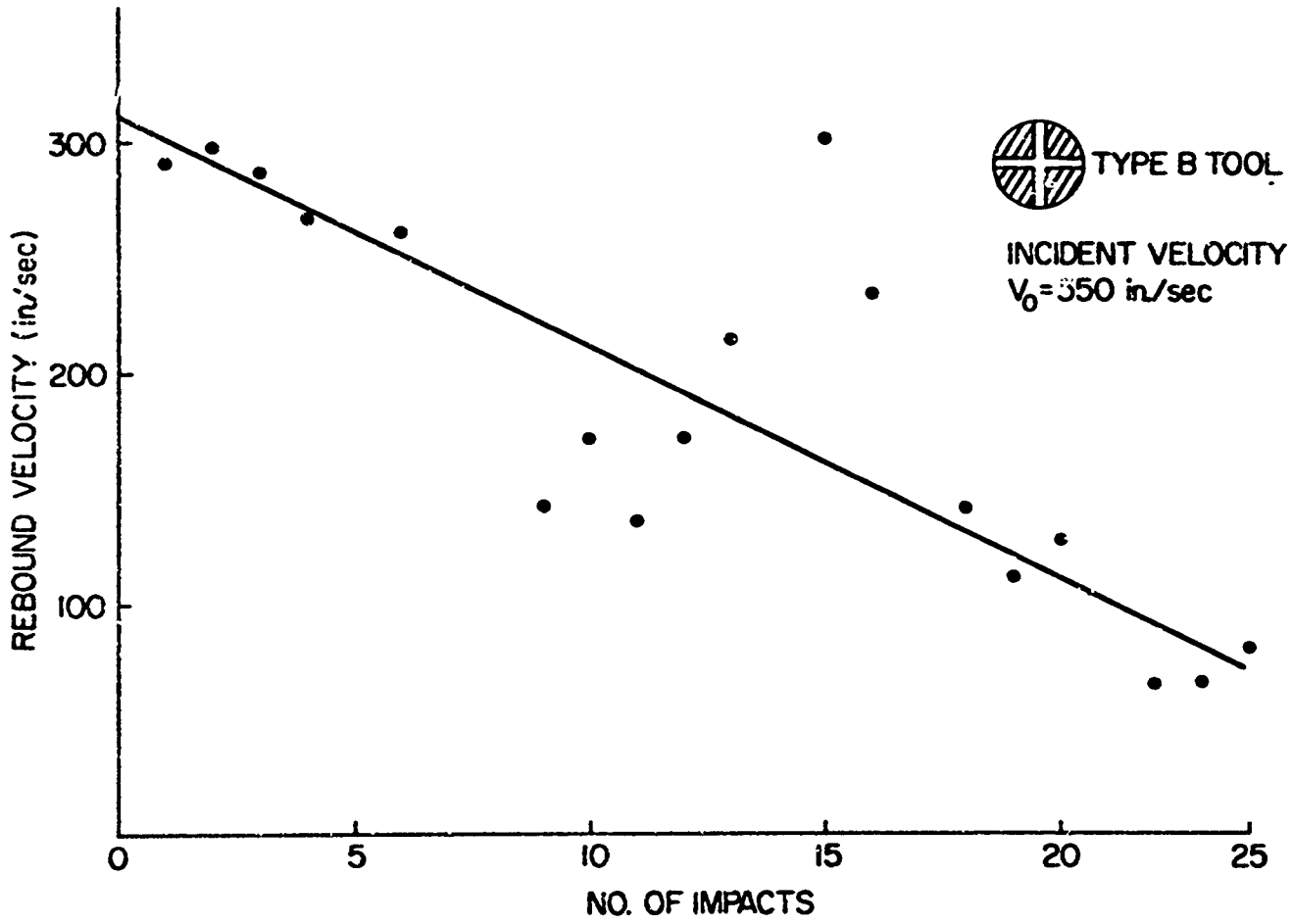

Figure 4-10- Effect of number of impacts on the rebound velocity for Type B tool.

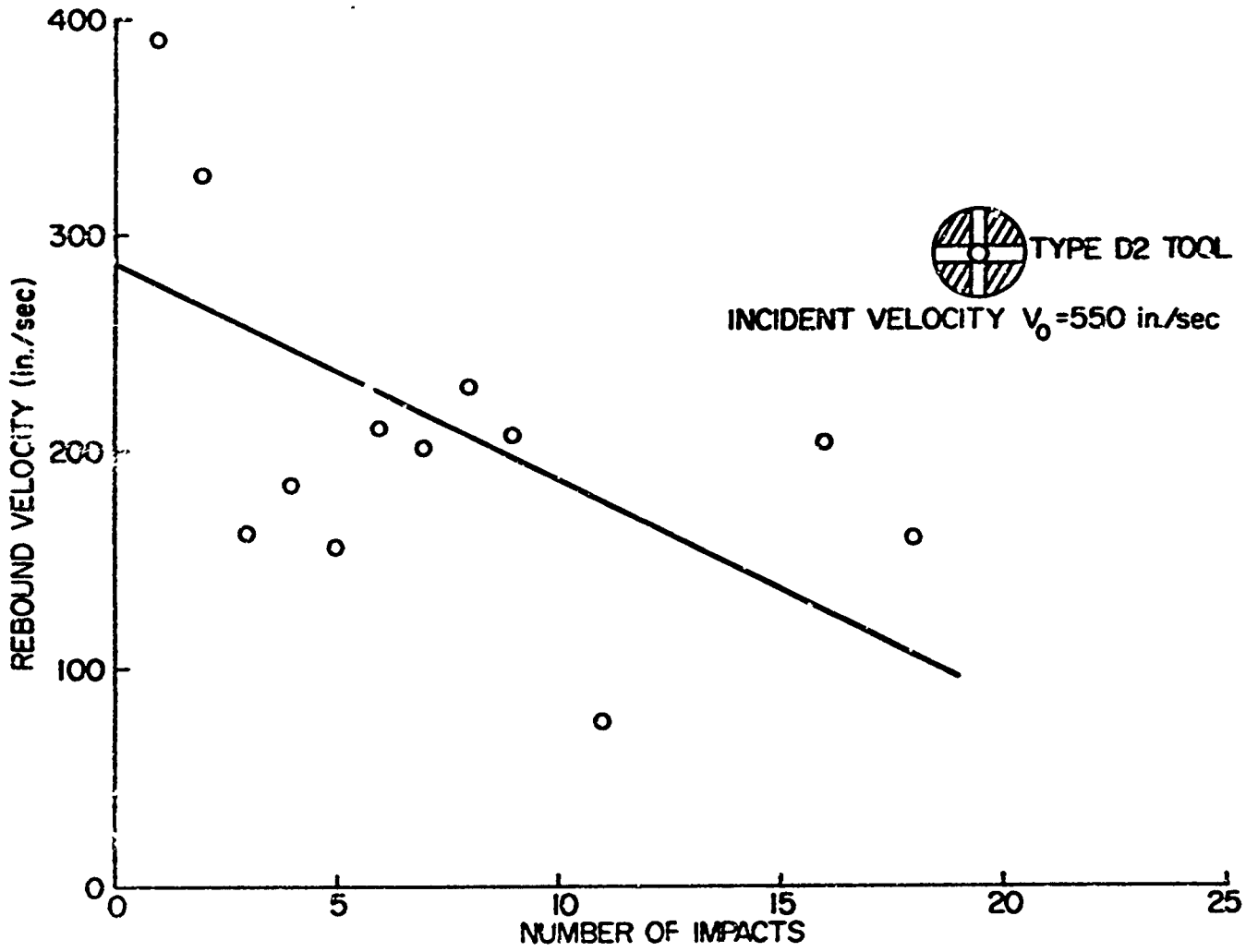

Figure 4-11 - Effect of number of impacts on the rebound velocity for Type D2 tool.

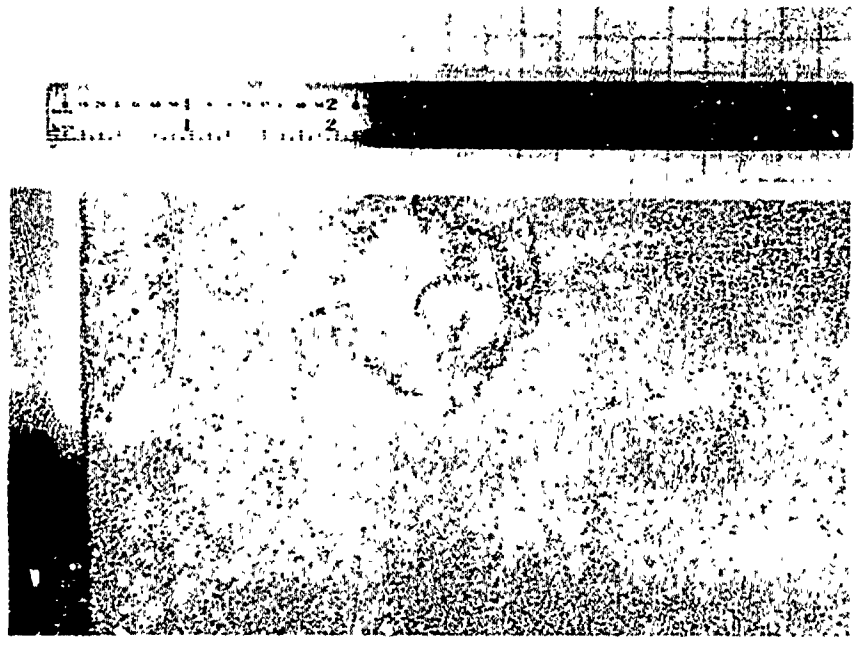

(a) with Type B Tool

(b) with Type D2 Tool

Figure 4-12 - Impact zone after twenty-five impacts (V_o = 550 in./sec.).

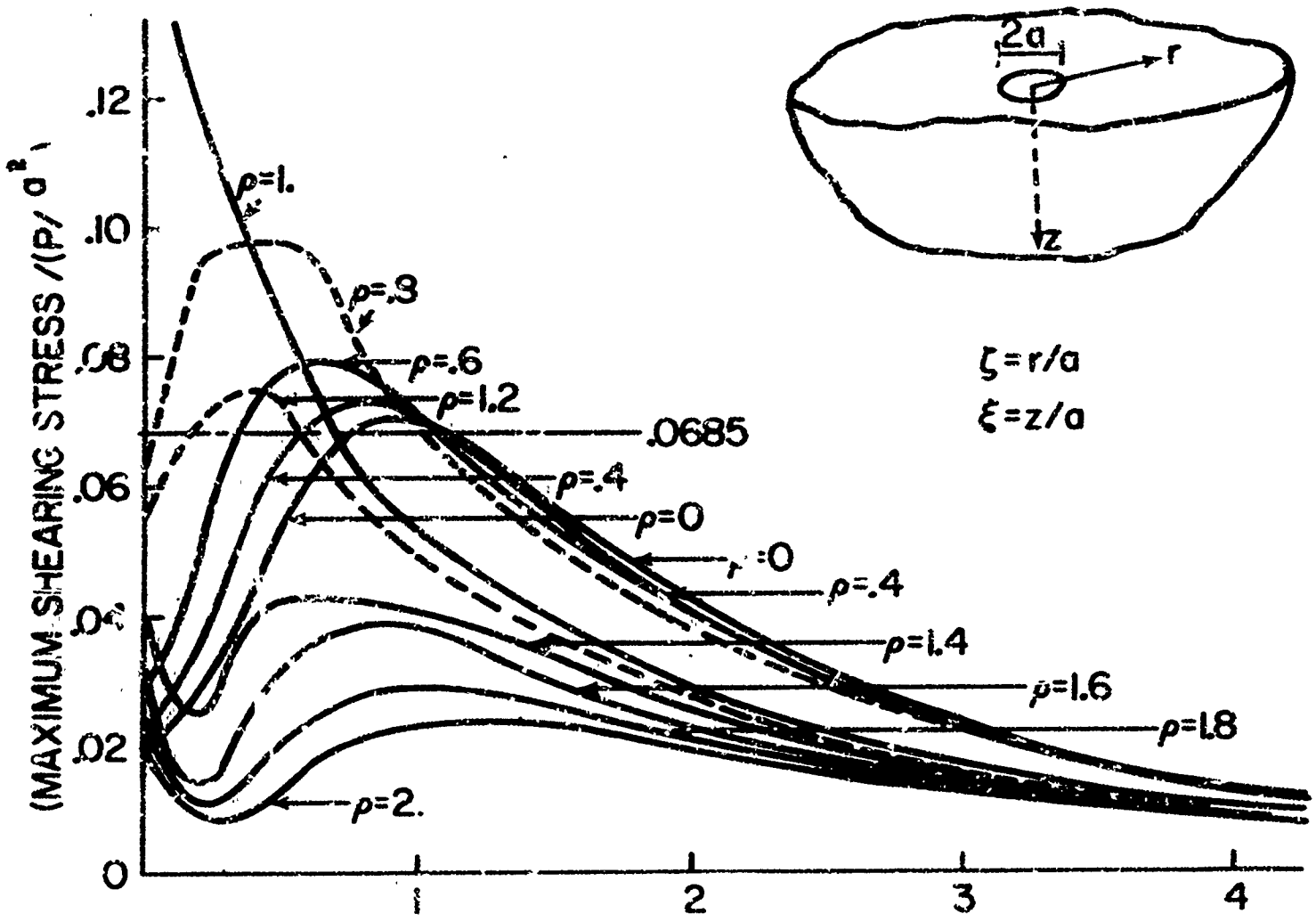

Figure 4-13 - Variation of maximum shearing stress, (normalized), with ρ and ζ.

(a) Type A Tool

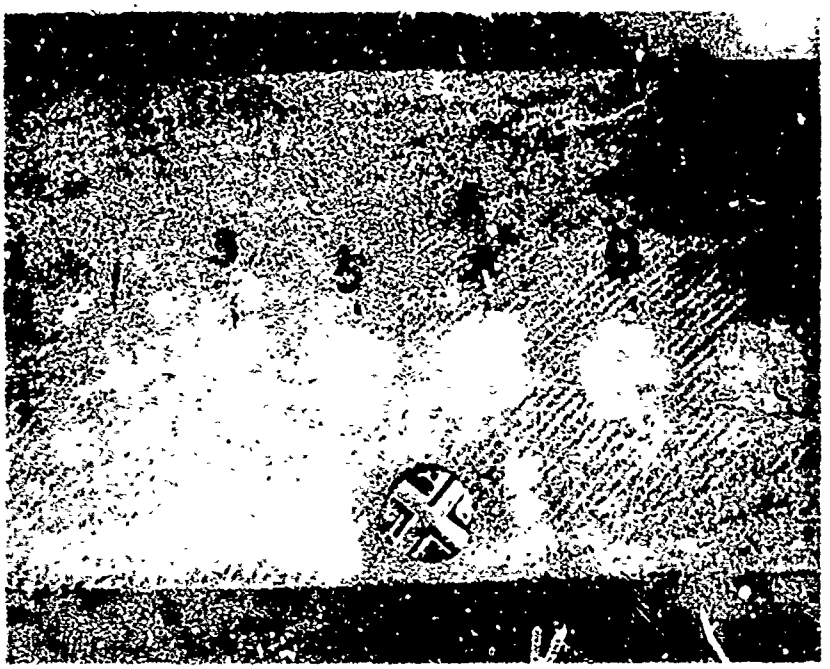

(b) Type B Tool

Figure 4-14 - Impact zone condition at different number of impacts.

(c) Type C Tool

(d) Type D1 Tool

(e) Type E2 Tool

Figure 4-14 - Continued

Figure 4-14 shows the impact zone condition at various number of impacts for various tip geometries. It is found that the less the area of tip the more efficient the tool in rock cutting. This is not surprising since with smaller area of contact the contact stress between tool and rock is higher and the maximum shearing stress is larger, accordingly. The direct result of higher maximum shearing stress is larger chip size in the fracture zone. The energy required to cut rocks can be reduced by a substantial amount without powderizing the rock.

In this experiment, the Type B tool has the highest efficiency in rock cutting, while the flat tip tool (Type A) has the lowest efficiency.

4-4 DISCUSSION

1. The analytical result on the rebound velocity of tools based on the one-dimensional theory of wave propagation in tool and bilinear rock model provides an upper bound to the actual rebound velocity.

2. Rebound velocity increases as the area of the tip of the tool is reduced, but the effect is not significant.

3. As the number of impacts at a specific area increases, chips accumulating in the fracture zone become a problem because more and more energy is consumed in powderizing the chips. The rebound velocity is reduced as the number of impacts is increased.

4. Stress concentration effects at sharp edges of the tool causes the damage in the rock surface. The smaller the area of tip the higher the efficiency in rock cutting, because it increases the chip size.

4-5 REFERENCES

1. Mahban, H., "Rock Behavior Under Impulsive Loading," Ph.D. Dissertation, The Ohio State University, 1970.

2. Lo, T. Y., "Analysis of Sonic Tool Impact on Rock," Part II, Section 1 of this report.

3. Sneddon, I. N., Fourier Transforms, McGraw-Hill, New York, 1951.

5 TOOL IMPACT ON A TRANSMISSION LINE

In the sonic drilling process, a short bouncing cylindrical tool is usually used between the transmission line of a transducer and the load. Therefore, we are interested in vibration and wave phenomena in both short (tool) and long (transmission line) cylindrical rods in the analysis of tool-line impact. The problem of impact on long cylindrical

rods has been studied extensively by researchers since Hopkinson [1] began in 1914. Almost all the researchers were interested in the wave phenomena in long rods. Little attention has been given to rods of small length-to-radius ratio; the reason being that the behavior of short cylindrical rods is very complicated according to the three-dimensional theory of elasticity. With the help of the computer, McNiven and Perry [2] found the approximate natural frequencies of axial vibration of short cylindrical rods. Bertholf [3] considered the wave propagation in a finite rod due to a step stress applied at one end of the rod while the other end is free. The above two studies on the short rod still give very little direct help for solving the present problem in which the contact force between tool and line is high in magnitude but short in duration. The contact time measured is less than 50 microseconds. Because of the difficulties involved, previous analysis on the tool-line impact are based on two simplifying assumptions. One is to assume that the one-dimensional theory of elastic wave propagation for long rods is still applicable to tools of short length during impact. The other is to treat the tool as a rigid body [4]. The stress waves produced in the transmission line, according to the above assumptions, are shown in Figure 5-1 (a) and (b) during the tool-line impact. Here we substitute for the transmission line a semi-infinite rod of the same diameter as the tool. A typical stress wave measured in the laboratory experiment for this tool line impact is shown in Figure 5-1 (c), which shows a considerably different stress wave shape from that shown in Figure 5-1 (a) and (b). Feng [5] conducted an experimental investigation of the longitudinal impact of steel rods and balls on the tip of a vibrating sonic transmission line. In his work a theoretical study on the ball-line impact was found to be in very good agreement with the experimental result. It is very interesting to note that the shape of a stress wave produced in his ball-line impact is very similar to the result obtained in a tool-line experiment as stated previously, Figure 5-1 (c).

A thorough study on the tool-line impact was conducted in the Laboratory of the Department of Engineering Mechanics at the Ohio State University. Special attention was given to the effect of end geometry on the rebound velocity of the tool, the energy loss during impact, the relationship between the incident velocity and rebound velocity, the stress waves produced, and the effect of the tip geometry of the transmission line.

5-1 THEORY OF IMPACT AND STRESS WAVES IN A ROD

During impact between a cylindrical tool and a transmission line, a large force $F(t)$ occurs at the contact surface. The force is equal to the area times the stress level of the wave that is transmitted into the line, as shown in Figure 5-2, where V_0 is the incident velocity, V_r is the rebound velocity, c is the wave velocity and $\sigma(t)$ is the

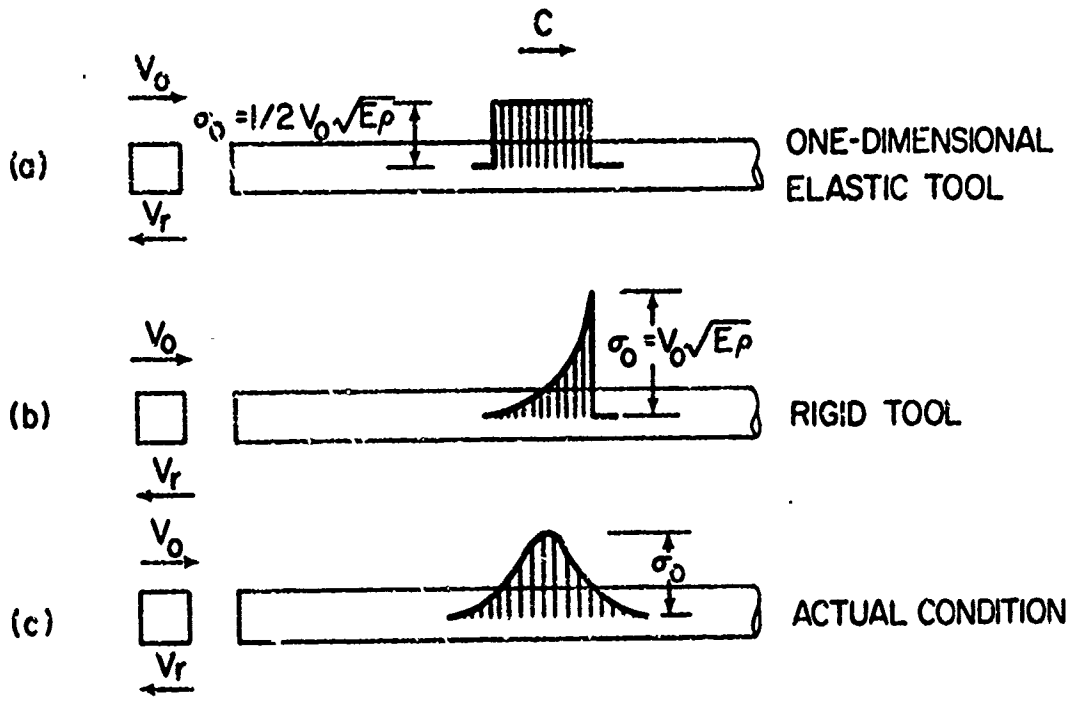

Figure 5-1 - Stress wave in the transmission line due to tool-line impact.

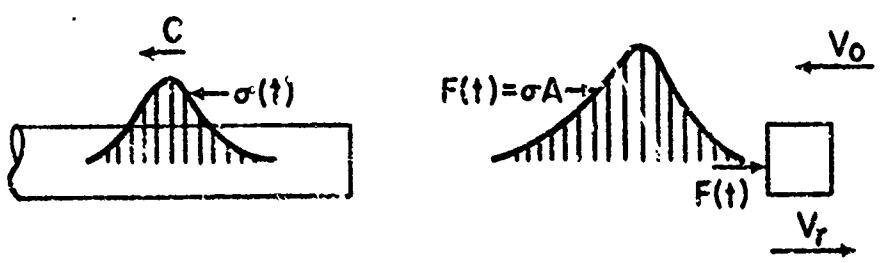

Figure 5-2 - Impact of tool and transmission line.

stress wave in the line. According to the principle of conservation of momentum, we have

$$\int F(t)dt = mV_r - (-mV_o)$$

or

$$A\int \sigma(t)dt = m(V_r + V_o) \qquad (5\text{-}1.1)$$

From the experimental result, $\sigma(t)$ is positive function of time (that is, it is always compressive). If we have $\sigma(t)$, then V_r can be calculated from the above equation as

$$V_r = \frac{A}{M}\int \sigma(t)dt - V_o \qquad (5\text{-}1.2)$$

where m is the mass of the tool. By the law of conservation of energy, the energy can be expressed by the following relationship.

$$E_o = E_t + E_r + E_L \qquad (5\text{-}1.3)$$

where

$E_o = \frac{1}{2}mV_o^2$ = original kinetic energy of the tool before impact

$E_t = \frac{1}{2E}\int \sigma^2 dV$ = energy transmitted into the transmission line, E is the Young's Modulus of the transmission line

E_r = Rebound kinetic energy of the tool

E_L = Energy loss during impact.

Since $\sigma(t)$ is, in general, a positive function of time, it can be proved that E_r and E_t in equation (5-1.3) increase or decrease at the same time, depending on the condition at the impact zone. This can be proved as follows:

Assume: $\sigma_1(t)$, V_{r1} are the stress and rebound velocity for a specific incident velocity and impact zone condition and that $\sigma_2(t)$, V_{r2} are the stress and rebound velocity for the same incident velocity after the impact zone condition is changed. Further, assume that $V_{r2} > V_{r1}$. Then

$$E_{r1} = \frac{1}{2}mV_{r1} \quad , \qquad E_{t1} = \frac{1}{2E}\int \sigma_1^2\, dV$$

$$E_{r2} = \frac{1}{2}mV_{r2} \quad , \qquad E_{t2} = \frac{1}{2E}\int \sigma_2^2\, dV$$

and

$$E_{r2} - E_{r1} = \tfrac{1}{2}m(V_{r2}^2 - V_{r1}^2) > 0 \qquad (5\text{-}1.4)$$

From observation of the experimental stress wave results, it is found that $\sigma_2(t) - \sigma_1(t) > 0$ for all t if $V_{r2} > V_{r1}$. Then,

$$E_{t2} - E_{t1} = \frac{A}{2E}\int(\sigma_2^2 - \sigma_1^2)d\ell$$

$$= \frac{A}{2E}\int(\sigma_2 - \sigma_1)(\sigma_2 + \sigma_1)d\ell$$

Since $(\sigma_2 - \sigma_1) > 0$ and $(\sigma_2 + \sigma_1) > 0$ we have

$$E_{t2} - E_{t1} > 0 \qquad (5\text{-}1.5)$$

Substituting equations (5-1.4) and (5-1.5) into equation (5-1.2) gives

$$E_o = E_{t1} + E_{r1} + E_{L1} = E_{t2} + E_{r2} + E_{L2}$$

$$E_{L2} - E_{L1} = (E_{t1} + E_{r1}) - (E_{t2} + E_{r2})$$

$$= (E_{t1} - E_{t2}) + (E_{r1} - E_{r2}) < 0$$

Hence,

$$E_{L1} > E_{L2} \qquad (5\text{-}1.6)$$

Therefore, we know that for a specific incident velocity V_o, the larger the rebound velocity the larger the energy must be that is transmitted into the line and the less the energy loss during impact. This is an important result from the above analysis.

5-2 EXPERIMENTAL PROCEDURE

A photograph and schematic diagram of the experimental set up is shown in Figure 5-3 (a) and (b). Two photo cells one inch apart are placed at the end of a spring gun to measure the time required for a tool to pass the one inch distance. With these values plus the correction required due to gravitational effect, the incident and rebound velocity can be calculated. The counter shown in Figure 5-3 is used to measure the incident velocity, while one of the two oscilloscopes measures rebound velocity. The stress wave produced due to impact is picked up by the other oscilloscope. By adjusting the spring deformation, we are able to control the incident velocity of the tool to about the level desired.

Figure 5-3 (a) - Experimental set-up

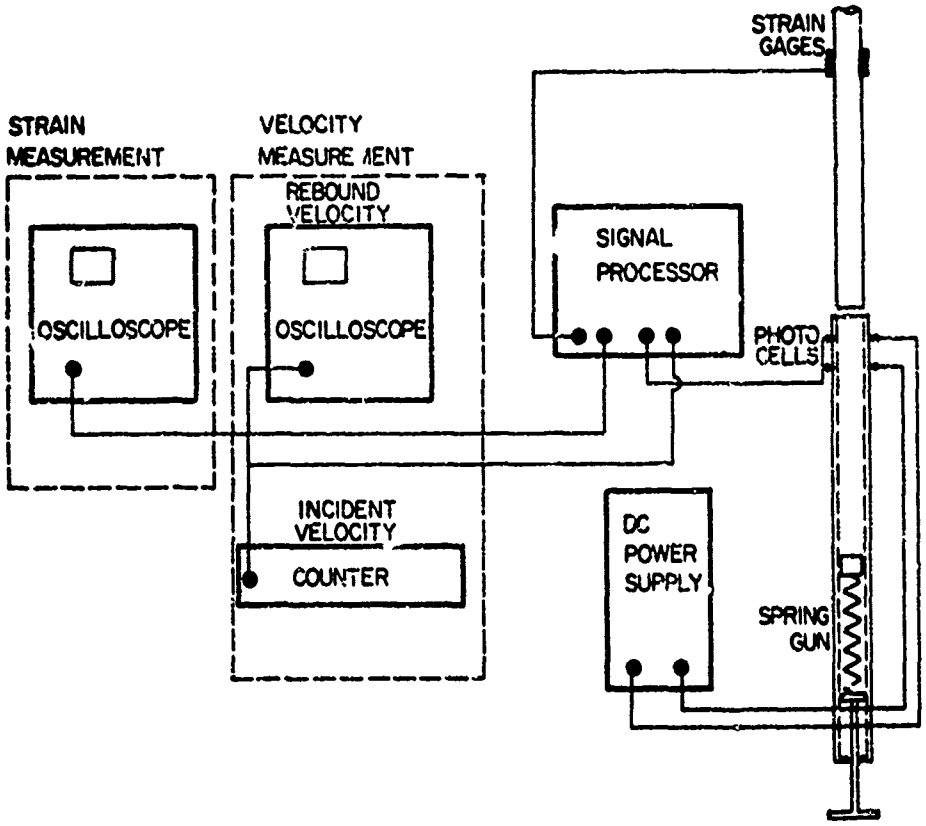

Figure 5-3 (b) - Schematic diagram of experimental set-up.

Figure 5-4 shows the various tools used in this study; all of them are 1 inch in diameter and 1 inch long. Four different end geometries of the tool were used in this experiment. All tools shown were made of cold-rolled steel. Another stainless steel flat tool was used to study the effect of material hardness on the rebound velocity.

5-3 RESULTS

(A) End Geometry of the Tool:

Four different end geometries were investigated for approximately the same impact velocity of 550 in./sec. Strain waves and rebound velocity were obtained and studied. There were several interesting results.

1. Secondary impact: When a tool approaches the transmission line, the axes of the tool and line usually are not perfectly parallel to each other. For tool Types 2, 3, 4 and 5, the contact between tool and line generally starts at a point on the periphery of the tool surface and a point on the surface of the transmission line tip. A very short time later, the surface of the tool rotates about the contact point and comes into complete contact with the surface of the transmission tip. This phenomena is called secondary impact. The elastic stress wave that goes into the transmission line has two peaks (Fig. 5-5 (b)(c)(d) and (e)). If the axis of the tool is perfectly parallel to the axis of the line only single impact will occur, and there is only one peak in the transmitted wave. Type 1 tool has a slightly curved surface. There is only one single impact in every circumstance (Fig. 5-5 (a)). This illustrates why the curves are more consistent for Type 1 tool for several impacts at the same incident velocity.

2. Percentage of Rebound Energy from the Line (Re) and the Energy Loss Due to Impact: We now define the percentage of rebound energy Re, as the ratio of E_r and E_o

$$Re = E_r/E_o = \left(\frac{V_r}{V_o}\right)^2 \qquad (5\text{-}1.7)$$

The value of Re for tools of different end geometry are shown in Table 3-1 for V_o = 550 in./sec.

Table 5-1 - Percent of Rebound Energy from the Line (V_o = 550 in./sec)

Type of Tool	1	2	3	4	5
Re	7.16%	2.39%	2.44%	3.00%	4.21%

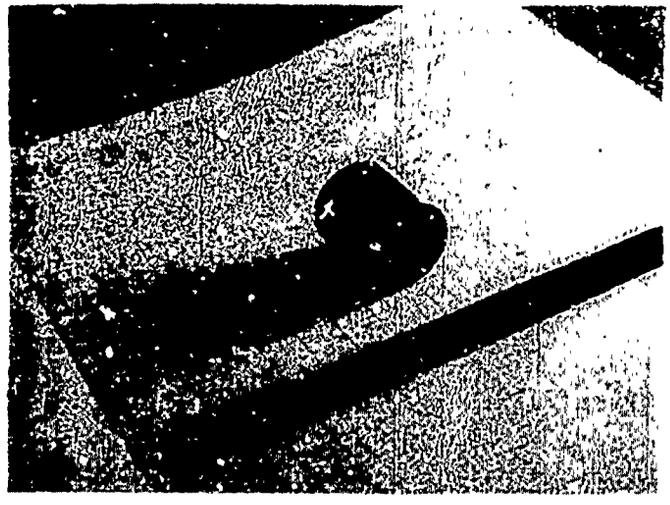

Type 1

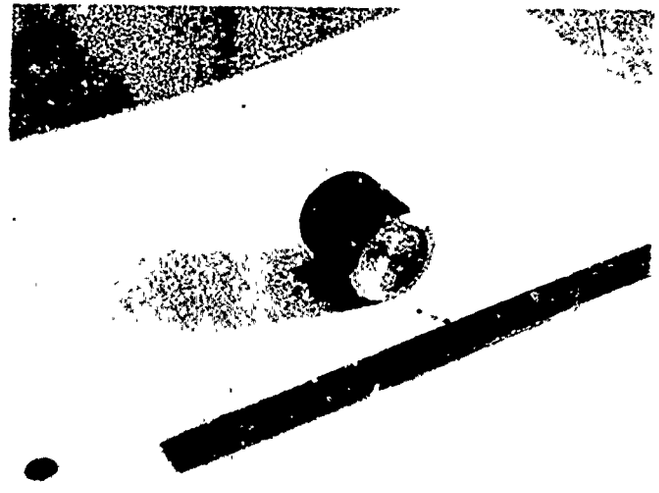

Type 4

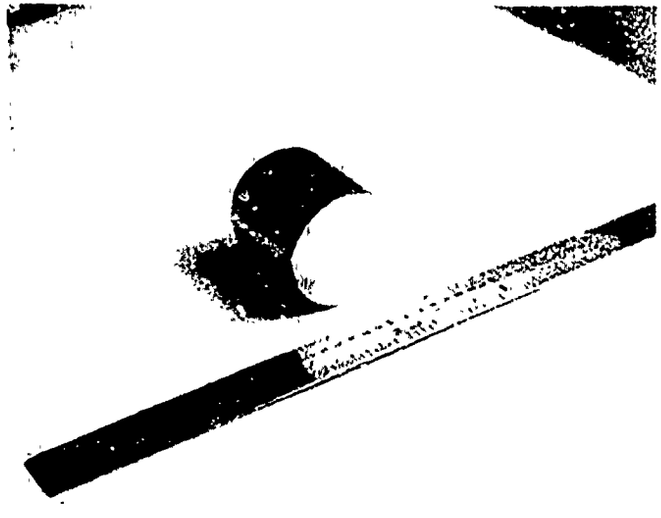

Type 2 & 3

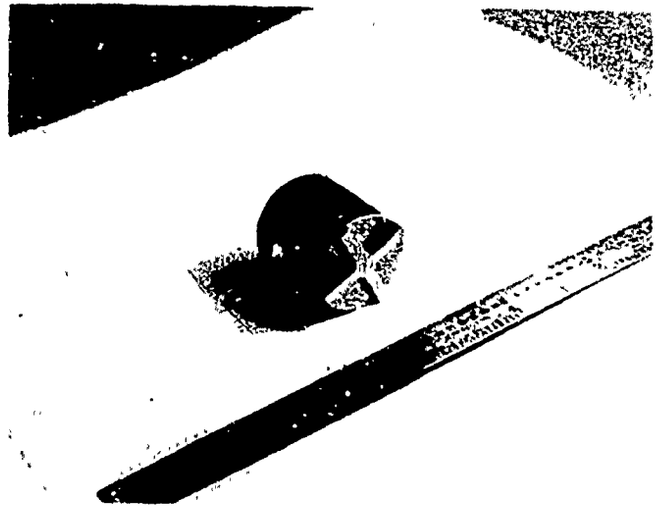

Type 5

Figure 5.4 - Tools

The figures in Table 5-1 show that the less the contact area the more the rebound energy from the line. Therefore, the energy loss due to impact is less for tools with a smaller area of contact according to the analysis in Section 5-1, so that energy loss is less for higher rebound velocity. This is in contradiction with the belief that a smaller area of contact would cause larger plastic deformation or more energy loss.

The values of Re are almost the same for the Type 2 Tool (flat end-cold rolled steel) and the Type 3 Tool (flat end-stainless steel). This tells us that the hardness of the tool material has little effect on the energy loss during impact, since stainless steel is much harder than cold-rolled steel. In general, a material with a low yield point stress would be expected to have a large plastic deformation during impact. This phenomena is another paradox in the consideration of energy loss during impact.

The above two contradictions can only be explained from the viewpoint that the energy loss due to plastic deformation is only a fraction of the total energy loss. The main cause of the loss of energy may be due to the cushioning effect of the air between the tool and transmission line; during impact, work has been done to compress the trapped air. Type 1 tool has the least area of contact, and the air between tool and line is more easily expelled from the point of contact; therefore less energy is lost in this case. Secondary impact for Type 2, 3, 4 and 5 tools is also another factor that causes energy loss, since some energy is always lost during impact, so that the more impacts the more the energy loss.

(B) Tip Geometry of Transmission Line:

To investigate the effect of tip geometry of a transmission line on the rebound velocity and stress wave produced, a tip shown in Figure 3-6 is attached directly on the end of a long rod in two different ways. Figure 5-7 shows the dimension of the tip and the means of connecting it to the transmission line. The stress waves produced under the impact of Type 1 and Type 2 tools are shown in Figures 5-8 and 5-9, respectively. The incident velocity of the tools is approximately 550 in./sec. There are two important features shown in these figures. The maximum stress is reduced by using an enlarged tip, and there is a secondary pulse shown. The reason for the above two phenomena is because the transmission line with an enlarged tip is no longer a prismatic cylindrical rod. Wave reflection occurs at sections where the cross-sectional area changes. This result suggests the possible desirability of having a lumped mass at the tip of the transmission line to reduce the peak of the stress wave into the body of the transducer.

Following is a table (Table 5-2) showing the percentage of rebound energy Re for V_o = 550 in./sec.

Figure 5-5(a)
Time Base:
5 μsec./division
ordinate (stress):
29.4 ksi/division

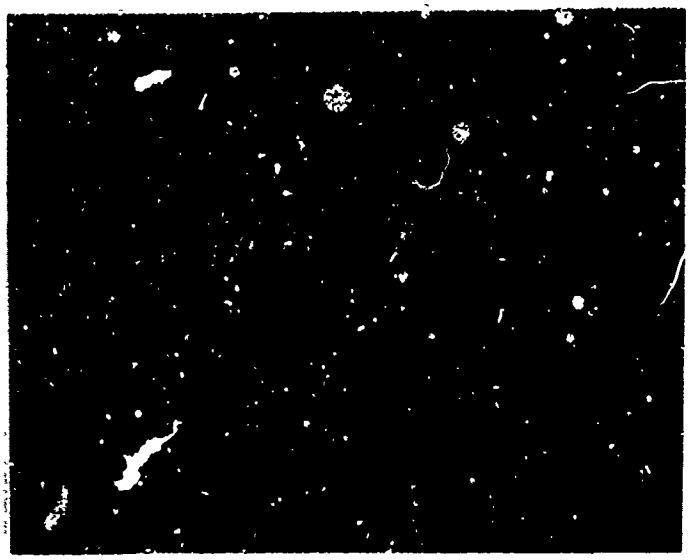

Figure 5-5(b)
Time Base:
5 μsec./division
ordinate (stress):
29.4 ksi/division

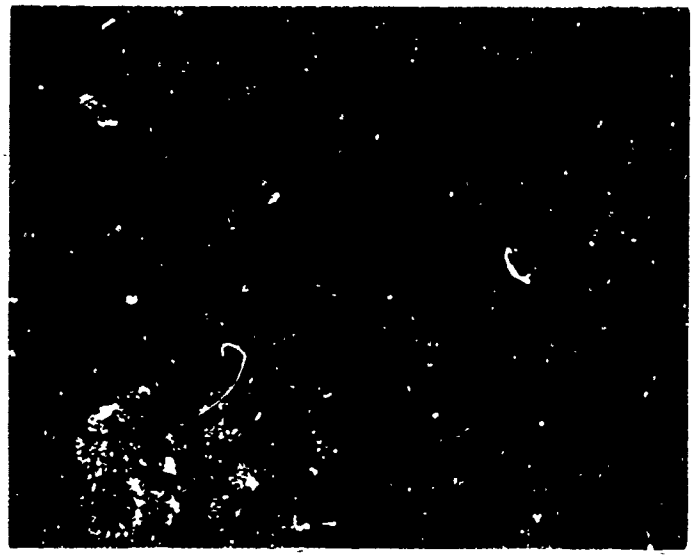

Figure 5-5(c)
Time Base:
5 μsec./division
ordinate (stress):
29.4 ksi/division

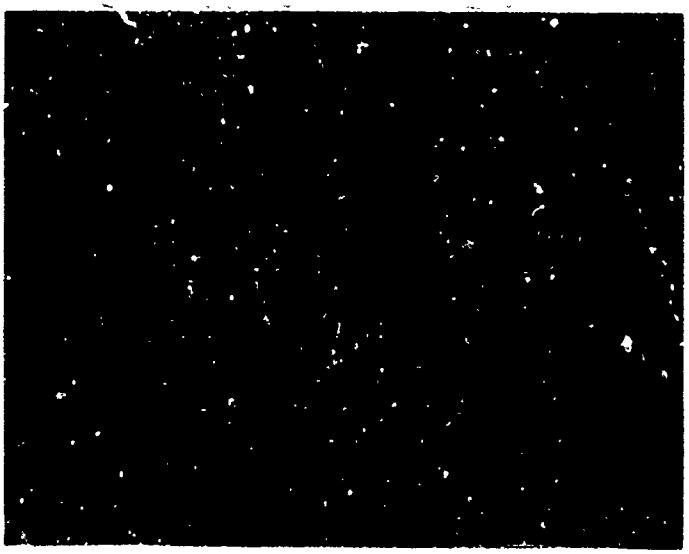

Figure 5-5(d)
Time Base:
5 μsec./division
ordinate (stress):
29.4 ksi/division

Figure 5-5(e)
Time Base:
5 μsec./division
ordinate (stress):
29.4 ksi/division

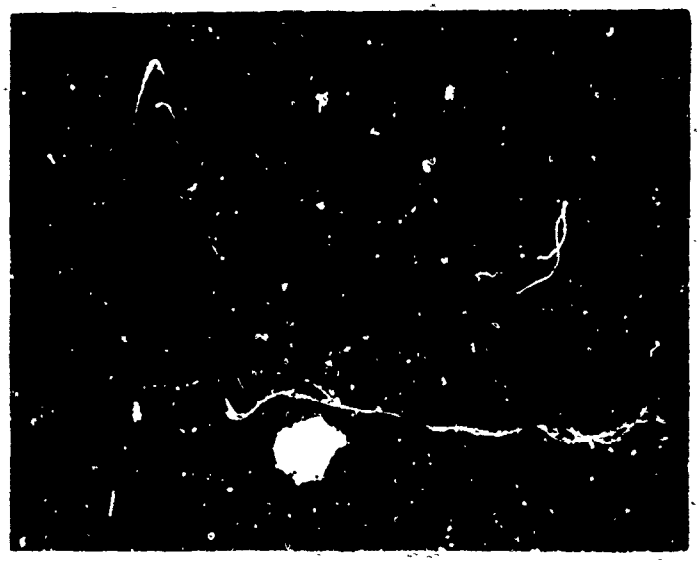

Figure 5-6 - Transmission line tip used in this experiment

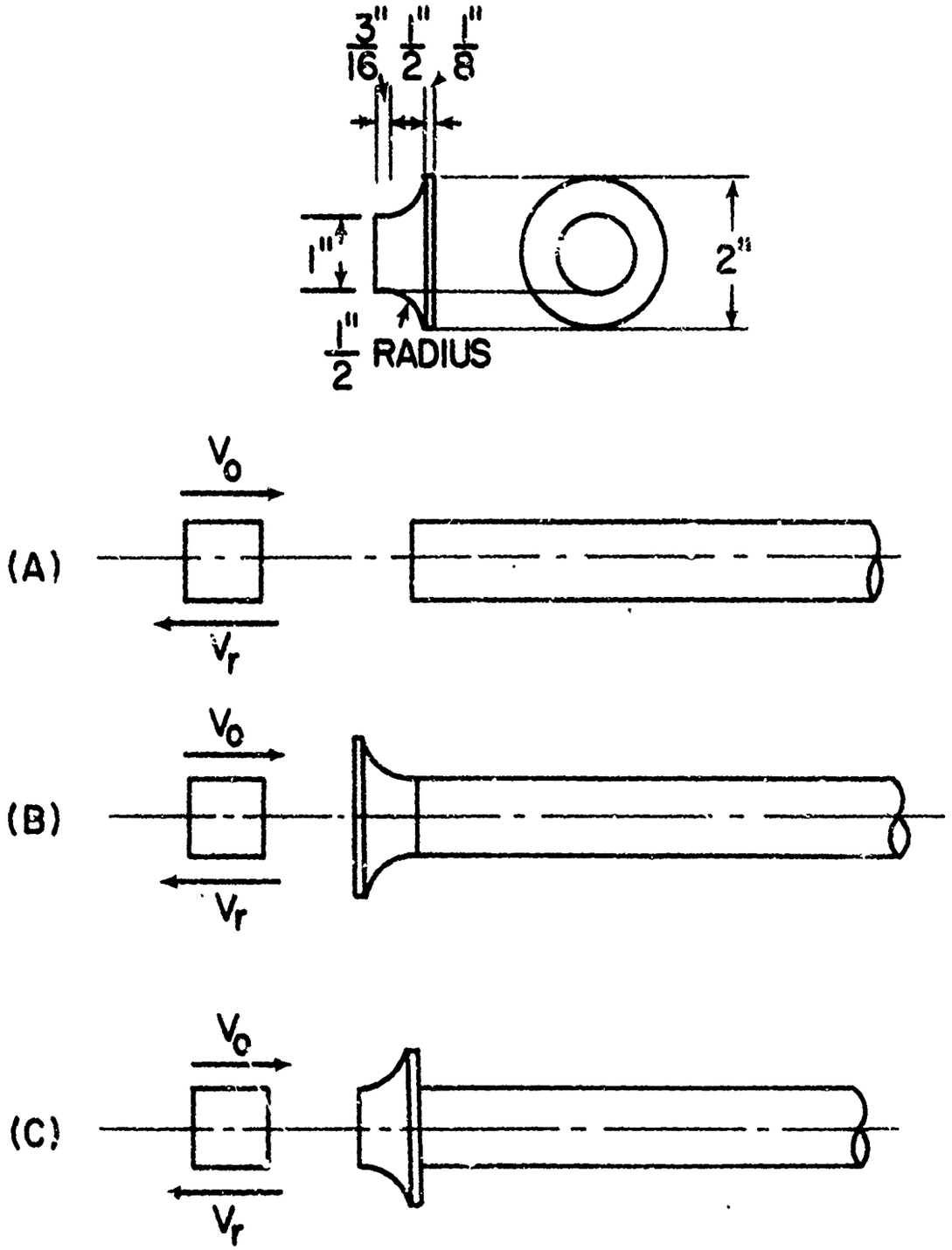

Figure 5-7 - Transmission line tip dimension and tip-transmission line assemblies.

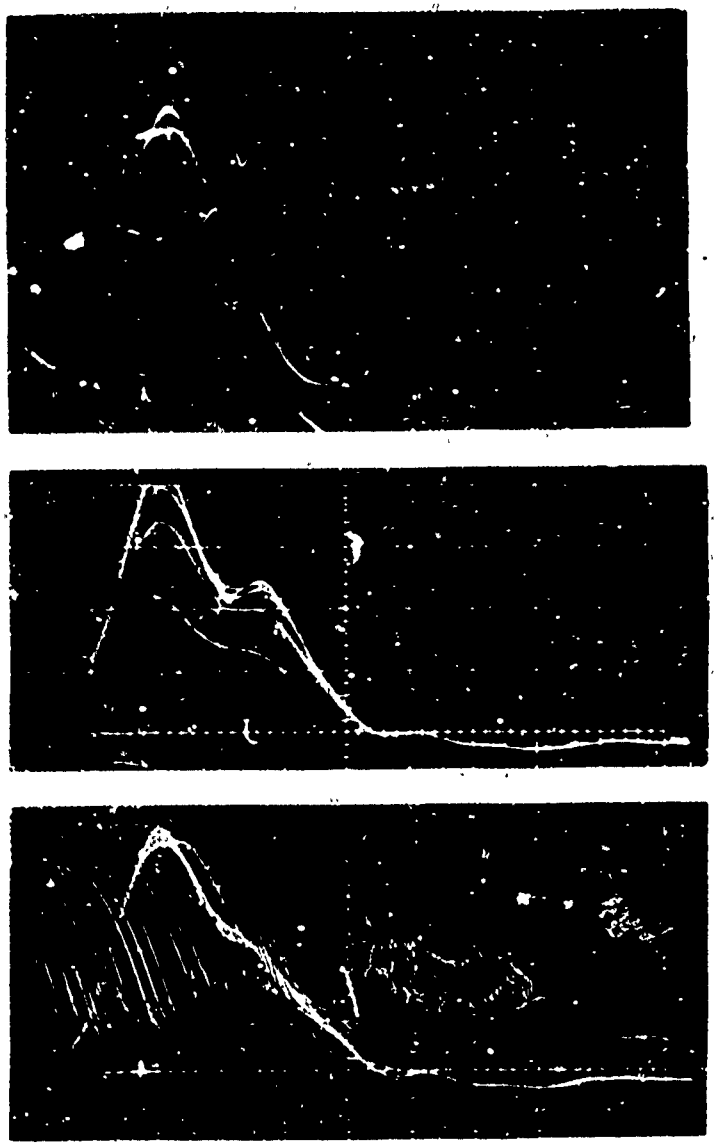

Figure 5-8 - Stress waves from tool impact.

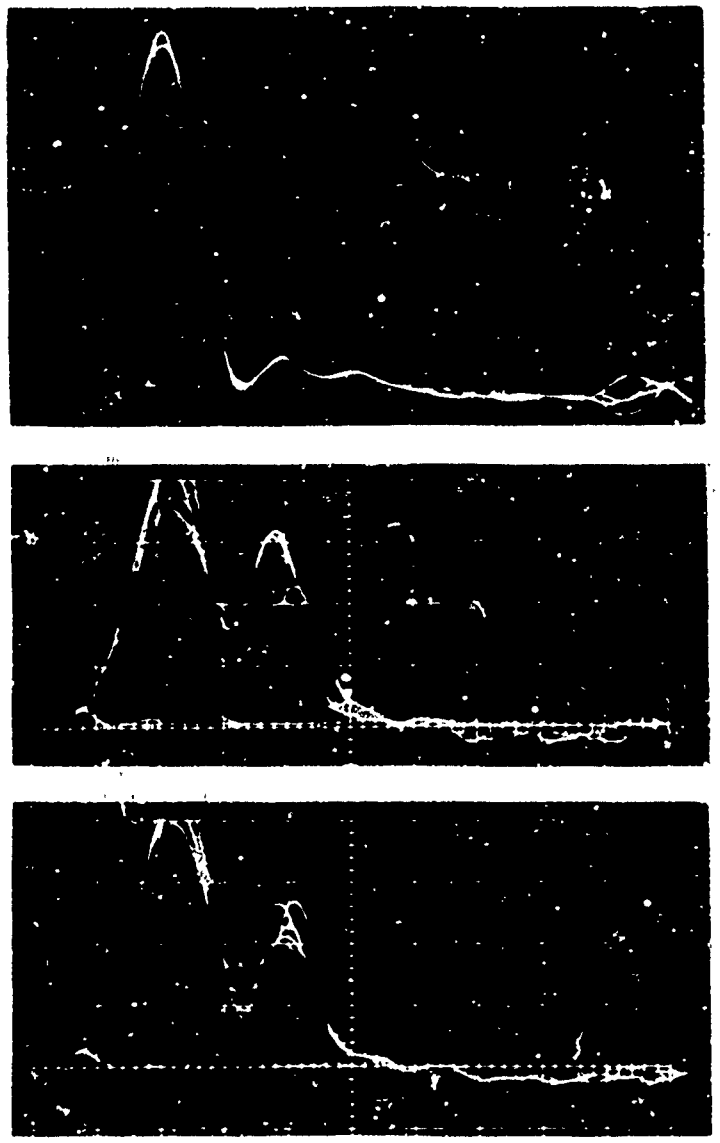

Figure 5-9 - Stress waves from tool impact.

Table 5-2 - Values of Re for Three Different Transmission Line Tip Geometries

Tip Geometry		(A) Without Enlarged Tip	(B) With Enlarged Tip	(C) With Inverted Tip
Re	Type 1 Tool	11.4%	9.5%	9.4%
	Type 2 Tool	2.7%	3.1%	2.7%

Table 5-2 shows that the rebound velocity is not affected by changing the area of transmission line tip. Comparing the value of Re in Table 5-1 (11.4%) and Table 5-2 (7.16%) for a Type 1 tool without an enlarged transmission line tip, there is a significant difference in this value. It is because the value in Table 5-1 is obtained when the tip of the tool is flattened out due to plastic deformation in persistent impacts which increases the area of contact between the tool and transmission line.

(C) Rebound Velocity of the Tool and Stress Waves in the Static Transmission Line:

The relationship between maximum stress and incident velocity of the tool are shown in Figures 5-10 and 5-11 for Type 1 (curved) and Type 3 (stainless steel flat tool), respectively. The relationship between rebound velocity and incident velocity of the tool are shown in Figures 5-12 and 5-13 for Type 1 (curved tool) and Type 3 (stainless steel flat tool), respectively.

The linear relationship between rebound and incident velocity shown in Figure 5-12 is in agreement with the results found by Feng for ball-line impact. The ratio V_r/V_o is smaller in this experiment because the tip of the tool has less curvature and has been flattened out due to persistent impact. Figure 5-12 does not have as good a result as Figure 5-13. This is mainly due to the fact that the impact of flat tool against transmission line is not consistent for all impacts. The rebound velocity varies considerably even for the same incident velocity.

5-4 DISCUSSIONS AND CONCLUSIONS

1. The incident-rebound velocity relation for tool-line impact a linear relationship which is in agreement with ball-line impact.

2. The smaller the area of contact between the tool and the transmission line, the higher the rebound velocity or the less the energy loss during impact.

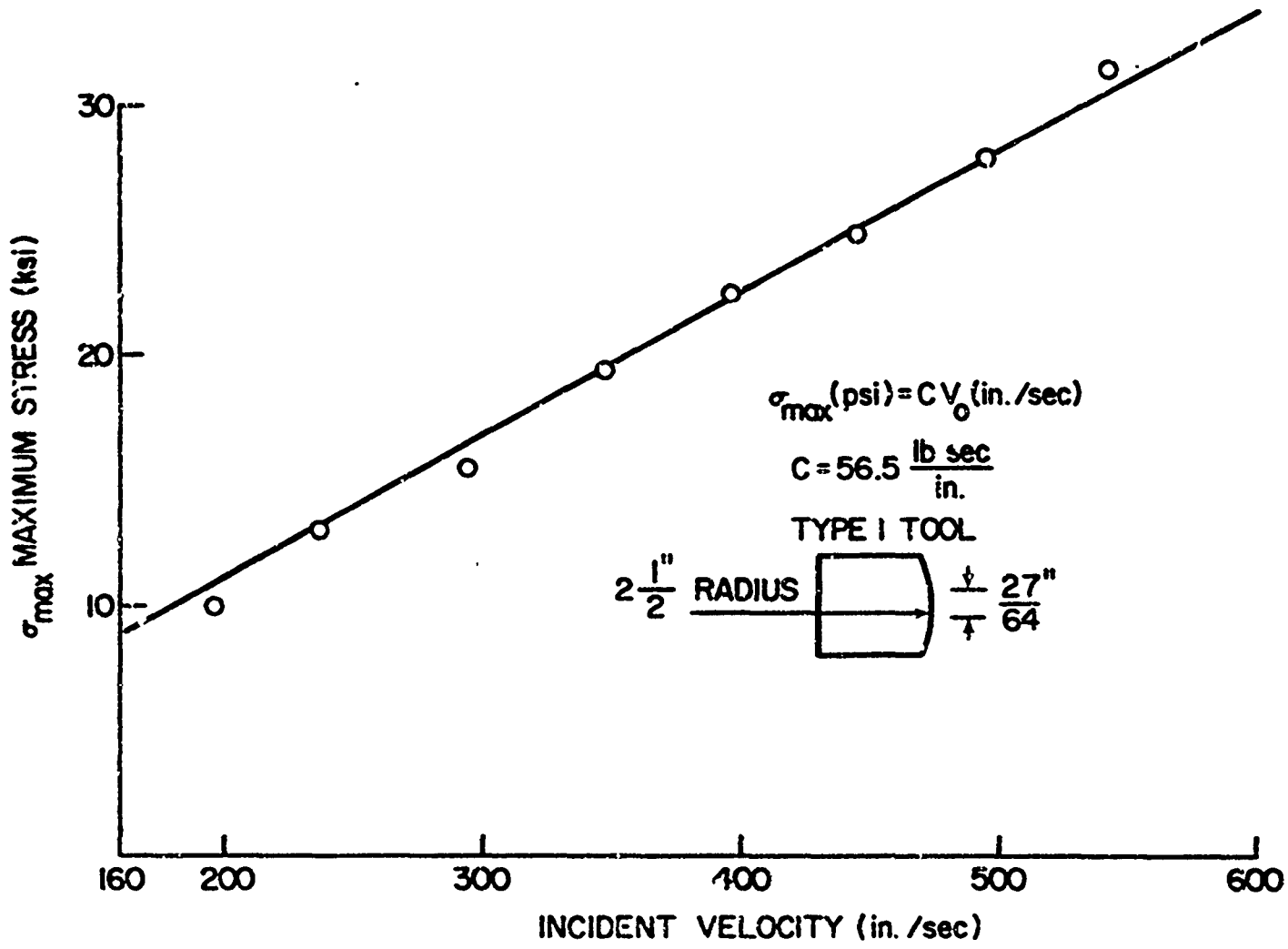

Figure 5-10 - Incident velocity-maximum stress for Type 1 tool.

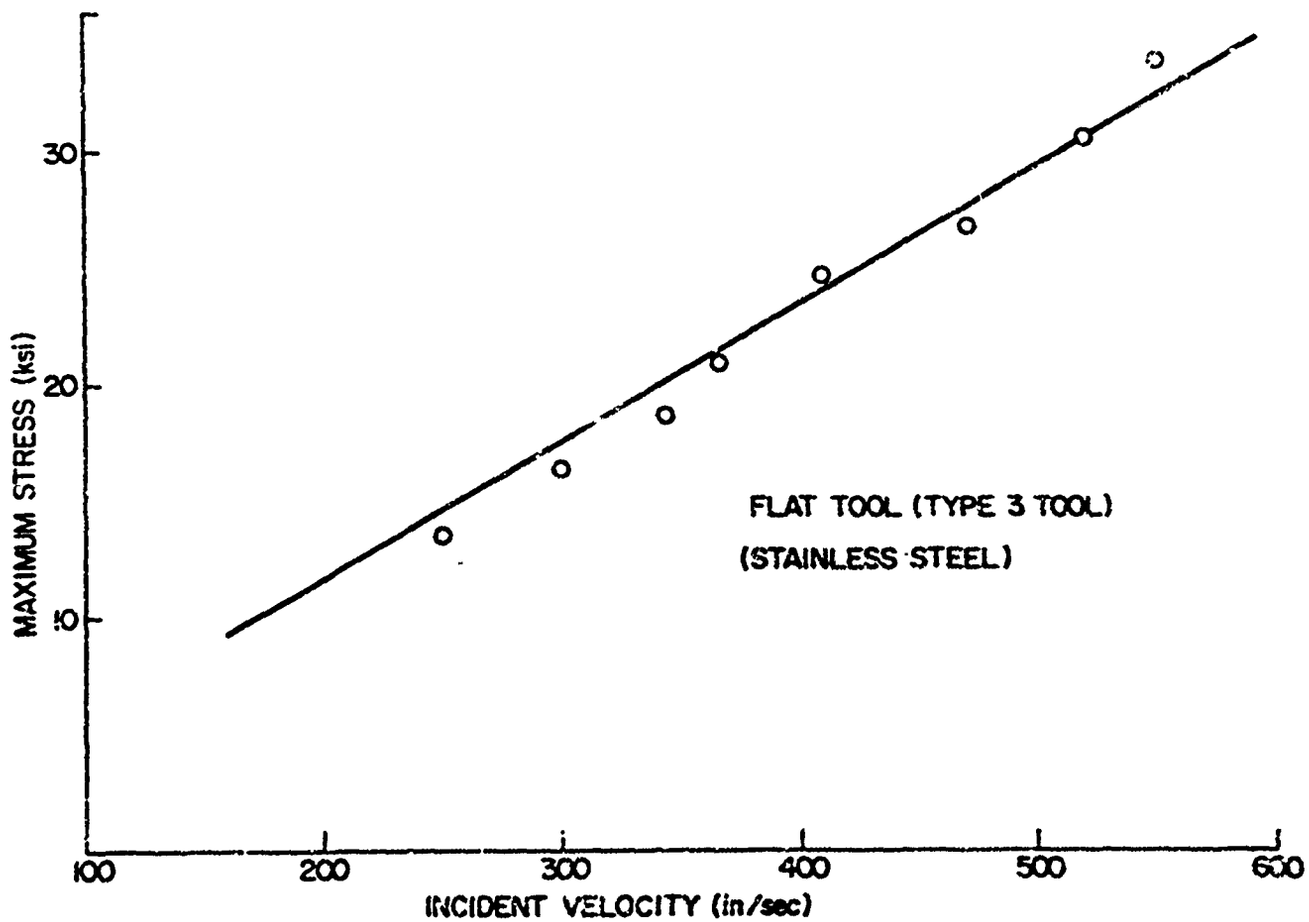

Figure 5-11 - Incident velocity - maximum stress for Type 3 tool.

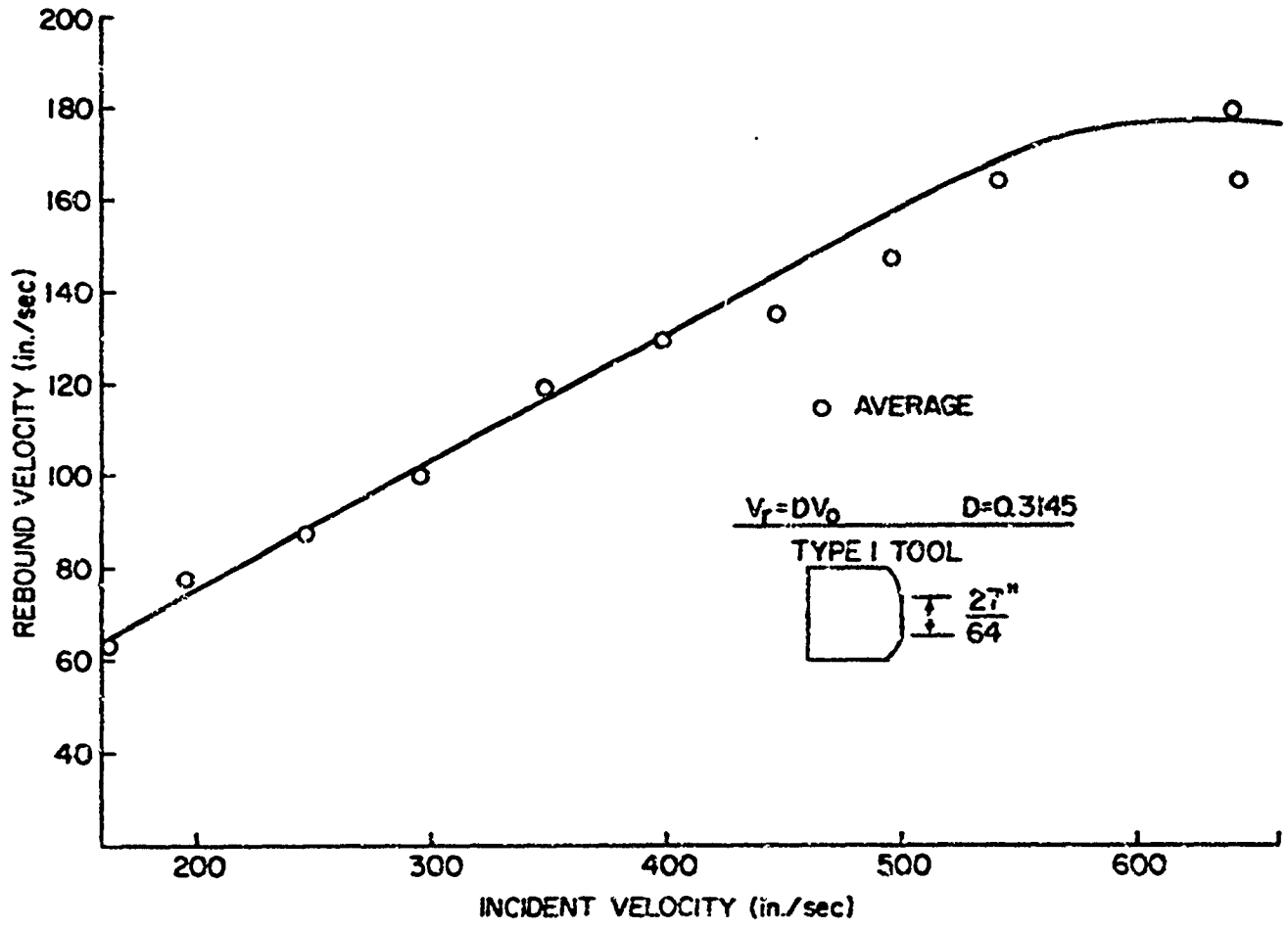

Figure 5-12 - Incident-rebound velocity relationship for Type 1 tool.

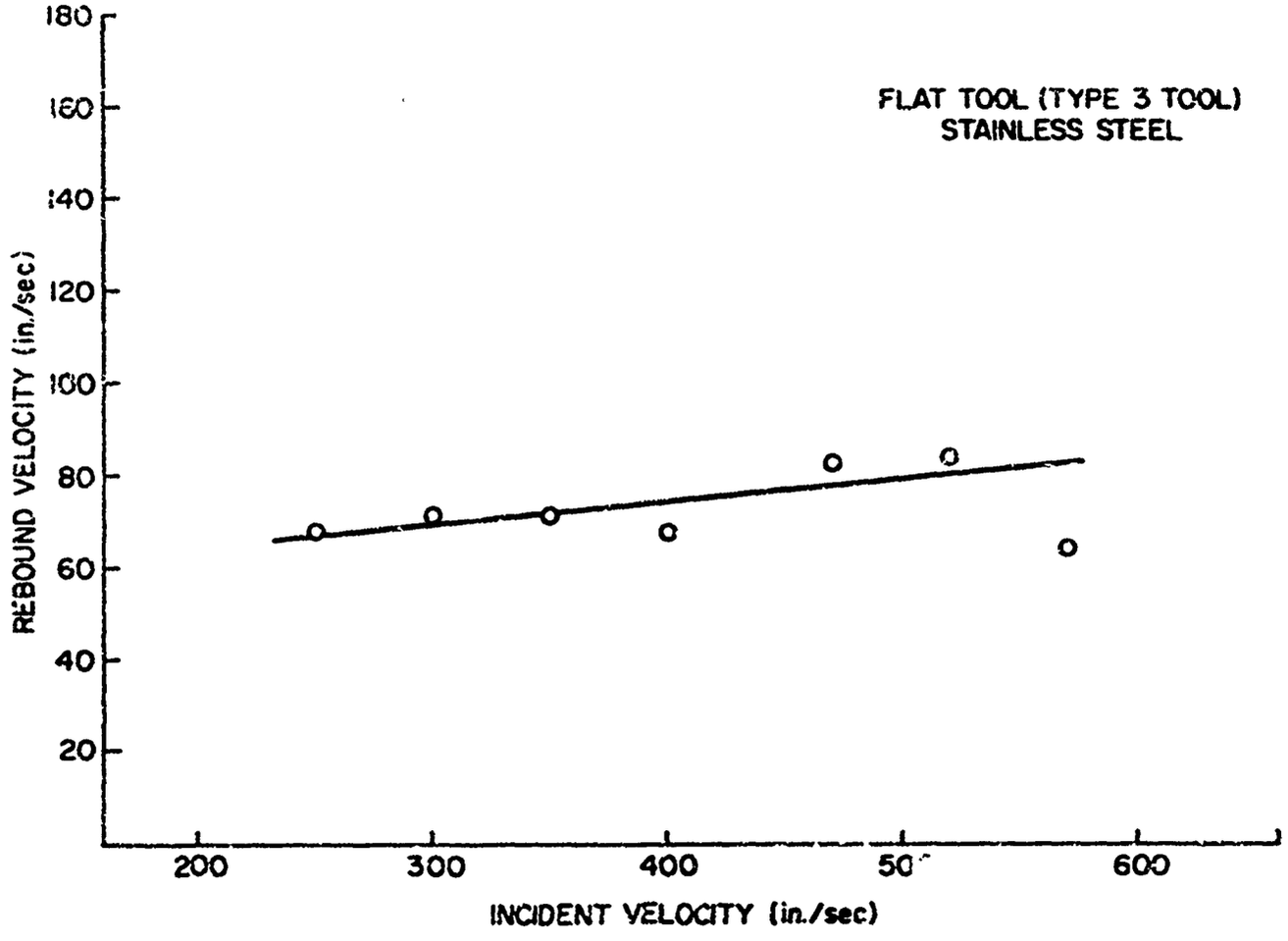

Figure 5-13 - Incident-rebound velocity relationship for Type 3 tool.

3. There is only a single impact between a curved face tool and transmission line, which Type 2, 3, 4 and 5 tools show secondary impact.

4. For the reasons stated in (2) and (3) above and in Section 5-3 (A), the curved tool is the most efficient tool end geometry of the tools tested.

5. A lumped mass at the tip of the transmission line has the effect of reducing the maximum stress wave transmitted into the line during impact.

6. Hardness of the tool has little direct effect on the improvement of rebound velocity. However, tools made of hard material can maintain the curvature of the end, and thus maintain the area of contact during impact.

5-5 REFERENCES

1. B. Hopkinson, "A Method of Measuring the Pressure Produced in the Detonation of High Explosives or by the Impact of Bullets," Phil. Trans. Roy. Soc. Lond. (A). 213, 437, 1914.

2. H. D. McNiven and D. C. Perry "Axially Symmetric Waves in Finite, Elastic Rods," J. Acoust. Soc. Am., 34, April, 1962.

3. L. B. Berthelf, "Numerical Solution for Two-Dimensional Elastic Wave Propagation in Finite Bars," J. Applied Mech., Sept., 1967.

4. S. Timoshenko and J. N. Goodier, Theory of Elasticity, Second Edition, McGraw-Hill.

5. C. C. Feng, "Energy Transfer in Sonic Impact Coupling," M. S. Thesis, The Ohio State University, 1969.

6 A DESCRIPTION OF THE SONIC INTERACTION PROCESS

Impact coupling is used as a means for transferring energy from the vibrating transducer to the load in a number of sonic processes. In this means of coupling, a small metallic mass, or tool, impacts repeatedly between the transducer and the load at rates of hundreds to thousands of cycles per second. Although the process is rapid and somewhat random, it is a continual sequence of two clearly defined events: (1) impact and rebound of the tool against the vibrating line and, (2) impact and rebound of the tool from the load.

The process is a complicated interaction involving a number of parameters of the sonic system. The transducer characteristics, in terms of energy storage level and Q, the transducer drive voltage, the

static force applied to the transducer, the mass and geometry of the tool and the characteristics of the load, all interact in determining the energy transfer characteristics of impact coupling. Thus, variation of one parameter in the process can easily affect several other parameters.

Because impact coupling has found many applications in sonic processes, such as grinding and riveting, as well as rock cutting, a number of studies have been made on various facets of the process. The first work in this regard was by Feng and Graff [1] in 1968. The first stress wave measurements of impact on a vibrating transmission line were reported at that time and the concept of "intercept" conditions between the tool and the line introduced. Graff [2] analyzed the case of intermittent contact between a vibrating transducer and a long rod. While the configuration studied was not the same as the small tool impact coupling arrangement, the role of static force in the impact coupling process was first brought out here. Feng [3], continuing the work reported in [1], performed a detailed analysis of impact coupling for the case of a spherical tool and a load in the form of a long, elastic rod. In this contribution, means for determining the steady-state impact conditions between the transducer tip and load were set forth. From this, power transfer was established. In addition, experimental results on the impact frequency for various gap settings between the transducer and load were found to be in accord with theoretical predictions. This work was also briefly summarized by Feng and Graff [4] and in part, has also been presented in [5].

In a later work, Feng [6] attempted the impact coupling interaction analysis for the case of a long tool, where the load under consideration was rock or concrete. The long tool aspect required that the wave propagation effects within the tool be considered, thus, greatly complicating the problem. Feng [7] also analyzed the problem of spring assisted impact coupling. In this work, a first attempt to assess the effect of an elastic support of the tool was made. Furthermore, first considerations of means for analyzing the impact of tools of irregular shape were made. In both studies just cited, the results were in terms of formal mathematical solutions, with numerical computations of the complex formula remaining to be done.

Libby [8] has obtained estimates of energy transfer to the work surface by impact coupling for metal deformation applications. In a later modification of this work Libby [9] has also brought in the recovery aspects of the transducer to incremental withdrawals of energy. This work was a precusor to some of the consideration in the present report.

Kendall [10] carried out an extensive study on sonic metal deformation. A part of this work was devoted to tool impact on the load. A major portion of the work involved a statistical analysis of the various parameters of the impact coupling process, such as transducer drive voltage, static force, tool mass and time of sonic deformation.

Several studies have been conducted on impact coupling into concrete and rock loads, with the main attention being given to the tool-load stage of the impact coupling sequence. Reference has already been made to the work by Feng [6] for the case of long tool impact into concrete. Mahban [11] conducted extensive studies on stress wave transmission into rock loads. In this work, means for experimentally determining the force-deformation characteristics of the rock for various tool tip configurations were given. This work was further extended by Mahban [12] in studies of the fracture zone in the rock, considerations of optimum pulse shape and incorpation of fracture criteria in the analysis of rock under impact. Lo [13] has analyzed the impact of a short tool on rock and established that a rigid mass model of the tool is accurate for such conditions of impact. More recently, Lo [14] has performed experiments in which sonic tools were propelled into single impact with the rock surface and impact, rebound and energy loss characteristics established.

A number of additional studies have been done on the tool-transducer tip stage of impact coupling. Graff [15] has attempted to extend the considerations used by Feng [3] for the case of a spherical tool to the more realistic case of tools of irregular shape. Discussion of optimum intercept points for tools having short and long impact contact times was also given. Experimental work by Shieh [16] provided information on characteristics of energy transfer to tools for differing geometry of contact between the tool and the line. The results also indicated that the simplifications incorporated into the theoretical developments by Graff [15] were too severe and did not accurately predict contact times between tool and load. Lo [17] has proceeded further in the study of tool impact on the transducer tip. Using a different experimental method than Shieh, Lo directly impacted tools of various geometries on sonic lines. Impact and rebound velocity and the transmitted stress wave was measured. The influence of the local contact geometry was assessed. Finally, Ma [18], as part of an extensive study of the transducer, has measured the transient response of the transducer to impact.

As indicated by the preceding survey, a wide range of studies on various aspects of impact coupling have been carried out. Despite the investigations, much is yet unknown on this means of energy transfer. In particular, the overall interaction problem involving the transducer, tool, load and static force parameters has been given only minimal attention. Thus, with the exception of the previously cited works by Graff [2] and Feng [6], the general interaction problem has received scant attention. The reason for this, of course, is that the important subprocesses of impact coupling, namely, tool-line and tool-load impact, have been under separate studies.

In the following, a qualitative explanation of the general interaction problem is put forth. This discussion, which is rather devoid of mathematics, is intended to show how the various parameters, such as drive voltage, transducer energy storage and Q, static force and tool-load parameters interact in impact coupling energy transfer.

6-1 VIBRATION AND ENERGY STORAGE OF THE TRANSDUCER

The first step in considering the interaction problem will be to review the basic vibration and energy storage characteristics of the sonic transducer. Thus, shown in Figure 6-1 is a schematic diagram of a full wavelength sonic transducer. Shown are the distributions of longitudinal displacement and stress along the body of the device. In particular, the maximum amplitude of vibration will occur at the tip of the horn and will have an amplitude designated as u_o. During sonic vibration, the transducer will act as an energy storage device having time varying amounts of elastic strain energy and kinetic energy.

As reviewed by Graff [19], the calculation of the instantaneous elastic strain energy is given by

$$U(t) = \frac{E}{2}\int_0^L \epsilon^2(x,t)dV \qquad (6\text{-}1.1)$$

where $\epsilon(x,t)$ is the axial strain distribution along the transducer and E is Young's modulus. The average strain energy is then given by

$$\overline{U} = \frac{1}{T}\int_0^T U(t)dt \qquad (6\text{-}1.2)$$

where T is the period of one cycle of vibration. Thus, given the vibration pattern (i.e., mode shape), which is to say $\epsilon(x,t)$, for a transducer, it is possible to compute the average strain energy contained in the device. Another energy expression used in transducer considerations is the maximum strain energy, given by

$$U_M = \frac{E}{2}\int_0^L \epsilon_M^2(x)dV \qquad (6\text{-}1.3)$$

where $\epsilon_M(x)$ represents the mode shape at maximum strain.

It should be noted that the tip vibration amplitude u_o may serve as a direct measure of the stored energy of the transducer. Thus, in rather general terms, it is possible to express the vibration mode of the transducer as

$$u(x,t) = u_o g(x/\lambda, \omega t) \qquad (6\text{-}1.4)$$

where $g(x/\lambda, \omega t)$ is the dimensionless expression for the mode shape, λ is the wavelength parameter and ω is the frequency parameter. Then, in general, $\epsilon(x,t) = \partial u(x,t)/\partial x$ so that strain will have the form

$$\epsilon(x,t) = \frac{u_o}{\lambda}\frac{\partial g}{\partial(x/\lambda)} = \frac{u_o}{\lambda} g' \qquad (6\text{-}1.5)$$

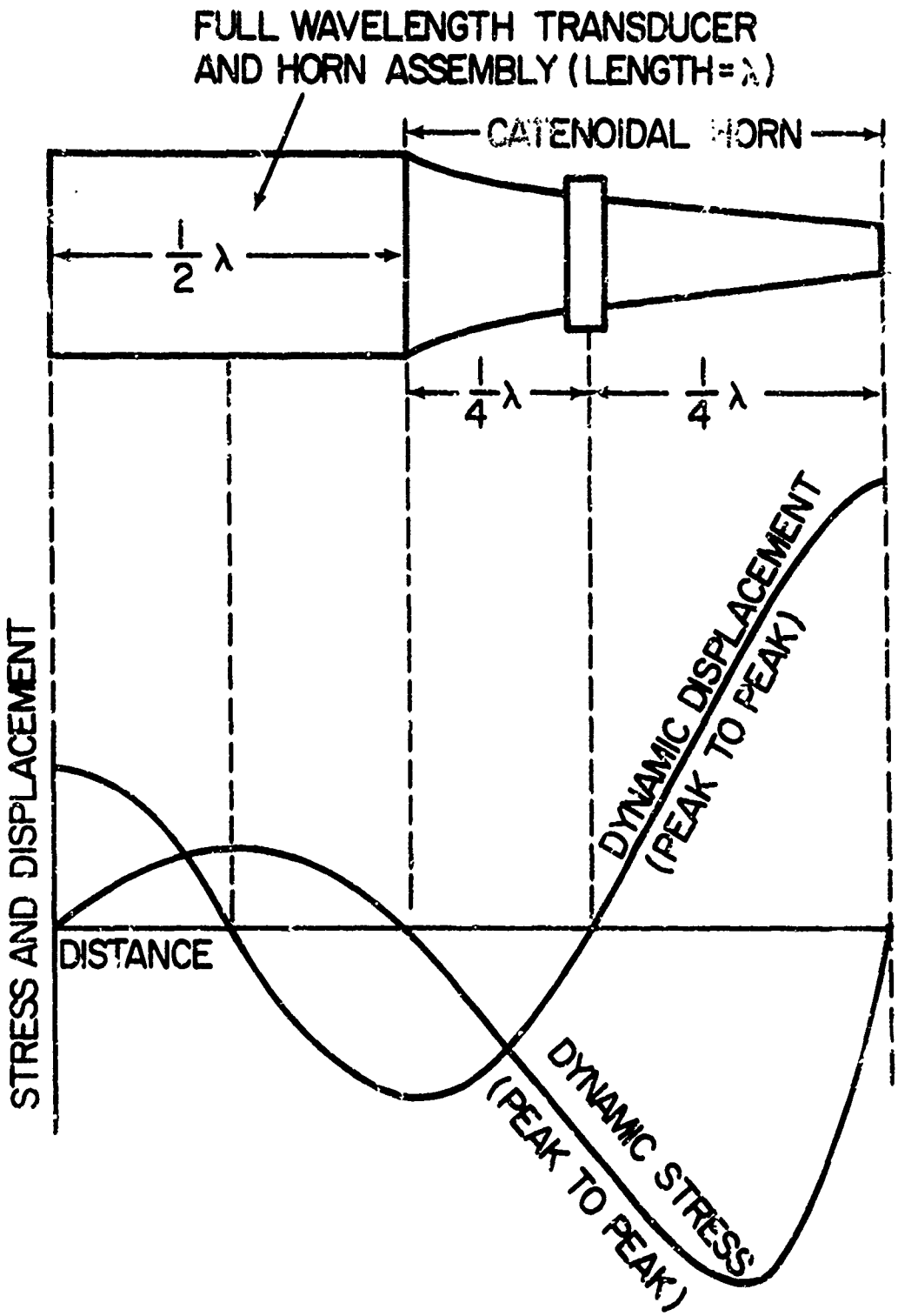

Figure 6-1 - Schematic diagram of a full wavelength transducer showing displacement and stress distribution along the length.

Inspection of expressions (6-1.1), (6-1.2) and (6-1.3) for $U(t)$, $\bar{U}$ and U_M then shows that

$$U(t),\ \bar{U},\ U_M \propto u_o^2 \tag{6-1.6}$$

That is, the elastic strain energy in the transducer varies as the square of the tip displacement.

The next consideration is the Q-factor of the unloaded sonic transducer. This is usually defined as

$$Q = \frac{2\pi U_M}{D} \tag{6-1.7}$$

where U_M is the maximum strain energy in the system and D is the energy dissipation per cycle. Now, the Q-factor is directly related to the time constant of a vibrating system. Thus, we may write for the transducer vibration

$$u(x,t) = u_t + u_s \tag{6-1.8}$$

where u_t is the transient and u_s is the steady-state response of the transducer. For U_t we may write the general form

$$u_t \sim e^{-t/T_c} \sin \omega t \tag{6-1.9}$$

where T_c is the time constant given by

$$T_c = 2Q/\omega \tag{6-1.10}$$

Thus, if any transient is imposed on the sonic transducer, such as a sudden withdrawal or addition of energy, or starting the transducer from rest or shutting down the driving voltage during steady vibration, the time constant will govern this change. Several examples of transient changes are shown in Figure 6-2 in the two curves A and B. Thus, in curve A, the transducer is started from rest with a certain drive voltage, say V_A. The energy builds up to a level U_A in the time period T_c. In curve B, the transducer is started from rest with a lesser drive voltage, say V_B, and driven to the lesser energy level U_B. Although $U_B < U_A$, the time period to reach that level is still T_c. Other transient changes are shown in the two curves. Thus, in A, at a slightly later period, the drive voltage is increased to a yet higher level, V_A' and the energy increases from U_A to U_A' in the time T_c. In curve B, a sudden withdrawal and a sudden addition of energy is shown. In both cases, the system energy either builds up or decays down to the former level U_B in time periods of T_c. Such sudden removals or additions are illustrative of what can occur during impact coupling. Finally,

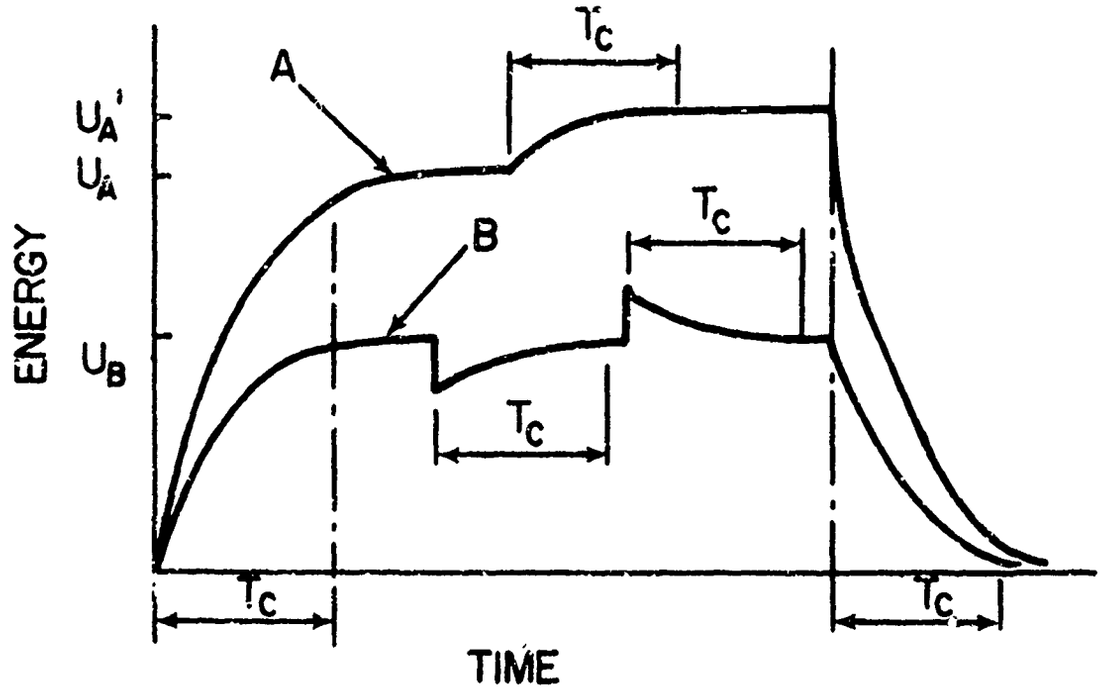

Figure 6-2 - Several examples of transient changes in the energy level of a sonic transducer.

the two curves illustrate the shut down behavior from the respective energy levels of U_A' and U_B'. Again, the time constant T_c governs.

To summarize, several parameters of the transducer have been brought in. They are the energy U, the tip displacement u_o, the Q-factor, the time constant T_c and the driving voltage V. In our further discussion, we will presume that a given voltage V will drive a transducer to a given energy level U and tip displacement u_o. It may thus be considered the independent variable of the system. Further, the transducer will have associated with it a given time constant T_c.

6-2 BASIC ASPECTS OF TOOL IMPACT ON THE TRANSDUCER

When a sonic tool impacts the vibrating transducer tip during impact coupling, the whole process is rather complex. The vibration level of the tip, the local geometry and material of the tip, the mass, geometry and velocity of the tool and location on the tip vibration trajectory at which impact occurs all influence the subsequent rebound of the tool. As previously mentioned, many facets of this complicated impact process have been previously analyzed, but complete understanding of all phases is still lacking. However, from the standpoint of the

present discussion of the overall interaction problem, detailed knowledge of the impact process is not required. Instead, only certain very general characteristics on the energy withdrawal (or addition) and force generated per impact are required.

The first fact to realize is that the duration of impact of the sonic tool is rather short, on the order of 30 μsec. This corresponds to about one-third of a cycle of sonic vibration. The second fact is that the recovery time of a sonic transducer is on the order of 10 milliseconds, or about 100 cycles of vibration. So, the time of impact is quite small relative to the recovery time. This enables the energy withdrawal or addition per impact to be considered as instantaneous from the standpoint of the recovery of the transducer to the impact. Thus, in curve B of the previous Figure 6-2, the examples of sudden energy withdrawal or addition can be considered the transient response to tool impacts.

A second consequence of the short impact duration is that the impact force may be approximated as an impulse or Dirac delta function in time from the standpoint of the gross motion of the transducer. To bring this aspect out, consider M as shown in Figure 6-3 (a). The transducer is acted upon by a static force F_s and a time varying force at the tip of the transducer, f(t). This latter force will in actuality be the sequence of impact forces from the tool. In Figure 6-3 (b), an idealized version of the sequence of force pulses acting on the transducer is shown. In actuality, the pulses would be of various amplitudes and intervals but, thinking in terms of averages it is justifiable to consider equal amplitudes and spacings. Also shown in the figure is the constant value of the static force, F_s. Again, the point is that the time between impacts and the duration of the individual impacts will be quite different. For impacts occurring at, say, 1000 impacts per second, the time between impacts would be 10^{-3} seconds (1 millisec). The impact duration is about 30 μsec or 0.03×10^{-3} seconds. Hence, it appears justifiable to represent f(t) by a sequence of Dirac delta functions. Thus,

$$f(t) = I \sum_{n=1}^{\infty} \delta(t - t_n) \qquad (6\text{-}2.1)$$

where I is the total impulse for a given impact and t_n is the time of the nth impact and is given by

$$t_n = nT_i \qquad (6\text{-}2.2)$$

where T is the time interval between impacts.

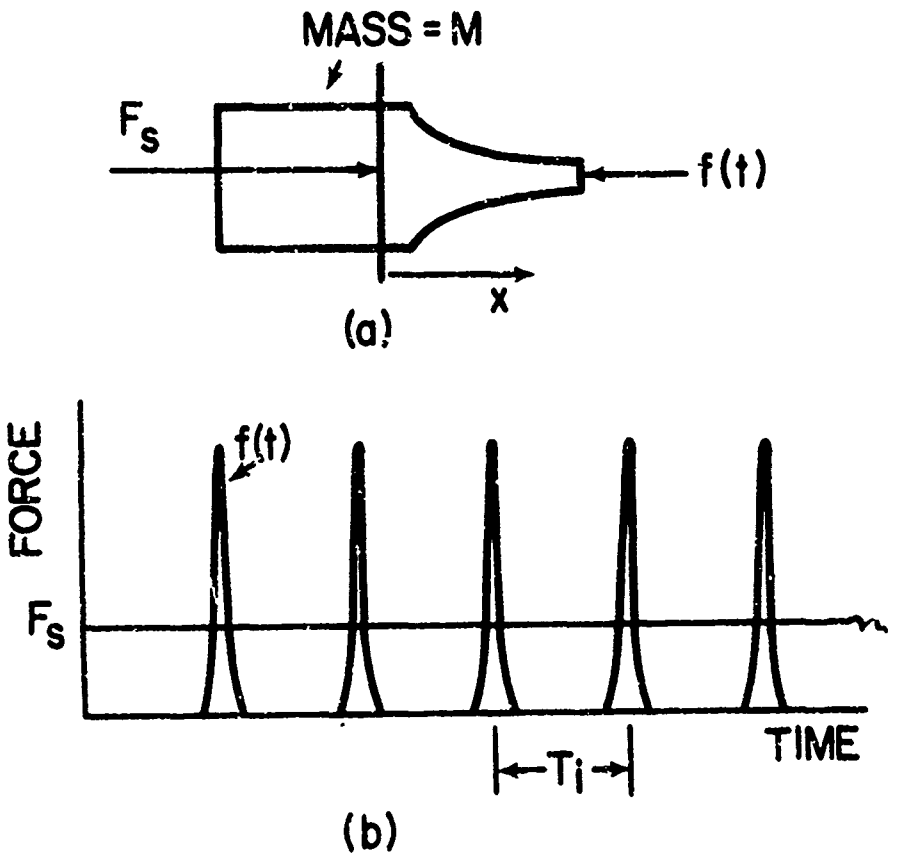

Figure 6-3 - (a) Transducer acted upon by the static force F_s and the impact force f(t). (b) Time distribution of the forces in the transducer.

It becomes rather easy to write the expression for the rigid body or gross motion of the transducer as

$$M\ddot{x} = F_s - f(t) = F_s - I \sum_{n=1}^{\infty} \delta(t - t_n) \qquad (6\text{-}2.3)$$

Integrating this gives

$$M(\dot{x} - \dot{x}_0) = F_s t - I \sum_{n=1}^{\infty} H(t - t_n) \qquad (6\text{-}2.4)$$

where $H(t - t_n)$ is the Heaviside function. Now, the velocity predicted by (6-2.4) has a sawtooth form, as shown in Figure 6-4. Thus, the constant force F_s causes a linear increase in velocity, but this is periodically offset by sudden velocity decreases due to the impact impulses.

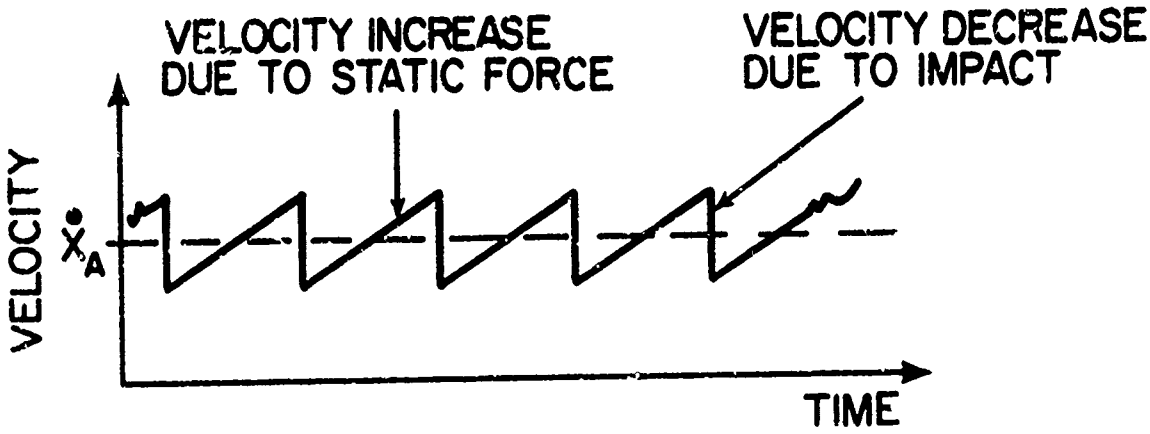

Figure 6-4 - Rigid body motion (velocity) of a sonic transducer acted upon by static force and impact.

If the proper balance holds between the static force and the impulse magnitude I and impulse intervals T_i, the resulting average velocity $\dot{x}_A$ will be constant. This is the condition shown in the just cited figure. The condition for proper balance is that

$$F_s T_i = I \tag{6-2.5}$$

This is merely a statement of impulse balance, so that the average net change in momentum of the transducer is zero.

These considerations clearly bring out the role of the static force in sonic processes. The force merely acts as an impulse balance on the transducer, counteracting the high amplitude, short duration forces from the tool impacts. Thus, the static force does no direct work on the load, in contrast to the role of static force in many deformation processes.

Continuing slightly further, it is of interest to consider some possible effects of changing the static force. As has been previously mentioned, the various parameters of the sonic system interact, so that in general it is not possible to change one parameter, such as static force, without modifying other parameters. Nevertheless, it is still possible to draw some limited information from single parameter variations. Thus, for the case of static force, it is seen from (6-2.5) that if F_s is increased to F_s', then either the time between impacts, T_i, must decrease or that the strength per impact, I, must increase. However, the impact strength will be largely determined by the energy level of the transducer and the tool characteristics. If these are

not changed, it is reasonable to assume that I remains constant. Then we may write

$$F_s T_i = I = F_s' T_i' \tag{6-2.6}$$

where $T_i' < T_i$ if $F_s' > F_s$.

Now, the time interval between impacts is made up of four time periods. Using Figure 6-5 as a reference, we have that

$$T_i = T_T + \Delta/V_I + T_L + \Delta/V_R \tag{6-2.7}$$

where T_T, T_L are, respectively the times of contact of the tool with the transducer and with the load. The velocities V_I and V_R are the velocities of impact with the load (V_I) and velocity of rebound from the load and subsequent impact with the transducer (V_T). The distance Δ represents the net gap between the transducer and the load; i.e., it is the distance between transducer and load minus the tool thickness. Writing (6-2.7) as

$$T_i = \Delta\left(\frac{1}{V_I} + \frac{1}{V_R}\right) + (T_T + T_L) \tag{6-2.8}$$

it is quite evident that if the time interval T_i is to become smaller due to an increase of static force, it is the gap Δ that must decrease. For a given strength of impact, the velocities V_I, V_R would remain the same as would the contact times T_T, T_L. This simple computation shows how, within certain restrictions on the constancy of the impulse I, that a variation of one parameter, F_s, causes variation in another parameter T_i.

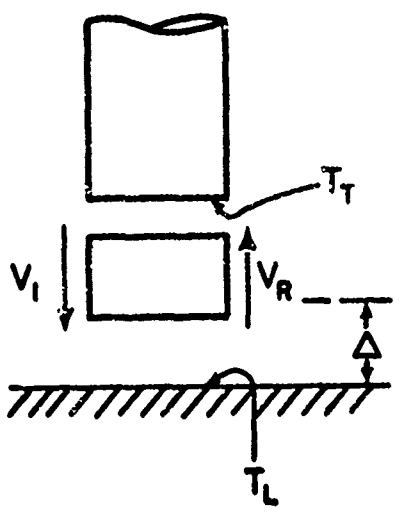

Figure 6-5 - Velocities of the impact tool in the transducer-load gap

6-3 TOOL-LOAD IMPACT AND THE STEADY STATE

Impact coupling is a two-stage process, with tool impact and rebound from the load being one of the stages. Whereas the stage of tool impact and rebound from the transducer may be considered as common to many sonic processes, the stage of tool impact with the load will differ for each application, since the load will be different. It is thus not possible to make general statements on tool-load impact other than to say that for a given impact velocity V_I, there will be a certain time of contact of the tool with the load, T_L and a subsequent rebound of the tool with velocity V_R. In general, $V_R < V_I$, so that a net loss of energy in the form of work done on the load will have occurred.

In fact, the lack of certainty on the tool-load impact conditions does not hinder further discussion of the sonic interaction problem, at least not at the present qualitative level. It is mainly necessary to realize that for a given load and a given sonic tool configuration, there will exist a relationship between the impact and rebound velocity, $V_R = f(V_I)$, that will be characteristic of that particular process. For a given case, it should be possible to establish the form of this relationship by theoretical or experimental means or a combination of both.

The main assumption required for further discussion is that in impact coupling energy transfer, that a steady state may be attained. By this is meant that for a given set of conditions (drive voltage, transducer energy level, tool, static force and load), an approximately constant bounce frequency of the tool in the gap is attained. There are, in fact, many good reasons to believe this is an excellent assumption. The analysis and experiments by Feng [3] showed, for a specific load, that such conditions resulted. This work followed earlier experimental observations in sonic riveting that a steady bouncing action was present. Referring again to Figure 6-5, what this means is that under steady state conditions, V_I and V_R remain approximately constant. Thus, the tool will strike the load with a velocity V_I, rebound from the load and strike the transducer with the velocity V_R and then again rebound from the transducer with the increased velocity V_I, with the process continuing to repeat this sequence.

6-4 INTERACTION OF VARIOUS PARAMETERS IN IMPACT COUPLING

The main parameters of a sonic impact coupling process have been mentioned previously. To recall, they are the voltage, energy level and tip displacement of the transducer, the static force on the transducer, the tool and the load. The first three parameters, voltage, energy and displacement are, in fact, directly related. In the following, we will be mainly interested in how the parameters of voltage, energy level and static force can interact in impact coupling. While the tool and the load characteristics will not be specified, it will be presumed that they will be invariant. Initially, only the simplest situation in terms of parameter variation will be considered, with more complex situations being introduced later.

(A) Limited Variations in Static Force

As the first and simplest case, assume a transducer is being driven at a voltage V_o with a resulting energy level U_o in the transducer. Let the static force be F_o. For these conditions, let there exist a steady-state impact action such that the time interval between impacts is T_o and the energy removed from the transducer per impact is ΔU_o. Finally, let the time constant for the transducer be T_c. The situation is summarized in Figure 6-6 (a).

Consider, now, that the static force is slightly increased to F_1 in one case, and decreased to F_2 in another case so that $F_1 > F_o > F_2$. As long as the variations are not too great, the only result of these changes will be to decrease or increase the time interval between impacts. Thus, for the case of increased force F_1, the time interval will decrease to T_1, while for the decreased force F_2, the time interval will increase to T_2, where $T_1 < T_o < T_2$. The resulting sequence of impacts for the two cases are shown in Figure 6-6 (b) and (c). Of course the time constant for the transducer remains the same, T_c. Further, the energy removal per blow, ΔU_o, remains the same.

At this point, what is meant by a "limited" increase of static force can be made clear. For a static force of F_o, the time interval between impacts was greater than the system time constant ($T_o > T_c$) so that the transducer has ample time to restore the energy loss ΔU_o between impacts. For increasing static force, the time interval between blows will decrease until it equals the system time constant. Thus, $T_1 \rightarrow T_c$, which is meant to be the situation illustrated in Figure 6-6 (b). Any further increase in static force, and thus further decrease of T_1 (so that $T_1 < T_c$) will result in impact before the transducer has fully restored itself to the original energy level U_o. This will complicate the interaction situation, since the energy removal per impact will be modified. Hence, this situation ($T_1 < T_c$) will be considered separately in the next section.

Finally, only brief remarks need be addressed to the case of decreasing static force, since this is of little practical interest. A transducer being operated in this situation, shown in Figure 6-6 (c), is merely being used quite inefficiently.

(B) Further Increase of Static Force

We now consider the situation where the static force has been increased to the extent that impacts are occurring before the transducer has completely restored to the original energy level U_o. The first thing to realize for this situation is that if the transducer has only recovered to an energy level U_o' before the next impact, where $U_o' < U_o$, then the energy removed by that next impact, $\Delta U_o'$, will be less than ΔU_o. The question is, how much less?

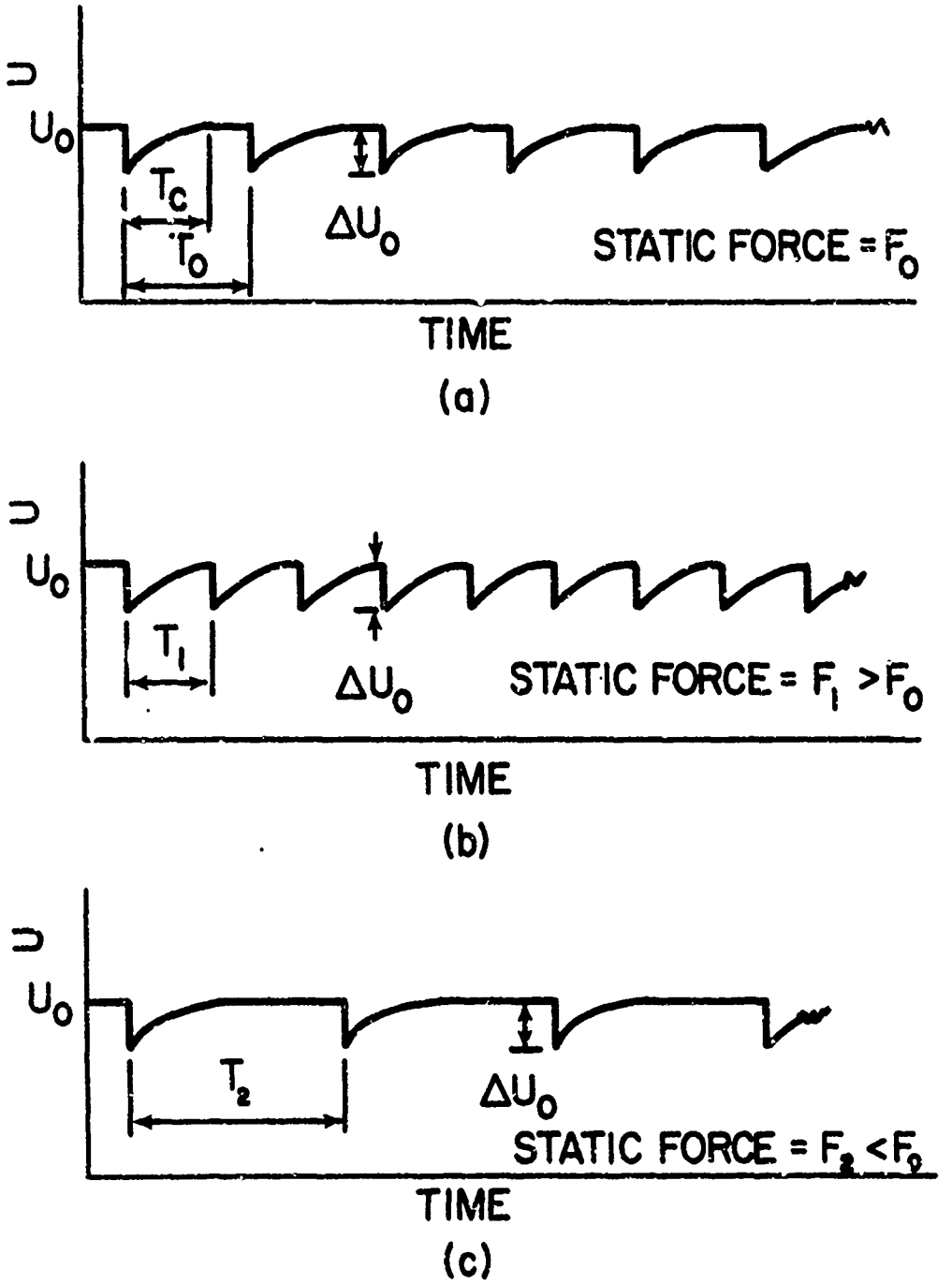

Figure 6-6 - Variations in impact rate due to variations in static force level.

The question of how much energy is removed from the transducer per impact has associated with it all the details of a given transducer tip, tool and load configuration. Lacking specific information on this, what will be done here is to assume that a constant percentage of the energy is removed per impact. For simplicity of discussion, the percentage figure will be somewhat arbitrarily selected as 20%. This means that for a given impact, 20% of the energy stored at the instant of impact will be removed by that impact.

To illustrate what can occur for various impact conditions, consider Figure 6-7 (a). This shows the case of an original energy level of U_o, with an impact then removing 20% of the energy, thus dropping the energy level to 0.8 U_o. Then various situations of recovery and subsequent impact are shown in the figure and tabulated below the figure. Thus, in case (b), the transducer has recovered to an energy level of 0.97 U_o when the second impact occurs. A 20% energy withdrawal from 0.97 U_o drops the energy to 0.78 U_o, where recovery then occurs to the level U_o in the time T_c.

With these preliminary considerations, it now becomes possible to proceed directly to the construction of various steady state sequences of impacts where, for a given sequence, the impact or energy removal always occurs at some given level of the original energy U_o. This is possibly best done by directly presenting such sequences and then following with an explanation.

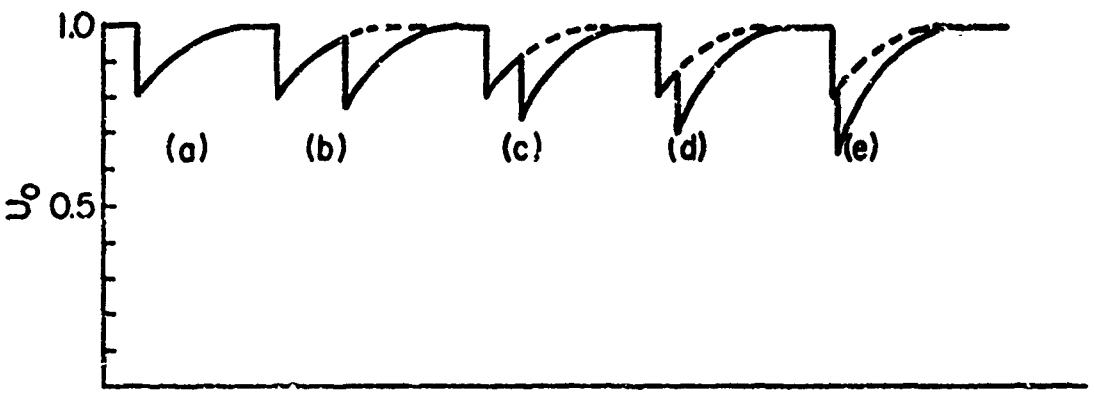

(a) Full recovery before next impact
(b) Next impact at 0.97 U_o; energy drops to 0.78 U_o
(c) Next impact at 0.92 U_o; energy drops to 0.74 U_o
(d) Next impact at 0.87 U_o; energy drops to 0.70 U_o
(e) Next impact at 0.81 U_o; energy drops to 0.65 U_o

Figure 6-7 - Impact and energy removal from a transducer at various stages of recovery from a previous impact.

Five steady state impact situations, (a) through (e), are shown in Figure 6-8. In (a), the simplest case of impacts occurring exactly at T_c is shown. This has been previously covered, but to review, the original energy level is U_o. An impact reduces the energy by 20%, to a level of 0.8 U_o from which recovery to U_o occurs in T_c. So, the maximum energy in the system is U_o, the minimum energy is 0.8 U_o and the average energy is about 0.92 U_o.

In the remaining situations (b) through (e), impacts occurring at maximum energy levels less than U_o are shown. To illustrate, consider (b). The maximum level that is attained before an impact is 0.95 U_o. At impact, a 20% withdrawal reduces the energy level to a minimum of 0.76 U_o, from which recovery begins. The time required to reach the previous level of 0.95 U_o is 0.5 T_c, as shown in the figure. At this point, impact again occurs, 20% of the energy is removed to a level of 0.76 U_o and the process repeats. Thus, for the case (b), maximum energy is 0.95 U_o, minimum is 0.76 U_o and the average energy is about 0.87 U_o.

In cases (c) through (e), this sequence of considerations is merely repeated. The differentiating factor for the various cases is that the energy level at which impact occurs is continually decreased. Thus, in (c) it is 0.9 U_o, in (d) it is 0.8 U_o and in (e), it is 0.7 U_o. In each succeeding case, the minimum energy and average energies are correspondingly lower and the impact times are correspondingly shorter. These various factors are summarized below the figure.

Now, the parameter that has been somewhat lost from the immediately preceeding discussion is the static force. The original consideration was to determine the steady state sequence corresponding to a given static force. We have, in fact, reversed the question and are now able to establish what static force corresponds to a given steady state sequence. This is done as follows: The impulse delivered to the transducer for an impact at a given energy level is I. If the energy level is U_o, the impulse is I_o; if the energy level is U_1, the impulse is I_1. If $U_1 < U_o$, then $I_1 < I_o$. The net effect is that the static force consistent with a given impact interval and impulse level will still be given by the basic expression (6-2.5); that is, $F_s T_i = I$.

It should be noted that we have about reached the limit of interpretation on the effects of a static force variation. Thus, suppose we know for the energy level U_o, that the impulse is I_o. The time interval for the energy to rebuild to I_o is T_o, so the necessary static force is $F_o = I_o/T_o$. If the static force is then increased to F_1, we must then find the set of conditions so that $F_1 = I_1/T_1$. What particular energy level U_1 that will yield this balance can only be found by analysis and experiment for the specific impact configuration, and cannot be established through the simple, qualitative considerations used in the present work. Thus, for example, it would not be known which of cases (b) through (e) of Figure 6-8 would yield this consistent set of conditions.

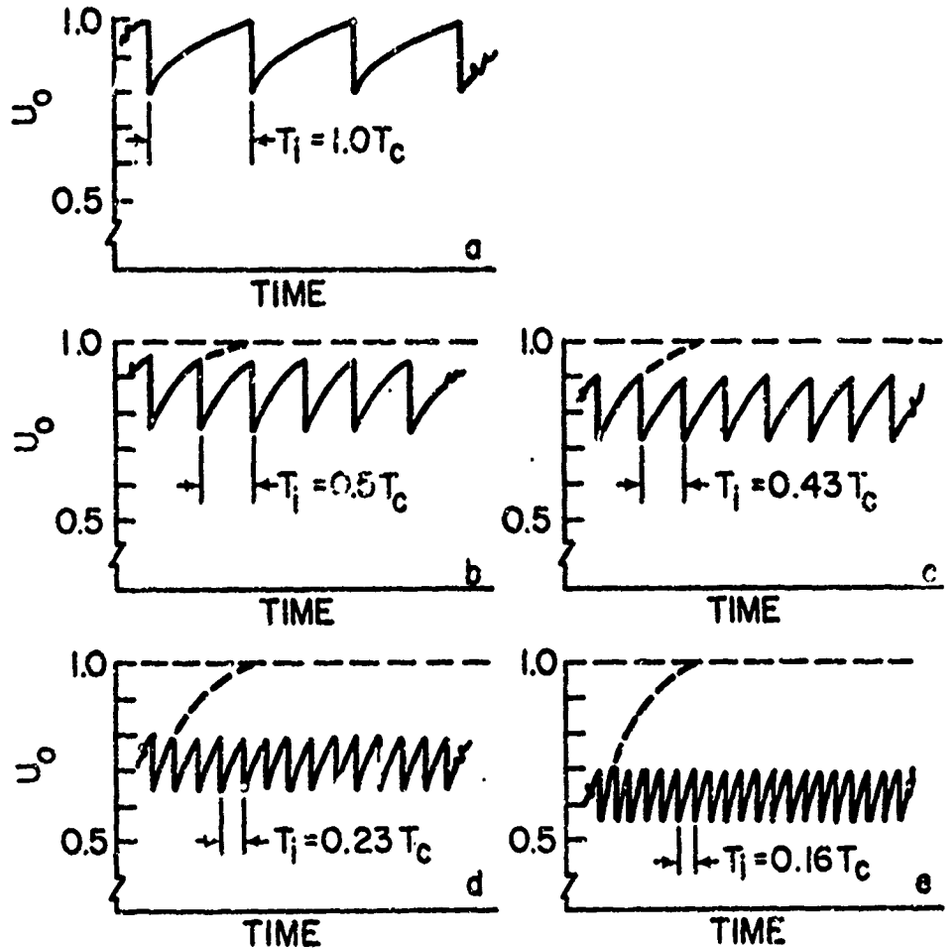

Case	Max. Energy	Min. Energy	Aver. Energy	T_i
(a)	U_o	0.8 U_o	0.92 U_o	1.0 T_c
(b)	0.95 U_o	0.76 U_o	0.87 U_o	0.5 T_c
(c)	0.9 U_o	0.72 U_o	0.82 U_o	0.43 T_c
(d)	0.8 U_o	0.64 U_o	0.73 U_o	0.23 T_c
(e)	0.7 U_o	0.56 U_o	0.63 U_o	0.16 T_c

Figure 6-8 - Sequences of steady-state impact at various energy levels.

(C) Effect of Voltage Variation

With the considerations that have been set forth in the preceeding section on the interrelationship of initial energy level, static force and impact times, it becomes a fairly simple matter to establish the effect of varying the voltage parameter.

As a first consideration here, suppose a system is operating at a voltage V_o, energy U_o and at a static force such that $F_oT_o = I_o$, where T_o is the same as the system time constant T_c. A situation such as this has already been depicted in Figure 6-8 (a). Again, I_o is the impulse per impact at the energy level U_o. Now let the voltage and, hence the energy, be increased to V_1 and U_1 respectively. At this increased energy level, the impulse per blow I_1 would be increased over the previous level. In the new force-impulse relationship, $F_1T_1 = I_1$, we see that either the time between impacts T_1 would have to increase or the static force would have to be increased over the previous level F_o. These various aspects are shown in Figure 6-9 (a) and (b). Thus, in (a), voltage increase without static force increase is shown, with the necessary lengthening of the time between impacts. In (b), a static force increase enables the rate of impact to be maintained constant. In both cases, there will be some transient period of behavior after the voltage is increased from V_o to V_1. No effort is made to depict the details of this.

We now wish to consider a more practical aspect of voltage increase. Now, suppose that the maximum average energy level that a given transducer can operate at is U_o. This level may be a limit established because of fatigue considerations, temperature rise considerations or some other criteria. Suppose, then, with a drive voltage V_o, the transducer is operating under impact at a maximum level of U_o, again as previously shown by Figure 6-8 (a). In fact, when the transducer is driven at voltage V_o, the maximum energy is indeed U_o but the average energy is less than U_o. Thus, while the voltage and maximum energy levels V_o, U_o are acceptable for no load conditions under impact load, the transducer is operating below capacity.

In order to bring the average energy level back to U_o, the transducer must be overdriven. That is, it must be driven at a voltage that, under no load conditions, might quickly result in transducer failure. The question is, what overdrive voltage should be applied? The answer to this is that any number of voltages may be applied, as long as the static force is also varied to keep in balance the impulse relation $F_sT_i = I$. Figure 6-10 shows several possibilities. In each case, the average energy remains at U_o.

Thus, in Figure 6-10 (a), an overdrive voltage is applied that corresponds to an energy level 1.07 U_o. The static force that is applied is such that the time interval between impacts is exactly equal to the time constant T_c. Since sufficient time is allowed for complete

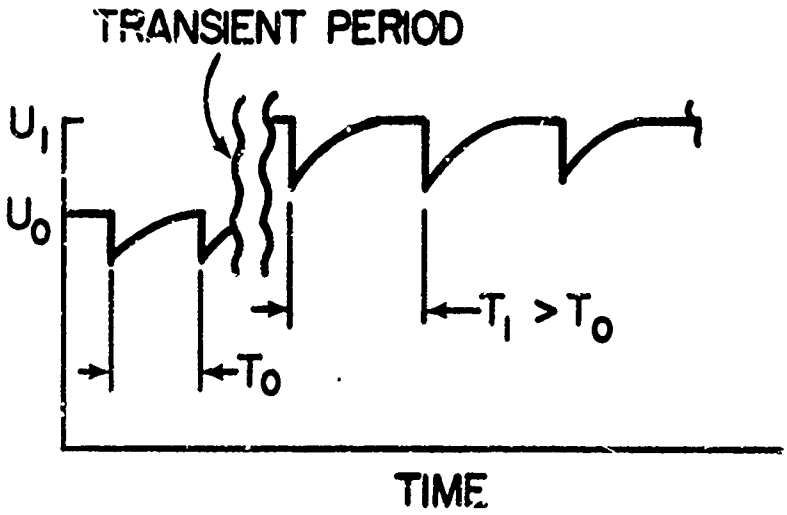

(a) Voltage increase $V_0 \rightarrow V_1$;
static force remains constant

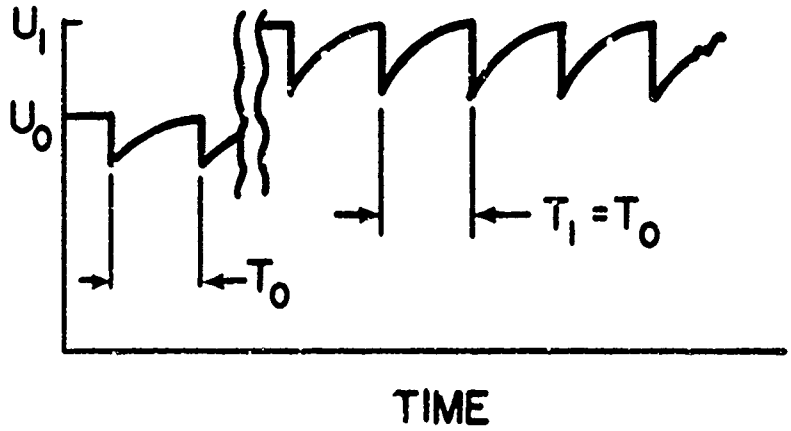

(b) Voltage increase $V_0 \rightarrow V_1$;
static force increased

Figure 6-9 - Influence on impact rate of a voltage increase (a) without and (b) with increases of static force.

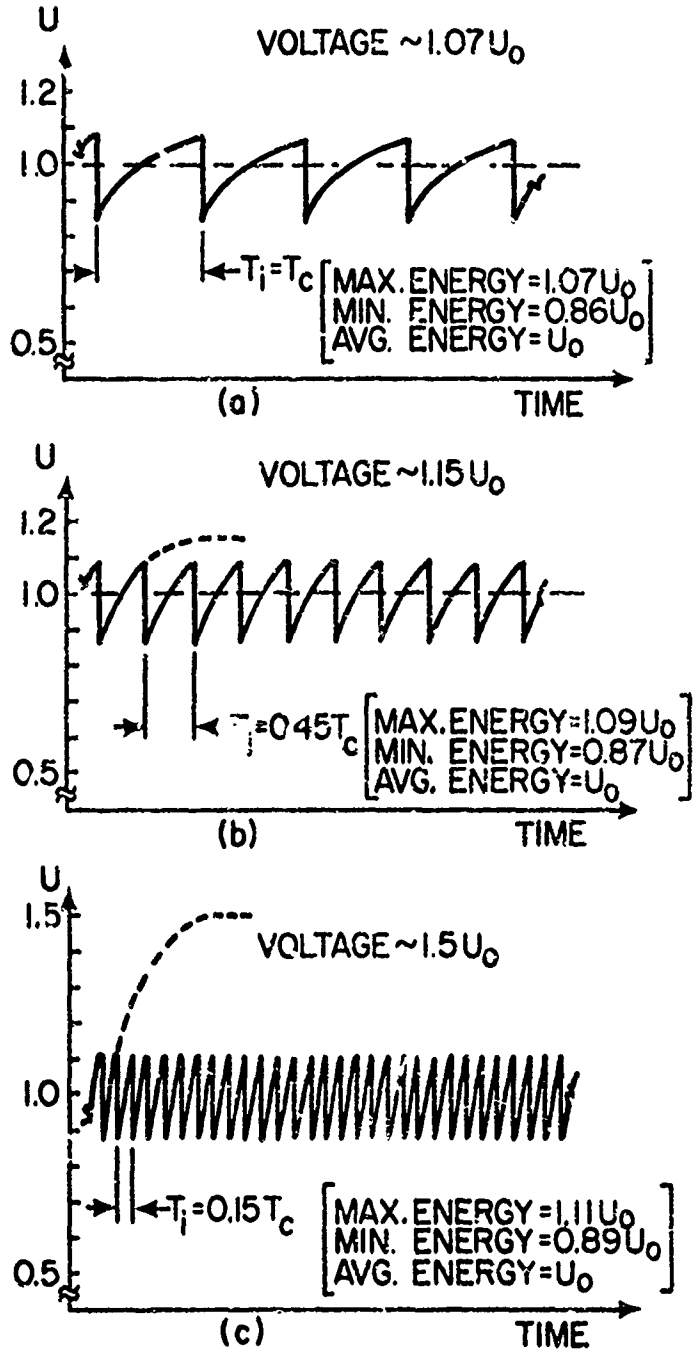

Figure 6-10 - Influence of various voltage overdrive conditions on the rate of impact.

recovery of the transducer, it builds up to the level of 1.07 U_o before each impact. With a 20% energy withdrawal, the level drops to 0.86 U_o; the average energy is at the limit capacity of U_o.

Different situations are shown in (b) and (c). Thus, in (b), an overdrive voltage consistent with an energy level of 1.15 U_o is applied. However, a static force is applied such that the maximum energy level never exceeds 1.09 U_o. A 20% removal at that level gives a minimum energy of 0.87 U_o with, again, an average energy level of U_o. The time interval between impacts is 0.45 T_c. In (c), an even more extreme case of overdrive is shown. The energy level consistent with the applied voltage is 1.5 U_o. However, by greatly increasing the static force, the rate of the impacts are greatly increased and the time interval between impact decreased to 0.15 T_c. At this rate, the maximum energy attained is 1.11 U_o. The minimum energy level is 0.89 U_o and the average is again U_o.

The basic result of using voltage overdrive is to enable a transducer to operate at an average energy level consistent with its no load capacity and, by also increasing static force, to greatly increase the rate of impacts.

6-5 SUMMARY

The objective of this work was to present a qualitative description of how the parameters of voltage, energy, static force and the system time constant interact in the impact coupling means of sonic energy transfer. In doing this, basic aspects of vibration and energy storage in the transducer were first reviewed, followed by review of basic aspects of tool impact on the transducer and the load and the concept of steady state.

There were two basic ways of considering the sonic interaction problem. In one way, the sonic parameter of voltage was considered to be held constant, and the static force increased. The result of such a force increase was to increase the rate of impact, but, also to reduce the average energy level in the transducer. In a second way, the voltage was increased so that the transducer was "overdriven." In this way, by applying various levels of static force, it was possible to increase the rate of impact to various levels, yet always maintaining an acceptable average stored energy.

At this point, the objective of a qualitative description of the interaction process in impact coupling has been accomplished. What is required in future work in this area is to make quantitative descriptions of specific processes. Thus, the no-load energy storage capacity of the actual transducers must be established, as well as the system time constants. The actual percentage of energy removal per impact for a given tool-transducer tip configuration must be established. Acceptable overdrive voltage levels must be found. These and other specific questions must be answered for given sonic processes.

6-6 REFERENCES

1. Feng, C. C. and Graff, K. F., "Impact on a Sonic Transmission Line," Engineering Experiment Station Report 220-Q3-68, see also Final Report on "Development of Sonic and Ultrasonic Power Devices for Application in Highway Engineering," Final Report, EES 220, Vol. 2, Chap. 22, 1970.

2. Graff, K. F., "Analysis of Intermittent Contact," Engineering Experiment Station Report 220-Q3-69, 1969. Also Vol. 2, Chap. 24 of EES 220 Final Report (see ref. 1).

3. Feng, C. C., "Energy Transfer in Sonic Impact Coupling," M.S. Thesis, The Ohio State University, 1969.

4. Feng, C. C. and Graff, K. F., "Impact Coupling: A Summary of Recent Investigations," Engineering Experiment Station Report 220-Q3-69, 1969. Also Vol. 2, Chap. 23 EES 220 Final Report (see ref. 1).

5. Feng, C. C. and Graff, K. F., "Impact of a Spherical Tool Against a Sonic Transmission Line," to appear in J. Accust. Soc. Amer.

6. Graff, K. F., Feng, C. C. and Kendall, L. A. "Mathematical Model of a Working Tool Excited by an Ultrasonic Transducer," Final Report on Engineering Experiment Station Project EES 291, 1970.

7. Feng, C. C., "Analysis of Spring-Assisted Impact Coupling," Final Report on Engineering Experiment Station Project WE 17, 1970.

8. Libby, C. C., "Estimates of Energy Transferred Incrementally to Metallic Work Surfaces Using a High-Power Sonic Transducer," Engineering Experiment Station Report 220-Q1-70, 1970. Also, Vol. 2, Chap. 25 of EES 220 Final Report (see ref. 1).

9. Libby, C. C., "Modifications of Paper, 'Estimates of Energy Transferred Incrementally to Metallic Work Surfaces Using a High Power Sonic Transducer'," Internal memorandum, 1971.

10. Kendall, L. A., "Sonic Impact Metal Deformation," Final Report on Engineering Experiment Station Project EES 320, 1970.

11. Mahban, H., "Stress Wave Transmission into Rock," Engineering Experiment Station Report 220-Q3-69, 1969. Also, Vol. 2, Chap. 27, EES 220 Final Report (see ref. 1).

12. Mahban, H., "Rock Behavior Under Impulsive Loading," Ph.D. Dissertation, The Ohio State University, 1970.

13. Lo, T. Y., "Analysis of Sonic Tool Impact on Rock," Semi-Annual Technical Report on the Project Sonic Rock Cutting, sponsored by Advanced Research Projects Agency through Bureau of Mines Contract HO-210010, June, 1971. See also Part II, Section 1 of this report.

14. Lo, T. Y., "Tool Impact on a Transmission Line," Part II, Section 4 of this report.

15. Graff, K. F. "Tool Impact on a Transmission Line," Chap. 3 of final report on Engineering Experiment Station Project EES 380, "Feasibility of Sonic Rock Crushing," 1971.

16. Shieh, L. C., "Energy Transfer into Sonic Impact Tools," Chap. 4 of EE 380 final report (see ref. 15).

17. Lo, T. Y., "Tool Impact on Rock," Part II, Section 5 of this report.

18. Ma, N. T., "Vibrational Characteristics of a Sonic Transducer," Part II, Section 3 of this report.

19. Graff, K. F., "Analysis of Stepped Horn Resonators," Engineering Experiment Station report 220-Q3-69, 1969. Also, Vol. 2, Chap. 3 of EES 220 Final Report (see ref. 1).